

https://dspace.org/

Weak shock wave reflections due to transverse waves in a conventional shock tube

Cachucho, André Rodrigues

2012-02-01
http://hdl.handle.net/10539/11234

Downloaded from a DSpace repository. https://dspace.org/

Weak shock wave reflections due to transverse waves in a conventional shock tube

André Rodrigues Cachucho

Faculty of Engineering and the Built Environment
School of Mechanical, Industrial and Aeronautical Engineering
University of the Witwatersrand

A project report submitted to the Faculty of Engineering and the Built Environment, University of the Witwatersrand, Johannesburg, in partial fullment of the requirements for the degree of Master of Science in Engineering.

· 2011 ·

Declaration

I declare that this report is my own, unaided work, except where otherwise acknowledged. It is being submitted for the degree of Master of Science in Engineering in the University of the Witwatersrand, Johannesburg. It has not been submitted before for any degree or examination at any other university.

Signed this ___ day of _____ 20___

_____

.

Abstract

Previous experimental work, utilising a unique large scale shock tube, shows that the four-wave shock reflection pattern, known as the Guderley reflection exists for Mach numbers below 1.10 on wedge angles of 10° and 15°. The current study proves for the first time that these rare reflections can be produced in a conventional shock tube for Mach numbers ranging from 1.10 to 1.40 and for various disturbances in the flow. Two shock tube configurations were tested, the first consisted of a perturbation source on the floor of the tube, and the second utilised a variable diverging section (10°, 15°, and 20°). A new principle was applied where the developed Mach reflection undergoes successive reflections off the upper and lower walls of a tube to produce the desired reflection. The high resolution images captured using a sensitive schlieren system showed evidence of the fourth wave, namely the expansion fan, for the majority of the results for both shock tube configurations. A shocklet terminating the supersonic patch behind the reflected wave was interestingly only observed for Mach numbers of approximately 1.20. The wave structures were similar to those observed in previous experimental work, except no evidence of the second shocklet nor the multi-patch geometry was found. Multi-exposure images of the propagating shock superimposed on a single image frame analysed with oblique shock equations estimated the velocities near the triple point. It was shown that the reflected wave is very weak, and that the flow behind the Mach stem is supersonic confirming the shock reflections to be indeed Guderley reflections.

Dream as if you'll live forever, live as if you'll die today . . .

James Dean

Acknowledgments

I would like to express my sincere thanks and appreciation to the following people:

Professor B. W. Skews, who, as my supervisor, provided essential advice, assistance and guidance in the key aspects of this dissertation. I am also very grateful for the funding I received from the National Research Foundation and the Merit Scholarship from the University of the Witwatersrand.

Mr. R. Paton who was always available to give a helping hand in setting up the acquisition instruments and in many circumstances helped me understand certain concepts related to the research being undertaken.

All my friends and colleagues, namely Nick Quarta, Omid Alimia and Steven Moss for their friendship and motivation.

The staff of the Mechanical Engineering Workshop for the manufacturing of the various shock tube components and for providing essential advice during the design and assembly of the shock tube. Special thanks goes to J. Cooper, M. van Wyk, A. Moller, and D. Smith for their invaluable experience and workmanship in manufacturing specialised shock tube equipment. Without their expertise this project would not be possible.

Finally, but not least, I would like to thank my Mother and Father for their support throughout my studies.

It is due to the generosity of those mentioned above, in putting their support, knowledge and expertise at my disposal, that I have been able to complete this research report.

Contents

List of Figures **iv**

List of Tables **viii**

List of Symbols **ix**

1 Introduction **1**

1.1 Background 1

1.2 Shock Waves 2

1.3 General Theory 2

1.4 Wave Diagrams 5

1.5 Shock Wave Reflections 6

1.5.1 Regular Reflection 7

1.5.2 Irregular Reflection 8

1.5.3 The von Neumann paradoxes 8

1.5.4 Guderley and Vasilev Reflections 10

2 Literature Review **14**

2.1 Numerical Solutions 14

2.2 Experimental Findings 22

2.3 Motivation 24

3 Objectives **26**

4 Experiment Design **27**

4.1 Dynamics of the Study 27

4.2 Existing shock tube 29
4.3 Modified Large-Aspect Ratio Tube 31
4.4 Shock Tube Configurations 33
4.4.1 First Configuration 33
4.4.2 Second Configuration 33

5 Apparatus **39**
5.1 First Shock Tube Configuration 39
5.2 Second Shock Tube Configuration 39
5.3 Data Acquisition Instruments 41
5.4 Optical System 42
5.4.1 Single Frame Camera 43
5.4.2 Multiple-Frame Camera 44
5.5 Control Panel 44
5.6 Diaphragm 45
5.7 Computing Facilities 46
5.7.1 Hardware 46
5.7.2 Software 46

6 Methodology **47**
6.1 Numerical Studies 47
6.2 Experimental Studies 47
6.3 Computational Fluid Dynamics Model 48

7 Discussion of Results **51**
7.1 Overview 51
7.2 Numerical Study 52
7.2.1 Summary 57
7.3 Experimental Results 57
7.3.1 The Expansion Wave 59
7.3.2 Evidence of the Shocklet 64
7.4 Quantitative Results 69
7.4.1 Initial Data 70

7.4.2 Refined Data 72
7.4.3 Summary 74

8 Conclusions **75**

References **77**

A Data Anaylsis **79**

B Testing Procedures and Precautions for Shock Tube Tests **82**

B.1 Testing Procedure for Large-Scale Diffraction (450mm) Shock Tube 82
B.2 Testing Precautions 84
B.3 Driver Clamping Procedure 85
B.4 Pre-Test Checklist 87
B.5 Test Log 88

C Driver Certificate of Manufacture **89**

D Shock Tube Engineering Drawings **91**

D.1 First Shock Tube Configuration - Perturbation Sources 92
D.2 Second Shock Tube Configuration - Diverging Section 93
D.3 Plunger section 94

List of Figures

1.1 Normal shock wave. 2

1.2 Galilean transformation. 3

1.3 The oblique shock wave as a result of flow over a wedge. 4

1.4 Pressure waves in a shock tube. 6

1.5 Velocity, temperature, density, and pressure distribution of the flow after diaphragm rupture 6

1.6 The 13 possible wave configurations. 7

1.7 Schematic for regular reflection (RR). 8

1.8 Schematic for simple Mach reflection (SMR). 8

1.9 Schematic illustration of Guderley's proposed reflection showing a Prandtl-Meyer expansion emanating from the triple point directly behind the reflected shock wave. 9

1.10 von Neumann reflection (vNR). 10

1.11 Schematic illustration of the wave configuration of a MR. 11

1.12 Schematic view of three different wave configurations: (a) vNR, (b) VR, and (c) GR. 12

1.13 Evolution-tree presentation of the transition criteria between various reflections (Vasil'ev et al. 2008). 12

1.14 Domains and the transition boundaries between various shock wave reflection configurations for $\gamma = 1.4$. 13

2.1 Expansion wave evaluation in high-resolution numerical study. 15

2.2 Numerical solution of the transonic small disturbance equations. 15

2.3 Refined numerical solution of the steady transonic small disturbance equations showing a sequence of triple points 16
2.4 Cross section of $\bar{M}$ showing sequence of triple points. 17
2.5 Defina et al. (2008) first solution for GR: Four-wave reflection patterns close to triple points T and T_1 for $F_0 = 1.7$ and $\theta = 10^\circ$. 19
2.6 The Vasilev reflection pattern close to the triple point for $F_0 = 1.93$ and $\theta = 10^\circ$ 20
2.7 The angle β of the reflected shock as a function of the distance x/h_M from the triple point 20
2.8 A schematic diagram of the computational domain. 21
2.9 Comparison between the nonlinear reflecting rarefaction problem and Guderley reflection. 21
2.10 Schematic of the shock structure produced by the reflection of the rarefaction wave off the sonic line. 22
2.11 Shock tube used by Skews et al. (2009). 23
2.12 Complex flow structure behind reflected shock wave. 23
2.13 Experimentally captured Guderley Mach reflection for a wedge angle of 15° and Mach number of 1.12 24

4.1 Schematic of developed reflection used by Skews et al. (2009) 27
4.2 Progression of developed irregular Mach reflection downstream for different time steps t_i showing the overall trajectory path of a triple point in a conventional shock tube. 28
4.3 Developed irregular Mach reflection due to the normal shock reflecting over a triangular perturbation source. 29
4.4 Developed irregular Mach reflection due to the cylindrical shock reflecting off the ceiling of the expansion chamber. 29
4.5 Existing shock tube layout. 30
4.6 Dimensions of expansion chamber and large-aspect ratio tube. 31
4.7 Rotational positions for observation window. 32
4.8 Plug design of large-aspect ratio tube. 32
4.9 Mounting plate with attached perturbation source. 33

4.10 Perturbation sources 34
4.11 Diverging section dimensions for the various ramp inserts. 34
4.12 20° ramp assembly. 35
4.13 Diverging section assembly. 36
4.14 Plunger section with accompanying pricker mechanism. 37
4.15 Wave diagram plots for a Mach number of 1.40 and various driver lengths. . 38
4.16 Driver assembly. 38

5.1 Schematic of first shock tube configuration. 39
5.2 Diverging shock tube configuration. 40
5.3 Newly manufactured diverging section and driver. 41
5.4 Replacement of a ramp section in the diverging section. 41
5.5 Pressure transducer ports on expansion chamber. 42
5.6 Schematic of a basic Z-layout schlieren system 43

6.1 Initial uniform quadrilateral mesh for second shock tube configuration with interval size of 15 mm 49

7.1 Static pressure contours of developed irregular Mach reflection propagating downstream for the rectangular perturbation source for $M_{ts} = 1.21$. 53
7.2 Trajectory path of triple points for $M_{ts} = 1.21$ and $M_{ts} = 1.31$ for an expansion chamber of 4.0 m. 53
7.3 Schematic of the uniform growth of the supersonic region behind the triple point as l_{vms} increases downstream. 54
7.4 Dynamics of the shock reflection in the shock tube for a 15° ramp angle, $M_{ts} = 1.31$, 4.0 m expansion chamber. 56
7.5 Reflected wave Mach number versus distance downstream for 15° ramp angles, $M_{ts} = 1.31$, 4.0 m expansion chamber. 57
7.6 General schlieren photograph captured through the viewing port showing the GR. 58
7.7 Incorrectly adjusted schlieren system showing no evidence of the flow features behind the triple point. 59

7.8 Original and contrasted image of GR clearly showing the expansion wave, 20° ramp angle, $M_{bts} = 1.107$. 60
7.9 Comparison between ω_{ir} and ω_{re} for the 10° ramp angle. 61
7.10 Summary of all the images showing evidence of the fourth wave of the GR as a black fan-shaped region immediately behind the reflected wave. 62
7.11 Comparison between the schlieren images obtained from the conventional shock tube and large scale shock tube. 63
7.12 Structure of GR with expansion wave immediately beneath reflected wave. . 64
7.13 GR with evidence of the shocklet produced by the perturbation sources. . . 65
7.14 Comparison between the shocklets produced by the 15° and 20° ramp angles for $l_{ec} = 2.0$ & 4.0. 66
7.15 Length of supersonic patch l_s behind the triple point. 67
7.16 Variation of supersonic patch size (l_s) with the virtual Mach stem length (l_{vms}). 68
7.17 Schematic of GR consisting of shocklet and secondary expansion wave. . . 69
7.18 Superimposed images using high speed camera for a 15° ramp angle and $M_{bts} = 1.206$. 70
7.19 Typical pressure trace record for $M_{bts} = 1.30$. 71
7.20 Initial Mach number data for captured GR. 72
7.21 Modified Mach number data for captured GR for $M_{bts} = 1.206$ (test 1 to 4), and $M_{bts} = 1.303$ (test 5). 73

A.1 Schematic of two superimposed irregular Mach shock reflections at time t_1 and t_2. 79
A.2 Oblique shock wave analysis of three overlaid images for the 15° ramp angle and $M_{bts} = 1.206$ 80

List of Tables

5.1 Diaphragm properties for driver section in the second shock tube configuration. 46

6.1 Inlet pressures for the first shock tube configuration 50

6.2 Inlet pressures for the second shock tube configuration based on the 15° ramp angle 50

7.1 Number of reflections undergone for the various shock tube configurations. 54

7.2 Summary of the observations for the entire parameter set. 69

7.3 Modified Mach number data for captured GR. 73

List of Symbols

3ST	Three shock theory.
4WT	Four wave theory.
a	Inverse Mach slope.
a_s	Speed of sound (m/s).
δ_i	Flow deflection angle (deg).
γ	Gas specific heat ratio.
GR	Guderley reflection.
l_{ams}	Apparent Mach stem length (mm).
l_{vms}	Virtual Mach stem length (mm).
l_s	Length of first supersonic patch (mm).
M_i	Mach number.
M_s	Incident wave Mach number.
M_{ts}	Incident wave Mach number of shock reflection at test section.
M_{bts}	Incident wave Mach number of shock reflection before test section.
ϕ_i	Shock wave inflow angle (deg).
R	Universal gas constant.
RR	Regular reflection.
T	Temperature (kelvin).
SMR	Simple Mach reflection.
θ_w	Wedge angle (deg).
vNR	von Neumann reflection.
VR	Vasilev reflection.
ω_{ir}	Angle between the incident wave and the reflected wave (deg).
ω_{re}	Angle between the reflected wave and the expansion wave (deg).

Chapter 1

Introduction

This section introduces the nature of shock wave reflections such as regular and irregular reflections, and further discusses the sub-domains of irregular reflections such as the von Neumann and the Guderley reflections. The nature of weak shock wave reflections, and an outline of the development of this specialised field of weak shock wave reflection is also covered. The equations presented in this chapter are crucial when calculating the correct initial conditions for the simulations presented in Chapter 3, and in determining the flow conditions behind a plane or oblique shock wave.

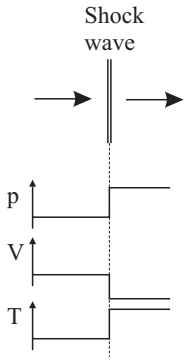
1.1 Background

Over the past century considerable research has been conducted in steady shock wave reflection as this phenomenon is very important in the field of aerodynamics. Strong shock waves of Mach numbers higher than 2.2 in air have been extensively studied, however in the supersonic civil aviation industry, lower Mach numbers are of particular interest. For example regular and irregular reflection interactions are critical in understanding various phenomena such as off-design inlet flows, inlet starting, and flow stalling. With regard to supersonic inlet flows the interactions and reflections of weak shock waves are very common for low and moderate Mach numbers from 1.0 to 2.0. However, in the case of weak shock waves the fundamentals of these waves have still not been entirely resolved, therefore leaving an obscure domain which has still not been completely investigated. (Ivanov 2010)

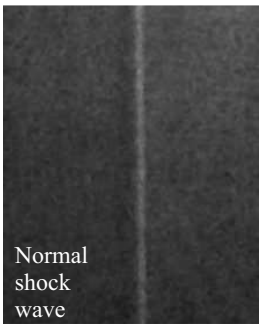
The most typical example of the uncertainty in the irregular reflection domain of weak shock waves is a shock reflection in the range of flow parameters where von Neumann's three shock theory (3ST) does not produce any solution even though experiments show that a Mach like reflection exists (Bleakney & Taub 1949). This paradox has raised considerable interest in developing new wave theories to better understand the nature of weak shock wave reflections. The following dissertation aims at exploring the weak shock wave irregular reflection domain using a novel experiment to produce a unique reflection called the Guderley reflection.

1.2 Shock Waves

A shock wave can be simply described by a spontaneous change in a flow, whereby the velocity decreases and the pressure increases through this region of sharp change. The discontinuity in the flow features are illustrated in Figure 1.1(a). The extremely thin region separating the supersonic velocity and relatively low pressure state to the state of relatively low velocity and high pressure is termed a shock wave. A schlieren photograph of a normal shock wave is shown in Figure 1.1(b), where the white vertical line represents the discontinuity between the supersonic flow on the left and subsonic flow on the right. The thickness of the shock wave is usually only a few mean free paths thick, the shock wave in general is curved, however many shock waves which occur in practical situations are straight or commonly known as normal shock waves. In normal shock waves the velocities both upstream and downstream of the shock are at right angles to the shock wave, however when there is a change in flow direction across the shock wave, the shock wave is termed an oblique shock wave (Oosthuizen & Carscallen 1997).



(a) Illustration of pressure, velocity and temperature variations across shock wave.



(b) Schlieren photograph of a normal shock wave.

Figure 1.1: Normal shock wave.

1.3 General Theory

The ratio between the velocity of the gas to the speed of sound in the gas is an important parameter when considering the compressibility of flows. This ratio is called the Mach number, given in Equation 1.1.

$$M = \frac{\text{gas velocity}}{\text{speed of sound}} \tag{1.1}$$

If the Mach number is smaller than one ($M < 1$) the flow is subsonic and information of the flow can propagate upstream therefore allowing the flow to anticipate any changes in area that may occur downstream. However, if $M > 1$ the gas is moving faster than the speed of sound, known as supersonic flow, and thus information cannot propagate upstream. This

means that a supersonic flow cannot go through any adjustments in flow before engaging with an obstacle (e.g. curve in a pipe).

The speed of sound is given in Equation 1.2

$$a_s = \sqrt{\gamma RT} \tag{1.2}$$

where γ is the ratio of specific heats of the gas, R is the gas constant being considered, and T is the temperature of the gas in Kelvin.

The inverse Mach slope for a uniform plane incident wave off a reflecting surface is given by Tesdall, & Hunter (2002) in Equation 1.3

$$a = \frac{\theta_w}{2\sqrt{M-1}} \tag{1.3}$$

where θ_w is the wedge angle in radians, and M is the incident Mach number. The inverse Mach slope is a useful value to determine the clarity of the flow features in a Guderley Mach reflection. The influence of the inverse Mach slope will be described in more detail in Section 2.1.

Galilean transformation

Attaching a frame of reference to a moving shock wave can transform the wave into a pseudo-stationary shock wave by superimposing the reversed velocity of the moving shock wave. Figure 1.2 illustrates this transformation whereby steady flow theories can then be applied to solve the regions in the flow field. This transformation will be utilised in analysing the flows for the three-shock configuration as will be shown in Appendix A.

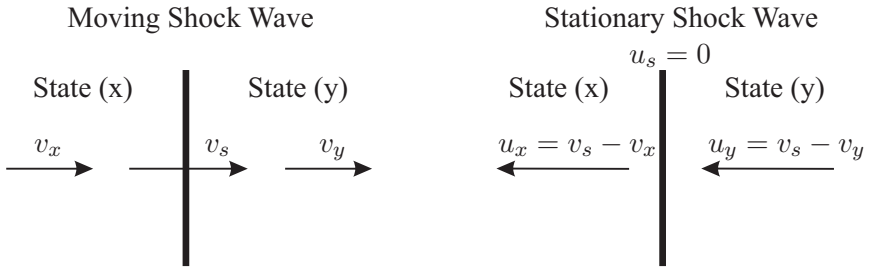


Figure 1.2: Galilean transformation.

The following Equations 1.4, 1.5, 1.6 are used to determine the required pressure and temperature ratios to produce a specific Mach number in a frame of reference with the shock stationary. These equations were used to calculate the appropriate initial conditions for the computational fluid dynamics (CFD) analysis discussed in Section 6.3.

$$M_y^2 = \frac{M_x^2 + \frac{2}{\gamma-1}}{\frac{2\gamma}{\gamma-1}M_x^2 - 1} \tag{1.4}$$

$$\frac{T_y}{T_x} = \frac{M_x^2 + \frac{2}{\gamma-1}}{\frac{2\gamma}{\gamma-1}M_x^2 - 1} \tag{1.5}$$

$$\frac{P_y}{P_x} = \frac{2\gamma}{\gamma+1}M_x^2 - \frac{\gamma-1}{\gamma+1} \tag{1.6}$$

Oblique Shock Waves

The preceding section was concerned with shock waves normal to the flow direction, however in many practical cases as shown in Figure 1.3, if a supersonic flow is required to change its flow direction by θ_w this results in a inclined shock wave being formed to the original flow direction. These inclined shock waves are generally called oblique shock waves. Similar to a normal shock wave, an oblique shock wave is a compressive wave which generates higher static temperatures and pressures while at the same time causing a drop in the Mach number. Note that the flow direction denoted by M_2 is parallel to the wedge angle θ_w.

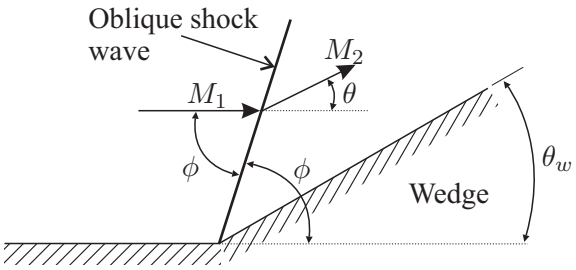


Figure 1.3: The oblique shock wave as a result of flow over a wedge.

The following equations, commonly referred to as the oblique shock equations, are derived by transforming the oblique shock into a normal shock. The derivation assumes that the flow is a steady two-dimensional planar adiabatic flow, that no external work is involved, and that the effects of body forces are negligible. The relationship between the downstream Mach number M_1, the upstream Mach number M_2, the resultant shock wave pressure ratio $\frac{p_2}{p_1}$, the oblique shock wave inflow angle ϕ, and the flow deflection angle θ are listed below (Zucrow & Hoffman 1976):

$$\frac{p_2}{p_1} = \frac{2\gamma}{\gamma+1}M_1^2 sin^2(\phi) - \frac{\gamma-1}{\gamma+1} \tag{1.7}$$

$$M_2^2 sin^2(\phi-\theta) = \frac{\frac{2}{\gamma-1} + M_1^2 sin^2(\phi)}{\frac{2\gamma}{\gamma-1}M_1^2 sin^2(\phi) - 1} \tag{1.8}$$

$$tan(\theta) = 2cot(\phi)\frac{M_1^2 sin^2(\phi) - 1}{M_1^2(\gamma + cos(2\phi)) + 2} \tag{1.9}$$

Equations (1.7), (1.8) and (1.9) are used in Section A to analyse the respective flows behind the shock waves presented in this study.

1.4 Wave Diagrams

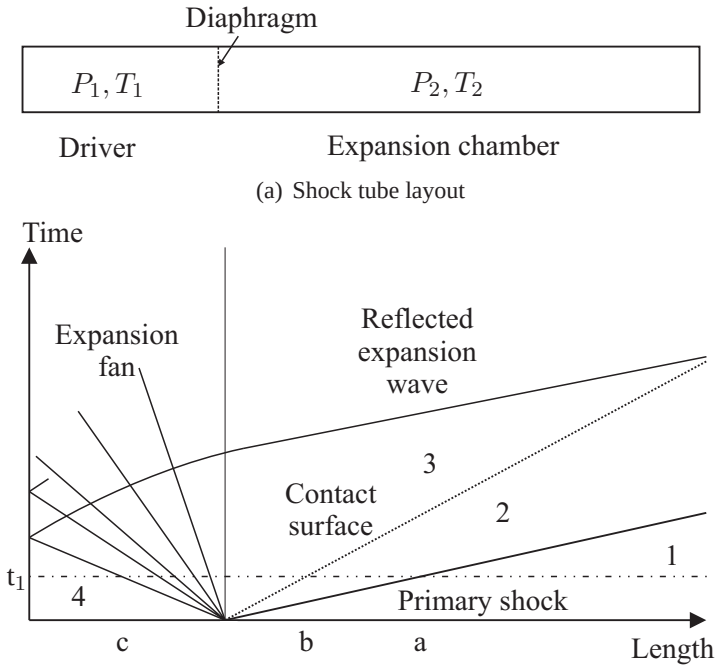
In order to design a fully functional shock tube it is important to understand the dynamics of the various waves in the shock tube at various operating conditions. The wave diagrams described below give insight into the operation of a general shock tube so that the length of the driver section can be correctly determined, as is presented as part of the Design Development in Appendix 4.4.2. Consider a "shock tube" in its simplest form which consists of a long constant area tube divided into two sections by a diaphragm. As shown in Figure 1.4(a), the sections to the left and right of the diaphragm are called the driver and expansion chamber respectively. Each section is filled with gas of different conditions p_1, T_1, m_1, γ_1 and p_2, T_2 m_2, γ_2, where p is the pressure, T is the temperature, m is the molecular weight and γ is the ratio of specific heats of the respective gas.

High pressure gas is contained in the driver, and low pressure gas, generally at atmospheric conditions, is contained in the expansion chamber. When the diaphragm is ruptured, either mechanically or by increasing the pressure of the gas in the driver, a shock wave propagates into the expansion chamber and an expansion wave simultaneously propagates into the driver as seen in Figure 1.4(b). *x* is the length downstream with its origin at the beginning of the driver, and *t* is the time with *t* = 0 at diaphragm rupture. The one-dimensional plot seen in Figure 1.4(b) is obtained from the time-dependent Euler equations for thermally and calorically perfect gases.

Analysing the wave diagram, it is seen that the head of the unsteady expansion wave reflects off the left wall of the driver section (*y*-axis) and is subsequently accelerated by its interaction with the centred expansion fan. Since the head of the reflected expansion wave has a larger velocity than the incident shock wave, the lengths of the driver and expansion sections have to be selected so that the time at which the reflected expansion reaches the end of the shock tube is delayed by as much as possible. The delay of both the reflected expansion wave and the incident shock wave allow for a maximised testing time, this implies having a relatively long driver.

Figure 1.5 illustrates the velocity, temperature, density, and pressure distribution of the flow at a constant point in time t_1 as seen in 1.4(b). It is seen that constant flow conditions are obtained between the the incident shock wave and the contact surface (region a-b), which is also indicated as region 2 shown in Figure 1.4(b). Notice that at the contact surface ($x = b$) the velocity and pressure remain constant, however there is a discontinuity in the temperature and density. The temperature of the gas is seen to increase at the shock wave and decrease through the expansion fan.

Note that the wave diagrams presented in Appendix 4.4.2 were produced using Kasimir 3 which is a commercially available shock tube simulation program developed by the Shock Wave Laboratory, RWTH Aachen University. The program is based on a one-dimensional



(a) Shock tube layout

(b) Wave diagram of events in shock tube

Figure 1.4: Pressure waves in a shock tube.

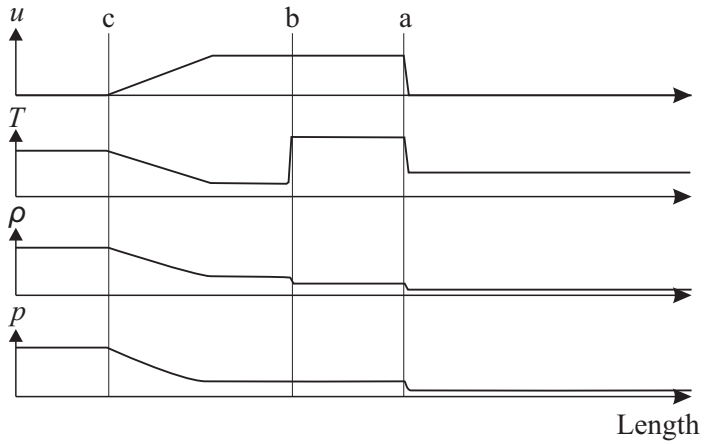


Figure 1.5: Velocity, temperature, density, and pressure distribution of the flow at a constant point in time t_1 after the diaphragm ruptures; position of the incident shock wave (*a*), contact surface (*b*), head of the unsteady expansion wave (*c*) (Tropea et al. 2007).

code which takes into account high temperature effects assuming chemical and thermal equilibrium.

1.5 Shock Wave Reflections

This section is critical in understanding the various shock wave reflections which occur for different flow conditions. This will make it easier to identify the observed shock wave configurations captured experimentally and allow the observations to be critically examined.

When a plane shock interacts with a wedge wall, a number of reflection patterns occur depending on the strength of the incident shock wave, the wedge angle θ_w and the gas specific heat ratio γ. There are 13 different wave configurations which are presented in the evolution tree in Figure 1.6 (Ben-Dor 2007). The first two branches present the regular (RR) and the irregular (IR) reflections, it is seen that the majority of the more complex reflections fall under the irregular reflection domain. Irregular reflections are divided into the strong shock and weak shock categories, namely Mach reflections, and three rare reflections (vNR, VR, and GR) that represent the von Neumann paradox conditions. It should be noted that in the context of this report the initially unnamed reflection ?R is now referred to as the Vasilev reflection (VR). In the present work only the weak shock wave domain or rather the von Neumann paradox conditions for irregular reflections will be investigated. This has been highlighted in yellow in Figure 1.6. Therefore, particular interest is centred on the von Neumann (vNR), Vasilev (VR), and the Guderley (GR) reflections. In order to obtain a better understanding of the characteristics of general shock wave reflections, the RR and MR are briefly described below.

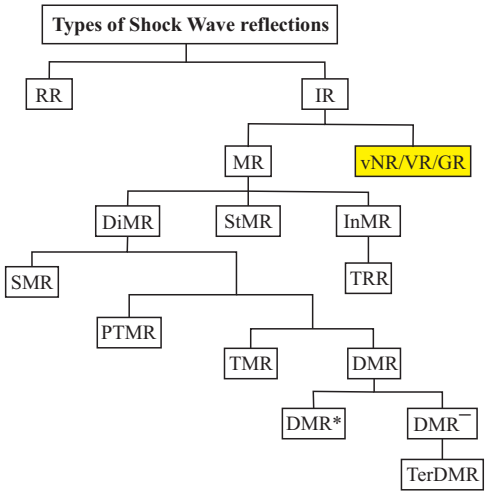


Figure 1.6: The 13 possible wave configurations (Ben-Dor 2007).

1.5.1 Regular Reflection

At lower shock strengths or larger wedge angles one observes the simplest wave configuration pattern consisting of two shock waves. This wave configuration is called the regular reflection (RR) as shown in Figure 1.7. As the plane shock wave moves over the wedge a reflected shock wave (R) is formed, which meets the incident shock wave (I) at the reflection point (r) on the wedge surface. In order to analyse the flow behind the two shock waves, the oblique shock theory is utilised (see Section 1.3, page 4).

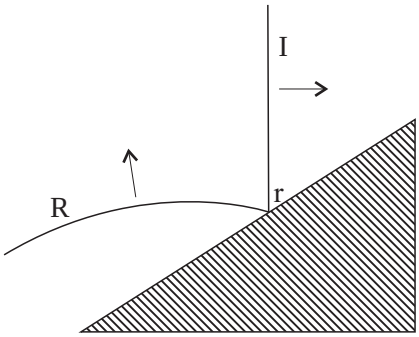


Figure 1.7: Schematic for regular reflection (RR).

1.5.2 Irregular Reflection

For smaller wedge angles the RR transforms into a simple Mach reflection (SMR) shown in Figure 1.8. The transition between RR and SMR results in the reflected and incident shock waves moving away from the surface and producing an additional single shock which is in perpendicular contact with the surface. This shock wave is called the Mach stem (M) and therefore the SMR consists of three shock waves. The point at which the three waves intersect is named the triple point (T), whereby a contact discontinuity originates as a result of the different flow conditions passing through the Mach stem and reflected shock wave. The contact discontinuity is commonly referred to as the slipstream (s). Various other irregular Mach reflections (e.g. DiMR, StMR) have been observed and classified as shown in Figure 1.6, however these reflection types are not relevant to the current work.

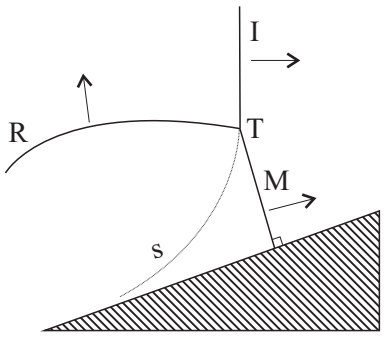


Figure 1.8: Schematic for simple Mach reflection (SMR).

1.5.3 The von Neumann paradoxes

To analyse the flow fields behind each wave in the RR and SMR, von Neumann formulated the two-shock and three-shock theory, which assumes that all shocks obey the Rankine-Hugoniot jump conditions, and all the waves are of negligible thickness and curvature. The theories presented excellent agreement for strong shocks, but for weak shocks serious discrepancies were found when comparing theoretical results with experimental observations. The conflict between experiment and theory is commonly referred to as the “von Neumann paradox”.

One discrepancy of the “von Neumann paradox” shows that the regular reflection exists in parameter regions where no physically realistic theoretical solution is possible. The second discrepancy, shows that a reflection configuration similar to the simple Mach reflection is observed for weak shocks (von Neumann 1963, Henderson 1987), even though no standard triple point configuration is compatible with the jump relations across the shocks and contact discontinuities. The latter discrepancy was called the “triple point paradox” as the predicted limits of the triple points where considerably different from those observed (Birkhoff 1950).

In order to resolve the paradox, Guderley (1947) proposed a theoretically consistent solution instead of the nonphysical branch in the von Neumann theory. The solution which used approximations of potential (isentropic) flow for weak shock waves concluded that a supersonic ($M>1$) patch exists in the region behind the triple point. But this could not eliminate the contradiction in von Neumann’s theory as it did not include a tangential discontinuity. Guderley’s proposed four-wave structure, as shown in Figure 1.9, consists of three important elements: a reflected shock wave which is directed towards incoming flow, a Prandtl-Meyer expansion emanating from the triple point, and a supersonic patch attached to the Mach stem (Guderley 1962).

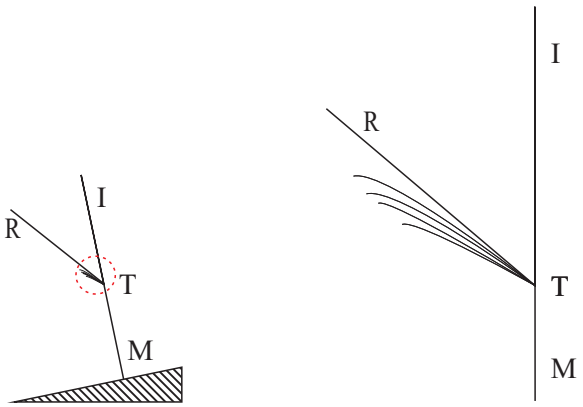


Figure 1.9: Schematic illustration of Guderley’s proposed reflection showing a Prandtl-Meyer expansion emanating from the triple point directly behind the reflected shock wave.

Although the four-wave theory resolves the apparent paradox, it was disregarded for decades due to the absence of high resolution experimentation and simulations to observe the really small supercritical patch behind the triple point. Intensive experimental (Bleakney & Taub 1949, Sternberg 1959, Sasoh & Takayama 1994) and numerical solutions (Colella & Henderson 1990, Brio & Hunter 1992, Tabak & Rosales 1994) could thus not resolve this wave configuration, therefore dismissing Guderley’s proposal.

The characteristics of the SMR-like reflection pattern as a result of the second discrepancy were first discussed in detail by Colella and Henderson (1990). With the use of the Euler equations and a second-order shock-capturing scheme with adaptive mesh refinement,

the authors named the observed reflection the von Neumann reflection (vNR) depicted in Figure 1.10. When comparing the SMR and vNR, it is seen that the SMR has a distinct discontinuity in slope between the incident and Mach shock near the triple point, alternatively the vNR consists of a single wave with a smoothly turning tangent joining the incident and Mach shock waves (Colella & Henderson 1990). It should be noted that the authors hypothesised the vNR as a possible resolution to the von Neumann paradox. But as is discussed in Section 1.5.4, the vNR appears in a parameter domain where there is a solution of the nonstandard 3ST, however the von Neumann paradox refers to situations in which wave configurations which look similar to SMR are in a domain in which the 3ST does not have any solution. Therefore, this suggests that the authors' hypothesis cannot resolve the von Neumann paradox.

Based on their results they also proposed a hypothesis that the reflected shock near the triple point degenerates into a continuous compression wave. However, there is some controversy concerning their results due to the numerical viscosity and grid resolution in their computations. It should also be mentioned that the discretisation of the Euler equations with shock-capturing schemes is known to always include some numerical noise in the algorithm, making Colella and Hendersons' results even more controversial (Ivanov et al., 2010).

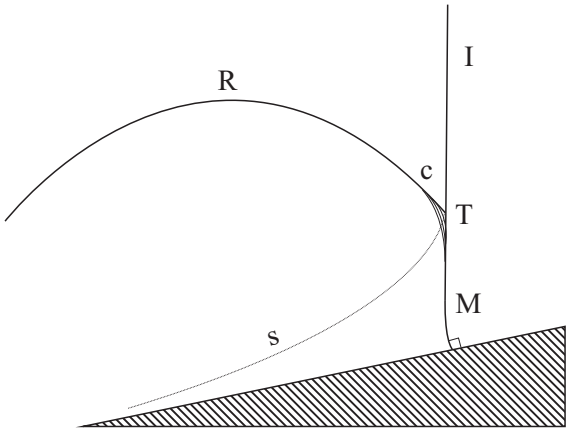


Figure 1.10: von Neumann reflection (vNR).

1.5.4 Guderley and Vasilev Reflections

This section outlines the weak shock wave reflection domain based on the experimental and numerical work published to date. The von Neumann reflection vNR, Guderley reflection GR, and the newly presented Vasilev reflection VR are described by the three-shock and four-wave theories (3ST & 4WT) respectively. Since the main objective of this work is to verify the existence of either the GR or VR, it is important that the transition criteria between the various reflections are understood, as will be described below. The following information in this subsection has been obtained from Ben-Dor (2007) and Vasilev et al.

(2008).

The three-shock theory (3ST) is used to analytically describe the MR wave configuration. Figure 1.11 represents the four flow discontinuities in a MR, indicating the corresponding intersection angles ϕ_i and flow deflection angles θ_i through each of the shock waves. Based on the assumptions of the 3ST, which states that the flow is inviscid and the contact surface is infinitely thin, this means that the streamlines on both the sides of the contact surface are parallel, i.e.,

$$\theta_1 \pm \theta_2 = \theta_3 \tag{1.10}$$

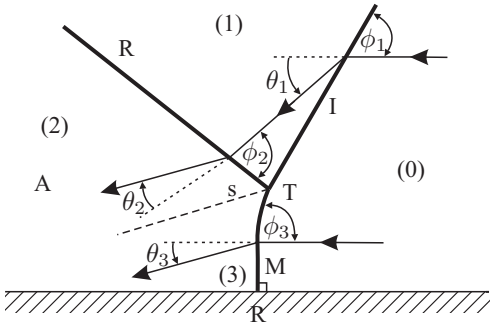


Figure 1.11: Schematic illustration of the wave configuration of a MR.

From Equation (1.10), the 3ST can be divided into two types:

- A "standard" 3ST where
$$\theta_1 - \theta_2 = \theta_3. \tag{1.11}$$
- A "nonstandard" 3ST where
$$\theta_1 + \theta_2 = \theta_3. \tag{1.12}$$

As will be shown subsequently, the standard 3ST solution is used to yield a MR, which is utilised in most textbooks to describe the boundary conditions across the slipstream. Alternatively the solution of nonstandard 3ST comprises of two cases: one where the solution is physical which results in a vNR, and another case where the solution is not physical which results in a new type of reflection, VR. The VR is an intermediate wave configuration between the vNR and the GR, and will be described subsequently in more detail. In the cases where the 3ST does not provide a physical or any solution, the four-wave theory (4WT) is utilised which is presented in Vasilev et al. (2008).

Figure 1.12 shows the three different wave configurations, vNR, VR, and GR, whereby the gray colour denotes the subsonic flow behind the triple point. In the vNR it is shown that the flow regions behind the reflected shock and Mach stem are subsonic. In the VR there is one supersonic region covering the area between the slip stream and the reflected shock wave with a Prandtl-Meyer expansion fan inside it. The GR consists of two supersonic

regions behind the triple point, whereby the one is similar to the VR and the second is located between the slipstream and the Mach stem. Note that both the supersonic patches in the GR are discontinuous across the slip stream. By analysing the number of supersonic regions near the triple point, the three wave configurations (vNR, VR, and GR) can be simply characterised.

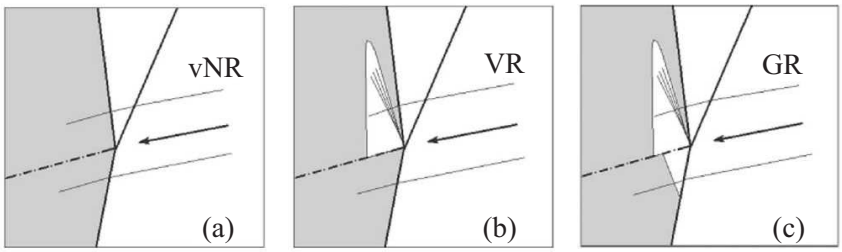


Figure 1.12: Schematic view of three different wave configurations: (a) vNR, (b) VR, and (c) GR. Gray denotes subsonic flow (Vasil'ev, Elperin & Ben-Dor 2008).

Based on the computational analysis of Vasilev et al. (2008), the weak shock wave reflection domain was investigated by means of the evolution of the (*I*-*R*)-polar combinations as the complementary wedge angle, $\theta_w^C = 90^\circ - \phi_1$, is decreased from an initial value of 41°, for which the reflection is a MR, to 31° which represents a GR for $M_s = 1.47$ and $\gamma = \frac{5}{3}$. The authors' work presents a full picture of the reflection phenomenon in the nonstandard-3ST domain and beyond it. The evolution of the types of reflection obtained for reducing θ_w^C are presented in Figure 1.13. It is seen that for the GR and the VR, the flow behind the reflected wave needs to be sonic for both cases, and as already discussed the flow behind the Mach stem must be subsonic for the VR and supersonic for the GR.

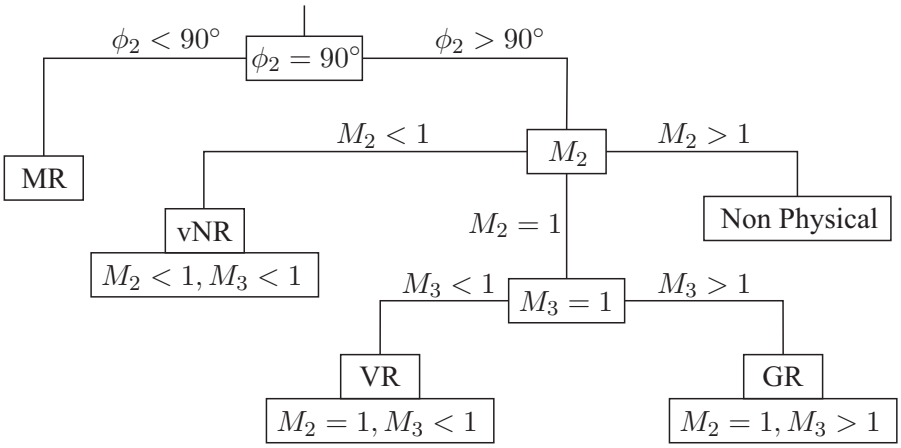


Figure 1.13: Evolution-tree presentation of the transition criteria between various reflections (Vasil'ev et al. 2008).

Progressing to the transition criteria shown in Figure 1.13, Figure 1.14 shows the domains of and the transition boundaries between the various shock wave reflection configurations in the (M_s, θ_w^C) plane for a diatomic ($\gamma = \frac{5}{3}$) gas. Curve 1 is the MR↔vNR transition curve,

i.e., $\phi_2 = 90^\circ$ on this curve. Above this curve $\phi_2 < 90^\circ$ and the reflection is MR. Curve 2 is the vNR↔VR transition curve, i.e., $M_2 = 1$ on this curve. Curve 3: The VR↔GR transition curve, i.e., $M_3 = 1$ on this curve. Curve 4: The curve on which $M_1 = 1$, below this curve no reflection exists as the flow behind the incident shock wave is subsonic. The domain below this curve is commonly referred to as the no-reflection domain (NR domain). Above curve 5 the 3ST has at least one mathematical solution and below it, the 3ST does not have any mathematical solution. Between curves 2 and 5, the 3ST has a non-physical solution. The von Neumann paradox discussed in Section 1.5.3 exists in the domain bounded by curves 2 and 4. Guderley proposed the four-wave concept which resolved the paradox in the domain bounded by curves 3 and 4. The reflection between curves 3 and 4 is a GR as shown in Figure 1.12(c), while the reflection that occurs inside the domain bounded by 2 and 3 is VR as shown in Figure 1.12(b). (Vasil'ev et al. 2008)

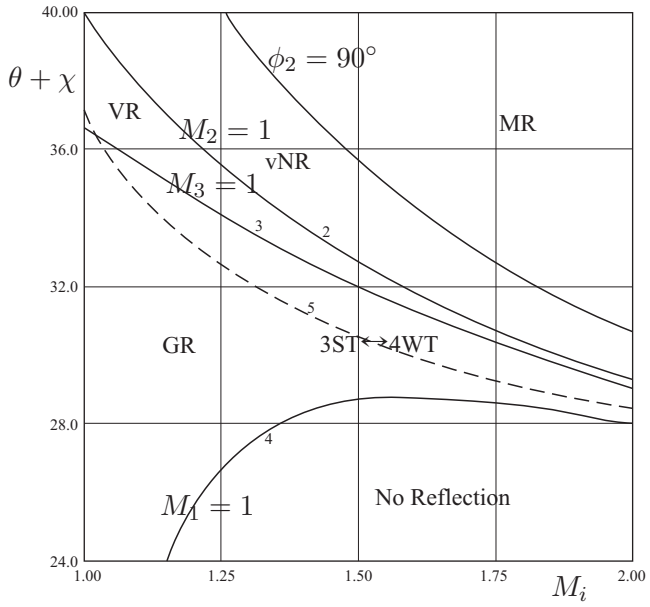


Figure 1.14: Domains of and the transition boundaries between various shock wave reflection configurations for $\gamma = 1.4$. Curve 1: The MR↔vNR transition curve, i.e., $\phi_2 = 90^\circ$. Curve 2: The vNR↔VR transition curve, i.e., $M_2 = 1$. Curve 3: The VR↔GR transition curve, i.e., $M_3 = 1$. Curve 4: The curve on which $M_1 = 1$. Below this curve the flow behind the incident shock is subsonic and therefore a reflection cannot take place. Curve 5: Above this curve, the 3ST has at least one mathematical solution and below it, the 3ST does not have any mathematical solution (Vasil'ev et al. 2008).

Chapter 2

Literature Review

Only recently, with the use of advanced high resolution simulations and experimentation has the flow field directly behind the triple point been resolved, showing evidence that the four-wave structure proposed by Guderley does in fact exist. This chapter discusses the key publications which have contributed to the progression in the field of weak irregular reflections with particular reference to the Guderley reflection.

2.1 Numerical Solutions

Vasil'ev & Kraiko (1999) with the use of a high-resolution numerical study using Euler equations showed that Guderley's proposed resolution might in fact be correct. Based on their study for a wedge angle of 12.5° and a Mach number of 1.47, they observed a supersonic patch and a narrow expansion fan centred on the triple point. Therefore, in the sub-domain where the three-shock theory has no solution, they found a four-wave structure which Guderley hypothesised in 1947. Figure 2.1 shows the expansion wave that exists directly behind the reflected shock combined with a supersonic patch outlined by the sonic line (M=1) and the slip stream.

In the same year Vasil'ev & Kraiko (1999) with the use of extensive calculations, formulated a four-wave theory (4WT) which completely resolved the von Neumann paradox. It was determined with the use of numerical results and a theoretical analysis that for weak shocks a very small logarithmic singularity with very large flow variable gradients were found in the vicinity of the triple point. The numerical results also showed that the curvature of the reflected shock wave at the triple point was approaching infinity. As a result of the large curvature of the reflected shock wave the subsonic flow behind it converges and becomes supersonic, similar to what is seen in Figure 2.1.

Similarly, evidence of Guderley's proposed resolution was also contained in numerical solutions of the steady transonic small disturbance equations as shown in Figure 2.2, therefore further reasserting the existence of the supersonic patch behind the triple point (Hunter & Brio 2000). Hunter & Brio (2000) also contemplated that a supersonic patch

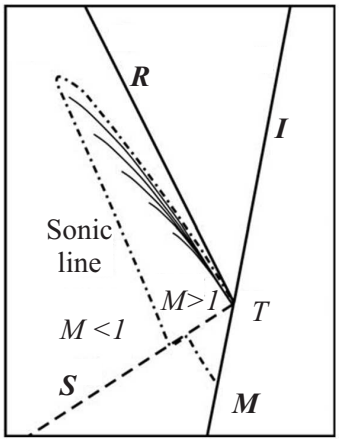


Figure 2.1: Expansion wave evaluation in high-resolution numerical study (Vasil'ev & Kraiko 1999).

could be terminated by a small shock existing behind the supersonic patch, and that there could be a series of such patches along the Mach stem. Zakharian (2000) with the use of Euler equations for weak shock reflection confirmed the validity of the results obtained by the steady transonic small disturbance equations, and showed that a tiny supersonic patch does occur behind the triple point as proposed by Guderley, but they did not discover an additional small shock as suggested by Hunter & Brio (2000). The solution determined that the supersonic and expansion fan region is approximately 0.5% of the Mach stem length, however the observed length of the supersonic patch is directly dependent on the resolution of the mesh behind the triple point and the mesh refinement technique utilised (Zakharian et al. 2000).

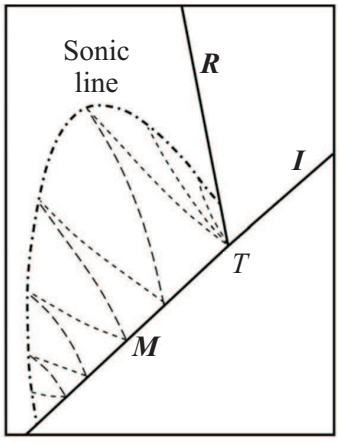
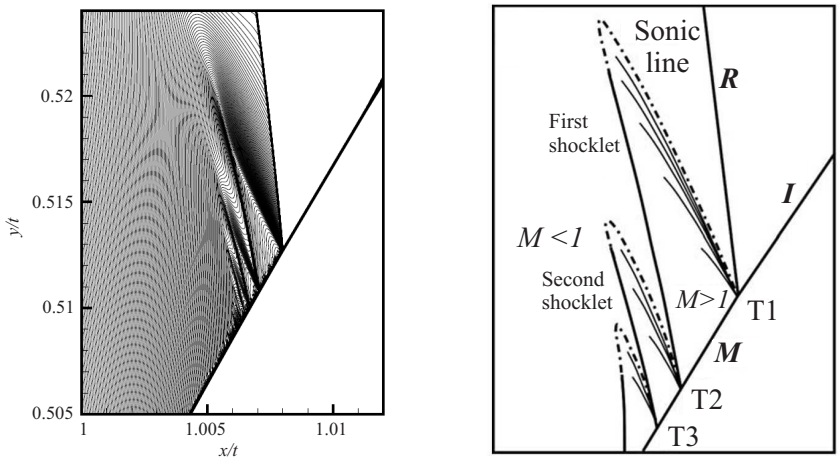


Figure 2.2: Numerical solution of the transonic small disturbance equations (Hunter & Brio 2000).

With the use of a self-similar solution and a highly refined mesh at the vicinity of the triple point, Tesdall et al. (2002) resolved a remarkably complex flow structure as shown in Figure 2.3(a). The numerical solutions were carried out for various inverse Mach slope (a)

values ranging from 0.3 to 0.8. All of the solutions contained a small region of supersonic flow behind the triple point, and it was discovered that this region decreased rapidly with increasing a. Note the most clearly defined flow features were observed for $a = 0.5$. (Tesdall et al. 2002)

Figure 2.3(a) illustrates the corresponding flow structure for $a = 0.5$ which consists of a sequence of triple points and tiny decreasing supersonic patches along the Mach stem. It was suggested that the supersonic patches are formed by the reflection of the weak shocks and expansion fans between the sonic line and the Mach stem. As shown in Figure 2.3(b), each expansion wave is centered at a triple point and reflects off the sonic line into a compression wave. The compression wave forms a shock wave that intersects the Mach stem reflecting as a succeeding expansion fan, resulting in a cascade of triple points. The expansion fan emanating at each triple point resolves the von Neumann paradox for weak shocks. However, the solutions question whether there is an infinite sequence of triple points in an inviscid weak shock Mach reflection. Tesdall and Hunter's (2002) findings therefore confirmed a new type of weak shock wave reflection, called the Guderley reflection (GR) (Tesdall et al. 2002).



(a) Detailed contour plot with 768×608 grid points for $a = 0.5$

(b) Schematic showing sequence of triple points

Figure 2.3: Refined numerical solution of the steady transonic small disturbance equations showing a sequence of triple points (Tesdall et al. 2002).

Following the detection of the Guderley reflection by Tesdall et al. (2002), a problem for the nonlinear wave system was studied numerically by Tesdall & Sanders (2006). The nonlinear wave system consisted of a 3×3 hyperbolic system that has a structure similar to that of the compressible Euler equations. At a set of parameters where a nonstandard solution for regular reflection occurs, a numerical solution remarkably similar to that observed by Tesdall et al. (2002) was obtained. The wave structure again consisted of a sequence of triple points along the Mach stem, with centred expansion fans emanating from each triple point.

The detection of this wave structure in the former system brought about another numerical analysis utilising full Euler equations (Tesdall et al. 2008). At a set of parameters where both regular and Mach reflection are impossible it was discovered that nearly identical solutions were again observed, therefore verifying the Guderley reflection further.

Based from the solution by Tesdall et al. (2008), the self-similar Mach number ($\bar{M}$) is plotted for a cross section directly behind the Mach stem and the triple point in order to analyse the sequence of triple points. Figure 2.4 shows the plot for $M = 1.04$ and a wedge angle of $11.5°$, where it is seen that shock/expansion wave pairs exist, where the large jump in the plot is the leading reflected shock, and the two corresponding smaller rises present the first and second shock respectively. Note that the crossing at $\bar{M} = 1$ indicates jumps across weak reflected shocks or across the sonic line. It was established that three supersonic regions exist in the vicinity behind the triple point. The height of the supersonic region was determined to be approximately 0.6% of the length of the Mach stem, which is 20% greater than Zakharian's (2000) results. The discepancy is a result of the advanced mesh refinement techniques utilised by Tesdall et al. (2008), and thus the improved overall resolution of the vicinity behind the triple point.

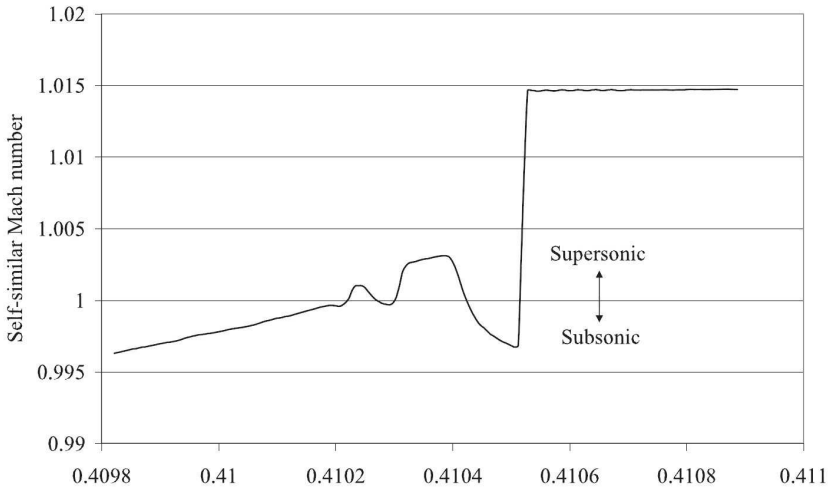


Figure 2.4: Cross section of $\bar{M}$ taken bottom-up slightly to the left and parallel to the Mach stem (Tesdall et al. 2008).

Based on the study conducted by Vasil'ev et al. (2008), the reflection of weak shock waves have been reconsidered analytically using shock polars. As discussed in Section 1.5.4, the solutions of the three shock theory (3ST) were classified as "standard-3ST solutions" and "nonstandard-3ST solutions". It was shown that there are initial conditions where the 3ST does not provide any solution, and the four shock theory (4WT) in these situations replaces the 3ST. Therefore, the 4WT which is derived by Vasil'ev et al. (2008), is used to describe the VR and GR wave configurations respectively. It was also shown that the four different wave configurations can exist in the weak shock reflection domain, the Mach reflection

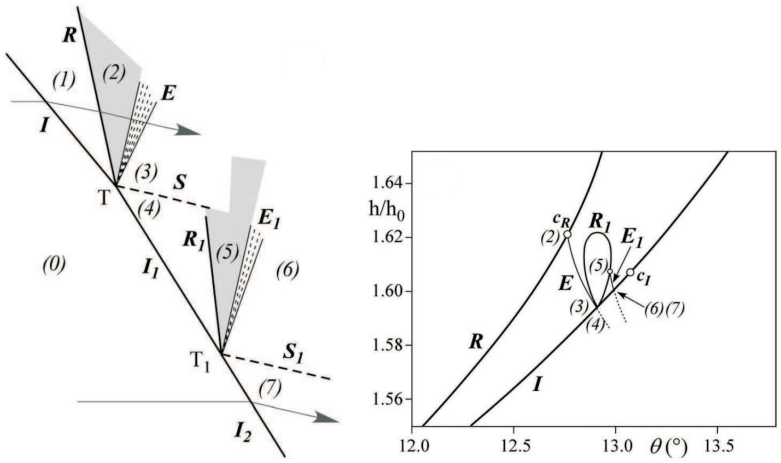
(MR), a von Neumann reflection (vNR), a Vasilev reflection (VR), and a Guderley reflection (GR). The domains and transition boundaries between these four wave configurations were also determined, as presented in Figure 1.14 on page 13.

Recently, Defina, Susin & Viero (2008) presented high-resolution numerical solutions of the depth averaged inviscid shallow water equations which provided new information on the weak shock reflection domain within the von Neumann paradox conditions. The authors computed shock reflections close to the Guderley and the Vasilev reflections which confirmed the validity of the four-wave theory, however they did not discover a complex sequence of supersonic patches predicted by Tesdall et al. (2002). The absence of the additional triple points and supersonic patches agrees with the suggestion by Vasil'ev et al. (2008) that the complex sequence of triple points only occurs during unsteady flow conditions, which is not the present case in the work of Defina, Susin & Viero (2008). It was noted that the four-wave model correctly predicts the wave pattern around the triple point but is not the solution of the GR, as the flow downstream of the Mach stem in the vicinity of the triple point is still supersonic and it is further turned towards the Mach stem. Defina, Susin & Viero (2008) therefore discuss a possible solution to better describe the developed wave characteristics of the GR. Note all results are based on the Froude number $F_0 = 1.7$ which is equivalent to the Mach number $M = 1.7$.

As seen in Figure 2.5(a), the solution looks at the general four-wave structure whereby the flow passing through incident shock I_1 deflects from $\theta_0 = 0$ to θ_4. This results in another triple point T_1 developing along I_1 with a corresponding four-wave reflection similar to that around T. The flow in region 7 is supersonic and similarly the flow is turned towards the Mach stem, and an addition triple point is then required along I_1. As seen in the shock polar presentation in Figure 2.5(b), for each triple point addition, the reflected shock polar reduces in size and flow conditions downstream of the expansion wave move closer toward the critical position for the incident shock, c_1. For an infinite number of triple points the solution will reach the critical condition along the incident polar shock, and the reflected shock will subsequently be reduced to a point (Defina, Susin & Viero 2008).

When comparing authors' results obtained for a Froude number of $F_0 = 1.7$ and a wedge angle of $\theta = 10^\circ$ and Vasilev and Kraiko's (1999) solution shown in Figure 2.1, both show that the sonic line is discontinuous when crossing the slip stream. Therefore, Defina et al.(2008) argue that the hypothesis given by Tesdall and Hunter (2002), for the developed sequence of triple points, seems unlikely to trigger the next supersonic patch when the compression wave forms from the reflection of the expansion fan off the sonic line (Defina, Susin & Viero 2008).

After the successful results obtained by Defina, Susin & Viero (2008), a similar paper on the VR within the framework of inviscid shallow water flow using improved high resolution



(a) Sketch of the reflection pattern (shaded area has $M < 1$)

(b) shock polar representation

Figure 2.5: Defina et al. (2008) first solution for GR: Four-wave reflection patterns close to triple points T and T_1 for $F_0 = 1.7$ and $\theta = 10^\circ$ (Defina, Susin & Viero 2008).

simulations was subsequently published. Their results again indicate the supersonic patch behind the reflected shock indicated by the thin dashed line shown in Figure 2.6(a). Note that Δ/h_M denotes the ratio between the grid size Δ and the length of the Mach stem h_M. They also confirmed the four-wave theory with the steady flow field and shock wave pattern close to the triple point. The following comparison between the analytical solution of the four-wave theory and the numerical results are superimposed in Figure 2.6(b). It is seen that the reflected shock, the Mach stem, the slip stream and the expansion fan have the directions predicted by the four-wave theory. Other quantitative comparisons between theory and computational results between the relative water depth and flow direction inside the supersonic patch gave errors smaller than 0.5% thus again confirming the validity of the four-wave theory.

The present numerical technique also allowed for the reconstruction of the shape of the reflected shock which is plotted in Figure 2.7. The plot consists of the computed angle β between the reflected shock and the x-axis, where the chosen coordinate system has the origin at the triple point with the y-axis tangent to the reflected shock at the origin. The plot gives a good indication of the curvature of the reflected shock which results in the acceleration of the flow from subsonic to sonic conditions behind the reflected shock wave for both the GR and VR (Vasil'ev et al. 2008). Their results also showed that the flow in the supersonic patch is not uniform, but is affected by a weak compression wave. It was suggested that the compression wave originates from the interaction of the supersonic flow in the patch with the subsonic flow immediately downstream, which results in a small deviation toward the reflected wall at the sonic line (Defina, Viero & Susin 2008).

In the most recent study related to the GR, Tesdall & KeyFitz (2010) formulate a problem

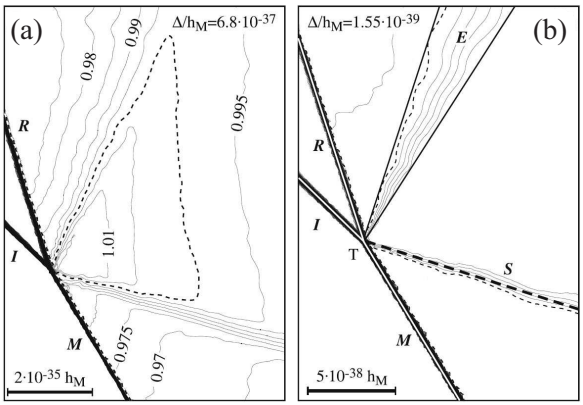


Figure 2.6: The Vasilev reflection pattern close to the triple point for $F_0 = 1.93$ and $\theta = 10°$: (a) The solid lines are iso-Froude contours and the thin dashed line is the sonic line; (b) the analytical solution of the four-wave model superimposed on the numerical solution (Defina, Viero & Susin 2008).

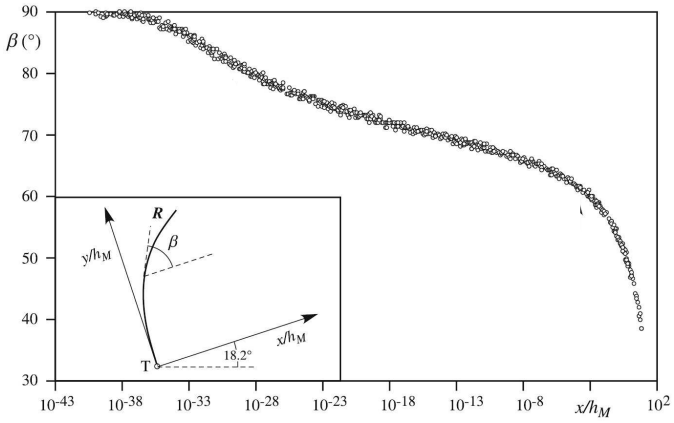


Figure 2.7: The angle β of the reflected shock as a function of the distance x/h_M from the triple point, indicating the curvature of the reflected shock wave which results in the acceleration of the flow from sonic to sonic conditions behind the reflected shock wave (Defina, Viero & Susin 2008).

for the unsteady transonic small disturbance equations (UTSD) equations which describes the effects of a rarefaction wave reflecting off a sonic line, as shown in Figure 2.8.

The solution of this problem is analogous to the weak shock reflection, known as GR, as the numerical work aims at modeling the behavior of the expansion fan interacting with the sonic line. The authors determine whether the reflection of the expansion fan and the sonic line form a compression wave which then steepens into a shock, as shown in Figure 2.9(a). The numerical results shown in Figure 2.9(b) confirms their study by showing that the expansion wave does in fact reflect off the sonic line forming a shock.

Unlike the GR, the numerical solution does not indicate any sign of a sequence of supersonic patches and shocks; however they do confirm the existence of a single shock which forms inside the supersonic region as depicted in Figure 2.10. Therefore, it is concluded that the

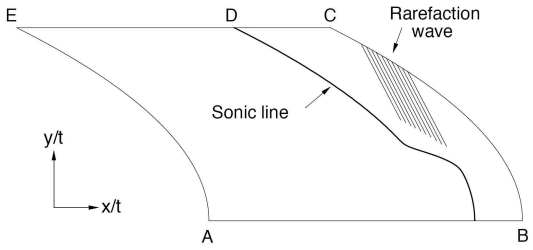
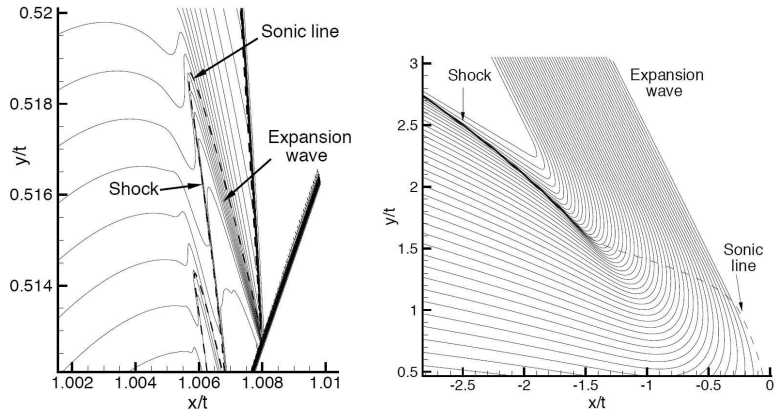


Figure 2.8: A schematic diagram of the computational domain. AB is the wall and BCDEA is the numerical boundary. In the region to the right of the sonic line, the flow is supersonic, and to the left it is subsonic (Tesdall & KeyFitz 2010).



(a) Numerical solution Tesdall & KeyFitz (2010).

(b) GR Tesdall et al. (2002)

Figure 2.9: Comparison between the reflecting rarefaction problem and Guderley reflection; both plots represent v-velocity contours. The region in (b) contains a single supersonic patch with the second patch visible at the bottom left. In both (a) and (b), the flow is supersonic to the right of the sonic line and subsonic to the left (Tesdall & KeyFitz 2010).

interaction of the rarefaction and the sonic line forms a transonic shock P_1P_2 coupled to the supersonic and subsonic regions across the sonic line and shock. The sonic line/shock is considered a new type of free boundary problem which has not previously been formulated or analysed, thus considerable work still needs to be conducted on this new type of free boundary problem.

To summarise the recent numerical results, the Guderley reflection solution has been found in two-dimensional shock reflection problems in UTSDE, the nonlinear wave system, the full compressible Euler equations, and the inviscid shallow water flow model. All the solutions show that the supersonic region is very small, therefore it is no surprise that the Guderley's proposed reflection could not for decades be detected experimentally. The numerical solutions also showed that the size of the supersonic region is proportional to the length of the Mach stem. It was estimated that a Mach stem of roughly one meter in length would be required to obtain sufficient resolution to experimentally observe the vicinity behind the triple point. This led to the unique experimental work conducted by

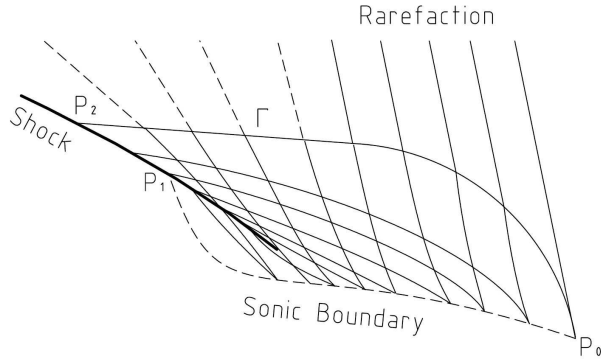


Figure 2.10: Schematic of the shock structure produced by the reflection of the rarefaction wave off the sonic line. The shock begins in the supersonic region, and P_1P_2 represents the transonic shock as shown (Tesdall & KeyFitz 2010).

Skews and Ashworth (2005) which is discussed in the following section.

2.2 Experimental Findings

Following the announcement of the Guderley Mach reflection found by Tesdall et al. (2002), Skews & Ashworth (2005) constructed a large-scale shock tube capable of producing Mach stem lengths an order of magnitude larger than those in conventional shock tubes. Figure 2.11 shows the basic size of the shock tube and a photograph of the facility. The facility consisted of a cylindrical cross-section driver, a short rectangular cross-section, a diverging driven section and a large rectangular cross-section whereby the cylindrical wave reflects off the roof producing the desired reflection pattern. The sketch shows in red some typical wave profiles as the shock propagates downstream. Note that Figure 2.11 represents the facility used by Skews, Li & Paton (2009) whereby a 15° diverging section is used instead of the 10° diverging section by Skews & Ashworth (2005).

The unique experimental study obtained high resolution schlieren photographs indicating small scale expansion structures behind the reflected shock. These results resembled the wave patterns observed by Vasil'ev & Kraiko (1999) and Tesdall et al. (2002), even though the incident shock wave generated was only approximately planar due to the cylindrical shock initially propagating through a diverging section. The tests were carried out on a 10° ramp with incident shock Mach numbers ranging from 1.05 to 1.1 (Skews & Ashworth 2005). Figure 2.12 is a photograph observed for M = 1.073 with a Mach stem length of 766mm. The first photograph is the original magnified schlieren image, and two images to the right were obtained using contrast adjustments and selected contrast thresholds (Skews & Ashworth 2005).

As shown in Figure 2.12, their results clearly detected the fourth wave, namely the expansion fan, and an indication of two accompanying shocklets as was observed by Tesdall

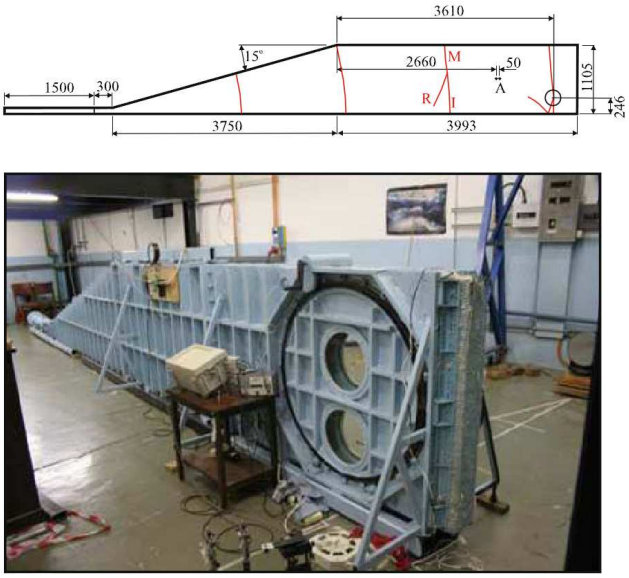


Figure 2.11: Shock tube used by Skews et al. (2009).

et al. (2002). The expansion wave is defined as the dark region directly behind the reflected wave, and the shocklet is the bright line underneath the reflected shock and the expansion wave. Since two shocklets (supersonic patches) were observed, this verified the numerical work produced by Tesdall et al. (2002), and in doing so resolved the von Neumann paradox. Analysis of the photographs determined that the expansion wave and terminating shocklet are estimated to be less than 2% of the length of the Mach stem, which is considerably larger than that predicted numerically.

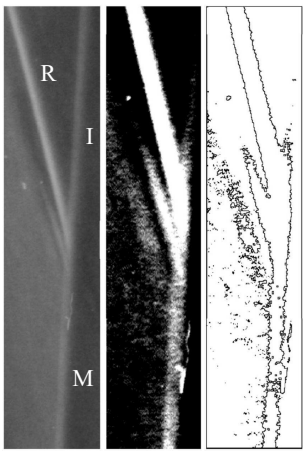
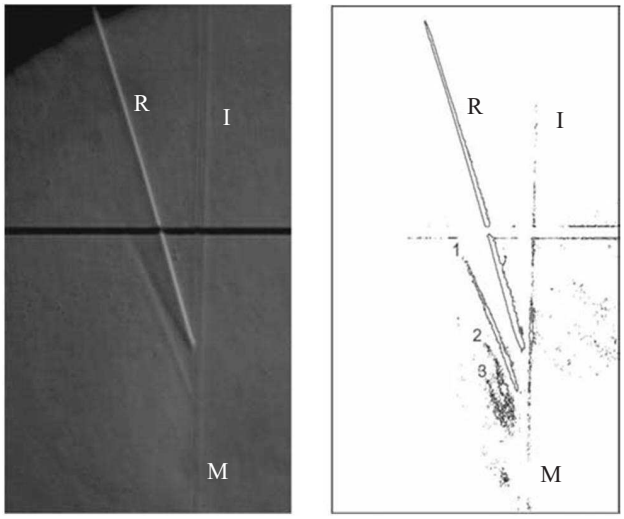


Figure 2.12: Complex flow structure behind reflected shock wave (Skews & Ashworth 2005).

As an extension to the recent experimental work, Skews et al. (2009) showed improved results of the Guderley Mach reflection for incident shock Mach numbers ranging from 1.05 to 1.1 on a 15° ramp. Figure 2.13(a) shows is an experimentally captured photograph where it is seen that there is clear evidence of the expansion fan directly behind the reflected

shock as proposed by Guderley (Skews et al. 2009). When analysing the contours in Figure 2.13(b), conclusive evidence of the first shocklet is found, indicated by 1, followed by two further regions (2 and 3) which strongly suggest the existence of the second and third shocklets. These results further satisfy Tesdall et al. (2002) observations, therefore ensuring the credibility of the solutions obtained numerically. However, it should be noted that the experimental observations of weak shock reflections off thin wedges does not show a defined slipstream even though a apparent Mach reflection occurs. This is probably because the weak shock reflection is really weak, making it difficult to observe the slipstream experimentally.



(a) Original schlieren image (b) Processed image to highlight shocklets

Figure 2.13: Experimentally captured Guderley Mach reflection for a wedge angle of 15° and Mach number of 1.12 (Skews et al. 2009).

In addition to the experimental photographs, quantitative data of the flow Mach numbers behind the major waves were determined using superimposed images. For an incident Mach number of approximately 1.125 it was found that the reflected wave is very weak with the flow Mach number ahead of the wave being less than 1.05 and the flow behind the wave being less than 0.98 respectively. The very weak flow Mach numbers in the vicinity of the triple point, called for very sensitive optical arrangements in order to capture the density gradients in the flow. It was mentioned that higher resolution tests utilising a shorter duration light source would better resolve the details of the flow features.

2.3 Motivation

Skews & Ashworth (2005) and Skews et al. (2009) discovered the existence of the Guderley reflection in the case of an approximately planar incident wave reflecting off a 10° and 15°

taper in a shock tube. Their results were only conducted for incident Mach numbers between 1.060 and 1.094, thus further study is required to investigate whether the Gurderley Mach reflection occurs for Mach numbers above this range ($M > 1.1$), and for a larger variation of tapered angles. Since all the experimental work conducted to date utilised a large diverging shock tube shown in Figure 2.11, high strength incident shock waves could not be achieved due to the decay in the incident shock wave strength along the length of the shock tube. Therefore, by using a smaller constant cross-sectional area shock tube the incident shock wave strength can be maintained.

Since there is limited experimental work in the weak irregular shock reflection domain, particularly the Guderley reflection, it is extremely important to find a practical means of observing this rare reflection without the use of a specially constructed facility. The idea of using a conventional shock tube to study these reflections came about when Skews (2007, personal discussion) observed a photograph of an expansion-fan-like region behind a reflected shock produced in a conventional shock tube. The observed Mach-like reflection consisting of an apparent expansion fan was accidentally produced by protruding pressure tappings in the shock tube facility. This led to the concept that a perturbation source instead of a ramp angle could be utilised to produce the Guderley reflection. The following experiment aims at verifying whether the Guderley reflection can be reproduced in a conventional shock tube utilising either a wedge angle or a perturbation source. Using a conventional shock tube will allow for a more practical method of studying the nature of these rare irregular reflections.

Chapter 3

Objectives

The primary objectives of this study in weak shock wave reflection domain were to:

1. Investigate whether the Guderley reflection exists in a Mach number range of 1.1 to 1.4 utilising a conventional shock tube.
2. Investigate what is the best means of producing the Guderley reflection, either by utilising a perturbation source or various ramp angles.

Chapter 4

Experiment Design

This chapter describes how the irregular Mach reflections will develop in the conventional shock tube facility, clearly outlining the difference between triple point propagation path in the previous experimental work and the underlining principle utilised in this study. An introduction to the shock tube layout and the required modifications are discussed. The two shock tube configurations, which consist of various perturbations sources and ramp angles are described below. Note that all the engineering drawings have been included in Appendix D.

4.1 Dynamics of the Study

As was discussed in the Literature Review, the Guderley reflection (GR) has already been observed experimentally by Skews et al. (2002) and Skews et al. (2009) using a unique large-scale shock tube layout seen in Figure 4.1. The GR was produced at the corner where the diverging section connects with the constant cross-sectional shock tube.

To produce a GR, the Mach stem of the reflection needs to be in the order of 1.0 m in length. Therefore, the shock tube utilised in Skews et al. (2009) and Skews & Ashworth (2005) required a height of approximately 1.1 m to provide sufficient space for the developed reflection to expand so that the expansion patch behind the triple point could be experimentally resolved. This shock tube facility was very impractical and expensive due to the size of the apparatus. The shock tube was limited to producing Mach stem lengths smaller than 1.1 m, and waves strengths weaker than M = 1.1.

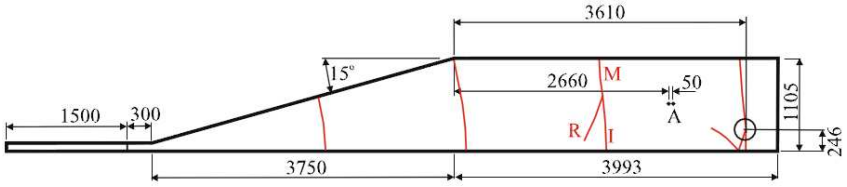


Figure 4.1: Schematic of developed reflection used by Skews et al. (2009)

Due to the limitations of the large scale shock tube, the current study makes use of a conventional shock tube to satisfy the first objective. An existing conventional shock tube layout described in Section 4.2 will be modified to accommodate various perturbations sources and ramp angles. Since the shock tube is only 0.45 m in height this means that a Mach stem of no larger than 0.45 m can be produced as the triple point thereafter interacts with the walls of the tube. Figure 4.2 shows the first reflection of the triple point off the floor of a conventional shock tube, where a new inverted reflection is created. As the reflection configuration propagates further downstream it reflects off the ceiling of the shock tube, inverting the reflection to its initial orientation. After a number reflections of the triple point it is seen that a jagged trajectory path is created. As seen in Figure 4.2, the Mach stem for the shock reflection before each triple point reflection transforms into the incident wave for the new shock reflection after the triple point reflection. A more detailed explanation of the dynamics of the multiple trajectory paths is described in the "Discussion of the Results" in Chapter 7.

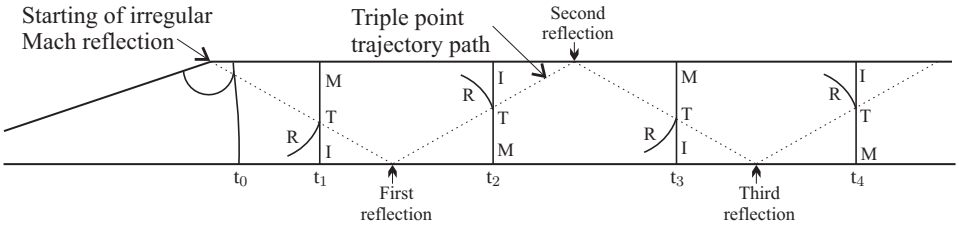


Figure 4.2: Progression of developed irregular Mach reflection downstream for different time steps t_i showing the overall trajectory path of a triple point in a conventional shock tube.

In Figure 4.2 it is seen that at any time interval t_i downstream, the actual length of the Mach stem is smaller than the height of the tube (0.45 m), which according to Vasilev & Kraikio (1999) would not be suitable to develop a Guderley reflection as the Mach stem is required to be in the order of 1.0 m. The following study is constructed on a hypothesis proposed by Skews (personal communication, 2008) which states that the Mach stem attached to the shock reflection is not the apparent Mach stem length observed at each time interval, but rather the overall vertical distance traveled by the triple point from where the reflection was created. Therefore, the overall vertical distance traveled by the triple point is named the virtual Mach stem length.

Utilising this hypothesis it is possible to produce virtual Mach stem lengths in the order of 2.0 m in a sufficiently long (9.0 m) conventional shock tube. The virtual Mach stem hypothesis will be tested by investigating whether the GR does in fact occur in the parameters of the experimentation, furthermore the relationship between the size of the supersonic region and the Mach stem length will also be investigated and discussed in Chapter 7.

With the application of this hypothesis, the current study makes use of two methods, utilising either a perturbation sources or a ramp angle, to satisfy the first objective of this research. The first method utilises a triangular perturbation source on the floor of the shock tube. A schematic shown in Figure 4.3 shows the interaction of the a normal shock wave with the perturbation source, resulting in a irregular Mach reflection which then propagates downstream.

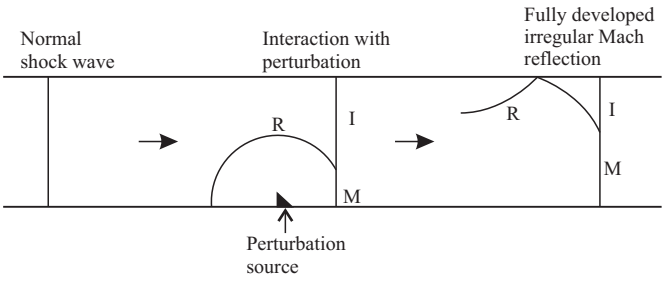


Figure 4.3: Developed irregular Mach reflection due to the normal shock reflecting over a triangular perturbation source.

The second method shown in Figure 4.4 utilises a diverging section similar to that used in the previous experimental work. This method produces an improved irregular Mach reflection as there is only a single change in direction as a result of the change in direction of the ceiling of the shock tube. By simply altering the angle of the diverging section the effects of various wedge angles on the developed irregular Mach reflection can be easily studied. The only issue of using the diverging section is that a cylindrical shock wave instead of a normal shock wave develops in the diverging section, but as discussed in Chapter 4.4 the radius of curvature of the incident shock wave is large and is not apparent in the experimental images obtained.

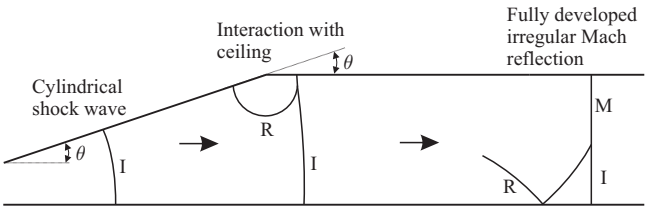


Figure 4.4: Developed irregular Mach reflection due to the cylindrical shock reflecting off the ceiling of the expansion chamber.

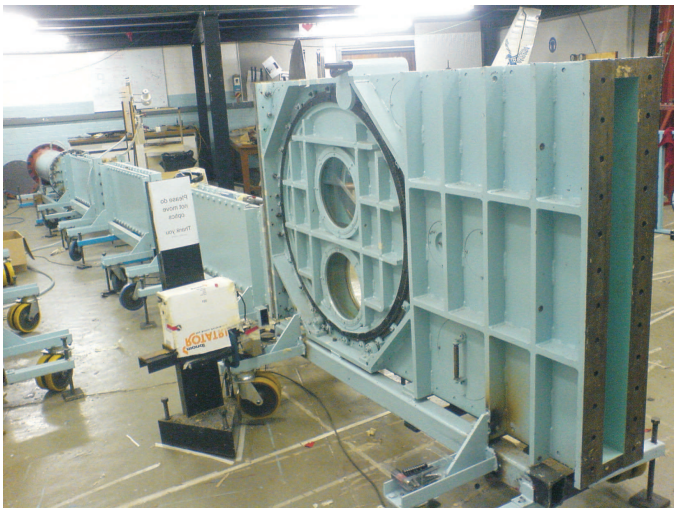
The following sections in this Chapter describe the existing shock tube facility and the modifications which were undertaken on the facility to conduct this study.

4.2 Existing shock tube

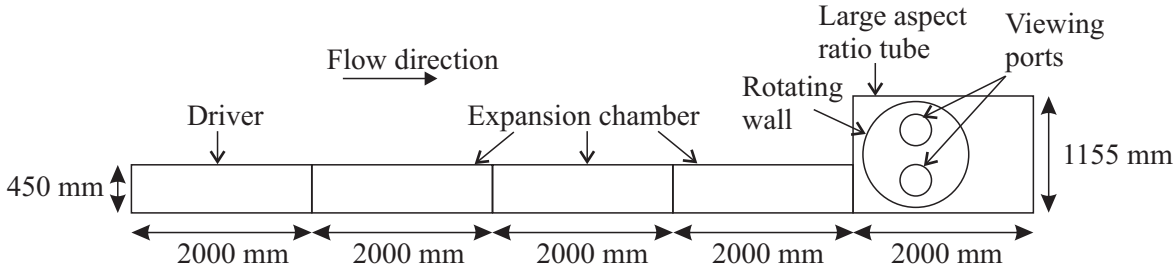
A newly manufactured shock tube, named the Lorenzo's tube, was the conventional shock tube utilised in the experimentation. The shock tube and the accompanying driver was

designed by a Master's student (2008) from the School of Aeronautical, Mechanical and Industrial Engineering, University of the Witwatersrand. Figure 4.5(a) shows the shock tube layout, where the Lorenzo's tube is attached to a large aspect-ratio tube consisting of two large rotating walls on either side of the tube; each wall consists of two fixed viewing ports. The rotating walls allow the viewing ports to rotate into various positions if the wave structure overshoots the viewing port.

The overall dimensions of the assembled shock tube are approximately 10 m in length, 1.2 m high and 0.1 m wide, as shown in Figure 4.5(b). It is seen that the expansion section consists of three sections each are 2.0 m in length making it is possible to shortened or lengthen the shock tube if necessary. The 0.305 m^3 pressure tested driver makes up the compression chamber, whereby a safe operating pressure of approximately 10 bar can be contained, producing a maximum Mach number of roughly 1.67 given that the conditions downstream are atmospheric (0.83 bar). It should be noted that the most vulnerable component in the shock tube are the viewing ports, which have been calculated using a safety factor of 2 to withstand a maximum driver pressure of 10 bar without inducing any stress cracks in the viewing ports.



(a) Photograph of shock tube assembly



(b) Schematic indicating internal dimensions of the shock tube assembly

Figure 4.5: Existing shock tube layout.

In order to pressurise the driver, a diaphragm (plastic sheet) is placed between the driver and the first expansion chamber. The bolts and nuts are fastened with the use of an impact wrench securing the diaphragm between the driver and the first expansion chamber section. When the driver is pressurised to the required pressure, the plunger is triggered, and a normal shock is generated due to the rupture of the diaphragm. The shock reflection travels down the expansion chamber where it is then photographed at the viewing port.

4.3 Modified Large-Aspect Ratio Tube

The main purpose of the experiment is to utilise a conventional shock tube to develop a GR. As shown in Figure 4.5(b) above, the internal heights of the expansion chamber and large-aspect-ratio tube are 450 mm and 1155 mm respectively. The internal height of the large-aspect ratio tube needed to be reduced by 705 mm so that a constant internal height of 450 mm could be maintained throughout the entire shock tube assembly. A constant internal height was achieved by the insertion of a plug-in section in the large-aspect ratio tube, illustrated by the hatched triangle in Figure 4.6.

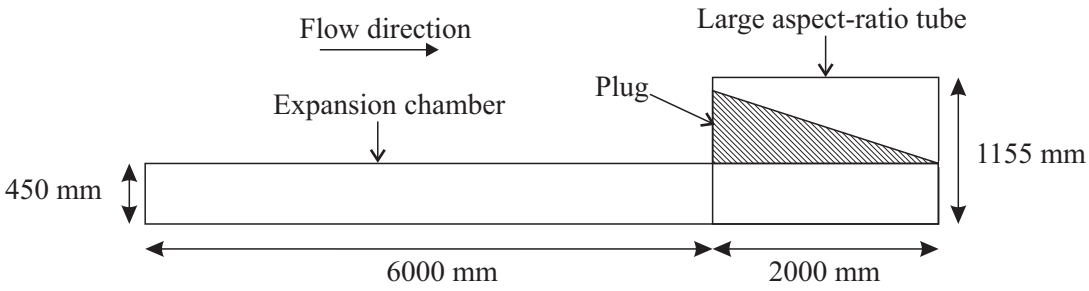


Figure 4.6: Schematic of internal dimensions for the existing expansion chamber and the large-aspect ratio tube.

The required length of the plug was determined by analysing the rotated positions of the observation window furthest downstream. Figure 4.7 shows two rotational positions for the observation window. It is seen that the plug only requires a length of approximately 1.0 m so that the full rotational capability of the observation window could be utilised.

Figure 4.8 shows the design of the plug which was constructed from mild steel. The wedge-shaped plug consists of a 1.0 m length standard 100 mm u-channel which is supported by a rectangular plate and a rib. The u-channel and rib were welded together, and then fastened onto the supporting plate, which was finally securely bolted onto an existing end-flange from the existing shock tube. The plug structure displayed in Figure 4.8 was designed for a maximum incident wave Mach number of 1.5. However, it should be noted that this structure was designed using a safety factor of 10, thus much larger Mach numbers can be supported.

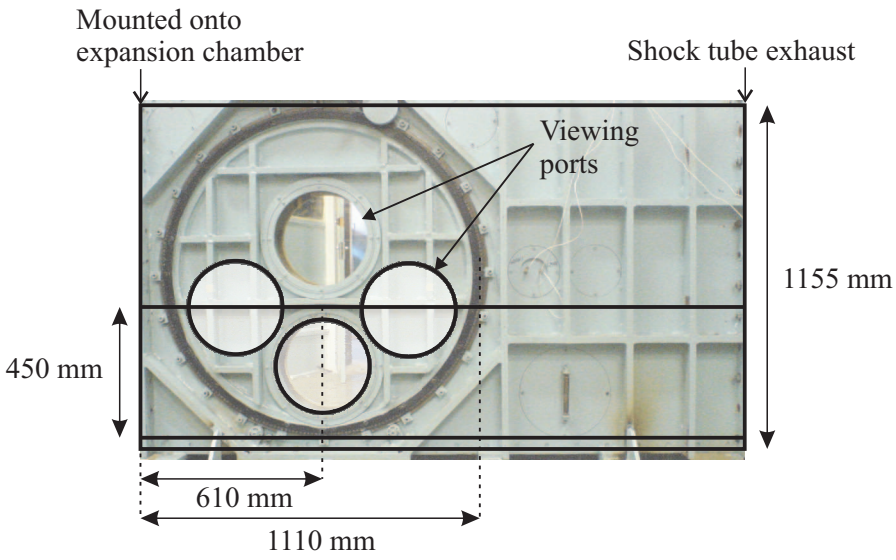


Figure 4.7: Rotational positions for observation window.

When the viewing ports are positioned vertically as shown in Figure 4.5, the u-channel of the plug assembly passes between the two viewing ports of the rotating wall. If the viewing ports are rotated to a different position, this will result in the ports sliding over the sides of the u-channel and possibly scratching the glass. Protective tape was adhered to both sides of the u-channel to prevent any damage to the viewing ports and the internal surface of the tube. Note that the engineering drawings for the given plug have been included in Appendix D. Both shock tube configurations (perturbation source and ramp angles) described below make use of the plug-in section as it is a fundamental part of the shock tube assembly.

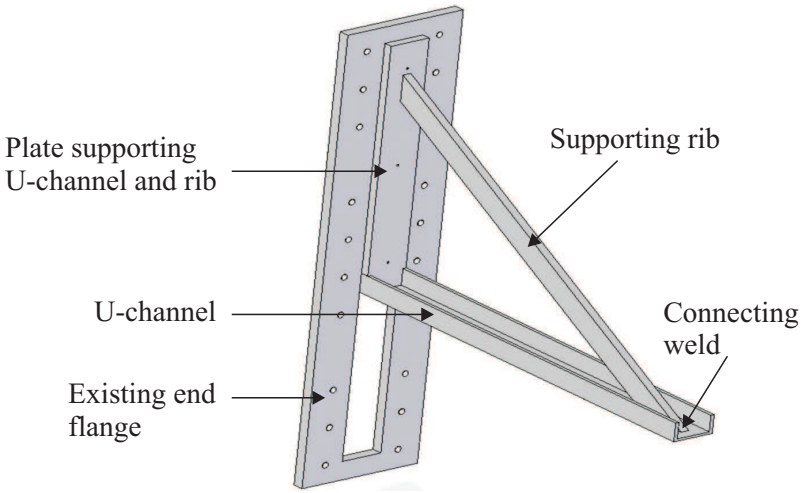


Figure 4.8: Design for plug which is inserted in the large-aspect ratio tube.

4.4 Shock Tube Configurations

The experiment consists of tests conducted on two different shock tube configurations. The first configuration consists of the existing shock tube described above including a mounting plate where various perturbation sources can be fastened. The second configuration makes use of a diverging section at the beginning of the expansion section. Note that testing was initially conducted on the first shock tube configuration, thereafter based on the experimental results it was decided that a second shock tube configuration would be necessary to produce an improved shock reflection.

4.4.1 First Configuration

The first configuration utilises the existing shock tube layout with two perturbation sources positioned in the expansion chamber. As shown in Figure 4.9, the perturbation source is fastened at the bottom of a mounting plate. The mounting plate can then be secured between any two sections of the expansion chamber. The mounting plate and perturbation source assembly provides flexibility in designing a number of inserts of various profiles. In this experiment only two inserts were manufactured.

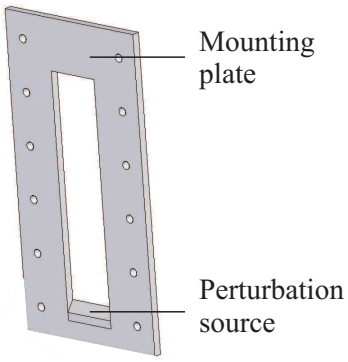
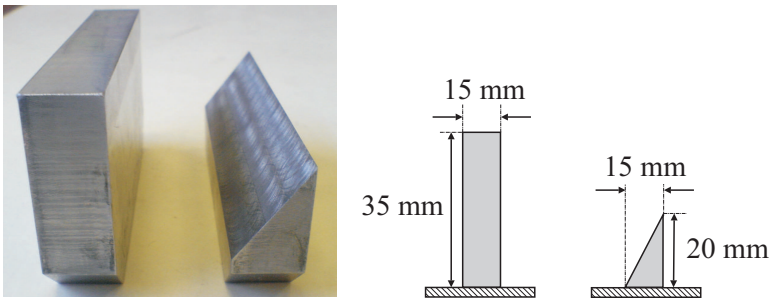


Figure 4.9: Mounting plate with attached perturbation source.

The two manufactured inserts are illustrated in Figure 4.10. The first insert has a plain rectangular profile with an overall perturbation height of 35 mm, whereas the second insert has a triangular profile with a height of 20 mm, and an angle of 53.1°. Note that the angle of the triangular profile is of no particular importance, and was merely chosen to reduce the strength of the second reflected shock produced when the shock passes over the perturbation source.

4.4.2 Second Configuration

After having completed testing with the first shock tube configuration, a new layout was designed based on the original setup used by Skews and Ashworth (2005) and Skews et al. (2009). The second setup consists of a diverging section at the beginning of the expansion chamber, ensuring the development of a clearly defined shock reflection as the flow field no



(a) Manufactured mild steel inserts (b) Dimensions for inserts

Figure 4.10: Perturbation sources

longer experiences an abrupt change in the area as was produced by the perturbation source which produced multiple reflected waves. The following configuration also required the construction of a new driver and plunger section.

Diverging Section

Three ramp inserts of 10°, 15°, and 20° were selected for the diverging section to produce the desired irregular Mach shock reflections. The 10° and 15° inserts were chosen as these are equivalent to the ramp angles utilised by Tesdall et al. (2002), Skews and Ashworth (2005) and Skews et al. (2009). This allows the current results to be compared with previous studies. In order to expand the testing domain, a 20° insert was also manufactured. The experiment investigates incident shock waves in the test section with Mach numbers in the range of 1.10 to 1.40.

Based on the dimensions of the expansion chamber, the outlet dimensions of the diverging section are 450×100 mm^2, where 100 mm is the internal width of the shock tube section. The inlet dimensions of the diverging section were chosen as 100×100 mm^2 as the best aspect ratio for efficient diaphragm rupture is 1:1. The corresponding length of the diverging section could thus be calculated based on the inlet and outlet dimensions. A diverging section length of 2000 mm was chosen which gave a ramp insert angle of approximately 10°. As shown in Figure 4.11, two ramp sections of 15° and 20° respectively could be contained individually within the diverging section using additional supports.

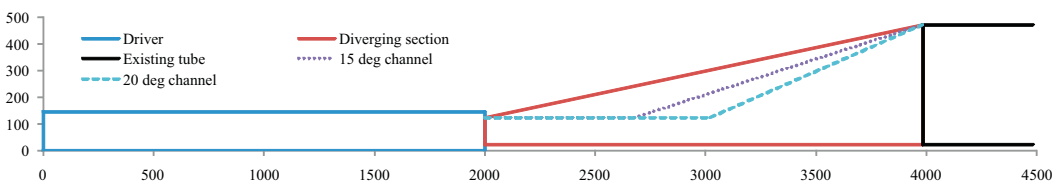


Figure 4.11: Diverging section dimensions for the various ramp inserts.

The ceiling, floor, and both the ramp sections of the diverging section were constructed from standard 100×50 u-channel sections which have been ground on both sides to provide a uniform surface to ensure a well sealed assembly. The manufactured 20° ramp section is shown in Figure 4.12, where it is seen that a horizontal channel is fastened onto a slanted channel to produced the desired ramp angle for the ceiling of the diverging section.

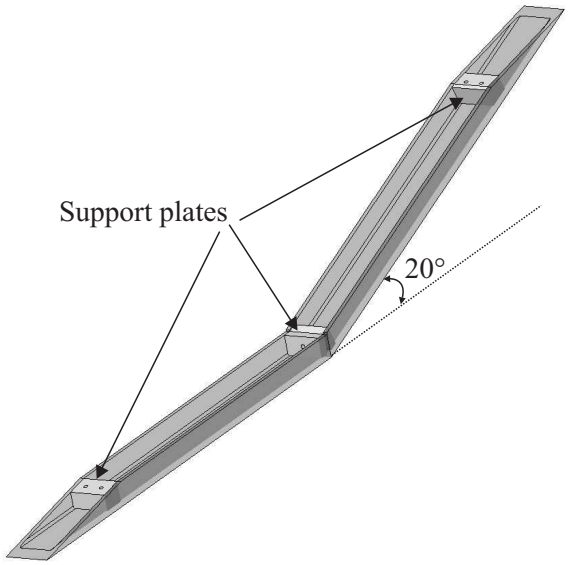


Figure 4.12: 20° ramp assembly.

Figure 4.13 shows the complete assembly of the 15° ramp section which is supported through the ceiling of the diverging section by four bolts. The following bolts can be removed and replaced by plugs to seal the ceiling of the diverging section when testing is conducted on the 10° ceiling, or alternatively the 20° ramp section may be inserted also supported by the four bolts. Thus with the use of the support holes through the ceiling, a number of different ramp sections can be manufactured to study a range of ramp angles.

Note that the insertion and removal of the ramp sectioned consists of removing one of the side plates, the ramp section was then carefully positioned within the diverging section and supported by the permanent 10° u-channel. Due to the considerable weight of the side plate, a hand operated winch was used to guide the side plate away from the shock tube and consequently reattaching it.

Plunger Section

The plunger section as seen in Figure 4.14 has a constant cross sectional area of 100×100 mm^2, a length of 300 mm, and includes a pricker mechanism. The ceiling and floor of the plunger section were also made of the standard u-channel which was utilised throughout the tube. The plunger section connects the driver to the inlet of the diverging section, the circular and rectangular flanges at each end fasten onto the corresponding circular flange of

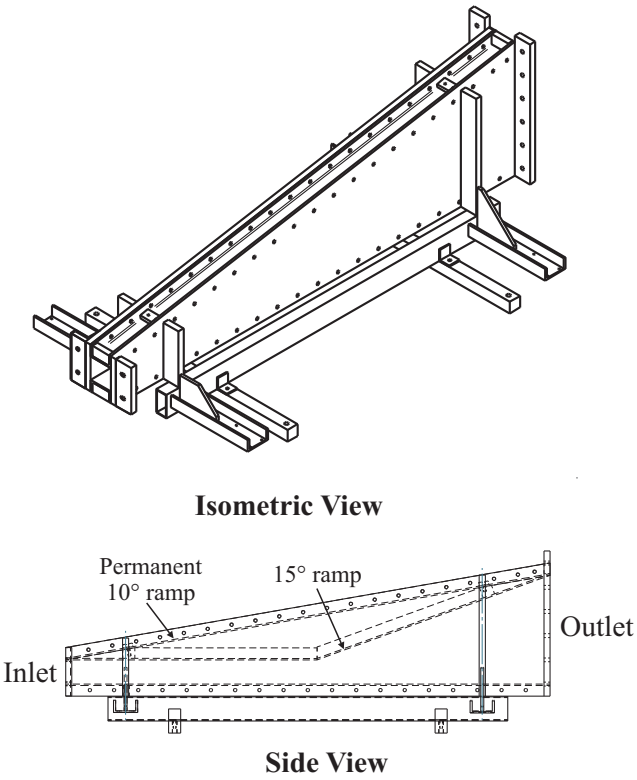


Figure 4.13: Diverging section assembly.

the driver and the rectangular inlet of the diverging section.

The pricker mechanism was used to rupture the diaphragm between the two circular flanges of the driver and the plunger section. As seen in Figure 4.14, the pricker mechanism fastens onto the external wall and consists of a stainless steel needle. The needle is manually triggered by pulling it back and engaging the catch, whereby it is then fired by a compressed spring. When the catch releases, the needle punctures and ruptures the distended diaphragm. Note that the pricker mechanism was easily adjusted to suite different testing conditions to ensure that there is sufficient travel in the needle to allow the diaphragm to consistently burst during tests. Once the diaphragm ruptures, the initially unsteady generated shock passes through the plunger section thus giving the shock wave sufficient time to develop into a well structured shock before entering the diverging section.

Driver

A new driver (pressure vessel) was designed to withstand a maximum pressure of 10 bar, capable of producing a maximum initial Mach number of approximately 1.67 if the downstream conditions are atmospheric. With an internal diameter of 154 mm, the internal cross sectional area of the driver was chosen to exceed that of the inlet area (100×100 mm^2) of the diverging section. This is important to produce a "clean" rupture for an effective shock wave to be generated.

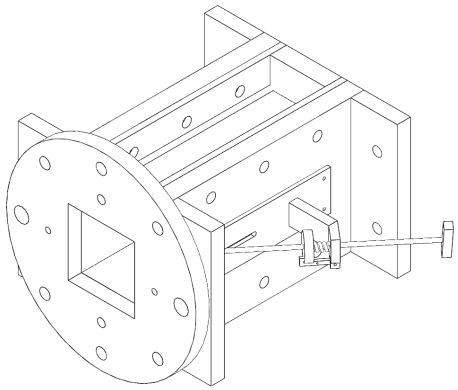
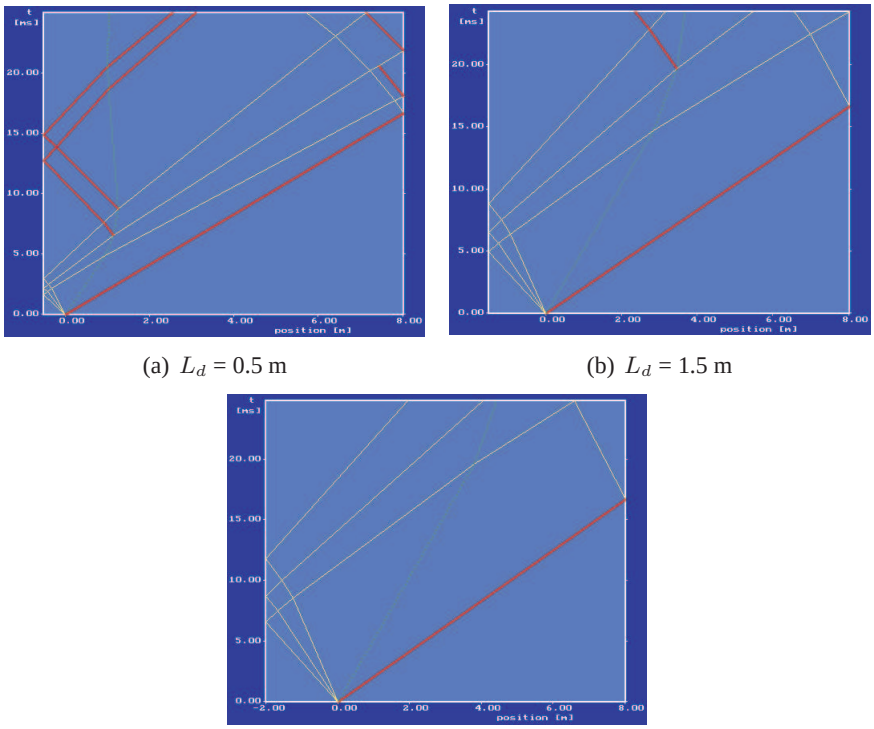


Figure 4.14: Plunger section with accompanying pricker mechanism.

The overall length of the driver was chosen by plotting the corresponding wave diagrams for varying driver lengths for a maximum intended Mach number of approximately 1.4. Figure 4.15 displays the wave diagrams for driver lengths of 0.5, 1.5, and 2.0 m respectively. Note that the plots resemble a simplified constant cross-sectional tube, as the diverging section could not be accounted for in the simulations. However, as Ashworth (2005) determined in his CFD simulations, the diverging section does not drastically change the effects of the rarefaction waves, and that only a slight deviation is seen from the expected linear curve (Skews & Ashworth 2005). Since the change in area of Ashworth's shock tube facility was a factor of 11, and the tube used in this investigation is only a factor of 4.5, this means that the effects of the area change are not as significant, and thus the wave diagrams are sufficiently accurate for the selection of the driver length. It is seen in Figure 4.15(c) that the testing time increases as the length of the driver increases, therefore a 2.0 m length driver was chosen as this provided a sufficient time interval between the incident and reflected expansion wave in the testing section.

Figure 4.16 shows the driver assembly. In order to easily manoeuvre the driver, a support stand was made which consists of a set of wheels and a guide rail so that the driver can be easily lodged or withdrawn from the plunger flange so the diaphragm can be replaced. The specifications of the driver and the pressure certificate are given in Appendix C.



(a) L_d = 0.5 m (b) L_d = 1.5 m

(c) L_d = 2.0 m

Figure 4.15: Wave diagram plots for a Mach number of 1.40 and various driver lengths.

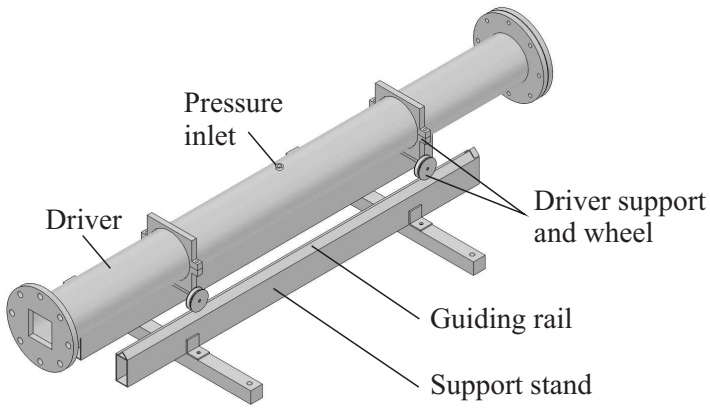


Figure 4.16: Driver assembly.

Chapter 5

Apparatus

This chapter briefly describes the two shock tube configurations and the instrumentation used in the experiment. The design, modifications and the functioning of the existing shock tube were outlined in the previous Chapter.

5.1 First Shock Tube Configuration

As described in Section 4.4, the first shock tube configuration consists of the existing shock tube configuration shown in Figure 4.5 combined with the triangular plug-in which maintains the height of the shock tube in the large-aspect ratio tube, and the perturbation mounting plate which supports the perturbation sources. Figure 5.1 is a schematic of the shock tube layout, were it is seen that the mounting plate can either be positioned at "A" between the first and second expansion chambers or at "B" between the second and third expansion chambers respectively. Both these positions were used to vary the distance in which the triple point of the developed reflection travels before arriving at the test section (large-aspect ratio tube). The important correlation between the overall distance traveled by the triple point and the virtual length of the Mach stem will be discussed in Chapter 7.

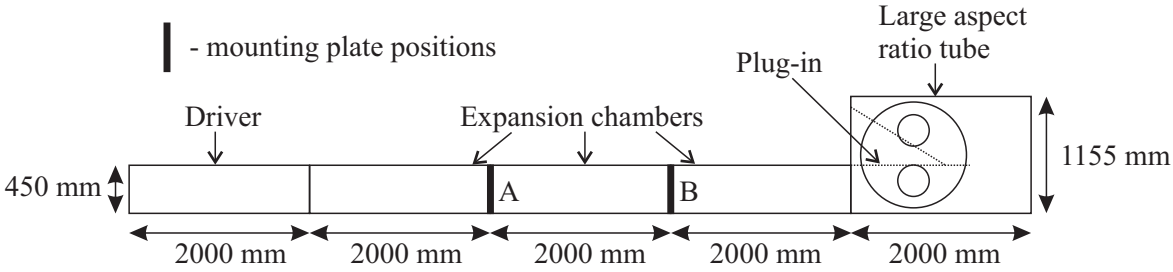
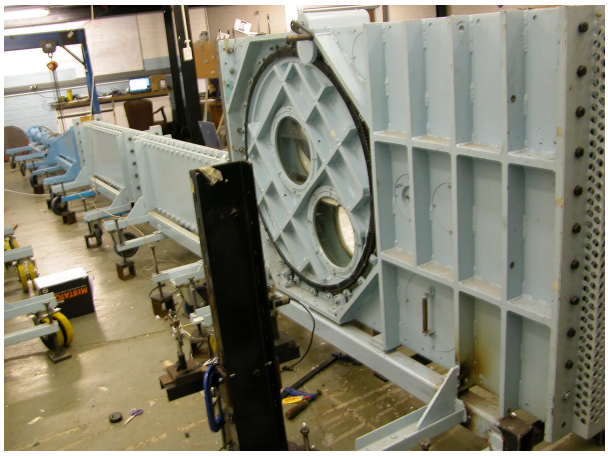


Figure 5.1: Schematic of first shock tube configuration.

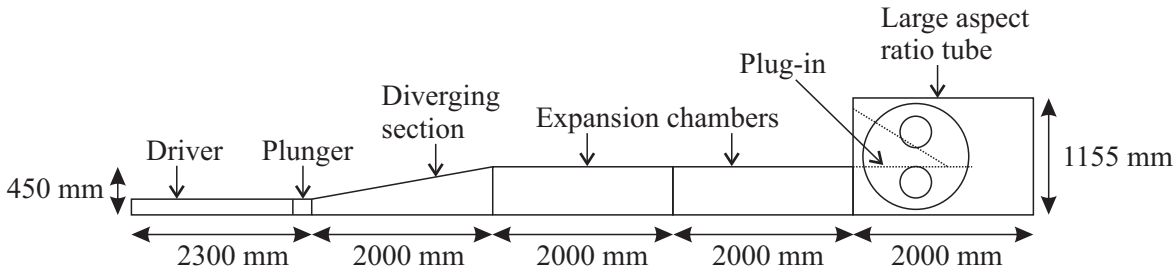
5.2 Second Shock Tube Configuration

The second configuration makes use of the newly designed driver and diverging section as shown in Figure 5.2. As seen in Figure 5.2(b) the configuration makes use of two constant

area expansion chambers and a varying area expansion chamber (diverging section). Either two expansion chambers as shown in Figure 5.2(b), or one expansion chamber can be utilised depending on the downstream propagation length required.



(a) Shock tube layout.



(b) Schematic of second shock tube configuration.

Figure 5.2: Diverging shock tube configuration.

Figure 5.3 below is an image of the newly designed driver and diverging section. The 15° and 20° ramp inserts are inserted into the diverging section by removing one of the side plates as shown in Figure 5.4. A chain block was used to support the side plate, while the ramp insert was manually placed into position and fastened onto the ceiling of the diverging section. Since the angle produced by the diverging section was critical for the developed reflection, it was important that the downstream edge of the ramp insert was correctly aligned with the expansion section. It should be noted that a 20μm paper gasket was taped to all joining surfaces and sections of the shock tube to reduce any leakages during the operation of the shock tube.

The driver was pressurised to 13 bar for the 1.4 Mach number runs, this meant that the driver was being pressurised above its maximum operating pressure of 10bar. However, the manufacturer of the driver verified that the driver could be safely operated at 13 bar since the flanges and the round tube of the driver were designed to withstand a maximum pressure of 16 bar.

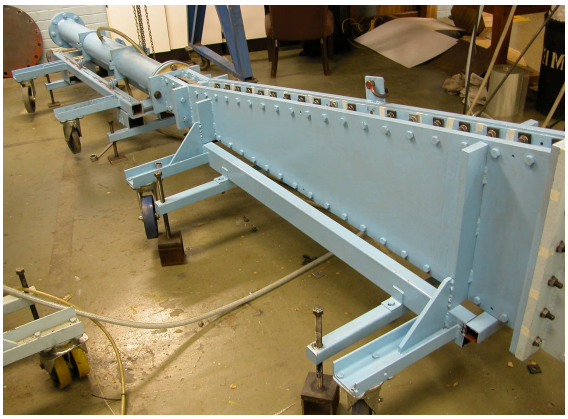


Figure 5.3: Newly manufactured diverging section and driver.



Figure 5.4: Replacement of a ramp section in the diverging section.

5.3 Data Acquisition Instruments

Data acquisition instruments were used to detect the shock passing by two high speed pressure transducers which consequently triggers a light source at a specified time delay in order to capture the wave at the viewing port.

Three pairs of transducer ports are located on the third expansion chamber, however only the pair furthest downstream were used as shown in Figure 5.5. The two pressure transducers are separated by 50 mm, and are situated at the centre height of the expansion chamber. By analysing the pressure traces the time delay between the two pressure spikes were used to determine the incident shock wave Mach number. The speed of the incident shock wave was then used to calculate the time delay required to capture the shock at the centre of the viewing port, given that the distance between the first downstream transducer and the centre of the viewing ports is approximately 790 mm. It should be noted that the large-aspect ratio tube consists of a number of transducer ports which were not utilised as none were located

in the constant cross-sectional area region.

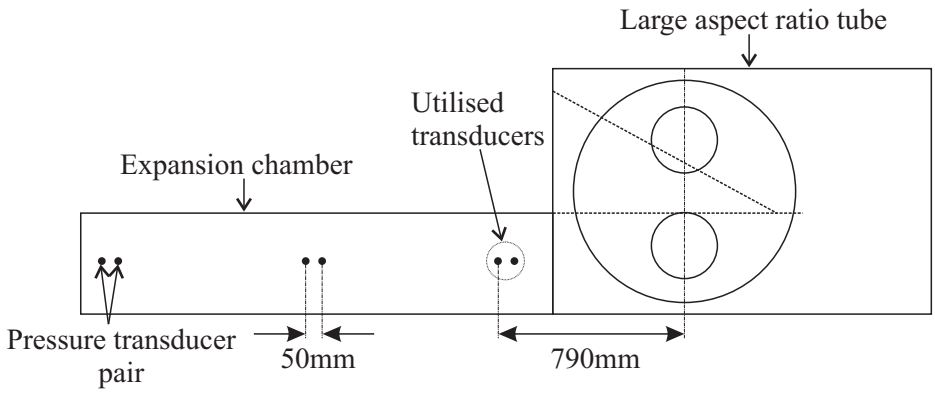


Figure 5.5: Pressure transducer ports on expansion chamber.

The following data acquisition instruments were used:

- Two high speed fast response PCB Piezotronics ICP® sensor piezo-electric pressure transducers (Model 113A21). Serial number: 14052 (Channel 2, downstream); Serial number: 14050 (Channel 4, upstream).
- High speed PCB ICP® sensor signal conditioner (Model 482A22) which amplifies the signals from the pressure transducers.
- Yokogawa DL1540 digital oscilloscope which receives the output signals from the signal conditioner and plots the voltage against time. The plots are then used to determine the respective Mach numbers for each experiment. The triggered output signal from the oscilloscope is then forwarded to the time delay unit.
- Time delay unit, Centre for Instrumentation Research, Cape Technickon with 50 to 99999 μs and 0 – 2.5V output. The time delay unit then utilises the specified time delay which triggers the xenon flash power supply (Model C3684), and as a result causes the xenon light source to emit one pulse of light.

5.4 Optical System

A general Z-layout schlieren setup was used to capture the wave structure produced by the perturbation sources and ramp inserts. In order to capture the weak irregular Mach reflection as well as the highly anticipated expansion fan and terminating shocklets a sensitive schlieren system was required.

The schlieren setup utilised is illustrated in Figure 5.6. As seen the system consists of two knife edges, one after the light source and the other before the camera. A xenon flash light source with an exposure pulse time of 1.9 μs is shone through a converging lens and focused on the first knife edge. The first knife edge consists of two razor blades separated by less

than 1 mm controlling the amount of light entering the system. The distance between the first mirror and the knife edge is exactly set to the focal length of the parabolic mirror. The second knife edge is a single razor blade, and functions mainly to adjust the sensitivity of the optical system. The distance between the second knife edge and the second mirror is also the mirror's focal length. The light bending around the second knife edge is then concentrated by a converging lens so that the image fits onto the digital camera's sensor.

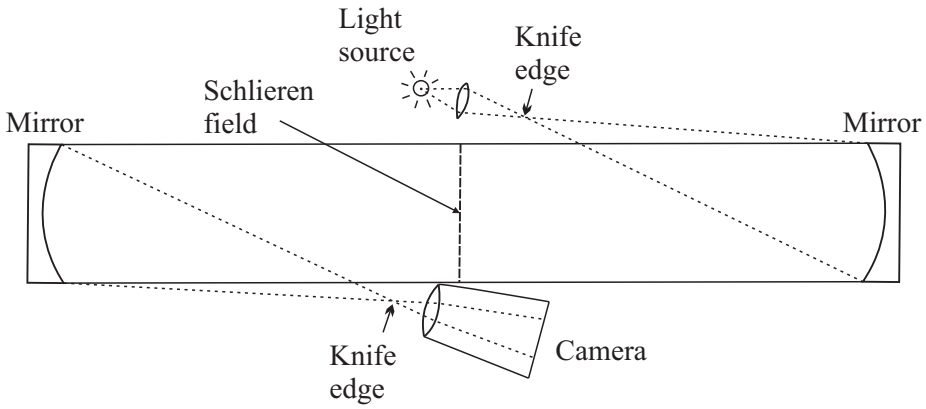


Figure 5.6: Schematic of a basic Z-layout schlieren system

The two parabolic mirrors mentioned above, have a diameter of 12.5 inch (312 mm) and a focal length of 1.905 m. These two mirrors were used at opposite ends of the viewing port (schlieren field) to produce a parallel beam of light passing through the test section. For the light to be parallel, the distance between the two mirrors must be larger than twice their focal length. It should be noted that all the components of the schlieren system were at the same level as the centre of the viewing port to ensure that a clear and undistorted image was obtained. However, as discussed in Chapter 7 the images produced by the schlieren system do not produce a uniformly sensitive image, this was due to the difficulty in aligning the schlieren system in the laboratory and the optical stigmatism produced by the converging lenses.

Two sets of images were captured: single-frame images using a Nikon D60 digital camera of 12.34 million pixels and multiple-frame images using a high speed camera of 0.5 million pixels. The setup of each camera is discussed below.

5.4.1 Single Frame Camera

The high resolution single-frame images were captured using a 1.9 μs xenon light source and one light-filter after the first knife edge. The filter was used to reduce the intensity of light entering the schlieren setup. The shutter of the camera was controlled manually by a wireless remote control, note that the camera was set on the bulb trigger mode. All the single-frame images were captured at least twice to ensure the repeatability of the results. The sensitivity of the system was continuously attuned by fine adjustments of the knife edges during testing resulting in varying illumination of the images. The sensitivity of the

camera was adjusted to suite the amount of light being cutoff by the first knife edge and the filter. Generally an ISO of 400 was utilised for the photographs. It should be noted that the flow pattern behind the triple point was best resolved when the knife edge was positioned parallel to the reflected shock wave allowing a high sensitivity in detecting the pressure gradients in the direction of the reflected shock wave.

5.4.2 Multiple-Frame Camera

The million frame per second camera manufactured by The Cooke Corporation was used together with a constant light source (a standard 45 W car lamp). Since the shutter of the camera is programmed (exposure, the delay between frames, and the number of frames) it was necessary to use a constant light source so that the viewing port was continuously lit to capture the propagating shock wave reflection. The multiple overlaid images of the moving shock wave reflection are then analysed to determine the trajectory path of the triple point so that the speed and direction of the flow behind each shock wave can be determined. Due to the low pixel resolution (0.5 million pixels) of the camera and the large field of view, the expansion patches were barely visible but the three main waves were clearly presented to obtain quantitative data of the wave velocities and the deflection angles. The procedure for analysing the multiple frame images is further discussed in Section 6 on page 47.

The specification of the high speed camera are given below.

- Manufacturer : PCO Computer Optics GmbH
- Serial : 335 CG 0073
- Trigger : TTL-signal
- Width : 1 μs...1 ms
- Delay : 0 μs...999 μs
- Cycle : 0 - 9

5.5 Control Panel

The control panel is located on a stand next to the data acquisition instruments such that the shock tube can be conveniently operated from a standing position. The control panel is supplied by a high pressure compressor with a limited pressure of 15 bar which is supplied to the driver. The control panel consists of the following components:

- Inlet hose from the high pressure compressor.
- A Wika pressure gauge connected to the driver via a 1/2” BSP radial connection, so that the static pressure can be measured. The gauge has a pressure range of 0 to 1000

kPa with a resolution of 5 kPa and an accuracy of 1%. (Make: Wika, SN: 720362, Catalog. No: 232.50.160)

- A pressure regulator to smooth out and reduce the pressure supplied from the compressor into the driver.
- A global-type 317 valve to control the pressure supplied from the compressor into the driver.
- A venting ball valve to release the pressure in the system, in case of an emergency such as a premature piercing of the diaphragm.
- An outlet hose which supplies the driver with pressure.
- A mercury thermometer to measure the ambient temperature. Temperature range of -5 to 50°C and a resolution of 0.2°C.

It should be noted that both the small and large drivers were pressurised from the same 15 bar pressure line.

5.6 Diaphragm

To obtain the various flow speeds required for the experiment, different diaphragm thicknesses and combinations of mylar sheeting were used. As mentioned before the diaphragm is inserted between the flanges of the driver and the plunger section respectively. The two flanges are lined with a rubber gasket so that an effective seal is produced around the diaphragm when the flanges are fastened together. The natural burst pressure is an important property of the diaphragm as this is the pressure in which the diaphragm ruptures without having to be manually ruptured.

As part of the calibrating process, various diaphragm thicknesses of one or multiple layers were ruptured to determine their corresponding natural burst pressures. The acceptable range of operating pressures for each diaphragm configuration was chosen to be less than 90% of the natural burst pressure to prevent premature bursting. The bursting pressure being the pressure in the driver when the pricker pierces the diaphragm.

For the driver in the first configuration a diaphragm of 125 μm was used, producing a natural burst pressure of 2.5 bar. None of the M = 1.2 and M = 1.3 tests in this setup exceeded a static pressure of 2.0 bar. For the driver utilised in the second shock tube configuration the diaphragm thickness, the number of layers and the corresponding natural burst pressures for each diaphragm arrangement are listed in Table 5.1.

Table 5.1: Diaphragm properties for driver section in the second shock tube configuration.

Diaphragm thickness (μm)	Number of layers	Natural pressure ($\pm$20 kPa)	Mach number produced
50	1	200	1.1
50	2	400	1.2
100	1	390	1.2
100	2	780	1.3
100	3	1200	-
100	4	1600	1.4

5.7 Computing Facilities

The following hardware and software was used for all the CFD simulations and CAD modeling.

5.7.1 Hardware

All simulations were carried out on three desktop computers from the Computational Modeling Computer Laboratory. The specifications of the computers utilised are given below:

- Processor: Intel(R) Xeon(R) CPU X3370 @ 3.00GHz
- RAM: 4.00GB

5.7.2 Software

All the software below was obtained from the School of Mechanical Engineering, University of the Witwatersrand, and all were academic versions.

Operating system: Microsoft Windows 7 Professional (64-bit)

Computational fluid dynamics software: Fluent from the software package Ansys 12.0 was used to develop the shock tube model and mesh generation. Simulations were thereafter run for different shock tube configurations and initial conditions.

Visualisation software: Tecplot 360 2009 was used for all the post-processing of the simulations obtained from Fluent.

Chapter 6

Methodology

This chapter discusses the research methodology for both the shock tube configurations. The ranges to be explored in each configuration are outlined, and the method in which the numerical and experimental work were analysed is discussed.

6.1 Numerical Studies

Numerical simulations were initially undertaken on both shock tube configurations to construct a better understanding of the dynamics of the developed shock reflections. Since previous experimental work already explored a range of low Mach numbers ($M_s < 1.1$), this study also aimed at determining whether the GR exists for higher Mach numbers. The simulations were performed for Mach numbers of 1.2 and 1.3 for the perturbation sources, and Mach numbers of 1.1, 1.2, 1.3, and 1.4 for the ramp angles. Two expansion chamber lengths (2.0 m and 4.0 m) were also simulated for the various Mach numbers to determine the effect of the virtual Mach stem length on the size of the supersonic region behind the triple point.

The computational work predicted the propagation path of the triple point downstream, and was not aimed at resolving the flow features in the vicinity of the triple point. The trajectory path of triple point for each condition was plotted and examined to determine whether the triple point would pass through the observation window during the experimental testing. Since the vicinity around the triple point is of concern, the wave velocities were measured in close proximity to the triple point. This allowed the numerical work to predict the strength of the reflected shock wave of the shock reflection. The velocity of the reflected shock wave could not be measured experimentally in the shock tube facility. A description of the numerical models are presented in Section 6.3.

6.2 Experimental Studies

The experimental tests were conducted using the same conditions as in the numerical study. These tests were performed utilising the operational manual, the pre-test check list, and the

test log presented in Appendix B. Calibration of the shock tube facility was first required to produce the desired shock wave strengths, thereafter the schlieren configuration needed to be constantly adjusted to capture the weak flow fields behind the triple point. All images were captured and the corresponding pressure traces recorded. The pressure traces were used to determine the velocity of the incident shock waves in all the images. All images then underwent contrast adjustments to clearly distinguish between the flow features of the GR. Various measurements from the images were taken to determine the size of the supersonic region and the velocities of flows behind each shock wave. This data was then compared existing published work.

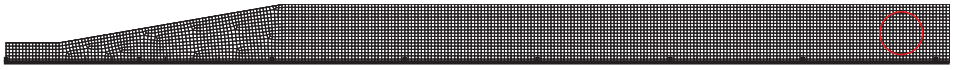
Tests which showed the best indication of the GR were then repeated and captured with a high speed camera so that the flow velocities in the vicinity of the triple point could be experimentally determined. This data together with the numerical data was then combined to obtain a better understanding of the nature of the captured GR.

6.3 Computational Fluid Dynamics Model

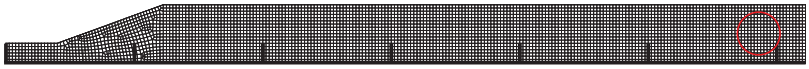
Numerous simulations were undertaken to determine the best model to effectively refine the irregular Mach reflection. The variables that where adjusted to obtain a converging solution where: the cell element type, the Courant number, the refining and coarsening adaption thresholds, the level of refinement per adaption, and the number of iterations before each adaption.

All the simulations were built using the two dimensional interface using Fluent on the commercially available Ansys 12 package. It should be noted that a number of two-dimensional simulations were also attempted using an in-house Euler solver developed in 1995 by a MSc student named Luke Felthun. The code, which is commonly referred to as “Luke’s code”, produced similar results to that obtained using Fluent, however due to the inability of Luke’s code to utilise parallel processing, the simulations required extensive processing time. Therefore, it was decided that Fluent would be best suited for all the simulations.

A density based solver was used to take into account the flow compressibility, and the fluid (air) was modeled as an ideal inviscid gas. An unsteady time setting was chosen for the transient analysis, and implicit and explicit models were attempted, both producing similar results. The final models were simulated using an explicit formulation with an initial uniform quadrilateral mesh of 15 mm interval size. The initial meshes for the 10° and 20° ramp angle shock tube configurations are shown in Figure 6.1. The red circle downstream in the shock tube represents the position of the viewing port.



10° ramp angle



20° ramp angle

Figure 6.1: Initial uniform quadrilateral mesh for second shock tube configuration with interval size of 15 mm

Since all the simulations were transient, dynamic mesh adaption was used to refine the region around the propagating shock wave configuration so that the weak reflected shock wave could be clearly resolved. A normalisation mesh adaption scheme was used, whereby the mesh was refined by analysing the density gradients in the flow. It was found that the coarsening and refining thresholds of nearly equivalent values had to be used (approximately 0.5% for the rectangular step and 0.5% for the triangular step) so that the weak reflected shock wave could be clearly defined at the furthest downstream position of the shock tube. For example, if a slightly larger coarsening threshold was used compared to the refining threshold, this would of resulted in the weak reflected shock wave decaying rapidly as it propagated downstream. Therefore, a large number of simulations were attempted with varying mesh adaptation values so that the weak reflected shock wave could be resolved effectively.

One to three million nodes were required to model the internal area of the shock tube. As expected more nodes were required for the triangular perturbation source in the first shock tube configuration, as the step produced a much weaker disturbance in the flow. It should be noted that each workstation utilised for the computations took approximately three days to run each simulation, this was mainly due to the extensive number of nodes present in each model as well as the continuous mesh adaption which was undertaken every 10 iterations. A initial Courant number of 1.0 was utilised, but later a value of 1.5 was used which produces equivalent results in half the processing time.

Inlet Conditions

The inlet pressure boundary conditions for the model were determined using Equations (1.4) to (1.6) to produce the required initial incident shock wave at the inlet of the shock tube. The inlet pressures required for the first shock tube configuration were easily obtained as a constant cross-sectional area is maintained throughout the expansion chamber, however for the second shock tube configuration the decaying cylindrical shock in the diverging section had to be accounted for. An iterative approach was taken to determine the initial incident shock wave Mach number at the inlet of the diverging section so that the required Mach number was produced at the outlet of the diverging section.

The inlet pressures presented in Tables 6.1 and 6.2 are given for an ambient temperature of 18°C and an atmospheric pressure of 0.83 bar. Table 6.1 tabulates the inlet conditions used for the first shock tube configuration for the two Mach numbers 1.2 and 1.3, and Table 6.2 the pressures used at the inlet of the shock tube, also tabulating the approximate decay percentages for the four Mach numbers and three ramp angles. The incident shock wave Mach numbers from the simulations were in an acceptable error range of 2.5% of the desired Mach numbers.

Table 6.1: Inlet pressures for the first shock tube configuration

Required Mach number	Gauge pressure total (Pa)	Static pressure (Pa)
1.2	133036	125606.7
1.3	167762.3	149815

Table 6.2: Inlet pressures for the second shock tube configuration based on the 15° ramp angle

Required Mach number	Initial Mach number	Decay (%)	Gauge pressure total (Pa)	Static pressure (Pa)
1.1	1.23	11	142704.1	132665.8
1.2	1.39	14	205544.4	173258.4
1.3	1.57	17	302479.0	224851.2
1.4	1.74	19	424234.1	279339.3

Chapter 7

Discussion of Results

The numerical and experimental results obtained during this study are presented here. The experimental results make up the majority of the discussion and where logical, the numerical results are used to construct a better understanding of the dynamics of the developed shock reflection.

7.1 Overview

This section looks at the results produced by the two shock tube configurations. For the first shock tube configuration comprising of the perturbation sources, tests were performed for incident Mach numbers of around 1.20 and 1.30. In the case of the second shock tube configuration with the three ramp angles, a wider range of incident Mach numbers (1.10 to 1.40) were studied. The main objective of this study was to determine whether the Guderley reflection (GR) could be produced in a conventional shock tube. Therefore, utilising the two shock tube configurations with the range of incident wave strengths, a large parameter set was explored to find the most likely conditions where the GR could occur.

The discussion begins by introducing the dynamics of the wave reflection in the shock tube using the numerical results obtained. The experimental images are then analysed and where logical numerical work is utilised to quantify certain aspects of the shock reflection. It should be noted that due to the weak incident shock wave Mach numbers ($1.1 < M_s < 1.4$), and the small disturbances in the flow (in particular the 10° ramp angle and the triangular perturbation), some of the the numerical results could not be clearly resolved and thus have not been included in this report.

Note that the Mach numbers of the shock reflections in the images refer to the Mach number measured just before the test section as shown in Figure 5.5 on page 42. This Mach number is denoted M_{bts}, which stands for the Mach number before the test section. However, for the numerical results the Mach number represents the speed of the shock reflection at the test section, this is denoted M_{ts}.

7.2 Numerical Study

As presented in the Literature Review, a number of computational techniques have already been developed to predict the complex flow structure in the vicinity of the triple point. However, the purpose of the CFD in this report aims at only determining the trajectory path of the triple point and the shock wave velocities. Due to the insufficient resolution of the simulations, as a result of the lack of processing power and the application of fundamental numerical models, the vicinity near the triple point could not be resolved to show the GR.

The following study is based on the hypothesis which suggests that the Mach stem attached to a Mach reflection at any time interval is the overall vertical distance travelled by the triple point of the Mach reflection. For a better understanding of what this means, we need to study the trajectory path of a given reflection. For example, consider the irregular Mach reflection produced by the rectangular perturbation source for a final incident shock wave Mach number of $M_{ts} = 1.21$. Figure 7.1 shows a static pressure contour of this reflection propagating downstream in the shock tube for various time steps. The simulation is modeled using a 2.0 m expansion chamber ($l_{ec} = 2.0$ m).

The first time step shows the undisturbed normal shock wave propagating to the right in the shock tube, where it interacts with the perturbation source producing an irregular Mach reflection. The succeeding images show the propagation path of the triple point downstream, as it first reflects off the ceiling and then the floor of the shock tube. The triple point of the reflection finally passes through the centre of the viewing port in the last time step. These simulations were completed before any experimentation was conducted to determine the position of the triple point in the viewing port, and to determine the number of triple point reflections which occurred in the shock tube before arriving at the viewing port downstream.

The number of reflections in the shock tube allows one to determine the overall vertical distance travelled by the triple point. Shown in Figure 7.1, the triple point travels approximately 2.5 shock tube heights upon arriving at the viewing port. This means that irregular Mach reflection according to the hypothesis has a virtual Mach stem length (l_{vms}) of 1.125 m but only an apparent Mach stem length (l_{ams}) of around 0.225 m. However, if the length of the expansion chamber is extended to $l_{ec} = 4.0$ m as shown in Figure 7.2, this allows the shock reflection to propagate further downstream, extending the virtual Mach stem length, and improving the likelihood of observing the GR. The solid and dashed lines in Figure 7.2 represent the trajectory paths for $M_{ts} = 1.21$ and $M_{ts} = 1.31$ respectively.

As expected the initial trajectory path of the triple point for the solid line shown in Figure 7.2 is identical to that shown in Figure 7.1. For a stronger shock wave it is shown that the trajectory angle is larger allowing the triple point for $M_{ts} = 1.31$ to pass by the periphery of the viewing port. The numerical work predicted the triple point position to within a radius of 30 mm of the actual position observed in the experimentation. The discrepancy between

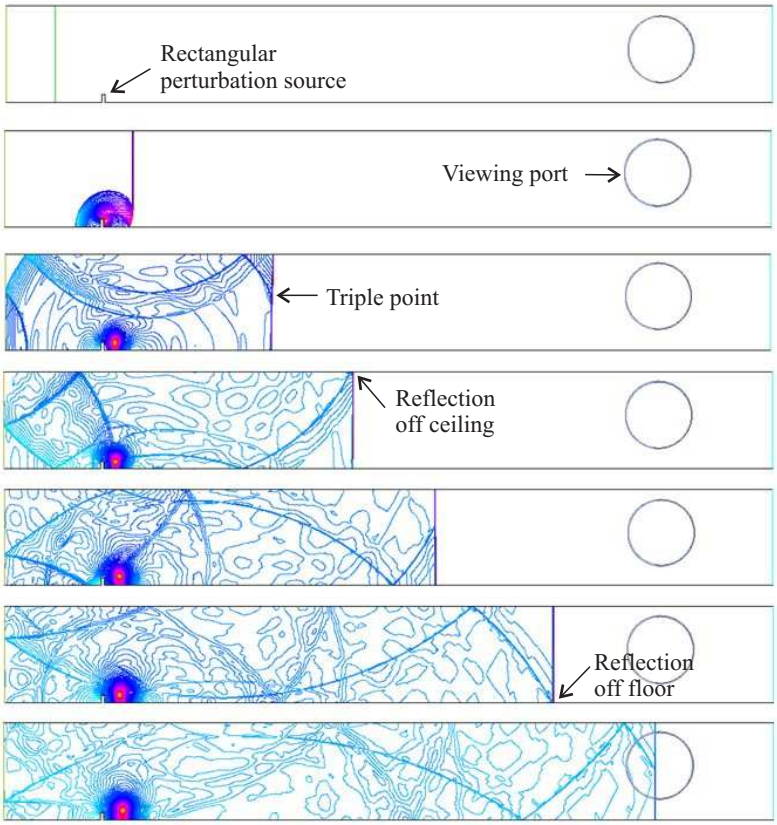


Figure 7.1: Static pressure contours of developed irregular Mach reflection propagating downstream for the rectangular perturbation source for $M_{ts} = 1.21$.

the results was because the Mach numbers produced in the experimentation generally deviated by around 5% compared to the values obtained in the numerical simulations. The simulations were also based on an inviscid model, thus neglecting the viscous effects of the air. The simulation nonetheless, provided a good approximation of the triple point position. For example, for the trajectory paths presented in Figure 7.2, experimentally both these reflections passed through the top of the viewing port, this compares well with that predicted numerically.

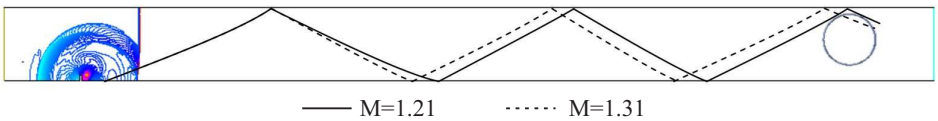


Figure 7.2: Trajectory path of triple points for $M_{ts} = 1.21$ and $M_{ts} = 1.31$ for an expansion chamber of 4.0 m.

Utilising the 4.0 m expansion chamber the virtual Mach stem length is almost doubled to $l_{vms} \approx 2.25$ m. Figure 7.3 shows the directly proportional relationship between the length of the expansion chamber and the growth of the virtual irregular Mach reflection according to the hypothesis described earlier. If the shock tube is assumed not to be bounded by an upper wall, the produced shock reflection continues to expand uniformly in time until the developed reflection is large enough to resolve the region behind the triple point. The

hypothesis suggests that the Mach stem remains virtually attached to the shock reflection regardless of the triple point reflections off the walls of the shock tube.

The aim of this study is to produce a Mach stem length in the order of 1.0 m so that the GR can be observed. However, utilising a conventional shock tube, the trajectory path of the triple point encounters the upper and lower floor of the tube a number of times depending on the length of the expansion chamber. Compared to the previous work by Skews et al. (2009), the triple point underwent only a single undisturbed trajectory path making no contact with walls of the shock tube due to the large-scale setup. At this stage it is unknown what the effect of the triple point reflecting in the shock tube has on the integrity of the flow features behind it. For a better understanding of the fundamental dynamics of the rebounding triple point, the numerical results are studied and discussed later.

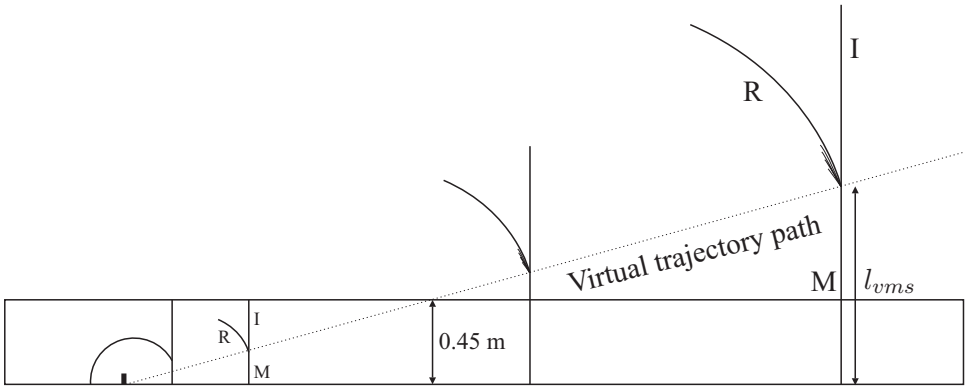


Figure 7.3: Virtual growth of irregular Mach reflection for a shock tube not bounded by an upper wall. This schematic shows the uniform growth of the supersonic region behind the triple point as l_{vms} increases downstream.

The number of reflections which occur in both shock tube configurations for the 2.0 m and 4.0 m expansion chamber are summarised in Table 7.1. The values presented in the brackets are the approximate virtual Mach stem lengths obtained for each configuration. For the different perturbation sources and ramp angles the number of reflections undergone remained the same for a specific Mach number, but the virtual Mach stem length varied by approximately 40 mm to 70 mm.

Table 7.1: Number of reflections undergone for the various shock tube configurations. Values in brackets represent the approximate virtual Mach stem lengths (l_{vms}).

Configuration	Expansion chamber length	Mach numbers 1.1	1.2	1.3	1.4
Perturbation source	2.0 m	-	2 (0.9 m)	2 (0.9 m)	-
	4.0 m	-	4 (1.8 m)	4 (1.8 m)	-
Diverging section	2.0 m	2 (0.9 m)	2 (0.9 m)	2 (0.9 m)	2 (0.9 m)
	4.0 m	3 (1.35 m)	4 (1.8 m)	5 (2.25 m)	5 (2.25 m)

The first image in Figure 7.4 shows the trajectory plot of the triple point for the 15° ramp angle and Mach number of $M_{ts} = 1.31$. This image describes the interchanging positions of the incident wave and the Mach stem after each triple point reflection in the shock tube. At a downstream distance of approximately 1.6 m, the shock reflection is initially formed at the corner of the tube where the triple point then follows a curved trajectory path until it encounters the floor at a downstream distance of 2.65 m. Note that before encountering the floor, the shock reflection configuration consists of the Mach stem (M_1) on top, and the incident wave (I_1) at the bottom of the triple point. The orientation of the shock reflection changes once the triple point rebounds, where the incident wave (I_1) before the triple point reflection becomes the new Mach stem (M_2) for the new trajectory path. Consequently it is seen that the trajectory path now propagates towards the upper wall (ceiling), where it then reflects off the ceiling at a downstream distance of approximately 3.5 m. Similarly, for the second triple point reflection, the incident wave (I_2) becomes the Mach stem (M_3) for the next shock reflection. Therefore, after each triple point reflection, the incident wave and the Mach stem interchange, whilst the reflected wave undergoes changes in orientation with respect to these two waves. It is seen that five triple point reflections occur before the shock reflection arrives at the end of the expansion chamber. A detailed investigation by Skews (1970) describes the trajectory by a triple point of a Mach reflection when reflected off a plane wall.

Shown in the Mach number plot in Figure 7.4, both the strength of the incident wave and Mach stem are plotted at the beginning of the diverging section at a downstream distance of 0.4 m. Since the vicinity around the triple point is of concern, the wave velocities were measured in close proximity to the triple point. As the normal shock enters the diverging section, a cylindrical shock wave is formed, where it then reflects off the corner at the end of the diverging section creating the desired initial shock reflection. As is seen in the plot, the strength of the initial cylindrical shock decays by 14% from 1.54 to 1.33 before interacting with the corner. The developed Mach stem (M_1) has an initial Mach number of M = 1.42 which is about 7% stronger then that of the incident wave (I_1). These two waves decay until the first triple point reflection off the lower floor, thereafter both the waves' Mach numbers increase in strength to almost similar values. The shock reflection then undergoes another trajectory path causing the waves to decay in strength once again until the triple point reflects off the upper wall, resulting in another amplification in shock strength at a downstream distance of 3.5 m. After a number of triple point reflections the incident wave Mach number gradually tends to a Mach number of roughly 1.30.

Figure 7.5 plots the reflected wave Mach number versus the downstream propagated distance. Similar to the incident wave and the Mach stem, the reflected wave undergoes continuous decay as it propagates downstream. After each reflection in the shock tube, the strength of the wave is seen to strengthen only by 0.1% to 0.3% which is neglegible compared to the 1% to 4% amplification experienced by the incident wave and Mach stem.

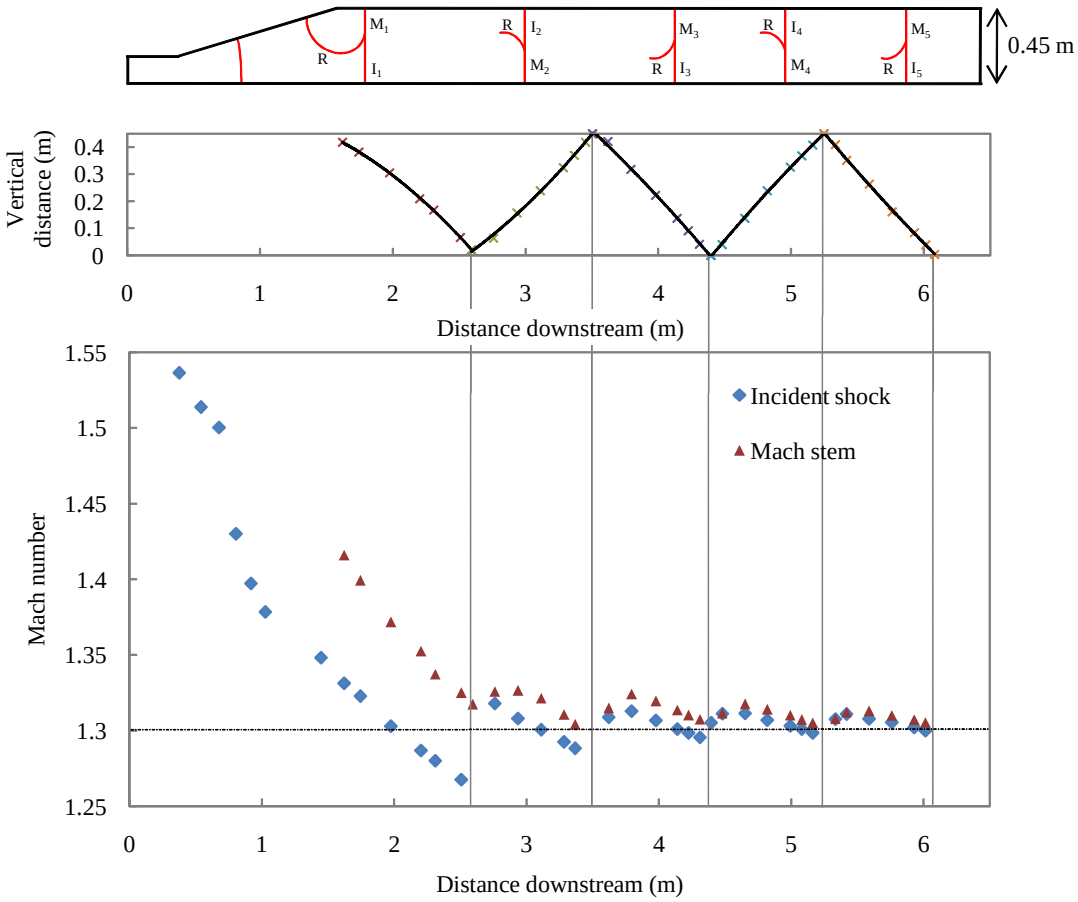


Figure 7.4: Dynamics of the shock reflection in the shock tube for a 15° ramp angle, $M_{ts} = 1.31$, 4.0 m expansion chamber. First image illustrates the change in orientation of the shock reflection downstream, second image illustrates the trajectory path of triple point downstream, and the third image plots the incident wave and Mach stem wave strength versus the downstream shock tube length.

The decay of the reflected wave appears more steady, with the wave gradually tending to M = 1.003. The reflected wave is very weak at the furthest downstream position and it is not surprising that the slip stream could not be resolved in the simulations.

Therefore, it is seen that each triple point reflection in the shock tube amplifies the waves in the shock wave configuration, preventing the shock reflection weakening significantly as it propagates downstream. This was an important factor in maintaining the shock strength after each triple point reflection, allowing the incident wave Mach numbers of approximately 1.4 to be produced, which could previously not be studied in the large-scale shock tube (Skews et al. 2009).

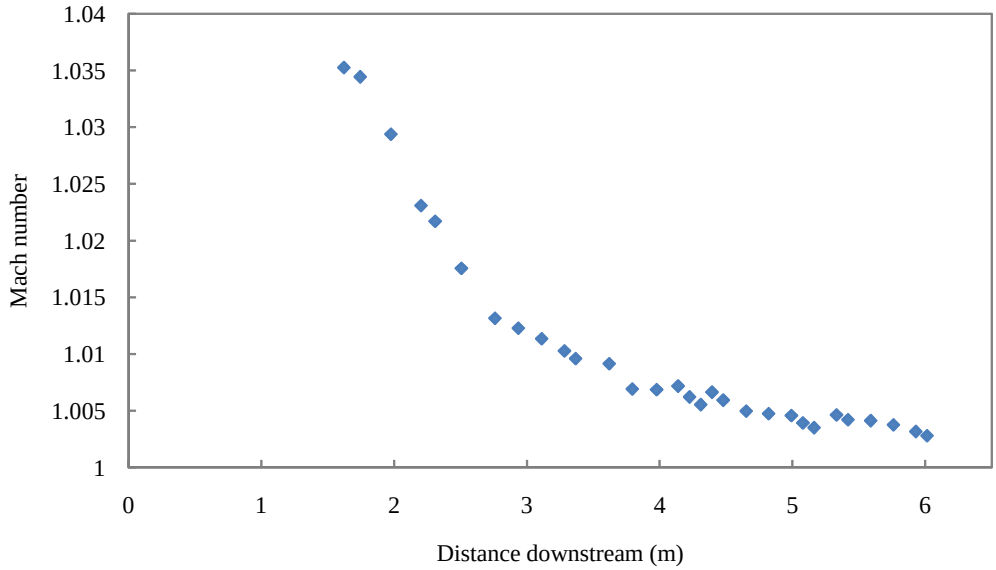


Figure 7.5: Reflected wave Mach number versus distance downstream for 15° ramp angles, $M_{ts} = 1.31$, 4.0 m expansion chamber.

7.2.1 Summary

The numerical results provide a means of determining the overall trajectory path and the wave velocities in each shock tube configuration. The number of triple point reflections in the shock tube and the virtual Mach stem length were determined for the various conditions; these are given in Table 7.1 on page 54. It was found that the Mach stem before each triple point reflection becomes the incident wave for the newly developed shock reflection. After each triple point reflection the Mach stem and incident wave strengthened by 1 to 4%, this establishes a very important technique to maintain the strength of the shock reflection downstream.

7.3 Experimental Results

Over 400 single-frame and 10 multi-frame schlieren photographs were captured during the experimentation. However, only the most qualitative images are presented in this study. Due to the large range of tests undertaken, the illumination of the images varied considerably as continual adjustments were made to the knife edges to find the best balance between the sensitivity and visibility of the images.

Figure 7.6 shows a general image capturing the entire viewing port using the schlieren system. The incident and reflected waves and the Mach stem have been labeled as I, R and M respectively. It is seen that the incident wave and Mach stem are presented by a gray vertical line, and the reflected wave is presented by the slanted white line extending to the top left corner of the photograph. The reason for the different colours identifying these shock waves is because of the angle at which the second knife edge cuts off the light

entering the schlieren system. In all the images the second knife edge was adjusted to match the angle of the reflected shock wave to improve the sensitivity of the flow captured in that direction. Note that in all the images the shock reflection pattern is presented with the incident shock wave on the top and the stationary air on the right.

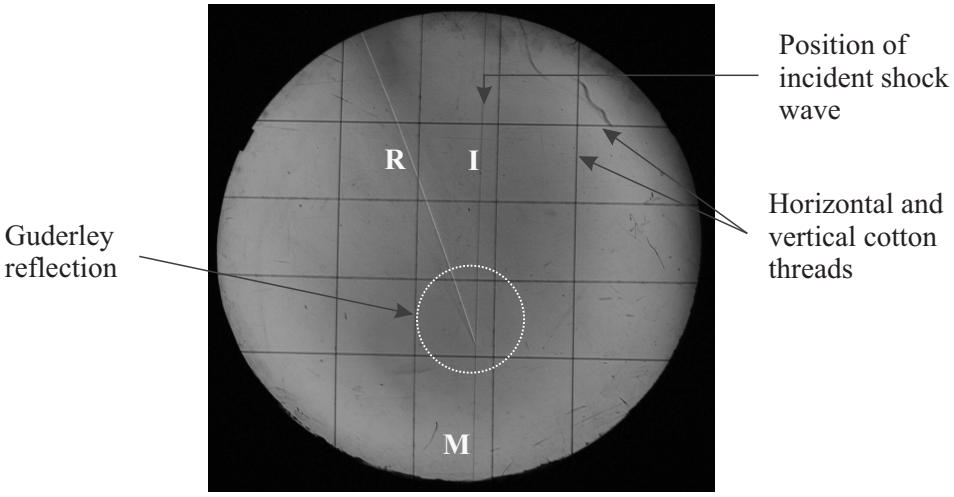


Figure 7.6: General schlieren photograph captured through the viewing port showing the GR. (20° ramp angle, $M_{bts} = 1.10$, 4.0 m expansion chamber) Virtual Mach stem, $l_{vms} = 1505$ mm; Actual Mach stem, $l_{ams} = 205$ mm

The vicinity behind or to the left of the triple point, encircled by the dotted white line shown in Figure 7.6, is the area of interest which was magnified and cropped to clearly observe the underlying flow features. The four vertical and horizontal lines in the image are cotton threads mounted across the viewing window each separated by 50 mm so that the shock reflection could be scaled relative to these threads. On close examination it is apparent that a dark streak exists directly beneath the reflected wave within the encircled dotted line. This streak which emanates from the triple point is called the expansion wave and is present in all the images shown in this report. The existence of this wave alone is evidence that the GR does in fact exist in a conventional shock tube thus supporting the main objective of this study. This observation also proves the virtual Mach stem hypothesis, as a Mach stem length of 205 mm shown in Figure 7.6 is too small to experimentally observed the GR, therefore the virtual Mach stem length of 1505 mm needs to be considered instead.

To capture the GR a very sensitive schlieren system was necessary. Particular trouble arose in obtaining images of uniform sensitivity, this is observed by the darker contrasted area seen in the centre of the viewing port shown in Figure 7.6. The least sensitive region is presented by the lighter contrasted periphery of the viewing port. It is believed this nonuniformity was attributed to the optical stigmatism of the converging lenses and the misalignment of the schlieren setup. Since the flow region of concern (circled region in Figure 7.6) only makes up a fraction of the schlieren photograph, the nonuniformity of the setup did not significantly effect the flow features being studied.

Figure 7.7 shows a GR of $M_{bts} = 1.236$ using the rectangular perturbation when the second knife edge has not been correctly adjusted. It is seen that the expansion region behind the reflected shock wave was not detected. This emphasises the importance of carefully setting the sensitivity of the schlieren system to observe the GR. This probably contributed to the GR not being detected before. Continuous adjustments of the knife edge was necessary throughout the experimentation to consistently capture the GR.

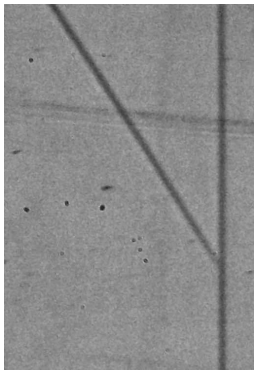


Figure 7.7: Incorrectly adjusted schlieren system showing no evidence of the flow features behind triple point. GR produced using a rectangular perturbation for $M_{bts} = 1.236$.

The two sections that follow concentrate on discussing the conditions in which the expansion patch and the shocklet were captured experimentally.

7.3.1 The Expansion Wave

Figure 7.8 shows the shock reflection observed for the 20° ramp angle, $M_{bts} = 1.10$, and 4.0 m expansion chamber. At this level of magnification the waves seem plane with an indication of a slight bend between the incident shock and the Mach stem. An expansion wave, centred on the triple point, is clearly seen by the black fan-shaped region immediately behind the reflected wave. This observation is similar to the primary patch predicted by Zakharian et al. (2000) and Vasil'ev & Kraiko (1999), however no clear evidence is found of a slipstream nor a shocklet in the images. The absence of the slip stream is mainly due to the orientation of the knife edge and the inability of the schlieren system to capture the really weak pressure gradients across the slip stream. Even with the most sensitive schlieren setup with the knife edge positioned correctly, the slip stream was not observed.

When analysing the expansion wave it is uncertain of the exact length it extends, as the patch gradually disappears the further it emanates from the triple point. It is estimated that the expansion wave shown in Figure 7.8 is approximately 96 mm in length, but since no shocklet is present this means that the size of the supersonic patch behind the triple point could not be determined. It should be noted that the size of the supersonic patch is determined by the point in which the shocklet terminates the expansion wave. Section 7.3.2 analyses the size of the supersonic region for the images which showed evidence of the

shocklet.

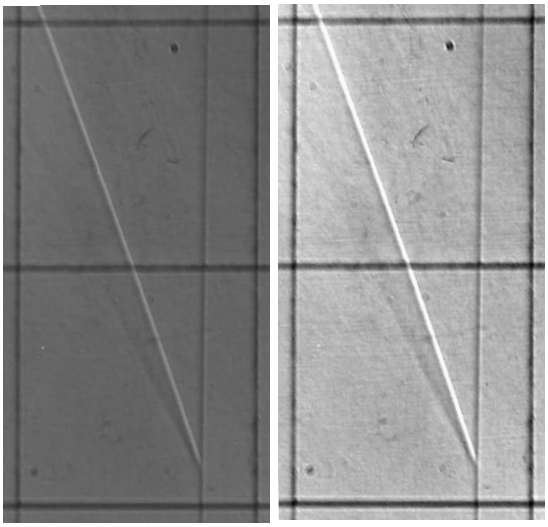


Figure 7.8: Original and contrasted image of GR clearly showing the expansion wave which is represented by the black fan-shaped region immediately behind the reflected wave. (20° ramp angle, $M_{bts} = 1.107$, 4.0 m expansion chamber, photo 276). $l_{vms} = 1208$ mm; $l_{ams} = 308$ mm

Figure 7.10 presents a series of tests for the perturbation sources and ramp angles, and compares the tests obtained for the 2.0 and 4.0 m expansion chambers. All the images clearly show the existence of the expansion wave, therefore confirming the fourth wave in the GR. For the very first time the GR is observed for incident shock strengths of 1.2 to 1.4, and for unconventional disturbances (perturbation sources) in the flow. All the images have been scaled identically so that direct comparisons can be made regarding the size of the various waves in the GR. It is observed that the visibility of the expansion wave is dependent on the strength of the incident shock as well as the angle of the ramp insert. Comparing similar Mach numbers shown in Figures 7.10(a) and (d), it is evident that the reflected shock is stronger for the 20° ramp angle, and the expansion wave is more clearly defined.

Comparing Figures 7.10(a) and (c) for the 10° ramp angle, it is seen that ω_{ir}, the angle between the incident and reflected waves, increases for stronger shock Mach numbers. The relationship between ω_{ir} and the incident Mach number is shown in Figure 7.9. It is seen that the data points for ω_{ir} correspond well with those predicted by the explicit formula for a reflected sonic wave presented by the solid trend line (Kobayashi et al. 1997). This suggests that the reflected wave of the GR is almost sonic which supports the numerically results which showed the reflected shock to be approximately 1.003. It was found that for the larger ramp angles the reflected wave strengthens resulting in the data deviated further away from the trend line.To understand the geometry of the GR, the angle ω_{re} between the reflected wave and expansion wave was analysed. Large scatter in ω_{re} was found for the

various Mach numbers with only a slight increase in ω_{re} as the shock strength increased. An average value of $\omega_{re} \approx 7^\circ$ was obtained for the 10° and 15° ramp angles, and $\omega_{re} \approx 9^\circ$ for the 20° ramp angle.

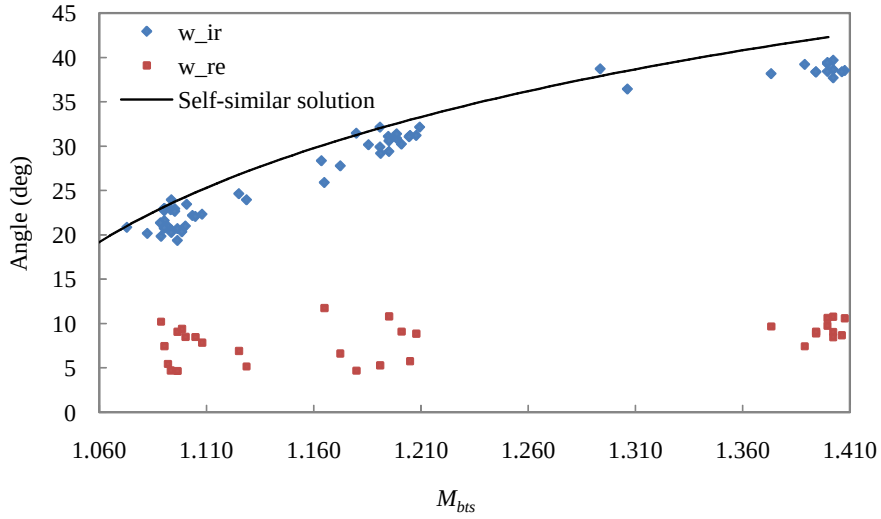
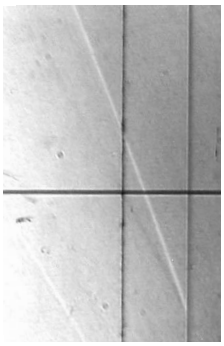


Figure 7.9: Comparison between the angles between the incident wave and the reflected wave (ω_{ir}), and the reflected wave and the expansion wave (ω_{re}) versus M_{bts} for the 10° ramp angle. The solid line represents the angle ω_{ir} predicted by a explicit formula for weak shocks (Kobayashi, 1997).

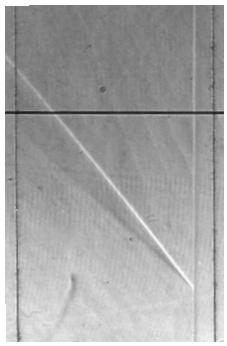
In the majority of the images in Figure 7.10 there are a number of transverse waves which trail the reflected wave. These waves should not be confused with shocklets, as they are weak waves which have no effect on the waves of the shock reflection. A transverse wave is shown to intersect the reflected shock in Figure 7.10(f) where it is seen that it does not effect the reflected wave in any way. The transverse waves are generally formed either during the rupturing of the diaphragm or when the shock front propagates downstream reflecting off any misaligned walls of the expansion chambers. The majority of the transverse waves produced during the rupture were dampened out by lining the walls of the shock tube directly after the driver with a carpet-like cover. This proved successful for the lower Mach numbers, but in the case of Mach numbers 1.30 and 1.40 numerous transverse waves were still produced, as shown in Figure 7.10. In future work, it is advised to extend the plunger section to allow more time for the shock wave to develop before entering the diverging section. This will minimise the number of transverse waves produced for the higher Mach numbers.



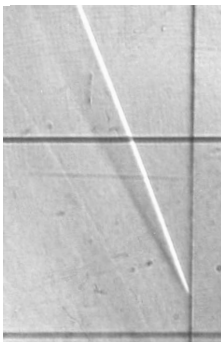
(a) 10° M1.106 (Photo 706)



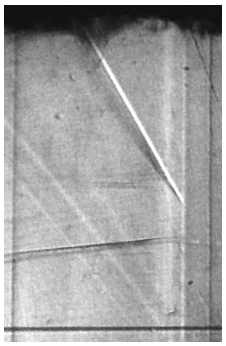
(b) 10° M1.172 (Photo 395)



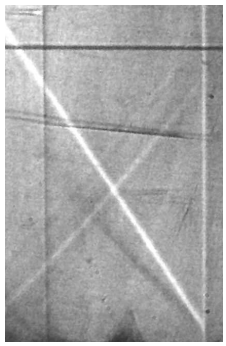
(c)10° M1.373 (Photo 637)



(d) 20° M1.107 (Photo 207)

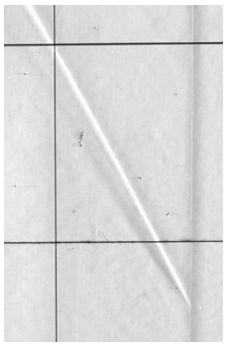


(e) Rect. M1.226 (Photo 1583)

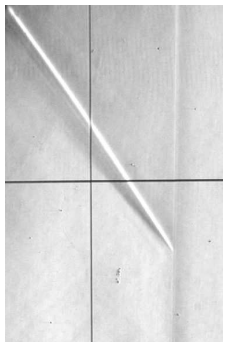


(f) Rect. M1.300 (Photo 1588)

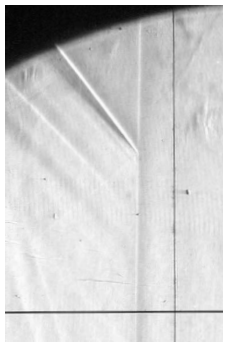
Shock reflections for 4.0 m expansion chamber



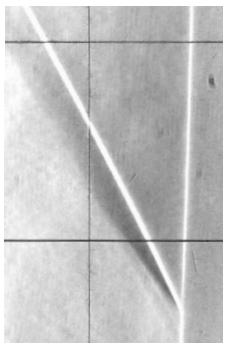
(g) 10° M1.208 (Photo 20)



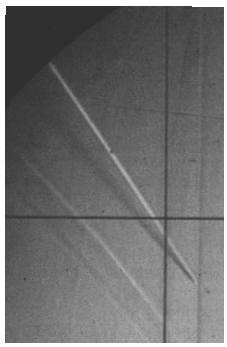
(h) 15° M1.301 (Photo 37)



(i) 15° M1.405 (Photo 45)



(j) 20° M1.206 (Photo 68)



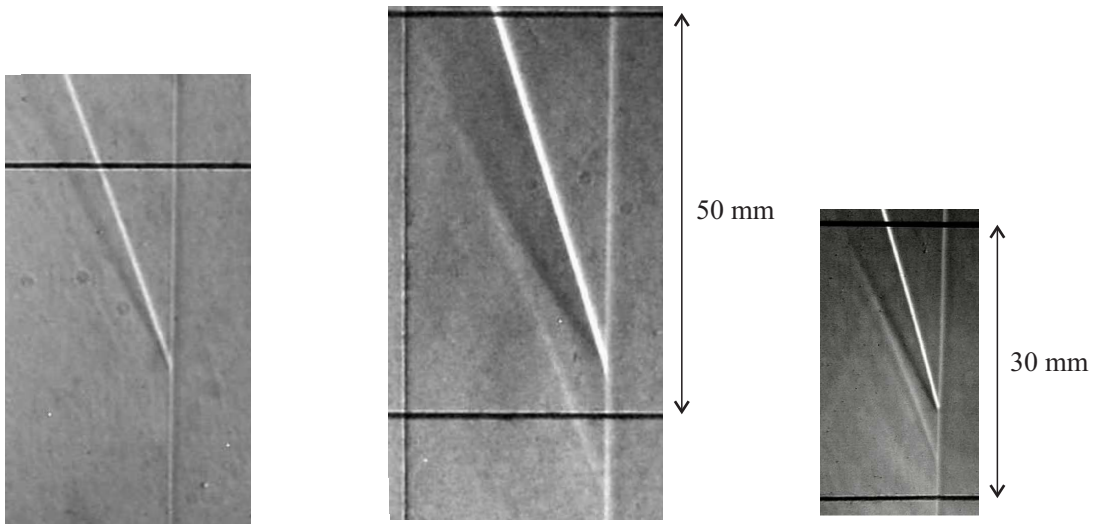
(k) Rect. M1.303 (Photo 795)

Shock reflections for 2.0 m expansion chamber

Figure 7.10: Summary of all the images showing evidence of the fourth wave of the GR as a black fan-shaped region immediately behind the reflected wave. All images are the same scale. Note the images obtained using the rectangular perturbations are denoted by Rect.

It has been proven thus far that the GR can be produced in a conventional shock tube. However, it is important to compare the shock reflections observed in this study to those shown in Skews et al. (2009). Shown in Figure 7.11 are three images obtained for a ramp angle of 15° and $M_{bts} \approx 1.10$. Figures 7.11(a) and (b) are from the current study utilising the 4.0 m expansion chamber whilst Figure (c) was presented in Skews et al. (2009). Again all three images have the same scale so that the size of the waves can be compared alongside each other. Figure 7.11(a) was captured 80% of the time for the following conditions, whilst Figure 7.11(b) was captured for the remainer 20% of the tests. According to Skews (2010, personal communication) the images in Skews et al. (2009) were also scarcely captured, requiring multiple tests to observe a single image showing evidence of the shocklet shown in Figures 7.11(c). This could be due to changes in atmospheric conditions, the manner in which the diaphragm ruptured, or the sensitivity of the schlieren system. These could of all contributed to not capturing the desired flow features repeatedly.

Comparing the Figures 7.11(b) and (c) it is seen that the flow features are almost identical, but the overall size of the GR presented in the conventional shock tube is considerably larger. This is because the virtual Mach stem length (l_{vms}) in Figure 7.11(b) is around 350 mm larger then the Mach stem produced in the large-scale tube shown in Figures 7.11(c). It should also be noted that the second expansion wave in Figure 7.11(b) is not visible, this could be a result of a less sensitive schlieren system. The lighter region below the expansion wave shown in Figures 7.11(b) and (c) represents the shocklet in the GR as predicted by Tesdall et al. (2002). These flow features were also found for a number of conditions presented in Section 7.3.2.



(a) 15° M1.097 (Photo 004) l_{vms} = 1174 mm

(b) 15° M1.097 (Photo 238) l_{vms} = 1153 mm

(c) 15° M1.07 (Skews, 2009) $l_{vms} \approx$ 800 mm

Figure 7.11: Comparison between the schlieren images obtained from the conventional shock tube (images (a) and (b)) and large-scale shock tube (image (c)).

From the above observation it can be stated that the large-scale shock tube and the

conventional shock tube are capable of producing almost identical results. The only real issue is the repeatability of obtaining these images, as the desired images are only captured on average once out of every five tests.

Summary

The series of tests all clearly showed the existence of the expansion wave immediately beneath the reflected wave confirming the existence of the fourth wave in the GR, as shown in the schematic in Figure 7.12. The virtual Mach stem hypothesis was verified as the GR was observed for apparent Mach stem lengths of $l_{ams} \approx 200$ mm which according to previous numerical work the supersonic region would be too small to resolve GR experimentally (Zakharian et al. 2000). Thus the only valid explanation for observing the GR was if the virtual Mach stem length of $l_{vms} \approx 1100$ mm was considered. Some tests showed evidence of a shocklet beneath the expansion wave, these images corresponded with those observed in Skews et al. (2009). However, the repeatability of these results were an issue, as on average only one out of every five tests showed evidence of a shocklet beneath the expansion wave. Therefore, this section concludes that the GR can be successfully studied in a conventional shock tube, and it further proves the virtual Mach stem hypothesis.

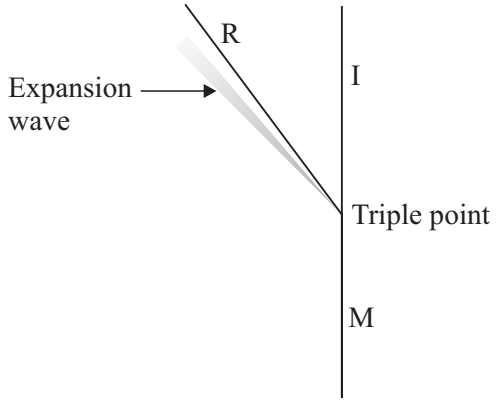
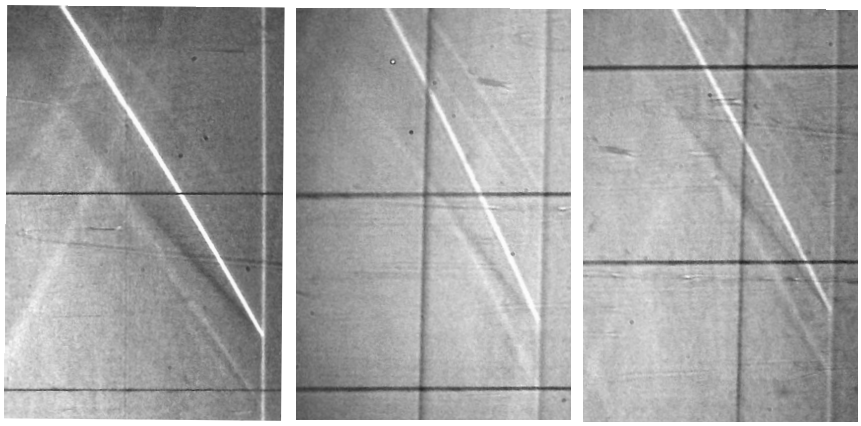


Figure 7.12: Structure of GR with expansion wave immediately beneath the reflected wave.

7.3.2 Evidence of the Shocklet

The three images shown in Figure 7.13 where obtained for the two perturbation sources using the 2.0 m expansion chamber and $M_{bts} \approx 1.20$. Initial evidence of the shocklet was observed for the rectangular perturbation source for $M_{bts} = 1.233$, shown in Figure 7.13(a). An expansion wave behind the reflected wave and a terminating shocklet are seen as predicted in Tesdall et al. (2002) and experimentally verified in Skews & Ashworth (2005) and Skews et al. (2009). The shocklet is represented by the distinct contrasting line almost parallel to the reflected wave immediately beneath the expansion wave. Directly below the shocklet a dark region is vaguely visible, suggesting that a second expansion wave may exist, but no sign of a second shocklet was observed. Figures 7.13(b) and (c) also show these distinct features for the triangular perturbation source for $M_{bts} = 1.187$ & 1.191.

Interestingly the shocklet was only observed for Mach numbers around 1.20 for both the perturbations, later it is shown that similarly the shocklet was only observed using the 15° and 20° ramp angles for $M_{bts} \approx 1.20$.



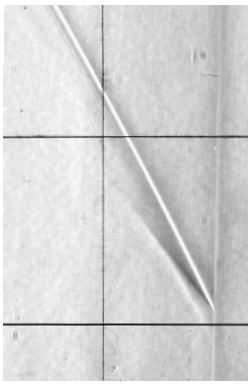
(a) Rect. M1.233 (Photo 885) (b) Tri. M1.187 (Photo 1459) (c) Tri. M1.191 (Photo 1461)

Figure 7.13: GR with evidence of the shocklet produced by the perturbation sources, where Rect. and Tri. denotes the rectangular and triangular perturbations respectively. The shocklet is the lighter area identified beneath the expansion wave. An expansion chamber of 2.0 m was used for these tests.

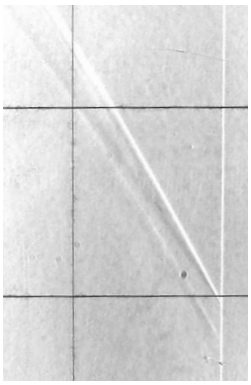
Figure 7.14 presents the images captured using the diverging section, it is seen that two different shock reflections occur when using the 2.0 m and 4.0 m expansion chambers. It should be noted that the GR comprising of a shocklet was mostly observed for $M_{bts} \approx 1.20$ and ramp angles of 15° and 20°. Seen in Figure7.14(a) for the 2.0 m expansion chamber, the shocklet is clearly seen emerging from the Mach stem below the triple point for both the images. The shocklet then intersects and terminates the expansion wave. It should be noted that as shown in Figure 2.9 on page 21, the shocklet is formed by the expansion wave reflecting off the sonic line in the vicinity of the triple point, which then intersects the Mach stem (Tesdall & KeyFitz 2010). Since it is not possible to observe the sonic line in the experimental images, we describe the shocklet as emerging from the Mach stem and terminating the expansion wave, this is essentially not what happens, but this allows the flow features to be described in a more understandable manner. Similar flow features are seen in Figure7.14(b) for the 4.0 m expansion chamber where the expansion wave and shocklet are more than double in length when compared to the images in Figure7.14(a). This is expected as the shock reflection shown in Figure7.14(b) has traveled nearly double the downstream distance compared to Figure7.14(a). This means that the shock reflection would have expanded by roughly twice the size allowing the flow features behind the triple point to be resolved more clearly as shown in Figure7.14(b).

The images obtained for the perturbations showed no sign of a second shocklet and second expansion wave as shown by Skews et al. (2009). In theory, according to Tesdall et al. (2002) there should be an infinite sequence of expansion waves and shocklets beneath the

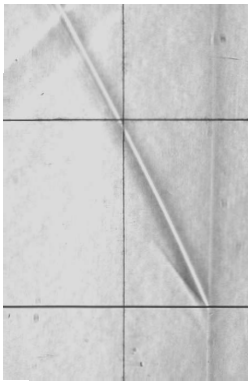
reflected wave for an inviscid flow. However, since the waves in this study are very weak and the viscous effects of the air are present, it is not surprising that the sequence of supersonic patches as observed in Tesdall et al. (2002) and Tesdall et al. (2008) were not resolved. It should also be mentioned that the triple point undergoes a number of reflections (2 to 5) off the ceiling and the floor of the shock tube, which could possibly dampen and degrade the integrity of the flow features behind the triple point. The extent of the degradation of the flow features (sequence of supersonic patches) are unknown and beyond the scope of this study.



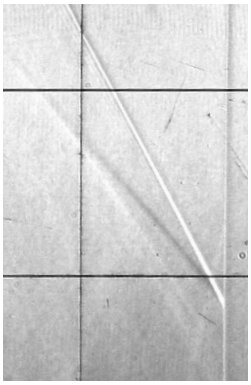
15° M1.204 (Photo 33)



15° M1.177 (Photo 119)



20° M1.206 (Photo 32)



20° M1.200 (Photo 193)

(a) 2.0 m expansion chamber.

(b) 4.0 m expansion chamber.

Figure 7.14: Comparison between the shocklets produced by the 15° and 20° ramp angles for $l_{ec} = 2.0$ & 4.0 m. Larger expansion waves are observed for the 4.0 m expansion chamber tests shown in (b). This is due to the larger virtual Mach stem length in (b).

In both the shock tube configuration tests, the GR has been observed with the expansion wave beneath the reflected wave, and in some cases evidence of the shocklet was also found. To determine the size of the supersonic patch, images with a clearly defined expansion wave and shocklet were required. Figure 7.15 indicates how the length of the supersonic patch was measured, the same measuring technique was adopted by Tesdall & Hunter (2002). It is seen that the size of the supersonic patch (l_s) is defined by the vertical distance between the 2^{nd} triple point and the region where the shocklet intersects or terminates the expansion wave. The 2^{nd} triple point is clearly defined in the images as the intersection of the shocklet

with the Mach stem, and the region encircled in Figure 7.15 indicates where the shocklet terminates the expansion wave. The latter region was approximated with an uncertainty of 5 mm as the point where these two waves intersect was not always clearly resolved.

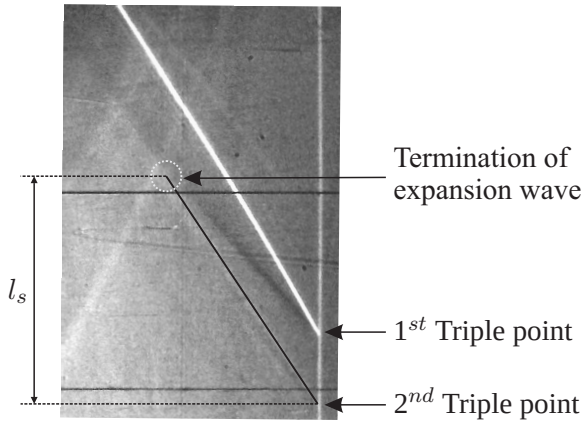


Figure 7.15: Length of supersonic region l_s behind the triple point (Photo 885).

Figure 7.16 is a plot of the size of the supersonic patch (l_s) versus the virtual Mach stem length (l_{vms}) for $M_{bts} \approx 1.20$. It is expected, as illustrated in Figure 7.3 on page 54, that the size of the supersonic patch is directly proportional to the virtual Mach stem length. When comparing similar data sets shown in Figure 7.16 it is seen that size of the supersonic patch does in fact increase for increasing virtual Mach stem lengths. The two linear trend lines for both the 15° and 20° ramp angles have similar gradients, meaning that the size of the supersonic patch increases at a certain rate regardless of the ramp angle. Since there were limited data points, it could not be conclusively determined whether there was genuinely a linear relationship. But it is suspected that if more data points were obtained they would follow a similar trend. More data points in the future can be obtained by studying the GR using two alternative expansion chamber lengths (e.g. 3.0m and 5.0m) to allow a different range of virtual Mach stem lengths to be explored. It is seen that the gradient between the two data points for the triangular perturbation is however much steeper than that obtained for the ramp angles. But since the two data points are in such close proximity to one another, no definitive statement can be made regarding the growth of the supersonic patch for the triangular perturbation.

Analysing the different supersonic patch sizes l_s in Figure 7.16, it is seen that l_s ranged from 24 mm for the 20° ramp angle for a virtual Mach stem of 1059 mm, to 78 mm for the 15° ramp angle and a virtual Mach stem of 1950 mm. The ratio between the supersonic patch size and the virtual Mach stem was found to be in the range of 2.3% to 4.8%. This compared reasonable well with the 2% obtained experimentally in Skews et al. (2009), but the experimental results still remain doubtful when compared to numerical work in Tesdall et al. (2008) where a value of 0.6% was obtained. However, it should be noted that their simulations were based on inviscid flows and a planar incident shock wave, and the experimental work in Skews et al. (2009) did not undergo a succession of triple point

reflections off the ceiling and the floor of the shock tube. These could be some reasons for the discrepencies between the results. It is seen that the size of the supersonic patches for the perturbation sources are 20 to 30 mm larger than that produced by the two ramp angles for similar l_{vms}. The 15° ramp angle produced a supersonic patch 11 mm larger than that obtained for the 20° ramp angle. It is unknown why these GRs resulted in considerably different supersonic regions, but it is suspected that that the planar incident wave produced for the perturbation tests could have an effect on the complex flow structure behind the triple point.

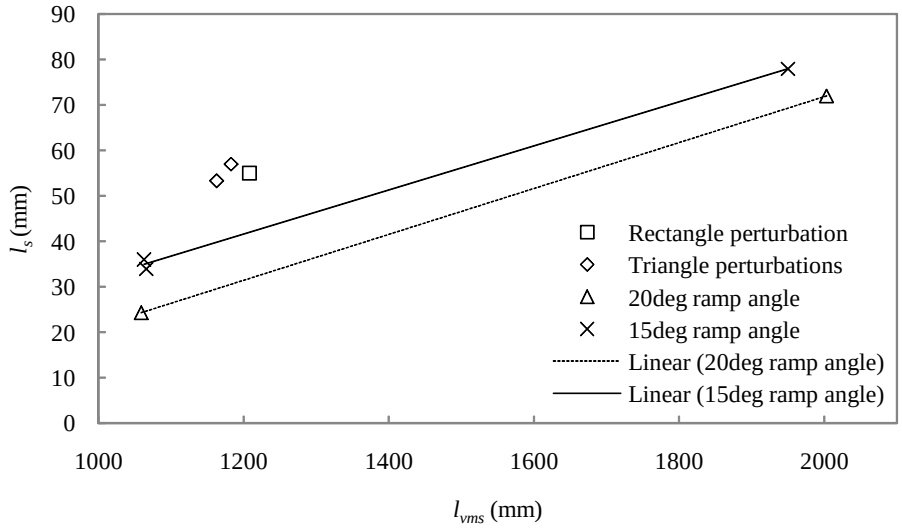


Figure 7.16: Variation of supersonic patch size (l_s) with the virtual Mach stem length (l_{vms}) for $M_{bts} \approx 1.20$.

Summary

Evidence of a single shocklet beneath the expansion fan was found for the two perturbation sources, and the 15° and 20° ramp angles. Interestingly only Mach numbers of approximately 1.20 showed evidence of the shocklet, and in some images an indication of a second expansion wave was also vaguely visible. Figure 7.17 is a schematic of the GR observed which includes the observed shocklet. The second expansion wave is complimented with a question mark as it was uncertain whether it was a true feature of the shock reflection. It was found that the size of the supersonic patch increased for larger virtual Mach stem lengths, therefore allowing the flow features behind the triple point to be better resolved when utilising the 4.0 m expansion chamber. However, a large variability in the supersonic patch size was obtained for the difference perturbations and ramp angles, with only the two ramp angles having similar linear growth rates. The sizes of the supersonic patches varied between 2.3% to 4.8% of the virtual Mach stem length, this compared reasonable well with the 2% obtained experimentally for lower Mach numbers in Skews et al. (2009).

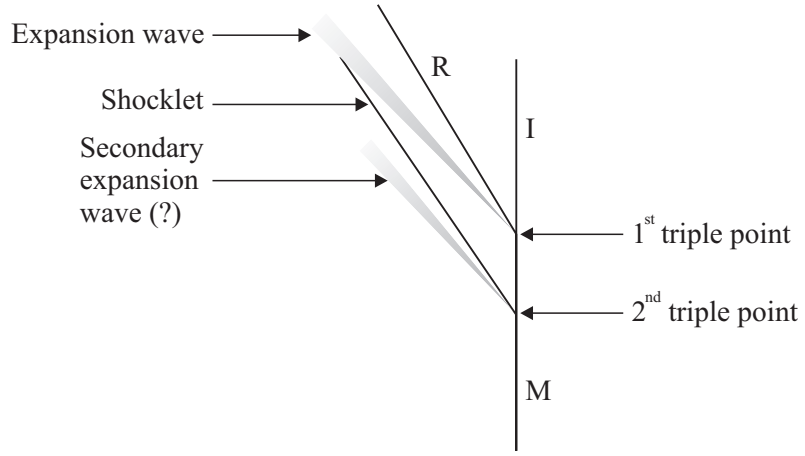


Figure 7.17: Schematic of GR wave structure consisting of a shocklet and an uncertain secondary expansion wave. This reflection was observed 1 out of every 5 tests conducted.

Table 7.2 summarises all the observations for the experimentation. “E” indicates that an expansion wave was observed, and “E & S” indicates that a shocklet was also observed in the GR. The tests with no entries “-”, are the tests whereby the triple point did not pass through the viewing port. It is seen that the majority of the parameter set showed evidence of the expansion wave, whilst only 7 of these conditions showed signs of the shocklet.

Table 7.2: Summary of the observations for the entire parameter set. “E” indicates that an expansion wave was observed, and “E & S” indicates that a shocklet was also observed in the GR. The tests with no entries “-” are the tests whereby the triple point did not pass through the viewing port.

Configuration	Expansion chamber length (m)	Mach numbers 1.1	1.2	1.3	1.4
Rectangular perturbation	2.0		E & S	E	
	4.0		E	E	
Triangular perturbation	2.0		E & S	E	
	4.0		-	-	
10° ramp angle	2.0	-	E	E	-
	4.0	E	E	-	E
15° ramp angle	2.0	E	E & S	E & S	E
	4.0	E & S	E & S	-	-
20° ramp angle	2.0	E	E & S	-	-
	4.0	E	E & S	E	-

7.4 Quantitative Results

The following section determines the nature of the flow behind each wave in the shock reflection by applying oblique shock equations to the superimposed images captured using the high speed camera. This allowed the shock reflections observed above to be categorised as either a GR or VR depending on whether the flow behind the Mach stem is supersonic

or not. Two measuring methods were utilised to determine the coordinates of the shock reflections relative to the grid shown in Figure 7.6. The first method presented in Section 7.4.1 consisted of scaling the image manually with reference to two vertical and two horizontal cotton threads each 50 mm apart. However, due to the presence of barrel distortion in the images a second method presented in Section 7.4.2 makes use of a two-stage spline technique which ensures that the asymmetric grid and the corresponding triple point co-ordinates were all mapped onto a grid of known size to correct the optical abberation.

7.4.1 Initial Data

Images for the 15° ramp angle and $M_{bts} = 1.20$ were analysed, as they showed evidence of the first shocklet as observed by Skews et al. (2009). A high speed camera was used to capture superimposed images with adjustable time delays and exposure times. An exposure of 3 μs was used to clearly distinguish the incident wave, the Mach stem and the the reflected wave so that the trajectory and velocity of the triple point could be determined. As a result of the poor pixel resolution, the clarity of the images were insufficient to capture the supersonic patches and shocklets. Each photograph consists of three to six overlaid images of the triple point with a set time delay of 70 μs between them. These images were scaled using two horizontal and two vertical guides, both 50 mm apart. A typical multi-frame image is shown in Figure 7.18.

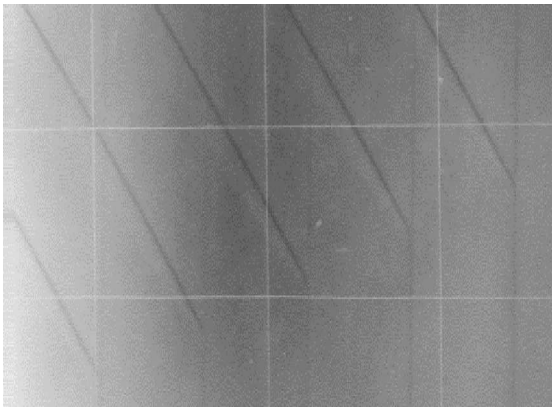


Figure 7.18: Five superimposed images taken at high magnification for a 15° ramp angle and $M_{bts} = 1.206$. Exposure time of 3 μs and a time delay of 70 μs between the triple points.

Due to the cylindrical incident wave produced in the diverging section, it is seen in Figure 7.4 on page 56 that the triple point trajectory path is curved as expected. All the waves in the vicinity of the triple point nonetheless appear to be planar in the photographs, as shown in Figure 7.18. This is mainly due to the very large radii of curvature of the waves and the optical magnification. When utilising the oblique shock equations to calculate the respective wave velocities, it was assumed that the incident and the reflected waves are planar near the triple point, implying that the flow regions in the vicinity of the triple point are uniform. A

pressure trace obtained just before the test section shown in Figure 7.19 indicates that there is very little decay in the pressure behind the incident wave. At a time of approximately 600 μs there is a jump in the pressure, this is the reflected wave trailing behind the shock reflection. The steadiness of the flow behind these two waves thus supports the uniformity of the flows in the oblique shock approach. A sample calculation given in Appendix A on page 79 determines the wave velocities and flow deflection angles.

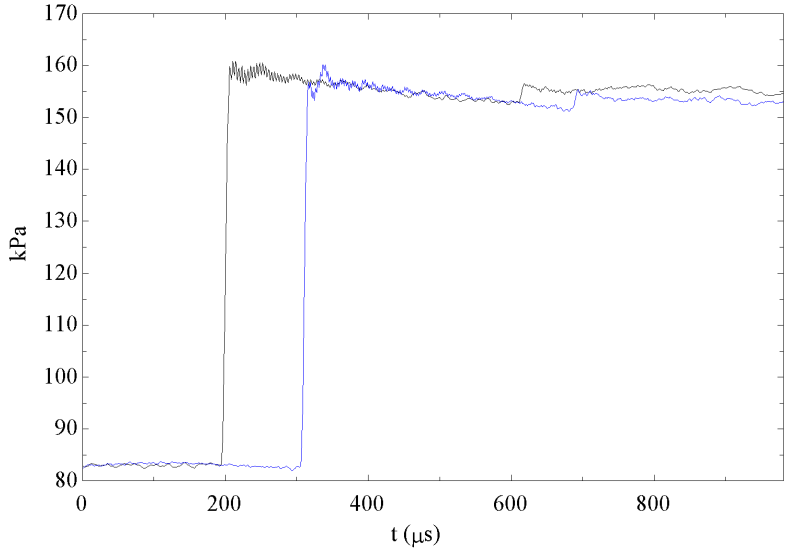


Figure 7.19: Typical pressure trance record for the two pressure transducers positioned before the test section, shown in Figure 5.5 on page 42. 15° ramp angle, $M_{bts} = 1.312$.

Four images were analysed for the 15° ramp angle and $M_{bts} = 1.206$ (test 1 to 4), and one for $M_{bts} = 1.303$ (test 5). Three positions of the triple point were used in each image to obtain well averaged results. Measurements were taken between the first and second shock, the second and third shock, and the first and third shock, where the respective triple point trajectory paths and the relative position of the reflected wave were determined using the drafting interface in Solid Edge V.19. Finally the wave velocities (M_1, M_2, and M_3) and the flow deflection angles (δ_1, δ_2, and δ_3) for the three regions (shown at Figure A.1 on page 79) were calculated as an average between the three shocks.

The analysis showed a slight amount of scatter for the tests 1 to 4, as shown in Figure 7.20. The repeatability of the data obtained in test 5 could not be commented on as it was the only overlaid image obtained for $M_{bts} = 1.303$. For all the tests the flow M_3 is just above sonic conditions, whilst the flow M_2 ahead of reflected wave is subsonic. These results are unrealistic and flawed, as according to the conservation of energy, a flow can only go from subsonic to supersonic if additional energy is added to the flow or if the area of the flow is decreased. None of these events occurred during the experimentation, and so it is possible that the non-physical data is a result of the uncertainty in the measurements. Since the reflected wave is very weak, a measurement error of the shock position as little as 0.5 mm was shown to change the nature of the flow from subsonic to supersonic or visa versa.

Therefore any distortion in the image could change the nature of the flow being calculated.

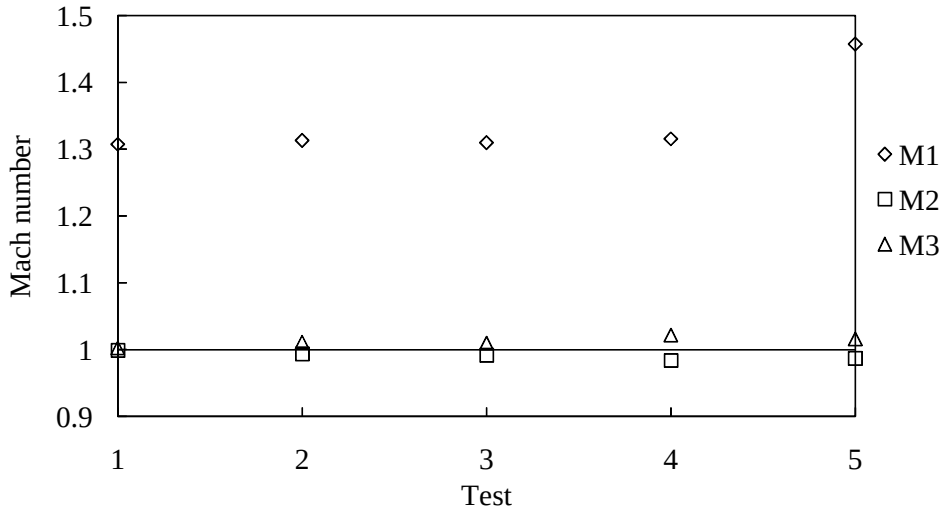


Figure 7.20: Initial Mach number data for captured GR for $M_{bts} = 1.206$ (test 1 to 4), and $M_{bts} = 1.303$ (test 5).

Similar results to those shown above were initially observed in Skews et al. (2009), where it was found that the flow changes from subsonic to supersonic. It was discovered that barrel distortion was the main calibration source of error in the images. Since the same setup was utilised in this study, barrel distortion was also an underlining factor to be considered. The effect of barrel distortion caused the corners of the blocks created by the grid not to be square, this increases particularly towards the periphery of the images. The distortion was believed to be attributed to the distortion produced due to the objective lens of the schlieren system. To resolve this problem the same image processing technique utilised in Skews et al. (2009) was applied to the images to reduce the above mentioned optical aberration. The modified results are given below.

7.4.2 Refined Data

A program developed by Mr. Paton transforms the asymmetric grids of the images into a grid of known size. This is achieved using a two-stage spline method which calculates the actual co-ordinates of the triple points relative to the corrected grid (Skews et al. 2009). The refined results where analysed in the same manner as before, with the three measurements taken off each image averaged. Since only six blocks of the grid were visible due to the high magnification as shown in Figure 7.18, only these blocks could be utilised for the grid correction. It was therefore necessary that each triple point and the accompanying intersection points with the grid, fell within the six grid block area to ensure that the spline method mapped the points accurately. The results are given in Figure 7.21.

It is first seen that the flow M_2 is now supersonic, with all the data points positioned above the sonic line ($M = 1$). The reflected wave is very weak, and the deflection (δ_2) through

it is also small, on average less than one tenth of a degree as shown in Table 7.3. All the tests determined the flow M_3 to be just below sonic conditions, a Mach number of around 0.99. Unlike the initial oblique shock calculations presented above, the refined results make physical sense, as the the flow goes from supersonic to subsonic when passing through the reflected wave. The barrel distortion in the images can therefore be singled out as the major calibration error in the schlieren system.

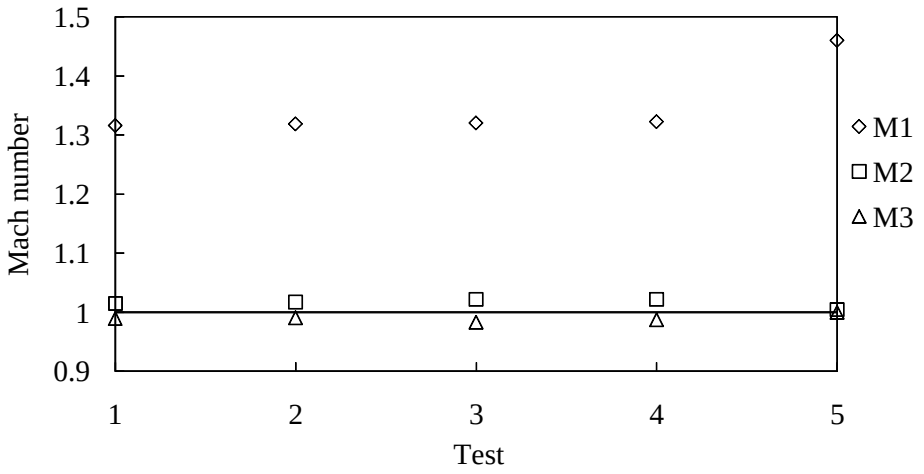


Figure 7.21: Modified Mach number data for captured GR for $M_{bts} = 1.206$ (test 1 to 4), and $M_{bts} = 1.303$ (test 5).

Table 7.3: Modified Mach number data for captured GR.

Test number	M_{bts}	Avg. M_1	Avg. M_2	Avg. M_3	θ (deg)	δ_1 (deg)	δ_2 (deg)
1	1.185	1.316	1.015	0.989	26.14	6.581	0.083
2	1.192	1.319	1.017	0.990	26.31	6.627	0.071
3	1.191	1.321	1.022	0.983	26.61	6.595	0.094
4	1.200	1.323	1.022	0.987	26.67	6.674	0.161
5	1.302	1.460	1.005	0.999	27.65	10.592	0.013

Since M_2 is supersonic, and the slopes between both the Mach stem and the incident wave are similar as shown in Figure 7.15, this means that the flow immediately behind the Mach stem is similar to the flow M_2 behind the incident wave. Hence, this means the flow behind the Mach stem is also supersonic. As shown in Figure 1.12 on page 12, the Guderley reflection consists of a supersonic region behind both the reflected wave and the Mach stem, whilst the VR consists of only a supersonic region behind the reflected wave. Therefore, because the flow is calculated to be supersonic behind the Mach stem in the current experiments, this suggests that the observed shock reflections are in fact GR, and not VR.

When analysing the flow structure predicted by Tesdall et al. (2002) in Figure 2.4 on page

17, it is seen that the flow immediately behind the reflected wave is subsonic followed by a sequence of diminishing supersonic patches along the Mach stem. The refined oblique shock data also predicts the flow M_3 behind the reflected wave to be subsonic behind the reflected wave, however the analyses cannot determine the nature of the flow further downstream of the reflected wave as the oblique shock equations are based on the planar wave assumption which models the flow as uniform in the three regions. The numerical results resolved a reflected wave with a radius of curvature of 2.20 m for the 2.0 m expansion chamber contrary to the planar wave assumption. The wave curvature could thus result in the flow accelerating from subsonic ($M_3 \approx 0.99$) to sonic or supersonic conditions, producing the first supersonic region. This supersonic region could represent the first supersonic patch behind the expansion wave as predicted by the computations of Tesdall and co-authors (Tesdall et al. 2002, Tesdall & Sanders 2006, Tesdall et al. 2008). The incident shock strength used for these computations are much weaker compared to the current experiments, and therefore it would be interesting to investigate whether the observations in the this report could be reproduced numerically.

7.4.3 Summary

The initial oblique shock analysis produced unrealistic results, whereby the subsonic flow ahead of the reflected wave turned into supersonic flow behind the wave. It was found that since the reflected wave was very weak, measurement uncertainties of 0.5 mm greatly affected the nature of the flow. Barrel distortion was found to be the main calibration source of error in the images. This led to a more refined analysis which determined the flow behind the reflected wave to be just below sonic conditions ($M_3 \approx 0.99$), and the flow deflection δ_2 through the weak reflected wave to be on average less than 0.10°. It was determined that the Mach number behind the Mach stem was approximately 1.02, which confirms that the reflections observed are in fact GR. The data could not be quantitatively be compared to Skews et al. (2009) due to the different incident Mach number strengths.

Chapter 8

Conclusions

The high-resolution experiments for both shock tube configurations showed evidence of the forth wave in the GR, confirming that the GR can be produced in a conventional shock tube. The majority of the images captured only the expansion wave behind the reflected shock, whilst a few images provided evidence of the shocklet terminating the expansion wave. The latter images showing identical flow features to those observed in Skews et al. (2009). This required the use of very sensitive optical arrangement.

Unrepeatable results were obtained showing evidence of the shocklet in the GR, these were only captured on average once in every five tests. Interestingly the shocklet was mostly observed for incident Mach numbers of around 1.20 for the 15° and 20° ramp angles. Vague evidence of the second expansion wave was observed, but the sequence of supersonic patches as predicted by Tesdall et al. (2002) could not be resolved.

The virtual Mach stem hypothesis was verified as the GR was observed, for the first time, in a conventional shock tube capable of only producing Mach stem lengths smaller than 0.4 m. Therefore, the Mach stem attached to the Mach reflection, is the overall vertical distance travelled by the triple point over the entire duration of the reflection. It was shown that the further the shock reflection propagated, the larger it expanded allowing the flow features to be better resolved. The triple point reflections in the shock tube were found to be a very important technique in maintaining the strength of the shock reflection downstream as a result of the amplification of the waves after each triple point reflection. This allowed Mach numbers as high as 1.40 to be achieved in this setup.

The supersonic patch size was found to vary between 2.3% to 4.8% of the virtual Mach stem length. For the 15° and 20° ramp angles a directly proportional relationship with similar gradients was observed when plotting the size of the supersonic patch with the virtual Mach stem length. The 15° ramp angle produced a better defined GR with supersonic patches 46% larger compared to the 20° ramp angle. The size of the supersonic region was considerably larger than that produced in Skews et al. (2009) as a result of the larger virtual Mach stem lengths produced.

An oblique shock analysis under the assumption of plane waves was conducted on superimposed images for the 15° ramp angle for $M_{bts} = 1.20$. It was shown that the reflected wave was very weak with the flow Mach number M_2 ahead of it being approximately 1.02 with a reference frame fixed to the primary triple point. It was determined that the flow behind the Mach stem was approximately 1.02, which confirms that the reflections observed for the 15° ramp angle and $M_{bts} = 1.20$ are in fact GR.

Very similar results were obtained for the perturbation sources and the various ramp angles, both showing evidence of the first shocklet underneath the expansion fan. Difficulty arose in determining which of the results correctly represented the GR as the size of the supersonic patch varied for both the shock tube configurations. The ramp angle configuration was the preferred setup, as the data could be easily compared with results from previous experimental work. The perturbation dimensions were complicated to parameterise as various shapes and sizes could be tested. Therefore, it is advised that in future studies the ramp angle configuration be utilised.

References

Ben-Dor, G. (2007), *Shock Wave Reflection Phenomena*, Springer Science+Business Media.

Birkhoff, G. (1950), *Hydrodynamics*, Princeton University Press.

Bleakney, W. & Taub, A. H. (1949), 'Interaction of shock waves', *Rev. Modern Phys.* pp. 584–605.

Brio, M. & Hunter, J. K. (1992), 'Mach reflection for the two-dimensional Burgers equation', *Phys. D* **60**, 194–207.

Colella, P. & Henderson, L. F. (1990), 'The von Neumann paradox for the diffraction of weak shock waves', *Journal of Fluid Mechanics* **213**, 71–94.

Defina, A., Susin, F. M. & Viero, D. P. (2008), 'Numerical study of the Guderley and Vasilev reflections in steady two-dimensional shallow water flow', *Physics of Fluids* **20**(9), 097102.

Defina, A., Viero, D. P. & Susin, F. M. (2008), 'Numerical simulation of the Vasilev reflection', *Shock Waves* **18**(9), 235–242.

Guderley, K. G. (1962), *The theory of transonic flow. Translated from the German by J.R.Moszynski.*, International Series of Monographs in Aeronautics and Astronautics. Div. II, Vol. 3. Oxford etc.: Pergamon Press. XIII, 344 p. .

Henderson, L. F. (1987), 'Regions and boundaries for diffracting shock wave systems', *Zeitschrift Angewandte Mathematik und Mechanik* **67**, 73–86.

Hunter, J. K. & Brio, M. (2000), 'Weak shock reflection', *Journal of Fluid Mechanics* **410**, 235–261.

Kobayashi, S., Adachi, T., Satoh, M. & Suzuki, T. (1997), 'On the formation mechanism of von Neumann reflection.', *Proc 21st Int Symp on Shock Waves* pp. 881–885.

Oosthuizen, P. H. & Carscallen, W. E. (1997), *Compressible Fluid Flow*, McGraw-Hill.

Sasoh, A. & Takayama, K. (1994), 'Characterization of disturbance propagation in weak shock-wave reflections', *Journal of Fluid Mechanics* **277**, 331–345.

Skews, B. W. (1970), 'Shock-shock reflections.', *C.A.S.I. Transactions* **4**, 16–19.

Skews, B. W. & Ashworth, J. T. (2005), 'The physical nature of weak shock wave reflection', *Journal of Fluid Mechanics* **542**, 105–114.

Skews, B. W., Li, G. & Paton, R. (2009), 'Experiments on Guderley Mach reflection', *Shock Waves* **19**, 95–102.

Sternberg, J. (1959), 'Triple-shock intersections', *Phys. Fluids* **2**, 179–206.

Tabak, E. G. & Rosales, R. R. (1994), 'Focusing of weak shock waves and the von Neumann paradox of oblique shock reflection.', *Phys. Fluids* pp. 1874–1892.

Tesdall, A. M., & Hunter, J. K. (2002), 'Self-similar solutions for weak shock reflection', *SIAM J. Appl. Math.* **63**, 42–61.

Tesdall, A. M. & KeyFitz, B. L. (2010), 'A continuous, two-way free boundary in the unsteady transonic small disturbance equations', *Journal of Hyperbolic Differential Equations* **22**, 1–22.

Tesdall, A. M., Sanders, R. & Keyfitz, B. L. (2008), 'Self-similar solutions for the triple point paradox in gasdynamics.', *SIAM J. Appl. Math.* **68**(5), 1360–1377.

Tesdall, A. M. & Sanders, R. T.and Keyfitz, B. L. (2006), 'The triple point paradox for the nonlinear wave system', *SIAM J. Appl. Math.* **67**, 321–336.

Tropea, c., Yarin, A. L. & Foss, J. F. (2007), *Springer Handbook of Experimental Fluid Mechanics*, Springer.

Vasil'ev, E. I., Elperin, T. & Ben-Dor, G. (2008), 'Analytical reconsideration of the von Neumann paradox in the reflection of a shock wave over a wedge', *Physics of Fluids* **20**(4), 046101.

Vasil'ev, E. & Kraiko, A. (1999), 'Numerical simulation of weak shock wave diffraction over a wedge under the von Neumann paradox conditions.', *Comp. Math. & Math. Phys.* **39**, 1335–1345.

von Neumann, J. (1963), *Collected Works*, Vol. 6, New York: Pergamon Press.

Zakharian, A. R., Brio, M., Hunter, J. K. & Webb, G. M. (2000), 'The von Neumann paradox in weak shock reflection', *Journal of Fluid Mechanics* **422**, 193–205.

Zucrow, M. J. & Hoffman, J. D. (1976), *Gas Dynamics*, Vol. 1, John Wiley & Sons.

Appendix A

Data Anaylsis

The following chapter presents a sample calculation using the oblique shock theory to determine the wave velocities in the shock reflection observed in Section 7.3. The flow in the three regions near the triple point were analysed as shown in Figure A.1. The regions labeled as 1, 2 and 3 represent the flow ahead of the incident wave, and behind the incident wave and the reflected wave.

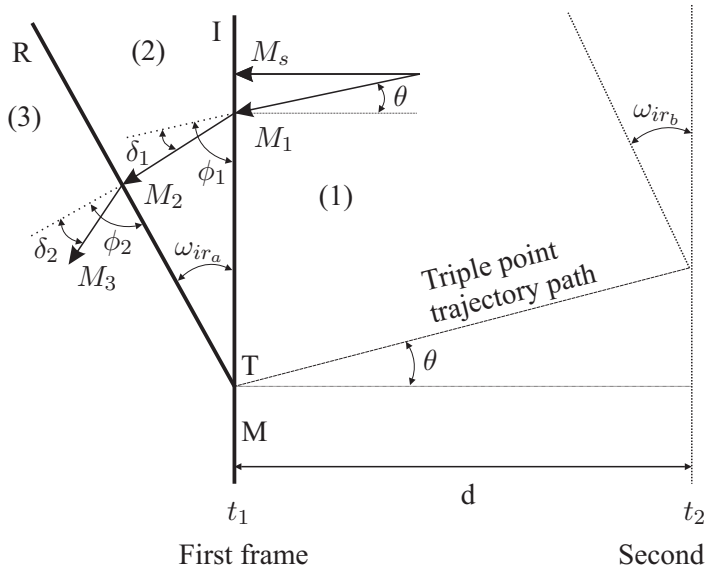


Figure A.1: Schematic of two superimposed irregular Mach shock reflections at time t_1 and t_2.

In order to analyse the flow in the three regions in the vicinity of the triple point, the flows were made pseudo-stationary by superimposing the reversed velocity of the triple point on the wave configuration. The deflection angles and the Mach numbers for the regions 1, 2 and 3 were then calculated using oblique shock wave theory for a steady two-dimensional planar adiabatic flow by applying Equations (1.8) and (1.9) on page 4. Before any measurements were obtained from the multi-frame images, the images needed to first be scaled correctly so that the grid represents a 50×50 mm^2 matrix. Thereafter, the triple point trajectory angle θ and the angles between the incident and reflected shock waves ω_{ir_a} and ω_{ir_b} were measured

using the drafting option on Solid Edge V.19.

Images were obtained using the high speed camera for the second shock tube configuration, where 5 to 6 overlaid frames were shot with a delay between each frame of 73 μs (this includes the exposure time of 3 μs). However, only 3 of the overlaid frames where required in the analysis. An image obtained for the 15° wedge angle for a Mach number of 1.2 will be used for this sample calculation. Figure A.2 shows the multiple-frames and the measurements obtained from the image.

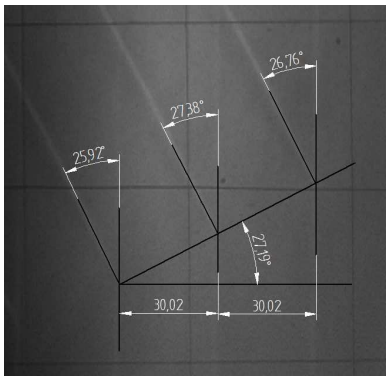


Figure A.2: Oblique shock wave analysis of three overlaid images for the 15° ramp angle and $M_{bts} = 1.206$

For the following calculation the Mach number M_s of the incident shock wave is determined by the displacement d travelled in a time interval $t_2 - t_1$ which is essentially the set delay time of the camera.

The velocity of the incident shock wave is given by:

$$V = \frac{d}{\Delta t} = \frac{0.03002}{73e^{-6}} = 411.23 \text{ m/s}$$

The Mach number of the incident shock wave for an atmospheric temperature of 21°C:

$$M_s = \frac{V}{a} = \frac{411.23}{20.048\sqrt{273.15 + 21}} = 1.190$$

The components of the Mach number M_s parallel to the triple point propagation path θ_1 is:

$$M_1 = \frac{M_s}{cos\theta_1} = \frac{1.190}{cos(27.19°)} = 1.338$$

The angle ϕ_1 which the incident wave makes with the propagation path:

$$\phi_1 = 90° - \theta_1 = 90° - 27.19° = 62.81°$$

The general oblique shock wave equations were then used to determine the diffraction angle δ_1 of the flow entering region (2) and the Mach number M_2 of the flow behind the incident

shock wave:

$$\begin{aligned}\delta_1 &= tan^{-1}\left(2cot\phi_1\frac{M_1^2sin^2(\phi_1)-1}{M_1^2(\gamma+cos(2\phi_1))+2}\right)\\ &= tan^{-1}\left(2cot62.81^\circ\frac{1.338^2sin^2(62.81^\circ)-1}{1.338^2(1.4+cos(2\times62.81^\circ))+2}\right)\\ &= 7.052^\circ\end{aligned}$$

and

$$\begin{aligned}M_2 &= \left(\frac{\frac{2}{\gamma-1}+M_1^2sin^2\phi_1}{\frac{2\gamma}{\gamma-1}M_1^2sin^2\phi_1-1}\right)^{1/2}/sin(\phi_1-\delta_1)\\ &= \left(\frac{\frac{2}{1.4-1}+1.338^2sin^2(62.81^\circ)}{\frac{2\times1.4}{1.4-1}1.338^2sin^2(62.81^\circ)-1}\right)^{1/2}/sin(62.81^\circ-7.052^\circ)\\ &= 1.026\end{aligned}$$

For the reflected shock wave, a similar approach is undertaken, whereby a new inflow angle ϕ_2 is used for the oblique shock analysis::

$$\phi_2 = \phi_1 - \delta_1 + \omega_{ir_a} = 62.81^\circ - 7.052^\circ + 26.68^\circ = 82.44^\circ$$

The Mach number of the flow entering the region (3) is similarly determined by applying the oblique shock equations with reference to the angle θ:

$$\begin{aligned}\delta_2 &= tan^{-1}\left(2cot\phi_2\frac{M_2^2sin^2(\phi_2)-1}{M_2^2(\gamma+cos(2\phi_2))+2}\right)\\ &= tan^{-1}\left(2cot82.44^\circ\frac{1.026^2sin^2(82.44^\circ)-1}{1.026^2(1.4+cos(2\times82.44^\circ))+2}\right)\\ &= 0.2136^\circ\end{aligned}$$

and

$$\begin{aligned}M_3 &= \left(\frac{\frac{2}{\gamma-1}+M_2^2sin^2\phi_2}{\frac{2\gamma}{\gamma-1}M_2^2sin^2\phi_2-1}\right)^{1/2}/sin(\phi_2-\delta_2)\\ &= \left(\frac{\frac{2}{1.4-1}+1.026^2sin^2(82.44^\circ)}{\frac{2\times1.4}{1.4-1}1.026^2sin^2(82.44^\circ)-1}\right)^{1/2}/sin(82.44^\circ-0.2136^\circ)\\ &= 0.992\end{aligned}$$

The same procedure is applied to the second frame with the shock wave configuration of angle ω_{ir_b}. It should be emphasised that the following analysis is very basic, however the values obtained should give a rough estimate of the flow velocities in each region.

Appendix B

Testing Procedures and Precautions for Shock Tube Tests

B.1 Testing Procedure for Large-Scale Diffraction (450mm) Shock Tube

Revision No.: 0
Revision Date: 2009.09.23

All test data for any given series of data to be recorded using LSDST-05 (Log sheet) as per the operating procedure listed below. Precautions as outlined in LSDST-02 must be adhered to at all times.

1. High pressure air receiver must be charged to supply driver of shock tube.
2. Before any given day's testing the pre-test inspection (LSDST-04) must be made and signed by the first operator for the day.
3. Switch on all instrumentation.
4. Close all valves on control panel except ball valves for driver static pressure and driver vent ball valves.
5. Open high pressure line globe valve.
6. If a flow visualisation system is set up and the xenon lamps are being used as the light source these must be switched onto external mode, i.e. must not flash repeatedly.
7. The diaphragm trigger plunger spring must be compressed and latched into the cocked position.
8. After greasing the top and bottom of the diaphragm material (to improve sealing and to secure it for closing the driver), fit a new, undamaged diaphragm sheet across the inlet to the expansion section.

9. Ensure that fingers and limbs are not in the diaphragm clamping area of the tube then close driver slowly and carefully from the rear.

10. Loosely fit all driver securing nuts manually.

11. Using the supplied pneumatic wrench and PPE (vibration-damping gloves, goggles, visor and hearing protection), tighten the driver securing nuts in the sequence labelled on the driver flanges i.e. 1-1-1, 2-2-2, 3-3-3 etc. as per the driver clamping procedure (LSDST-03).

12. Switch on operator headlamp and switch off test area lights (if the test includes the schlieren photography or similar flow visualisation, otherwise the test area lights must be left on).

13. The oscilloscope must be triggered on (must say “waiting for trigger”) and the delay time must be input on the delay box.

14. Hearing protection as provided must be worn by all persons inside the testing room from this point on until the end of a single test. Check that no unauthorised persons have entered the venue and that interlocks are still active.

15. Close the driver vent ball valve.

16. The pressure regulator valve at the top must be opened to 15 – 20the desired testing pressure as indicated on the unit.

17. The control globe valve must be slowly opened to pressurise the driver section. Blow the whistle at approximately half the required driver pressure to alert persons outside of the venue of the impending test in case of a premature burst.

18. Close the control globe valve once the required driver pressure has been attained.

19. Blow the whistle again and wait 3 - 5 seconds before the plunger string is pulled to prick the diaphragm. If flow visualisation is required, the operator headlamp must be switched off and the camera hand trigger must be closed and held closed until the blast can be heard.

20. The operator headlamp must be switched on (if necessary) and the panel supply globe valve immediately closed.

21. The driver vent ball valve must be opened to allow remaining air in the driver to be vented.

22. Switch on the test area lights.

23. Loosen the driver section securing nuts as per the driver clamping procedure (LSDST-03).

24. Remove the loosened nuts manually and open the driver by pushing it slowly and carefully at the rear.

25. Remove and dispose of the burst diaphragm.
    At the end of any given day's testing:

26. Close the high pressure line globe valve.

27. Open all valves on the control panel.

28. Move the downstream blast barrier from the testing position and remove the muffler from the shock tube exhaust.

29. Remove all diaphragm material trapped in the test section.

B.2 Testing Precautions

Revision No.: 0
Revision Date: 2009.09.23

1. In the event of a failed diaphragm burst (diaphragm does not rupture or only slowly leaks following trigger release), the panel supply globe valve must be closed and the driver vent valve slowly opened to safely vent the driver. As venting may cause the diaphragm to rupture, the whistle must be blown at the start of this procedure and all hearing protection must be worn.

2. Make sure all the bolts for the driver section are screwed in correctly so as not to strip the bolts.

3. Apply grease on bolts every 20 tests to ensure long-life of bolt threads

4. When placing diaphragm between gaskets, make sure the diaphragm grain direction is correct, the grain direction must be vertical.

5. All doors must be locked and if any unauthorised person enters the testing room, the testing procedure must be aborted immediately. The unauthorised person must be asked to leave the room for testing to proceed.

6. Blast barriers must be placed correctly and under no circumstances may anyone walk in-front of the shock tube outlet when testing.

7. Always make sure the plunger is re-set before clamping the driver section with the new diaphragm set.

8. Make sure the oscilloscope has recorded a pressure trace before commencing the next test.

9. A whistle must be used at least 30s before testing of the shock tube.
10. Hearing protection must be worn before testing of the shock tube.

B.3 Driver Clamping Procedure

Revision No.: 0
Revision Date: 2009.09.23

1. Ensure that wrench socket is securely fitted to the pneumatic wrench and that all personal protective equipment (vibration-damping gloves, goggles, visor and hearing protection) is worn.

Tightening Before Test

2. Ensure that the pneumatic wrench is set to turn clockwise (tighten).
3. Fit the socket of the pneumatic wrench over the nut at the “1” position at the top of the driver flange.
4. Loosely holding the socket to ensure safe operation, tighten the nut by depressing the trigger, allowing the wrench to run for 3 seconds after it has stopped turning freely.
5. Once the pneumatic wrench has stopped turning remove it from the nut.
6. Fit the socket of the pneumatic wrench over the next “1” position clockwise from the top as seen from the rear of the driver.
7. Repeat steps 4 – 6 for the remaining “1” position nut.
8. Fit the socket of the pneumatic wrench over the nut located at the “2” position clockwise next to the first “1” position as seen from the rear of the driver and repeat steps 5 – 7 for the “2” positions.
9. Repeat 8 for positions “3” to “6”.

Loosening After Test

10. Ensure that the pneumatic wrench is set to turn counter-clockwise (loosen).
11. Fit the socket of the pneumatic wrench over the nut at the “1” position at the top of the driver flange.
12. Loosely holding the socket to ensure that the nut and / or socket do not fly free, loosen the nut by depressing the trigger until the socket turns freely.
13. Once the pneumatic wrench has stopped turning remove it from the nut.

14. Remove the nut from the socket and remove the washer from the bolt (if necessary).
15. Fit the socket of the pneumatic wrench over the next “1” position clockwise from the top as seen from the rear of the driver.
16. Repeat steps 4 – 6 for the remaining “1” position nut.
17. Fit the socket of the pneumatic wrench over the nut located at the “2” position clockwise next to the first “1” position as. seen from the rear of the driver and repeat steps 5 – 7 for th.e “2” positions.
18. Repeat 8 for positions “3” to “6”.

Flow Research Unit

Pre-Use inspection - **Large-Scale Diffraction (450mm) Shock Tube**

Month .....

If In Order	
If Faulty	X
No Tests	

Document No.	LSDST-04
Revision No.	0
Revision Date	2009.09.23

Item	Inspection conducted	1	2	3	4	5	6	7	8	9	10	11	12	13	14	15	16	17	18	19	20	21	22	23	24	25	26	27	28	29	30	31	Remarks	RP
1	Walling downstream of shock tube exhaust undamaged (excludes minor scratches, chips etc.)																																	
2	Shock tube clear of debris and other loose materials																																	
3	Muffler fitted to shock tube exhaust																																	
4	Lateral barriers placed at exhaust of shock tube																																	
5	Downstream barrier placed at exhaust of sock tube and **casters locked**																																	
6	Test section window frames secure																																	
7	Supply valve and connection inspected for leaks																																	
8	Supply hose inspected for leaks or other damage																																	
9	Supply hose is not twisted or severely bent																																	
10	Control panel valves and connections inspected for leaks																																	
11	Driver free of loose materials and undamaged																																	
12	Driver gaskets in good condition																																	
13	Driver closing nuts and bolts in good condition																																	
14	Whistle available and in working order																																	
15	**All** required personal protective equipment (PPE) [vibration-damping gloves, hearing protection, goggles] present and in good condition																																	
16	User headlamps present and in working order																																	
17	Instrumentation cabling secured off floor of working area																																	
18	Venue is clear of all unauthorised personnel																																	
19	Magnetic interocks and test lights have been enabled																																	

RP	Name - Responsible Person	Signature - Responsible Person	Name - Supervisor	Signature - Research Officer

Responsible persons are those operators duly trained in the operation of the Large-Scale Diffraction (450mm) Shock Tube by the Research Officer of the Flow Research Unit as notarised above

Flow Research Unit

Test log - **Large-Scale Diffraction (450mm) Shock Tube**

Date .....
Static Pressure .....
Static Temperature .....
Sound Speed .....

If In Order	
If Faulty	X

Document No.	LSDST-05
Revision No.	0
Revision Date	2009.09.23

Test	Time	Diaphragm Thickness [µm]	Driver Safely Closed	Blast Barriers In Place	Blast Barrier Casters Locked	Muffler Fitted	Pressure Regulator Setting [kPa]	Required Driver Pressure [kPa]	Trigger Delay [µs]	Venue Clear of Unauthorised Persons	Interlocks Activated	Successful Burst	Approximate Driver Pressure at Burst / Fail [kPa]	Approximate Wave Travel Time Between Speed Pressure Transducers [µs]	Wave Velocity [m/s]	Wave Mach Number	Camera Image Name / Number	Driver Safely Opened	Diaphragm Cleared from Driver	Diaphragm Cleared from Test Section	Signature	Responsible Person
1																						
2																						
3																						
4																						
5																						
6																						
7																						
8																						
9																						
10																						
11																						
12																						
13																						
14																						
15																						
16																						
17																						
18																						
19																						
20																						

End of Day Checklist

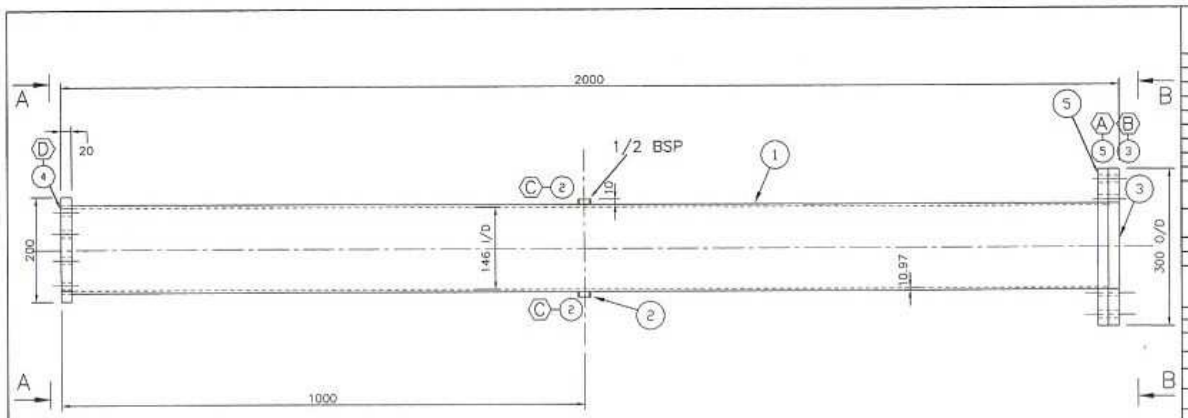
Item	/ X
High pressure line globe valve closed	
All valves on control panel opened	
Blast barriers moved away from exhaust	
Muffler removed from shock tube exhaust	
Diaphragm material removed from test section	

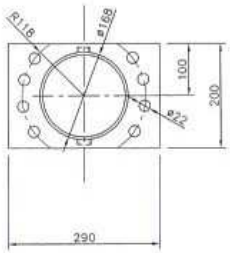
End of Day

Time of Conclusion .....
Responsible Person
.....
Signature (RP)
.....

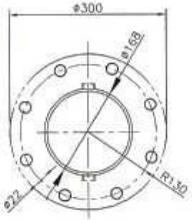
Appendix C

Driver Certificate of Manufacture

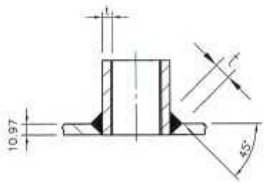




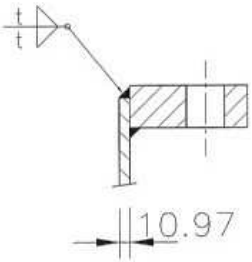
VIEW ON A–A



VIEW ON B–B



SOCKET TO PIPE
WELD DETAIL



FLANGE TO PIPE

VESSEL DATA

DESIGN CODE		RSA/CIF 81 07A09
DESIGN PRESSURE	kpa	1000
DESIGN TEMPERATURE	°C	25
OPERATING PRESSURE	kpa	1000
OPERATING TEMPERATURE	°C	25
HYDROSTATIC TEST PRESSURE	kpa	1300
CORROSION ALLOWANCE	mm	NIL
X-RAY		NONE
HEAT TREATMENT		NONE
JOINT FACTORS: SHELL		0.7
ENDS		0.85
MASS FULL OF WATER	kG	±497
EMPTY		±152
CUBIC CAPACITY	m³	0.053.5
ELECTRODES		E7018,ER70S-6 & ARGO-5 EM12K F7A0

NOZZLE SCHEDULE

MARK	SIZE	QTY	NOZZLES SCH	O.D.	WALL	FLANGES TYPE	RATE	FACE	REMARKS
A	168 I/D	1	80	300	20		PN16	FF	END FLANGE
B	168 I/D	1	N/A	300	20	N/A	N/A	N/A	BLANK FLANGE
C	1/2"	2	N/A	21.30	3000#	N/A	N/A	N/A	INSERT PLUG
D	168 I/D	1	80	290x200	20		PN16	FF	DRIVER FLANGE

ITEM	QTY	DESCRIPTION	MATERIAL	REMARKS
5	1	END FLANGE 168 I/D	BS1501-151-430A	300 O/D
4	1	DRIVER FLANGE 290x200x20	BS1501-151-430A	168 I/D
3	1	BLANK FLANGE	BS1501-151-430A	300 O/D
2	2	15 BSP SOCKETS	ASTM-A105	3000#
1	1	PIPE 146 I/D	ASTM-A106-GRB	SCH 80

MATERIAL LIST

REV	DATE	BY	DESCRIPTION
0	24.02.2010	K.P.	FIRST ISSUE

This drawing is subject to return on demand and must not be copied or passed on to any third party, or used directly or indirectly for any other purpose than the design and construction to the order of ARLEC Engineering Works CC.

	DATE	NAME
DRAWN	24.2.10	K.PRETT
CHECKED		
APPROVED		

SHEET 1 OF 1

SCALE 1:7.5

33.5 LITRE HORIZONTAL DRIVER ASSEMBLY

ARLEC

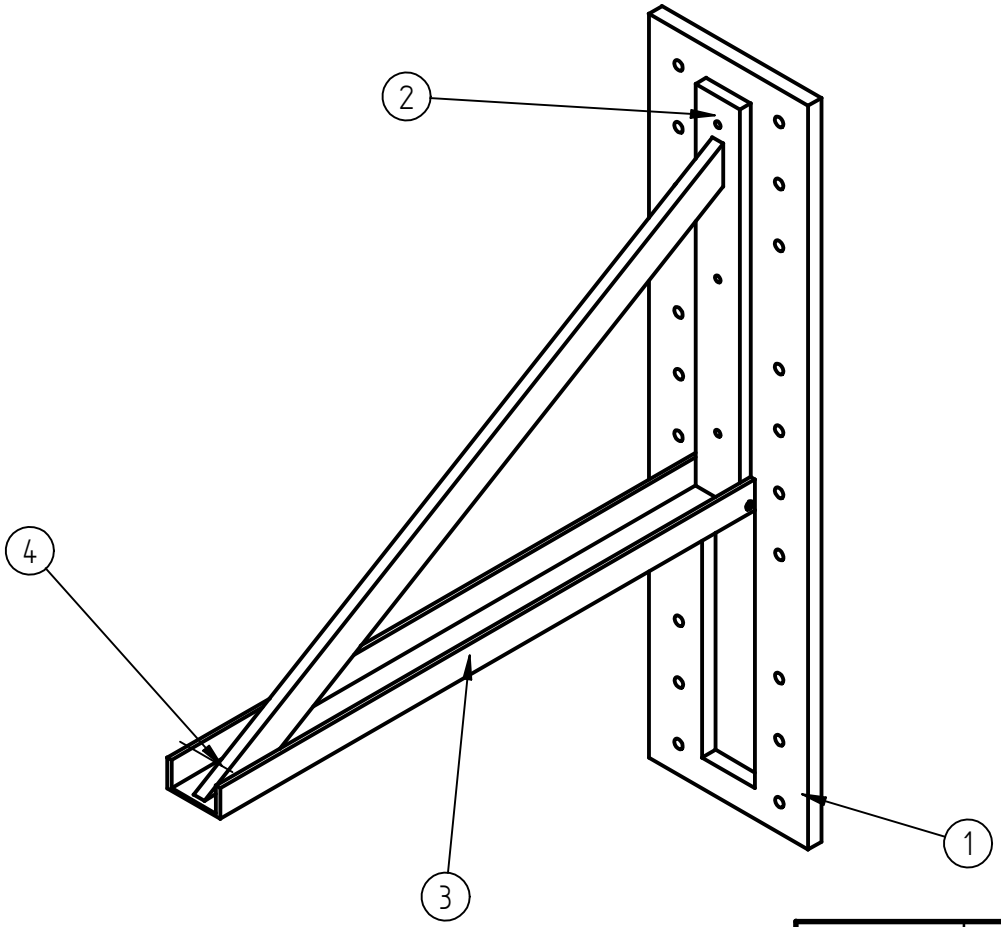
ARLEC DRG No WIT501

REV 0

Appendix D

Shock Tube Engineering Drawings

D.1 First Shock Tube Configuration - Perturbation Sources



Item Number	Title	Quantity
1	Existing End Plate	1
2	Support Plate	1
3	U-Channel	1
4	Rib Support	1

	NAME
DRAWN BY	Andre Cachucho (0501252N)
SUPERVISOR	Prof. B. W. Skews
ENG APPR	
DATE	24/04/2008

ALL DIMENSIONS ARE IN MILLIMETERS.
TOLERANCES UNLESS OTHERWISE STATED
± 0..2MM OR TO STANDARDS DICTATED BY
MATERIALS USED. ANGLES IN DEGREES ± 0.5 °

UNIVERSITY OF THE WITWATERSRAND

SCHOOL OF MECHANICAL, AERONAUTICAL AND INDUSTRIAL ENGINEERING

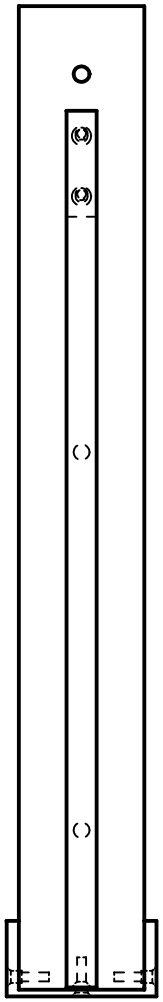
TITLE End Plate Assembly

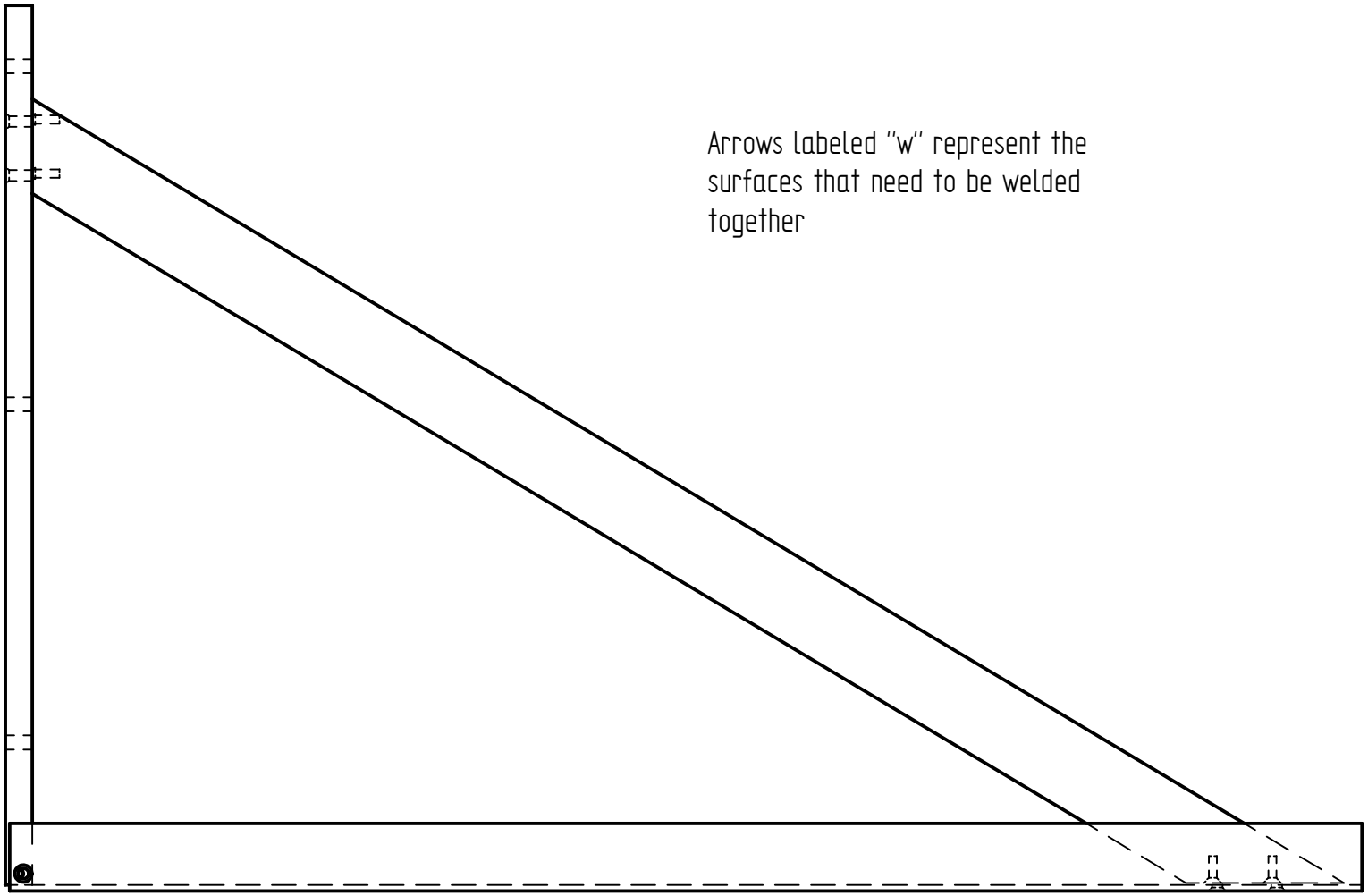
QUANTITY: 1

REV

SCALE: 1 : 10 | WEIGHT: | 1 of 10

SOLID EDGE ACADEMIC COPY





Arrows labeled "w" represent the surfaces that need to be welded together

	NAME
DRAWN BY	Andre Cachucho (0501252N)
SUPERVISOR	Prof. B. W. Skews
ENG APPR	
DATE	24/04/2008

ALL DIMENSIONS ARE IN MILLIMETERS.
TOLERANCES UNLESS OTHERWISE STATED
± 0..2MM OR TO STANDARDS DICTATED BY
MATERIALS USED. ANGLES IN DEGREES ± 0.5 °

UNIVERSITY OF THE WITWATERSRAND

SCHOOL OF MECHANICAL, AERONAUTICAL AND INDUSTRIAL ENGINEERING

TITLE End Plate Assembly (welding)

QUANTITY: 1

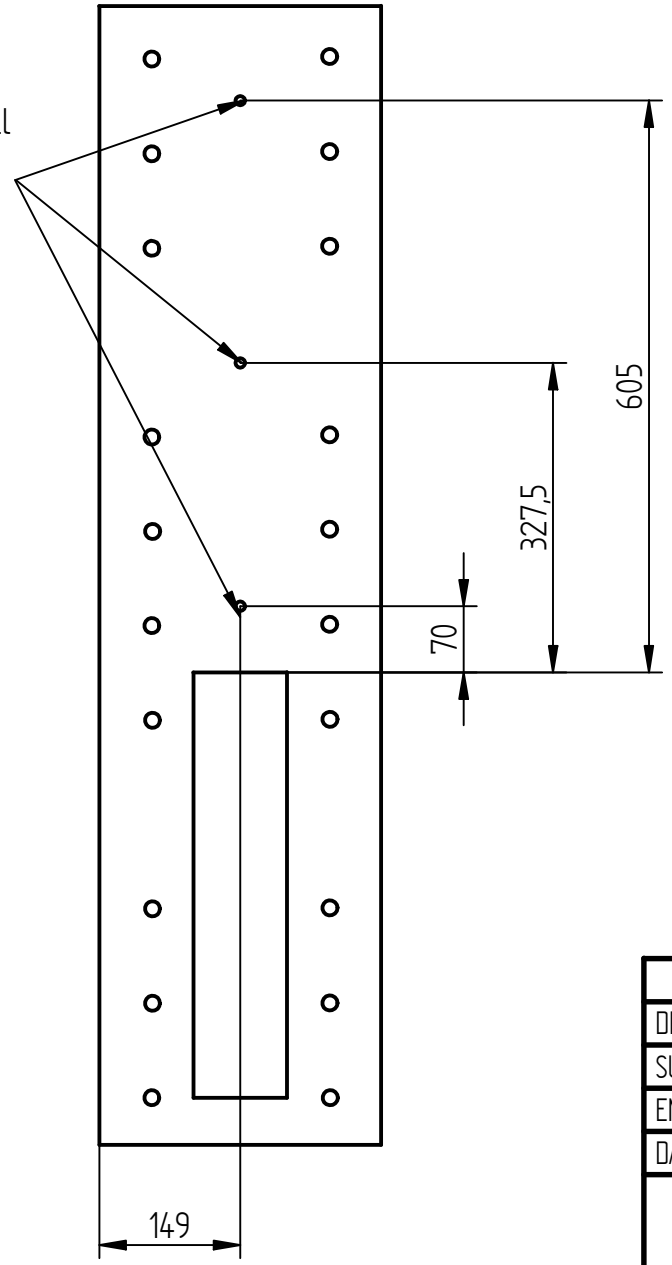
REV

SCALE: 1 : 5

WEIGHT:

SOLID EDGE ACADEMIC COPY

Holes need to be drilled into existing End Plate All holes are M10.



	NAME
DRAWN BY	Andre Cachucho (0501252N)
SUPERVISOR	Prof. B. W. Skews
ENG APPR	
DATE	24/04/2008

ALL DIMENSIONS ARE IN MILLIMETERS.
TOLERANCES UNLESS OTHERWISE STATED
± 0..2MM OR TO STANDARDS DICTATED BY
MATERIALS USED. ANGLES IN DEGREES ± 0.5 °

UNIVERSITY OF THE WITWATERSRAND

SCHOOL OF MECHANICAL, AERONAUTICAL AND INDUSTRIAL ENGINEERING

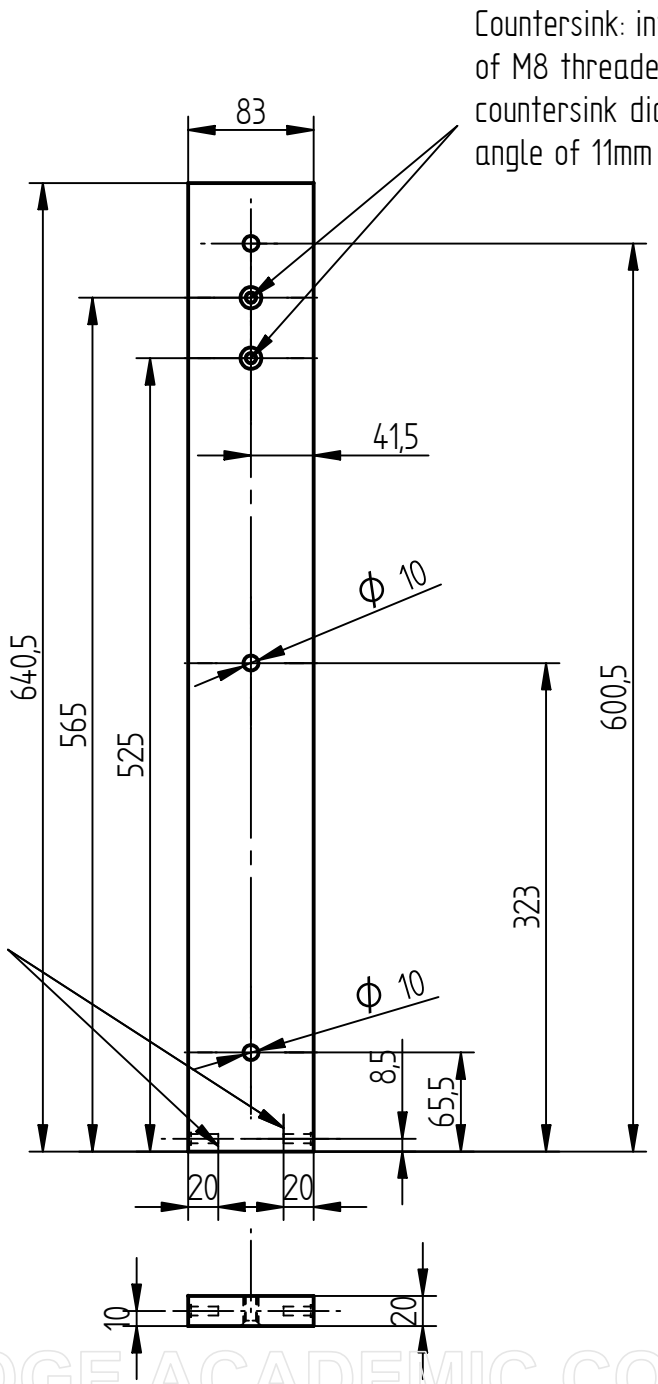
TITLE Existing End Plate

QUANTITY: 1

REV

SCALE: 1 : 8 | WEIGHT: | 2 of 10

SOLID EDGE ACADEMIC COPY



	NAME
DRAWN BY	Andre Cachucho (0501252N)
SUPERVISOR	Prof. B. W. Skews
ENG APPR	
DATE	24/04/2008

ALL DIMENSIONS ARE IN MILLIMETERS.
TOLERANCES UNLESS OTHERWISE STATED
± 0..2MM OR TO STANDARDS DICTATED BY
MATERIALS USED. ANGLES IN DEGREES ± 0.5 °

UNIVERSITY OF THE WITWATERSRAND

SCHOOL OF MECHANICAL, AERONAUTICAL AND INDUSTRIAL ENGINEERING

TITLE Support Plate

QUANTITY: 1

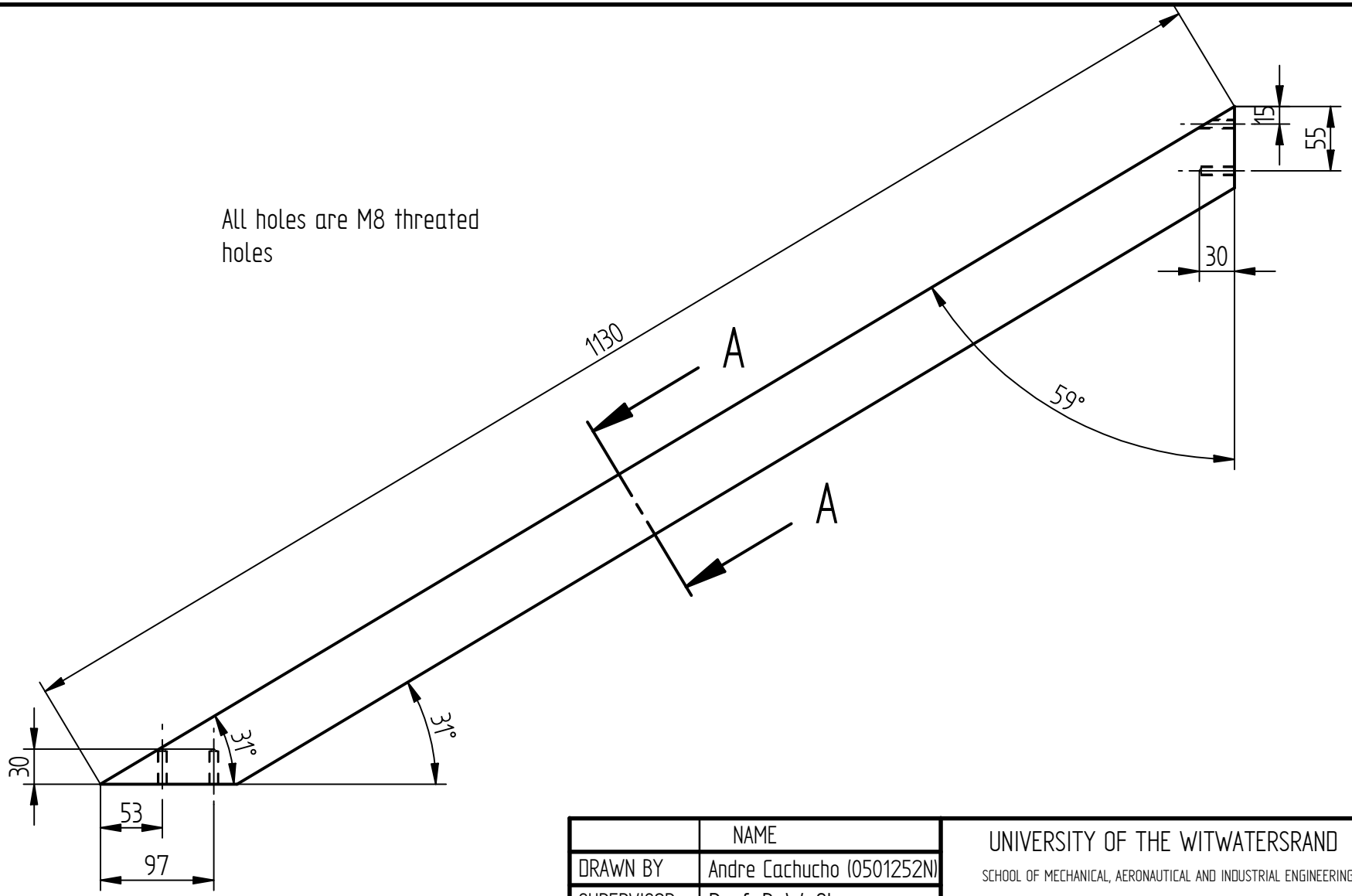
REV

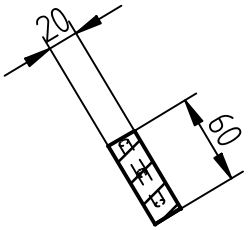
SCALE: 1 : 4

WEIGHT:

SOLID EDGE ACADEMIC COPY

All holes are M8 threated holes





SECTION A–A

	NAME
DRAWN BY	Andre Cachucho (0501252N)
SUPERVISOR	Prof. B. W. Skews
ENG APPR	
DATE	24/04/2008

UNIVERSITY OF THE WITWATERSRAND

SCHOOL OF MECHANICAL, AERONAUTICAL AND INDUSTRIAL ENGINEERING

TITLE Support Rib

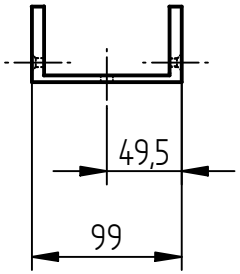
ALL DIMENSIONS ARE IN MILLIMETERS. TOLERANCES UNLESS OTHERWISE STATED ± 0..2MM OR TO STANDARDS DICTATED BY MATERIALS USED. ANGLES IN DEGREES ± 0.5 °

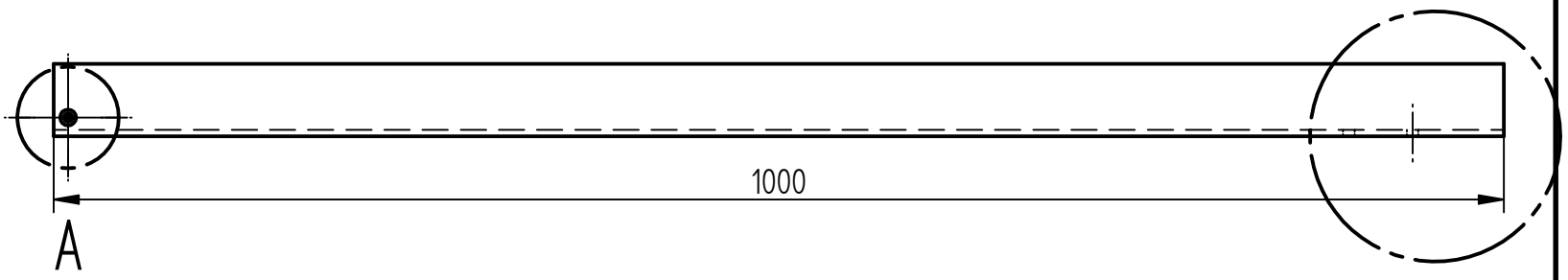
QUANTITY: 1

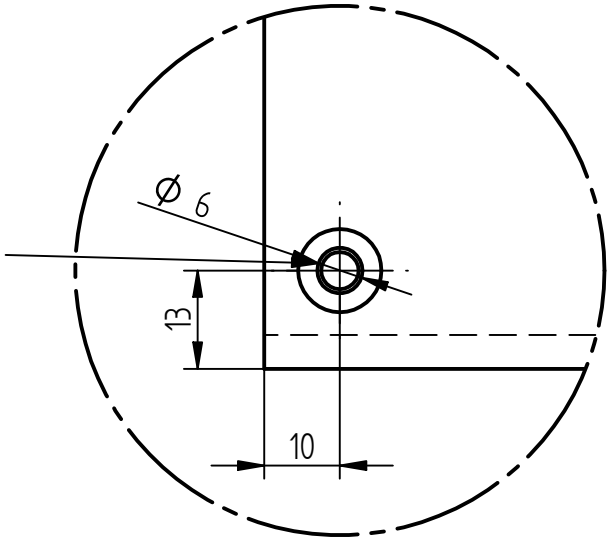
REV

SCALE: 1 : 5 | WEIGHT: | 4 of 10

SOLID EDGE ACADEMIC COPY

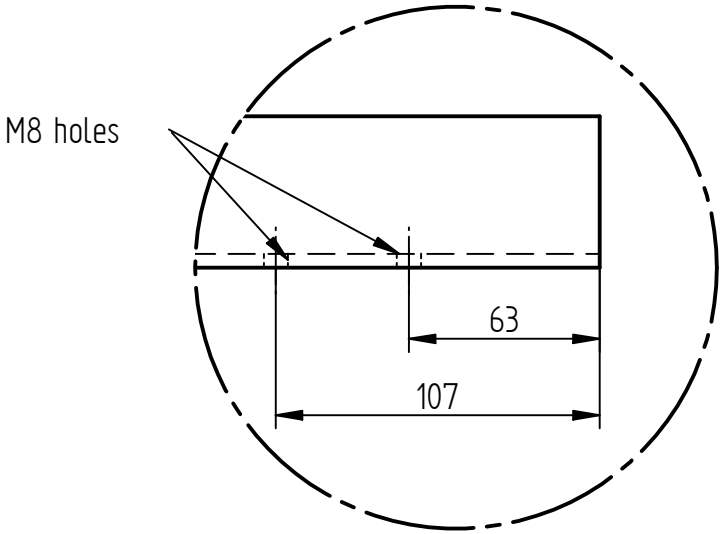






Both holes are: M6 CSK threaded holes, with countersink diameter and angle of 11mm and 90 degrees

DETAIL A



DETAIL B

Since the U-channel has slanted internal sides, they will have to be machined such that the support plate can be properly fitted and bolted onto the area shown in Detail A.

	NAME
DRAWN BY	Andre Cachucho (0501252N)
SUPERVISOR	Prof. B. W. Skews
ENG APPR	
DATE	24/04/2008

ALL DIMENSIONS ARE IN MILLIMETERS. TOLERANCES UNLESS OTHERWISE STATED ± 0..2MM OR TO STANDARDS DICTATED BY MATERIALS USED. ANGLES IN DEGREES ± 0.5 °

UNIVERSITY OF THE WITWATERSRAND

SCHOOL OF MECHANICAL, AERONAUTICAL AND INDUSTRIAL ENGINEERING

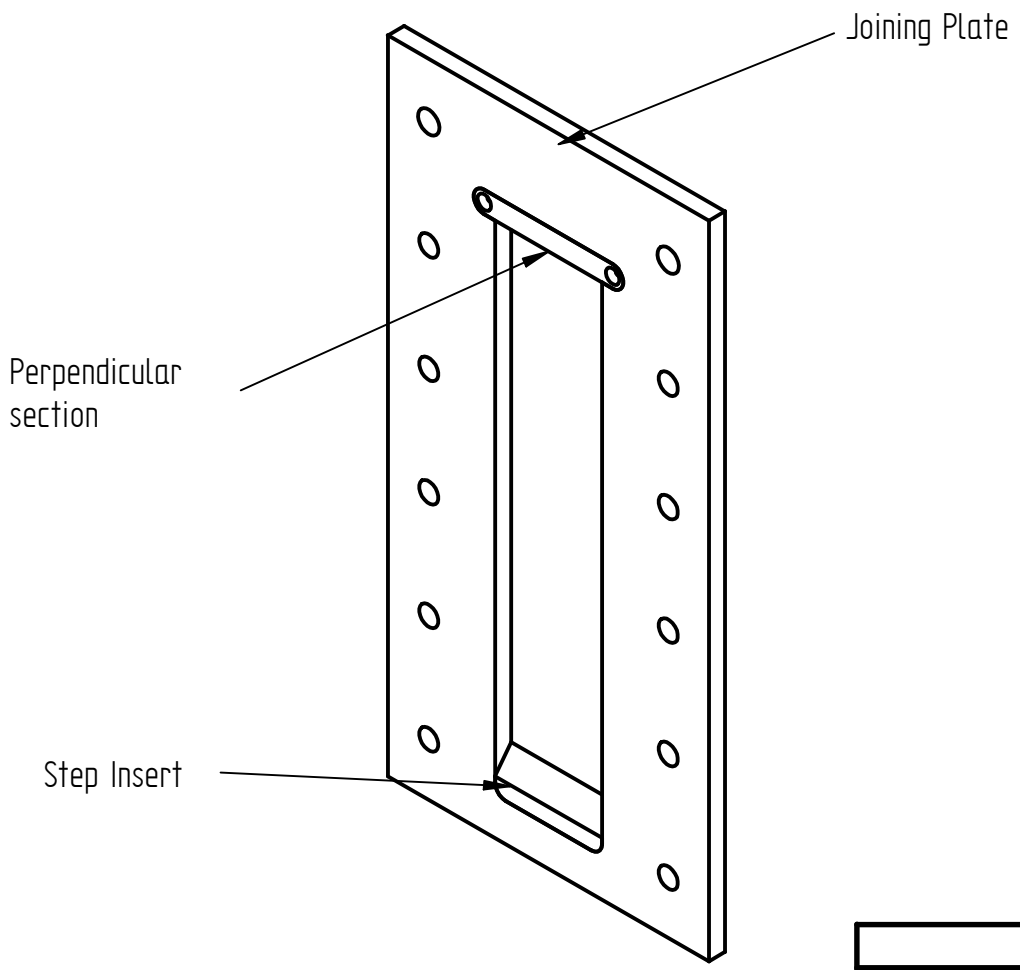
TITLE U-Channel std. 100 x 50 steel channel

QUANTITY: 1

REV

SCALE: 1 : 5 | WEIGHT: | 5 of 10

SOLID EDGE ACADEMIC COPY



	NAME
DRAWN BY	Andre Cachucho (0501252N)
SUPERVISOR	Prof. B. W. Skews
ENG APPR	
DATE	24/04/2008

ALL DIMENSIONS ARE IN MILLIMETERS.
TOLERANCES UNLESS OTHERWISE STATED
± 0..2MM OR TO STANDARDS DICTATED BY
MATERIALS USED. ANGLES IN DEGREES ± 0.5 °

UNIVERSITY OF THE WITWATERSRAND

SCHOOL OF MECHANICAL, AERONAUTICAL AND INDUSTRIAL ENGINEERING

TITLE Middle Plate Assembly

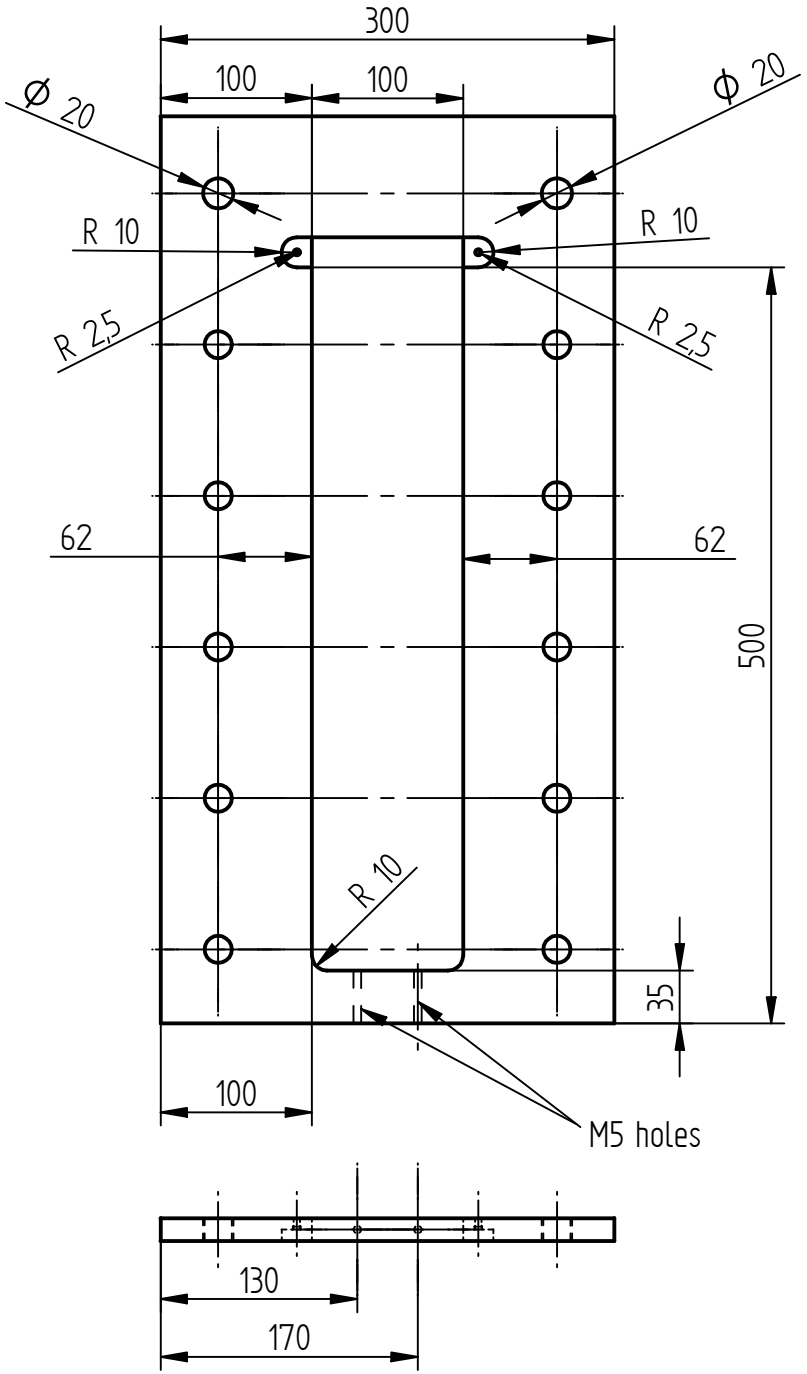
QUANTITY: 1

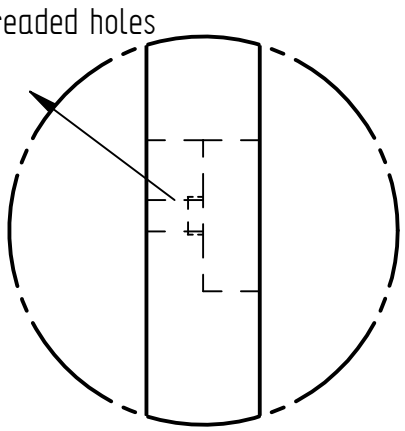
REV

SCALE: 1 : 5

WEIGHT:

SOLID EDGE ACADEMIC COPY

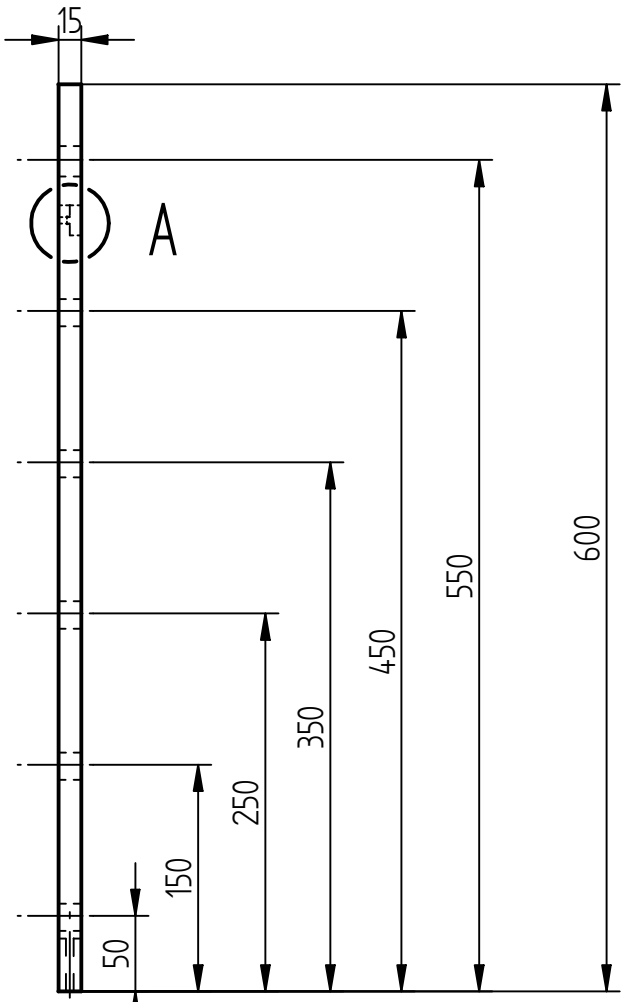




DETAIL A

All the bolt holes are M18 in diameter except for the ones indicated on the drawing.

This plate should use a 16mm standard mild steel plate and then machined down to a thickness of 15mm



	NAME
DRAWN BY	Andre Cachucho (0501252N)
SUPERVISOR	Prof. B. W. Skews
ENG APPR	
DATE	24/04/2008

ALL DIMENSIONS ARE IN MILLIMETERS.
TOLERANCES UNLESS OTHERWISE STATED
± 0..2MM OR TO STANDARDS DICTATED BY
MATERIALS USED. ANGLES IN DEGREES ± 0.5 °

UNIVERSITY OF THE WITWATERSRAND

SCHOOL OF MECHANICAL, AERONAUTICAL AND INDUSTRIAL ENGINEERING

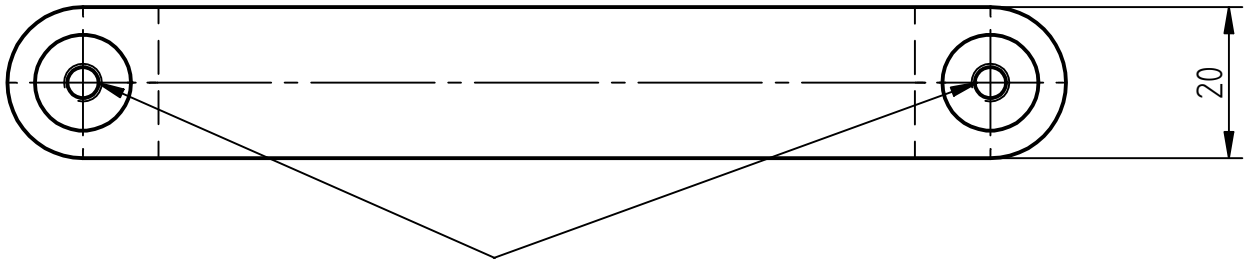
TITLE Joining Plate

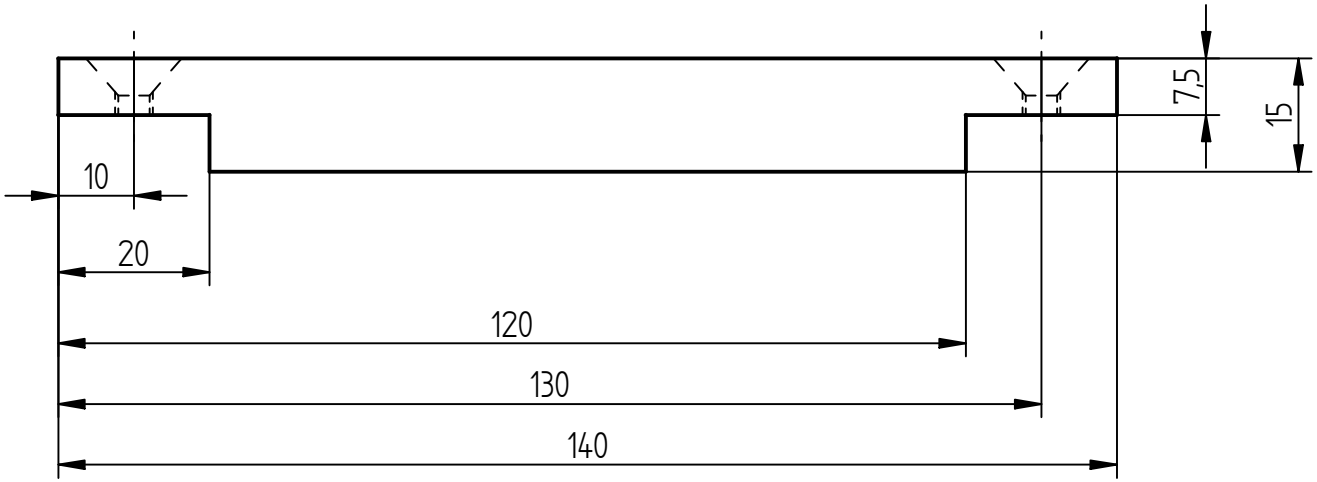
QUANTITY: 1

REV

SCALE: 1 : 5 | WEIGHT: | 7 of 10

SOLID EDGE ACADEMIC COPY





	NAME
DRAWN BY	Andre Cachucho (0501252N)
SUPERVISOR	Prof. B. W. Skews
ENG APPR	
DATE	24/04/2008

ALL DIMENSIONS ARE IN MILLIMETERS.
TOLERANCES UNLESS OTHERWISE STATED
± 0..2MM OR TO STANDARDS DICTATED BY
MATERIALS USED. ANGLES IN DEGREES ± 0.5 °

UNIVERSITY OF THE WITWATERSRAND

SCHOOL OF MECHANICAL, AERONAUTICAL AND INDUSTRIAL ENGINEERING

TITLE Perpendicular Section

QUANTITY: 1

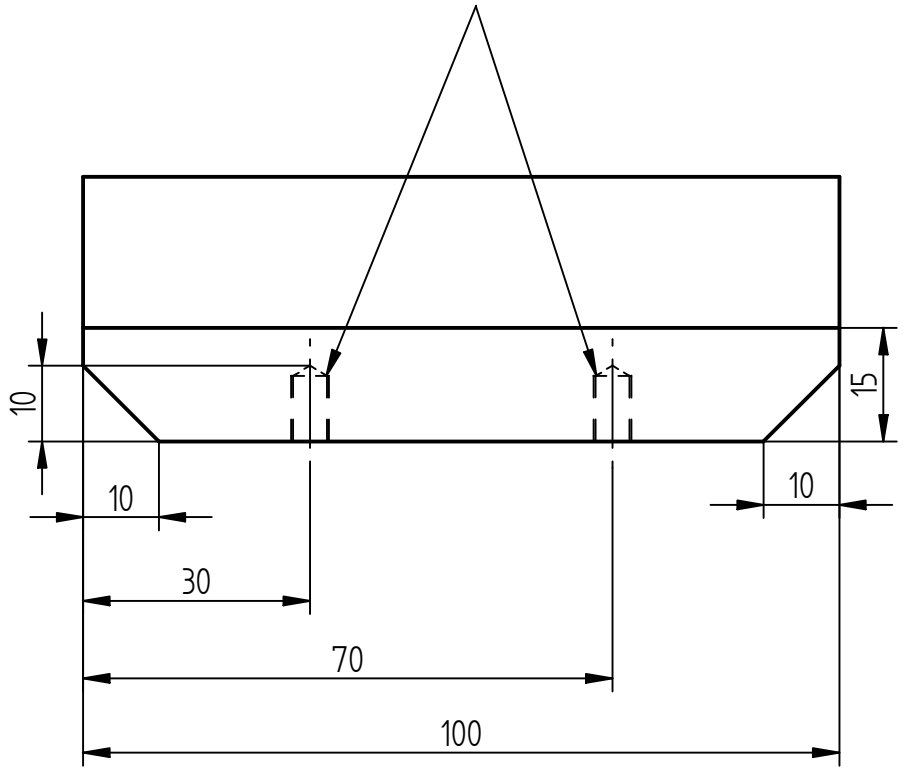
REV

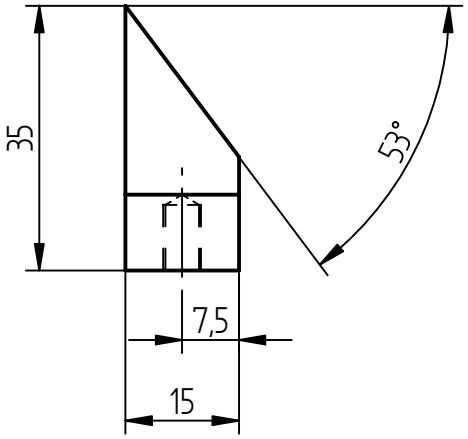
SCALE: 1 : 1

WEIGHT:

SOLID EDGE ACADEMIC COPY

M5 Threated holes





	NAME
DRAWN BY	Andre Cachucho (0501252N)
SUPERVISOR	Prof. B. W. Skews
ENG APPR	
DATE	24/04/2008

ALL DIMENSIONS ARE IN MILLIMETERS.
TOLERANCES UNLESS OTHERWISE STATED
± 0..2MM OR TO STANDARDS DICTATED BY
MATERIALS USED. ANGLES IN DEGREES ± 0.5 °

UNIVERSITY OF THE WITWATERSRAND

SCHOOL OF MECHANICAL, AERONAUTICAL AND INDUSTRIAL ENGINEERING

TITLE Triangular Step No.1

QUANTITY: 1

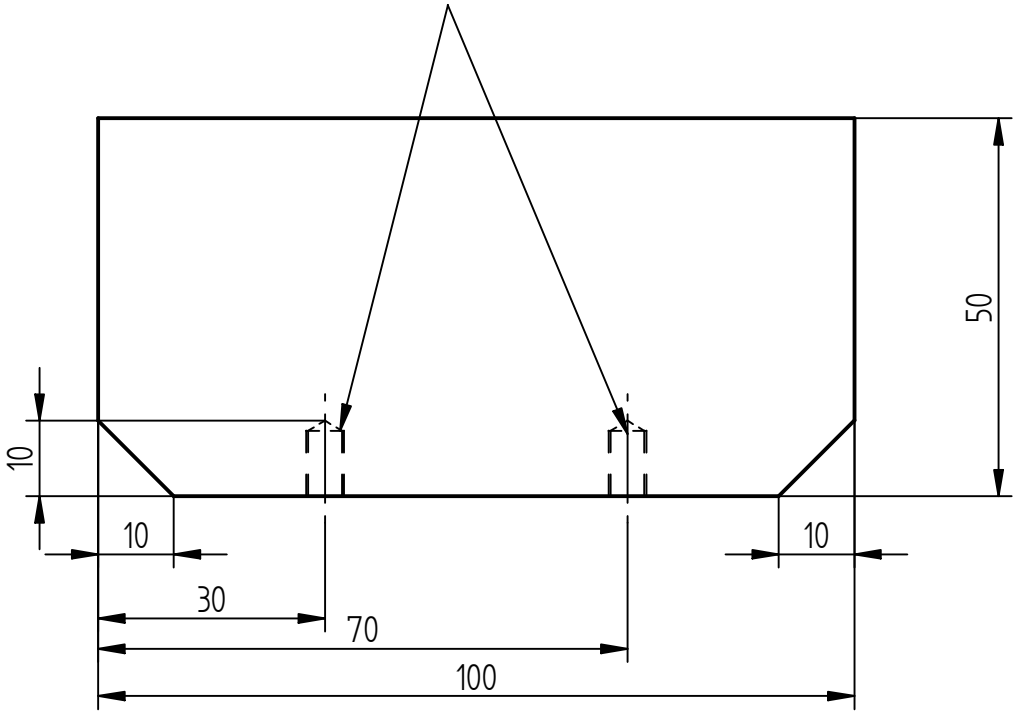
REV

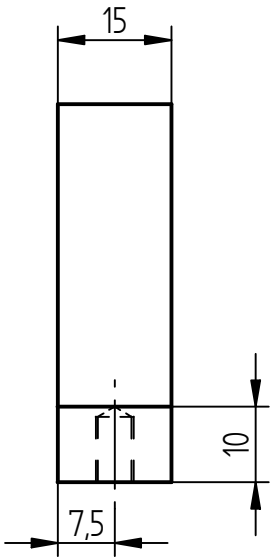
SCALE: 1 : 1

WEIGHT:

SOLID EDGE ACADEMIC COPY

M5 Threated holes





	NAME
DRAWN BY	Andre Cachucho (0501252N)
SUPERVISOR	Prof. B. W. Skews
ENG APPR	
DATE	24/04/2008

ALL DIMENSIONS ARE IN MILLIMETERS.
TOLERANCES UNLESS OTHERWISE STATED
± 0..2MM OR TO STANDARDS DICTATED BY
MATERIALS USED. ANGLES IN DEGREES ± 0.5 °

UNIVERSITY OF THE WITWATERSRAND

SCHOOL OF MECHANICAL, AERONAUTICAL AND INDUSTRIAL ENGINEERING

TITLE Rectangular Step No.1

QUANTITY: 1

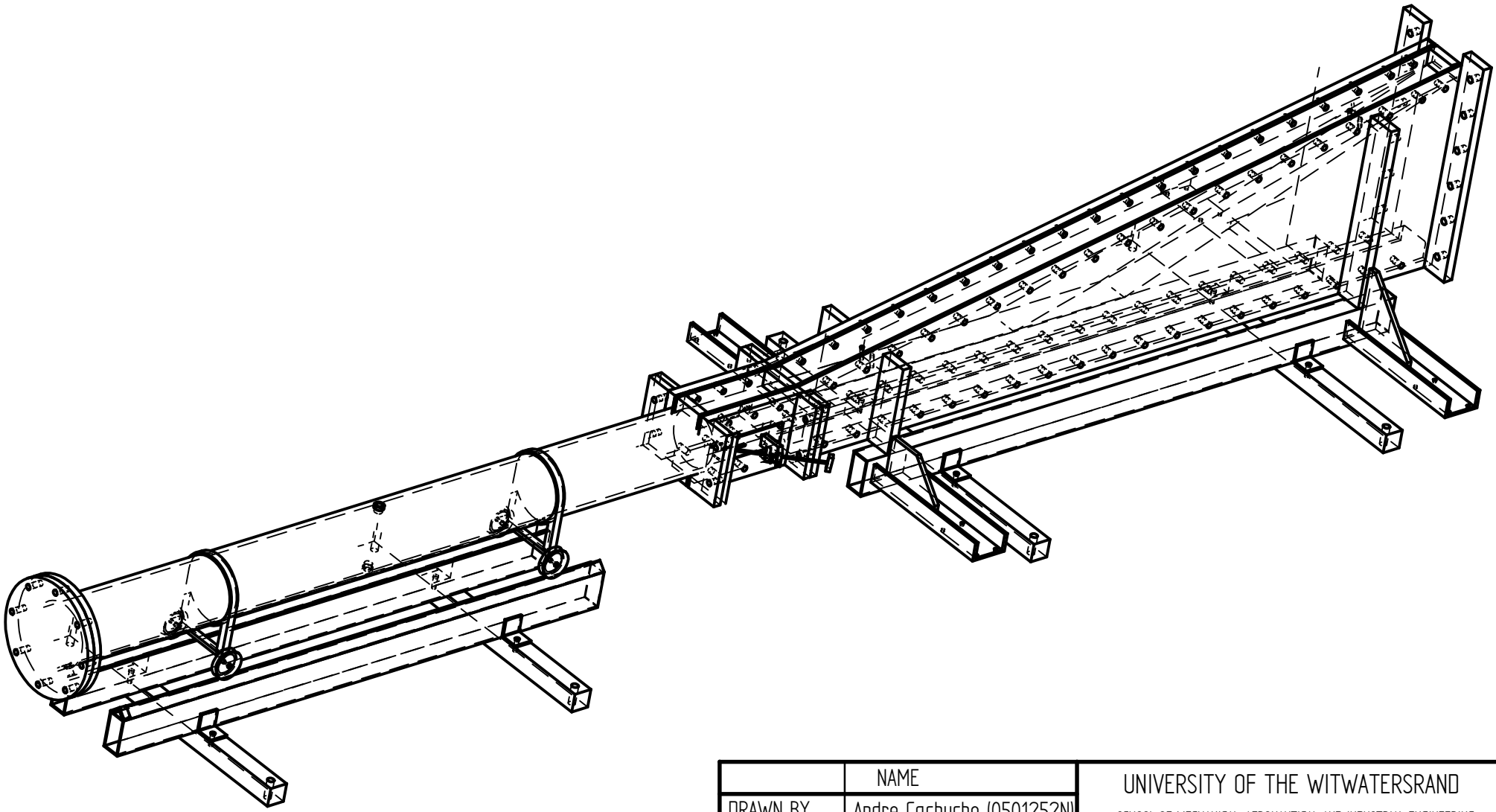
REV

SCALE: 1 : 1

WEIGHT:

SOLID EDGE ACADEMIC COPY

D.2 Second Shock Tube Configuration - Diverging Section



	NAME
DRAWN BY	Andre Cachucho (0501252N)
SUPERVISOR	Prof. B. W. Skews
ENG APPR	
DATE	14/09/2009

ALL DIMENSIONS ARE IN MILLIMETERS.
TOLERANCES UNLESS OTHERWISE STATED
± 0..2MM OR TO STANDARDS DICTATED BY
MATERIALS USED. ANGLES IN DEGREES ± 0.5 °

UNIVERSITY OF THE WITWATERSRAND

SCHOOL OF MECHANICAL, AERONAUTICAL AND INDUSTRIAL ENGINEERING

TITLE: Driver and diverging section assembly

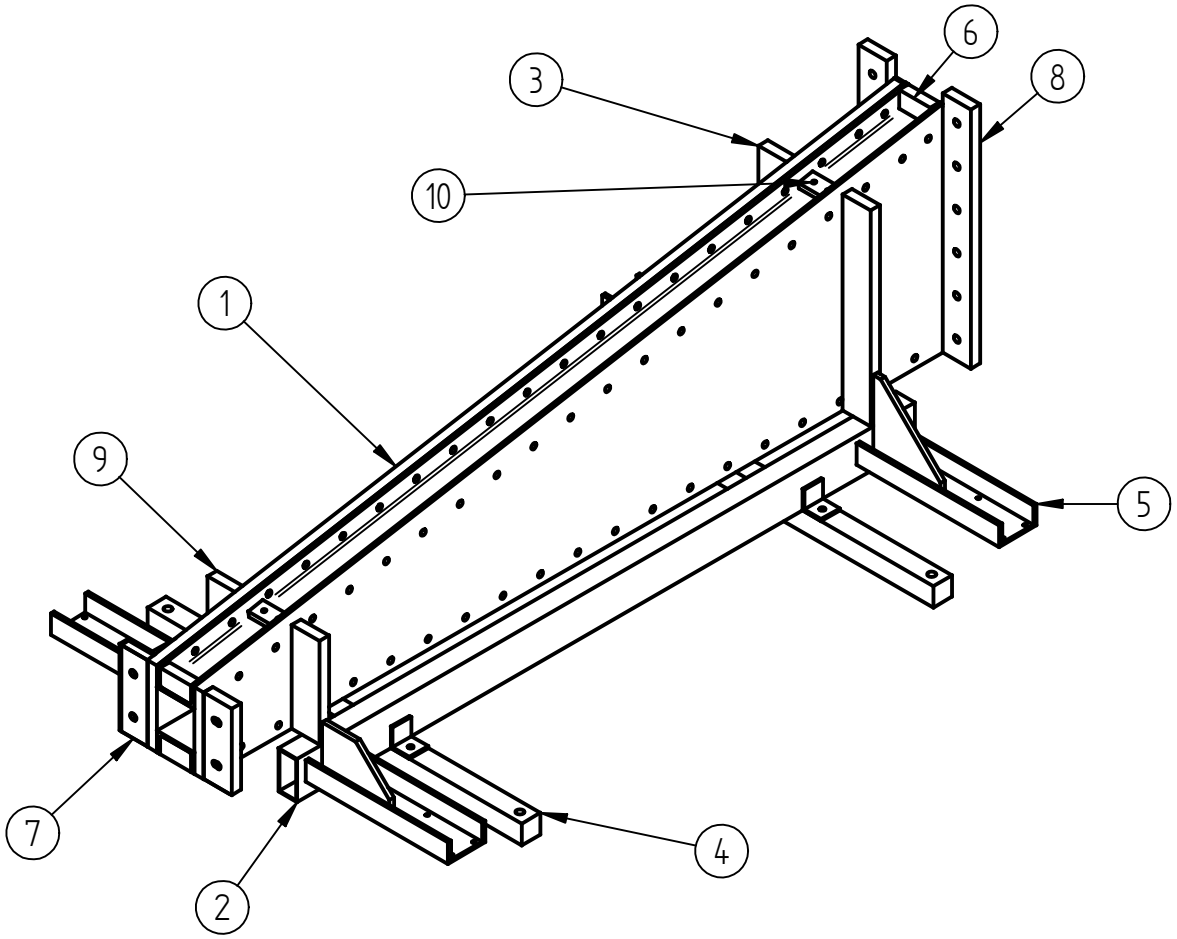
QUANTITY: 1

REV

SCALE: 1 :13.33 | WEIGHT: | 1 of

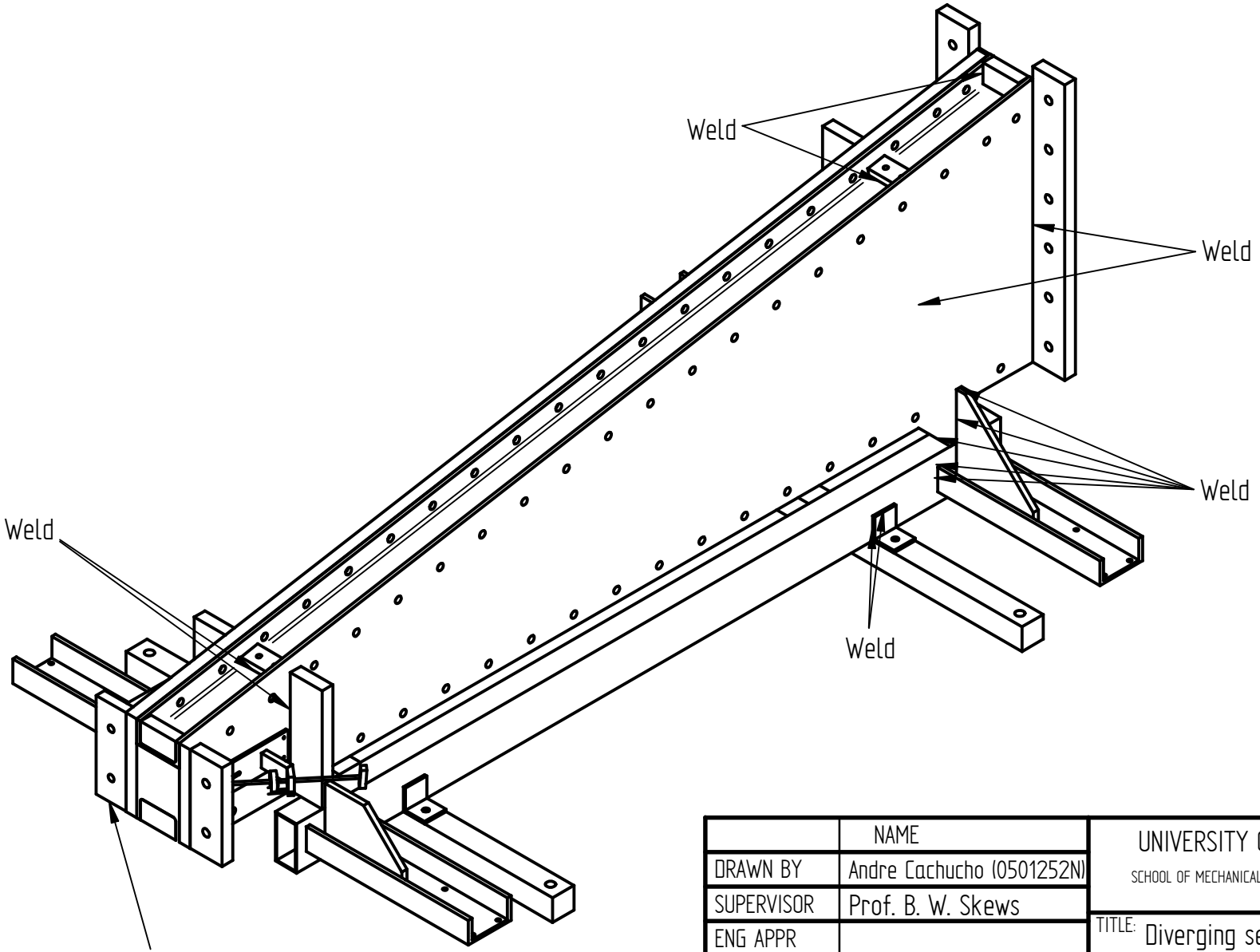
SOLID EDGE ACADEMIC COPY

Item Number	Title	Quantity
1	Section walls including top and bottom u-channel	1
2	Caster support rail	2
3	Large reinforcing flange	2
4	Stabliser assembly	2
5	Caster support assembly	4
6	Top and bottom flanges	4
7	Driver flange	1
8	End-section flange	2
9	Small reinforcing flange	2
10	Channel support insert pieces	2



	NAME	UNIVERSITY OF THE WITWATERSRAND SCHOOL OF MECHANICAL, AERONAUTICAL AND INDUSTRIAL ENGINEERING	
DRAWN BY	Andre Cachucho (0501252N)		
SUPERVISOR	Prof. B. W. Skews		
ENG APPR		TITLE: Diverging section assembly – Part List	
DATE	07/10/2009		
ALL DIMENSIONS ARE IN MILLIMETERS. TOLERANCES UNLESS OTHERWISE STATED ± 0..2MM OR TO STANDARDS DICTATED BY MATERIALS USED. ANGLES IN DEGREES ± 0.5 °		QUANTITY: 1	REV
		SCALE: 1 : 8.33 WEIGHT:	1 of

SOLID EDGE ACADEMIC COPY



	NAME
DRAWN BY	Andre Cachucho (0501252N)
SUPERVISOR	Prof. B. W. Skews
ENG APPR	
DATE	07/10/2009

ALL DIMENSIONS ARE IN MILLIMETERS.
TOLERANCES UNLESS OTHERWISE STATED
± 0..2MM OR TO STANDARDS DICTATED BY
MATERIALS USED. ANGLES IN DEGREES ± 0.5 °

UNIVERSITY OF THE WITWATERSRAND

SCHOOL OF MECHANICAL, AERONAUTICAL AND INDUSTRIAL ENGINEERING

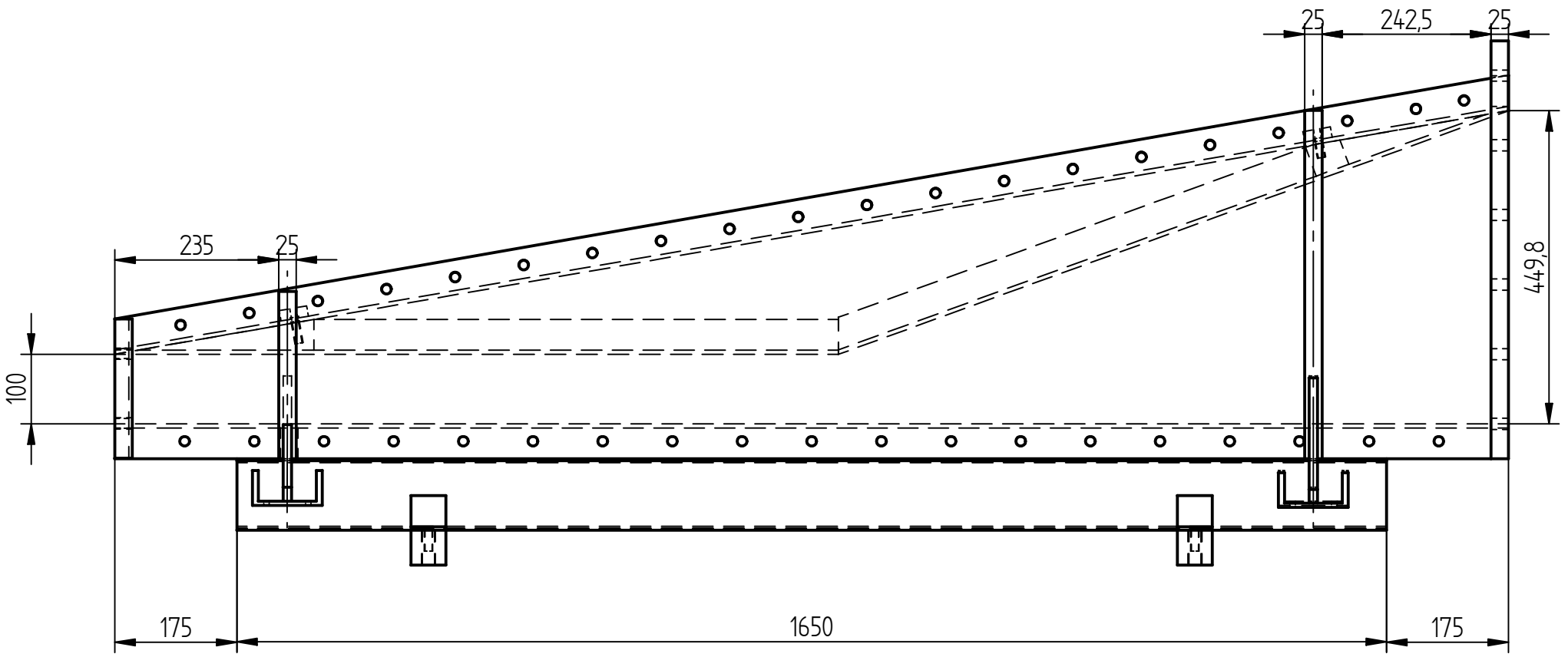
TITLE: Diverging section assembly – Welds

QUANTITY: 1

REV

SCALE: 1 : 8.33 | WEIGHT: | 1 of

SOLID EDGE ACADEMIC COPY



	NAME
DRAWN BY	Andre Cachucho (0501252N)
SUPERVISOR	Prof. B. W. Skews
ENG APPR	
DATE	07/10/2009

ALL DIMENSIONS ARE IN MILLIMETERS.
TOLERANCES UNLESS OTHERWISE STATED
± 0..2MM OR TO STANDARDS DICTATED BY
MATERIALS USED. ANGLES IN DEGREES ± 0.5 °

UNIVERSITY OF THE WITWATERSRAND

SCHOOL OF MECHANICAL, AERONAUTICAL AND INDUSTRIAL ENGINEERING

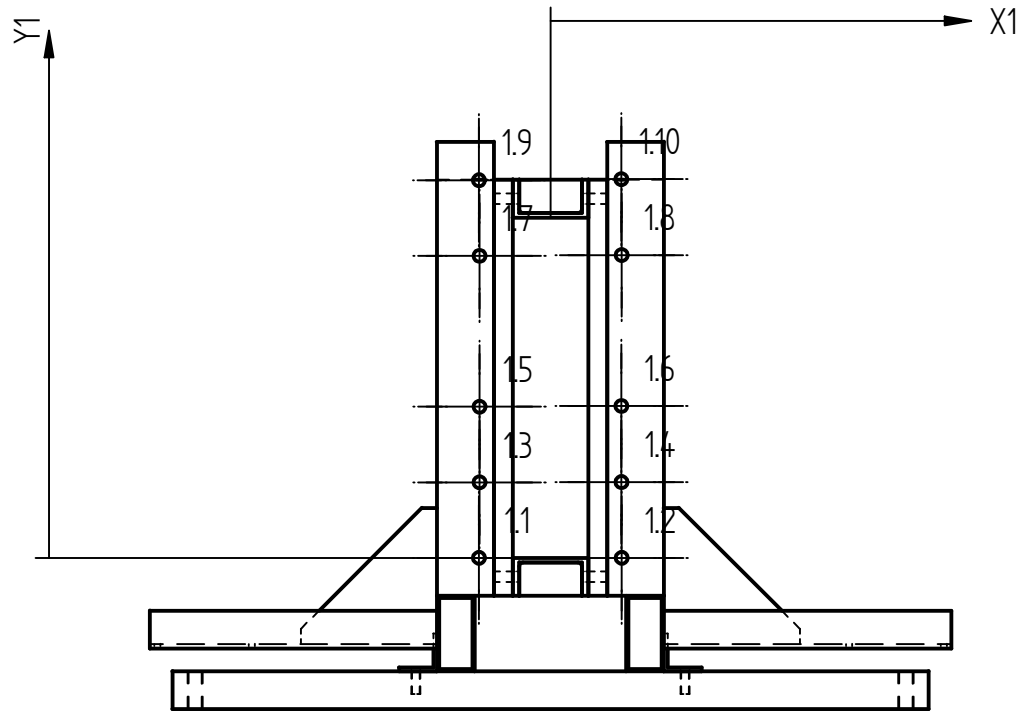
TITLE: Diverging section assembly

QUANTITY: 1

REV

SCALE: 1 : 8.33 | WEIGHT: | 1 of

SOLID EDGE ACADEMIC COPY



Hole Table			
Hole	X	Y	Size
1.1	-94,55	0	Φ 16
1.2	94,25	0	Φ 16
1.3	-93,87	99,9	Φ 16
1.4	93,88	100,25	Φ 16
1.5	-93,82	199,95	Φ 16
1.6	93,82	200,9	Φ 16
1.7	-93,88	399,45	Φ 16
1.8	93,98	400,5	Φ 16
1.9	-94,55	499,45	Φ 16
1.10	93,68	500,9	Φ 16

	NAME
DRAWN BY	LORENZO LACOVIG
SUPERVISOR	Prof. B. W. Skews
ENG APPR	
DATE	19/06/2007

ALL DIMENSIONS ARE IN MILLIMETERS.
TOLERANCES UNLESS OTHERWISE STATED
± 0..2MM OR TO STANDARDS DICTATED BY
MATERIALS USED. ANGLES IN DEGREES ± 0.5 °

UNIVERSITY OF THE WITWATERSRAND

SCHOOL OF MECHANICAL, AERONAUTICAL AND INDUSTRIAL ENGINEERING

TITLE Driven Section Front Flange Hole Table

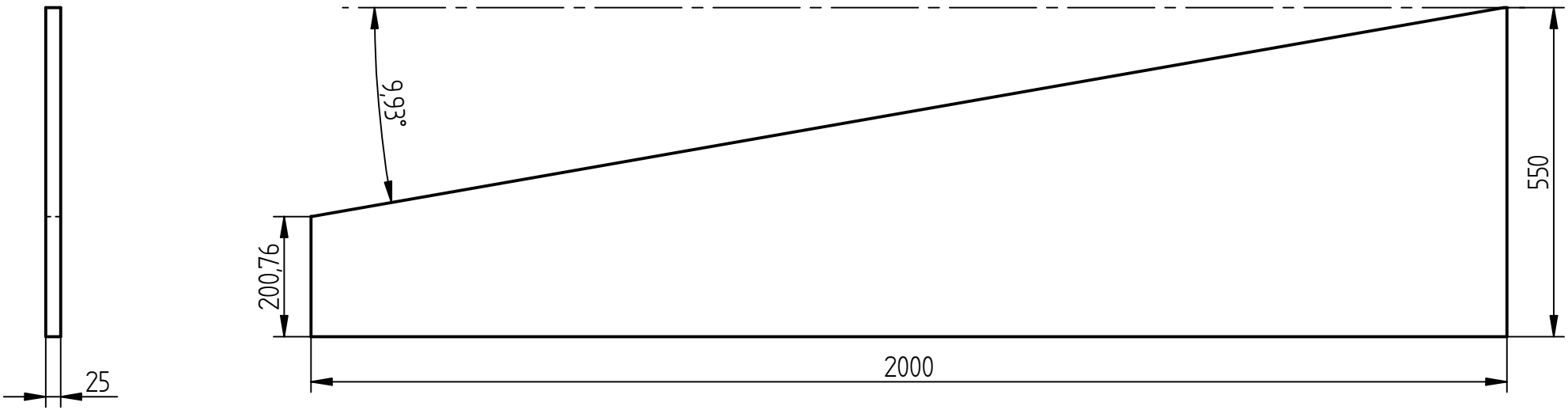
QUANTITY: 1

REV

SCALE: 1 : 10

WEIGHT:

SOLID EDGE ACADEMIC COPY



	NAME
DRAWN BY	Andre Cachucho (0501252N)
SUPERVISOR	Prof. B. W. Skews
ENG APPR	
DATE	07/10/2009

ALL DIMENSIONS ARE IN MILLIMETERS.
TOLERANCES UNLESS OTHERWISE STATED
± 0..2MM OR TO STANDARDS DICTATED BY
MATERIALS USED. ANGLES IN DEGREES ± 0.5 °

UNIVERSITY OF THE WITWATERSRAND

SCHOOL OF MECHANICAL, AERONAUTICAL AND INDUSTRIAL ENGINEERING

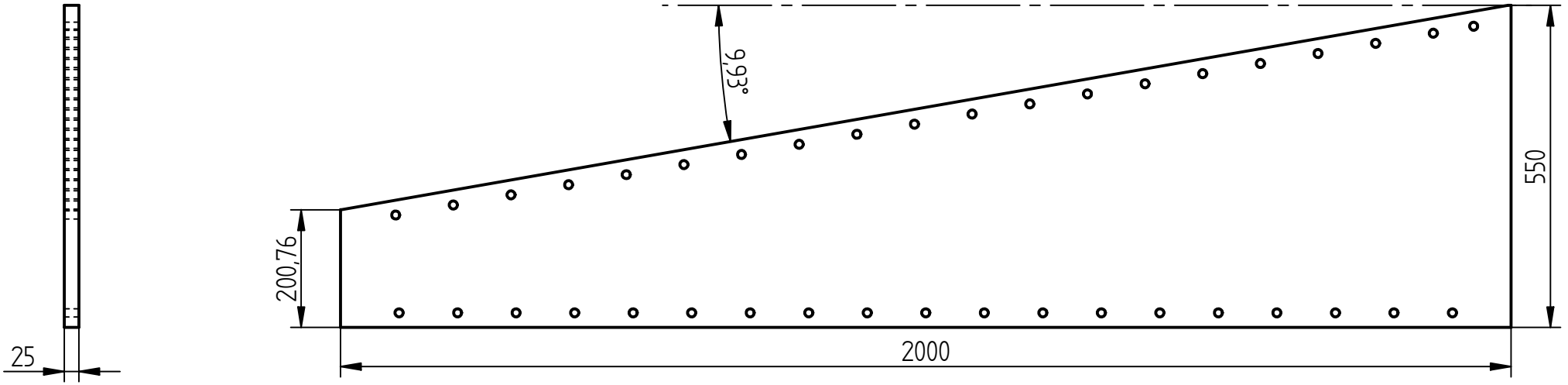
TITLE: Driver section wall 1 of 3 (mild steel plate)

QUANTITY: 2

REV

SCALE: 1 : 0.1 | WEIGHT: | 1 of

SOLID EDGE ACADEMIC COPY



	NAME
DRAWN BY	Andre Cachucho (0501252N)
SUPERVISOR	Prof. B. W. Skews
ENG APPR	
DATE	07/10/2009

ALL DIMENSIONS ARE IN MILLIMETERS.
TOLERANCES UNLESS OTHERWISE STATED
± 0..2MM OR TO STANDARDS DICTATED BY
MATERIALS USED. ANGLES IN DEGREES ± 0.5 °

UNIVERSITY OF THE WITWATERSRAND

SCHOOL OF MECHANICAL, AERONAUTICAL AND INDUSTRIAL ENGINEERING

TITLE: Driver section wall 1 of 3 (mild steel plate)

QUANTITY: 2

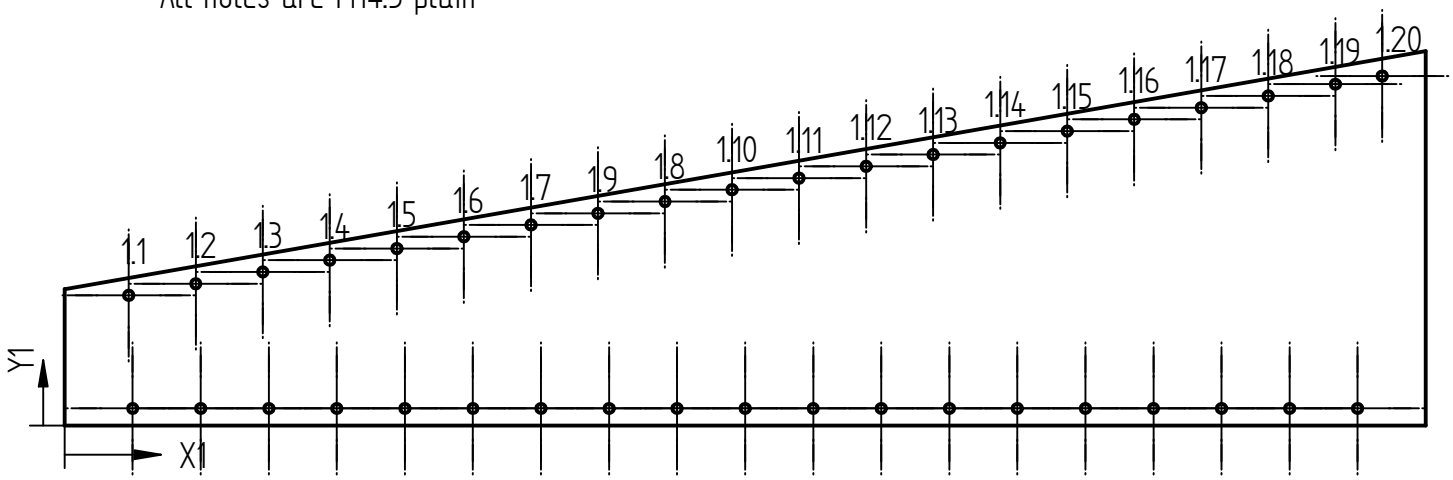
REV

SCALE: 1 : 0.1 | WEIGHT: | 1 of

SOLID EDGE ACADEMIC COPY

Hole Table		
Hole	X	Y
1.1	94,2	191,1
1.2	192,7	208,3
1.3	291,2	225,6
1.4	389,7	242,8
1.5	488,2	260,1
1.6	586,7	277,3
1.7	685,2	294,6
1.8	882,2	329,1
1.9	783,7	311,8
1.10	980,7	346,3
1.11	1079,2	363,5
1.12	1177,7	380,8
1.13	1276,2	398
1.14	1374,7	415,3
1.15	1473,2	432,5
1.16	1571,7	449,8
1.17	1670,2	467
1.18	1768,7	484,3
1.19	1867,2	501,5
1.20	1936,2	513,6

All holes are M14.5 plain



	NAME
DRAWN BY	Andre Cachucho (0501252N)
SUPERVISOR	Prof. B. W. Skews
ENG APPR	
DATE	07/10/2009

ALL DIMENSIONS ARE IN MILLIMETERS.
TOLERANCES UNLESS OTHERWISE STATED
± 0..2MM OR TO STANDARDS DICTATED BY
MATERIALS USED. ANGLES IN DEGREES ± 0.5 °

UNIVERSITY OF THE WITWATERSRAND
SCHOOL OF MECHANICAL, AERONAUTICAL AND INDUSTRIAL ENGINEERING

TITLE: Driver section wall 2 of 3: 10degree hole table (mild steel plate)

QUANTITY: 1

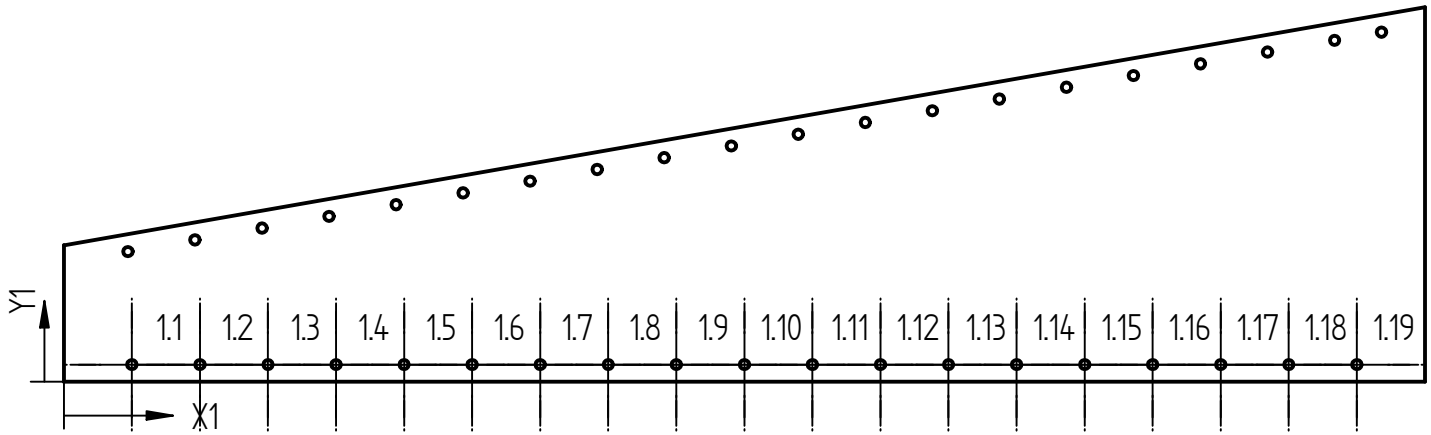
REV

SCALE: 1 : 11.11 | WEIGHT: | 1 of

SOLID EDGE ACADEMIC COPY

Hole Table		
Hole	X	Y
1.1	100	25
1.2	200	25
1.3	300	25
1.4	400	25
1.5	500	25
1.6	600	25
1.7	700	25
1.8	800	25
1.9	900	25
1.10	1000	25
1.11	1100	25
1.12	1200	25
1.13	1300	25
1.14	1400	25
1.15	1500	25
1.16	1600	25
1.17	1700	25
1.18	1800	25
1.19	1900	25

All holes are M14.5 plain



	NAME
DRAWN BY	Andre Cachucho (0501252N)
SUPERVISOR	Prof. B. W. Skews
ENG APPR	
DATE	07/10/2009

ALL DIMENSIONS ARE IN MILLIMETERS.
TOLERANCES UNLESS OTHERWISE STATED
± 0..2MM OR TO STANDARDS DICTATED BY
MATERIALS USED. ANGLES IN DEGREES ± 0.5 °

UNIVERSITY OF THE WITWATERSRAND

SCHOOL OF MECHANICAL, AERONAUTICAL AND INDUSTRIAL ENGINEERING

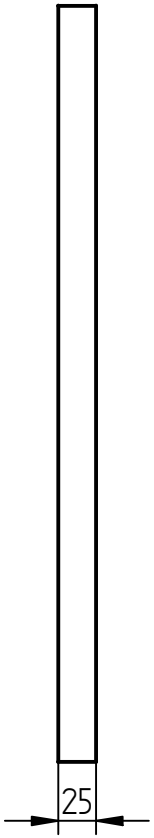
TITLE: Driver section wall 3 of 3: Horiz hole table (mild steel plate)

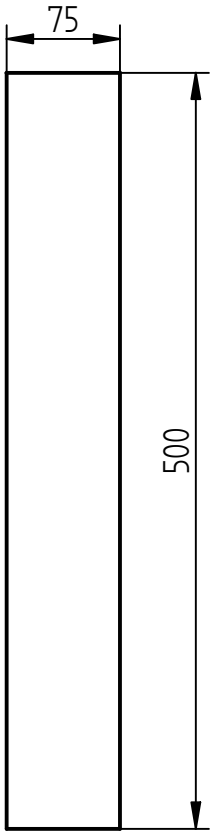
QUANTITY: 1

REV

SCALE: 1 : 11.11 | WEIGHT: | 1 of

SOLID EDGE ACADEMIC COPY





	NAME
DRAWN BY	Andre Cachucho (0501252N)
SUPERVISOR	Prof. B. W. Skews
ENG APPR	
DATE	07/10/2009

ALL DIMENSIONS ARE IN MILLIMETERS.
TOLERANCES UNLESS OTHERWISE STATED
± 0..2MM OR TO STANDARDS DICTATED BY
MATERIALS USED. ANGLES IN DEGREES ± 0.5 °

UNIVERSITY OF THE WITWATERSRAND

SCHOOL OF MECHANICAL, AERONAUTICAL AND INDUSTRIAL ENGINEERING

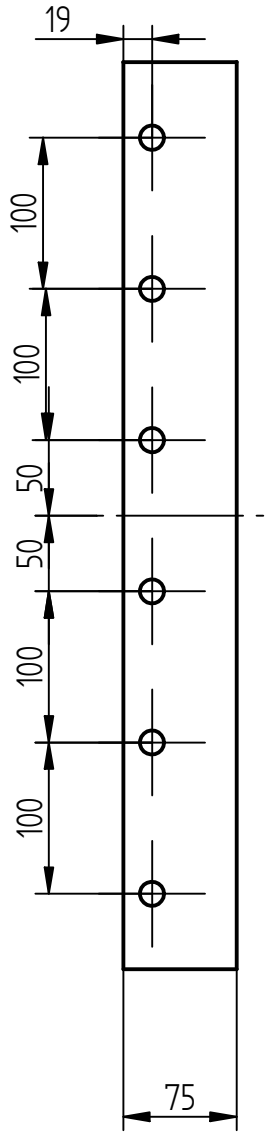
TITLE: Large reinforcing flange

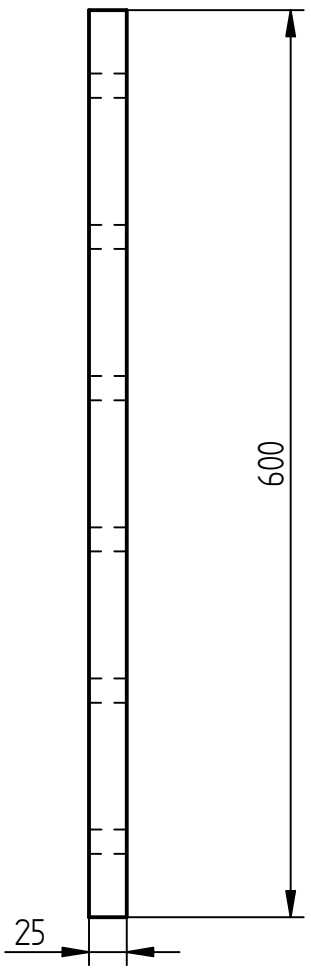
QUANTITY: 2

REV

SCALE: 1 : 0.5 | WEIGHT: | 1 of

SOLID EDGE ACADEMIC COPY





	NAME
DRAWN BY	LORENZO LACOVIG
SUPERVISOR	Prof. B. W. Skews
ENG APPR	
DATE	09/06/2007

ALL DIMENSIONS ARE IN MILLIMETERS.
TOLERANCES UNLESS OTHERWISE STATED
± 0..2MM OR TO STANDARDS DICTATED BY
MATERIALS USED. ANGLES IN DEGREES ± 0.5 °

UNIVERSITY OF THE WITWATERSRAND

SCHOOL OF MECHANICAL, AERONAUTICAL AND INDUSTRIAL ENGINEERING

TITLE Driven Section Side Flange
[mild steel plate]

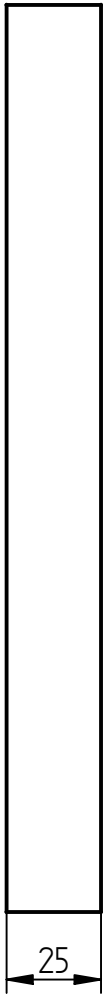
QUANTITY: 2

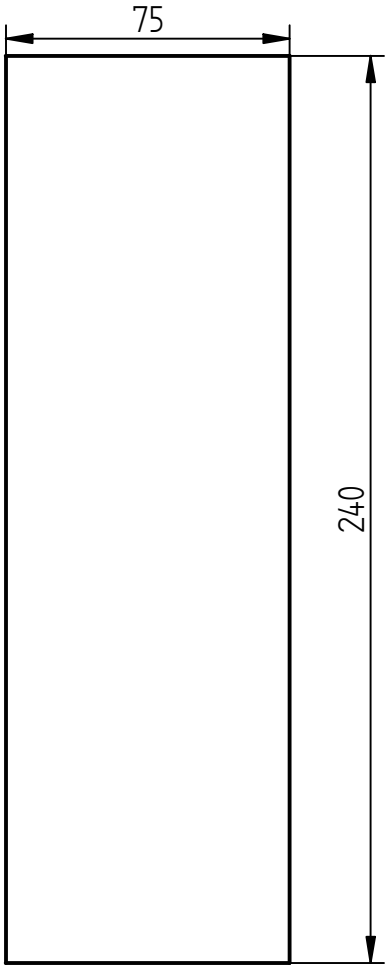
REV

SCALE: 1 : 5

WEIGHT:

SOLID EDGE ACADEMIC COPY





	NAME
DRAWN BY	Andre Cachucho (0501252N)
SUPERVISOR	Prof. B. W. Skews
ENG APPR	
DATE	07/10/2009

ALL DIMENSIONS ARE IN MILLIMETERS.
TOLERANCES UNLESS OTHERWISE STATED
± 0..2MM OR TO STANDARDS DICTATED BY
MATERIALS USED. ANGLES IN DEGREES ± 0.5 °

UNIVERSITY OF THE WITWATERSRAND

SCHOOL OF MECHANICAL, AERONAUTICAL AND INDUSTRIAL ENGINEERING

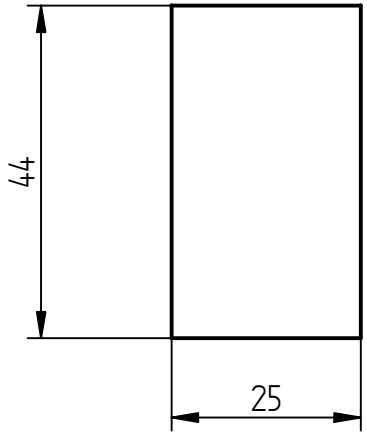
TITLE: Small reinforcing flange

QUANTITY: 2

REV

SCALE: 1 : 0.5 | WEIGHT: | 1 of

SOLID EDGE ACADEMIC COPY





These flanges are required for both the plunger section and the diverging section

	NAME
DRAWN BY	Andre Cachucho
SUPERVISOR	Prof. B. W. Skews
ENG APPR	
DATE	14/09/2009

ALL DIMENSIONS ARE IN MILLIMETERS.
TOLERANCES UNLESS OTHERWISE STATED
± 0..2MM OR TO STANDARDS DICTATED BY
MATERIALS USED. ANGLES IN DEGREES ± 0.5 °

UNIVERSITY OF THE WITWATERSRAND

SCHOOL OF MECHANICAL, AERONAUTICAL AND INDUSTRIAL ENGINEERING

TITLE Top or Bottom Flange
[mild steel plate]

QUANTITY: 8

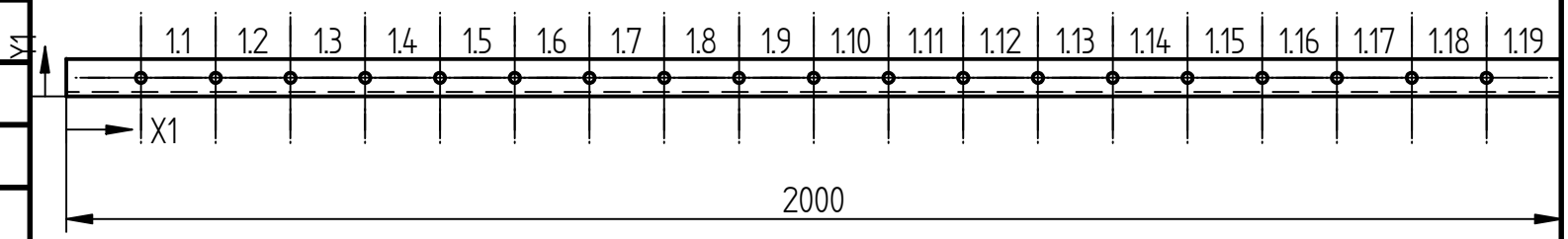
REV

SCALE: 1 : 1

WEIGHT:

SOLID EDGE ACADEMIC COPY

Hole Table		
Hole	X	Y
1.1	100	25
1.2	200	25
1.3	300	25
1.4	400	25
1.5	500	25
1.6	600	25
1.7	700	25
1.8	800	25
1.9	900	25
1.10	1000	25
1.11	1100	25
1.12	1200	25
1.13	1300	25
1.14	1400	25
1.15	1500	25
1.16	1600	25
1.17	1700	25
1.18	1800	25
1.19	1900	25



All plain holes are M14.5

	NAME
DRAWN BY	Andre Cachucho (0501252N)
SUPERVISOR	Prof. B. W. Skews
ENG APPR	
DATE	07/10/2009

ALL DIMENSIONS ARE IN MILLIMETERS.
TOLERANCES UNLESS OTHERWISE STATED
± 0..2MM OR TO STANDARDS DICTATED BY
MATERIALS USED. ANGLES IN DEGREES ± 0.5 °

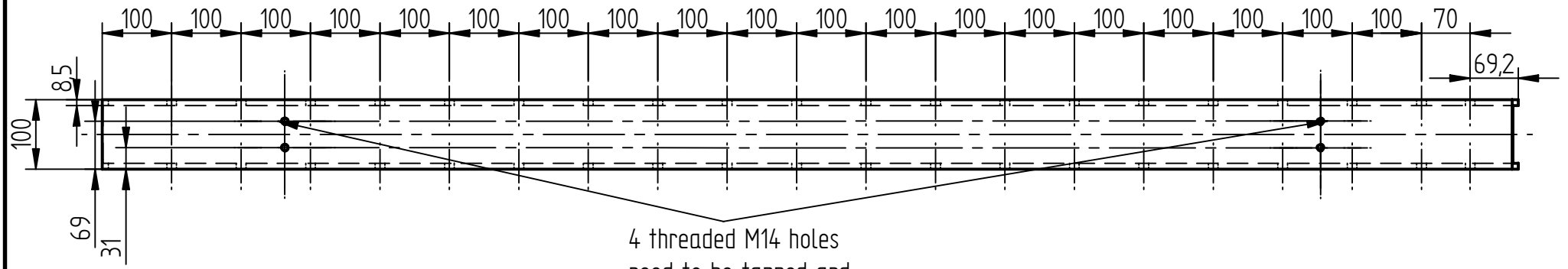
UNIVERSITY OF THE WITWATERSRAND
SCHOOL OF MECHANICAL, AERONAUTICAL AND INDUSTRIAL ENGINEERING

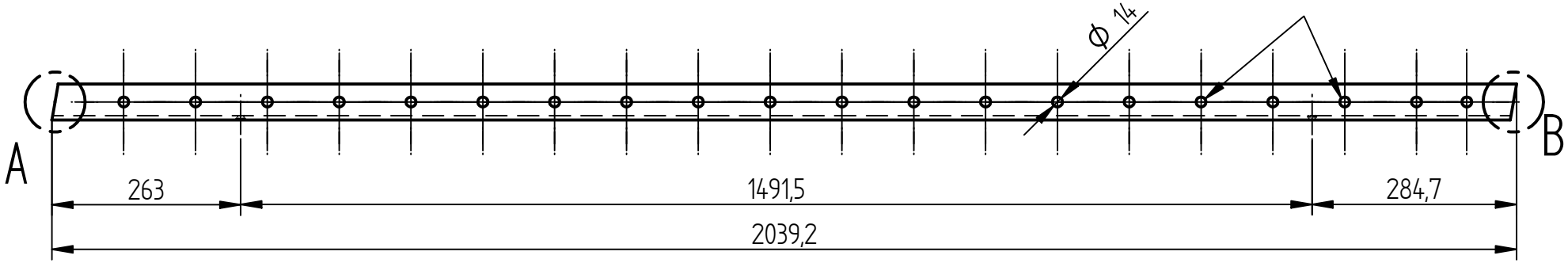
TITLE: Floor Std Steel U-channel (100x50)

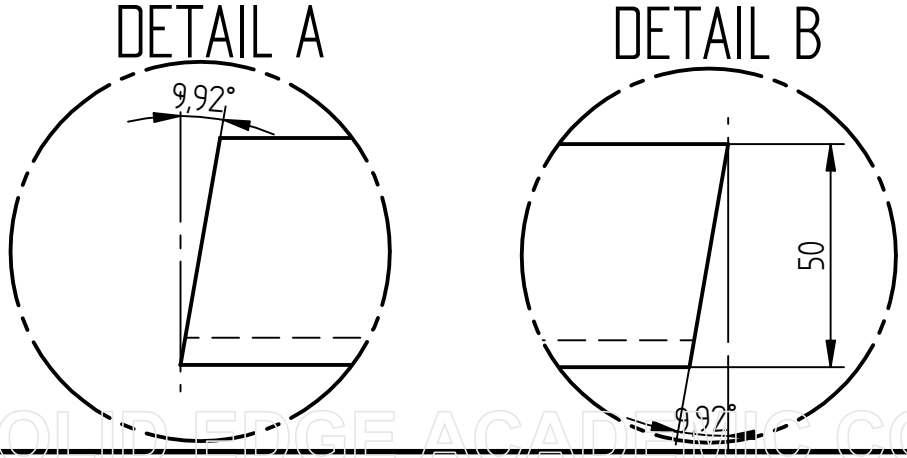
QUANTITY: 1 | REV

SCALE: 1 : 0.5 | WEIGHT: | 1 of

SOLID EDGE ACADEMIC COPY







	NAME
DRAWN BY	Andre Cachucho (0501252N)
SUPERVISOR	Prof. B. W. Skews
ENG APPR	
DATE	07/10/2009

ALL DIMENSIONS ARE IN MILLIMETERS.
TOLERANCES UNLESS OTHERWISE STATED
± 0..2MM OR TO STANDARDS DICTATED BY
MATERIALS USED. ANGLES IN DEGREES ± 0.5 °

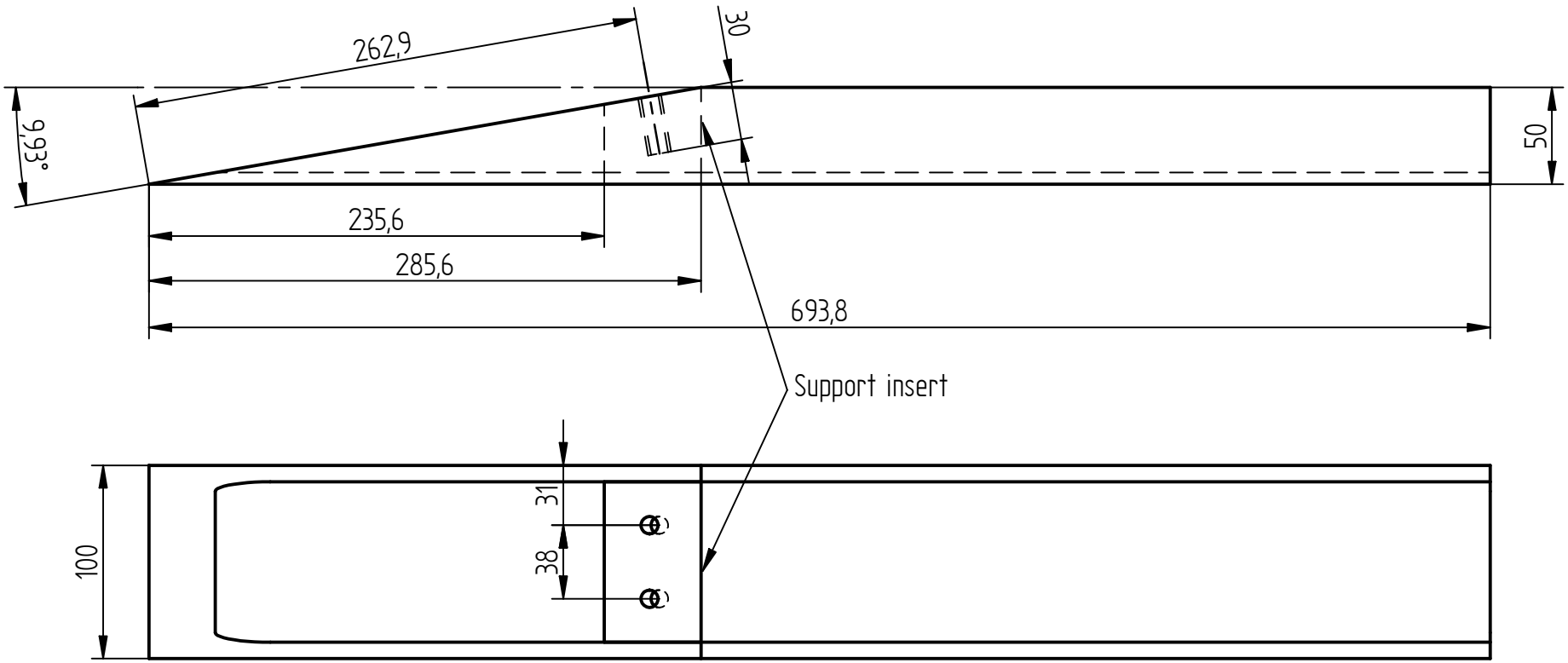
UNIVERSITY OF THE WITWATERSRAND
SCHOOL OF MECHANICAL, AERONAUTICAL AND INDUSTRIAL ENGINEERING

TITLE: 10 degree U-channel
Standard steel U-channel (50x100)

QUANTITY: 1 | REV

SCALE: 1 : 8.33 | WEIGHT: | 1 of

SOLID EDGE ACADEMIC COPY



NB: Weld support inserts (Blocks) before machining

	NAME
DRAWN BY	Andre Cachucho (0501252N)
SUPERVISOR	Prof. B. W. Skews
ENG APPR	
DATE	07/10/2009

ALL DIMENSIONS ARE IN MILLIMETERS.
TOLERANCES UNLESS OTHERWISE STATED
± 0..2MM OR TO STANDARDS DICTATED BY
MATERIALS USED. ANGLES IN DEGREES ± 0.5 °

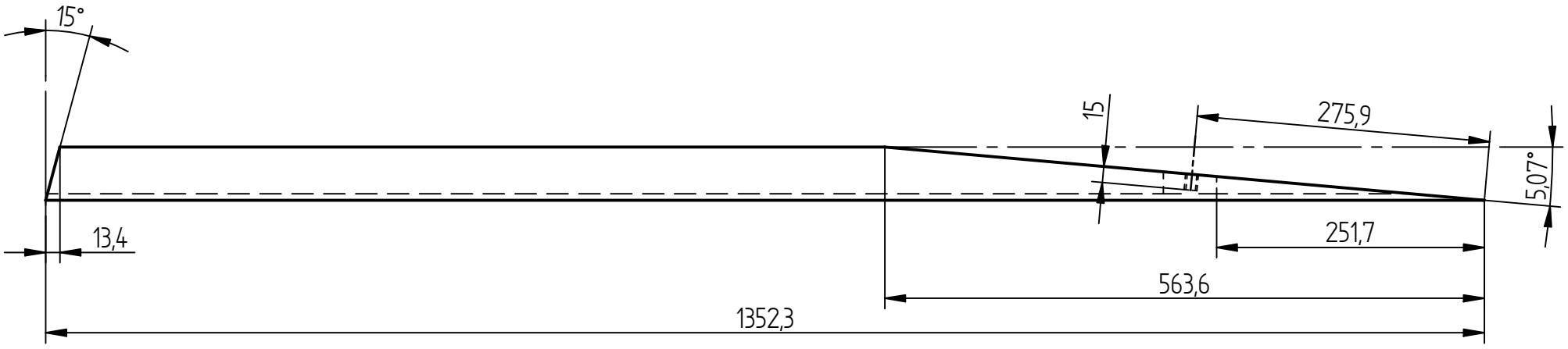
UNIVERSITY OF THE WITWATERSRAND
SCHOOL OF MECHANICAL, AERONAUTICAL AND INDUSTRIAL ENGINEERING

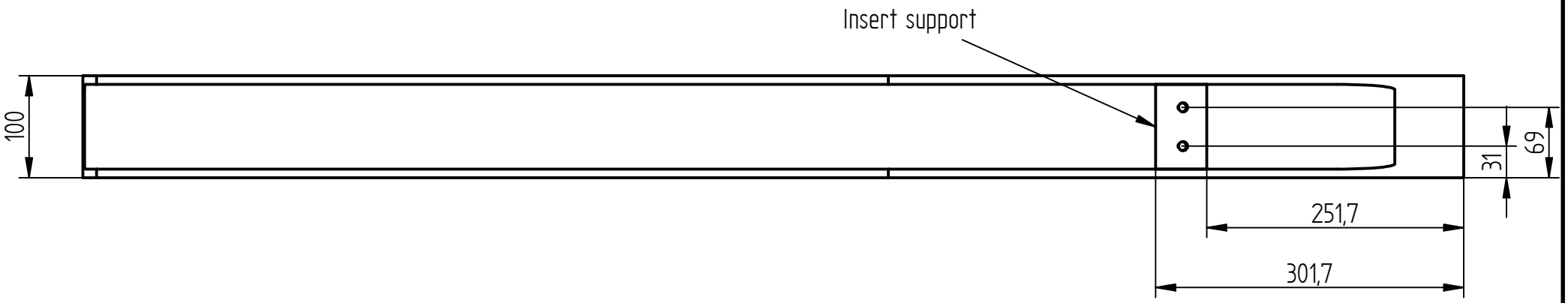
TITLE: Horizontal section: 15 degree
Std steel U-channel (50x100)

QUANTITY: 1 | REV

SCALE: 1 : 3.33 | WEIGHT: | 1 of

SOLID EDGE ACADEMIC COPY





NB: Weld support inserts (Blocks) before machining

	NAME
DRAWN BY	Andre Cachucho (0501252N)
SUPERVISOR	Prof. B. W. Skews
ENG APPR	
DATE	07/10/2009

ALL DIMENSIONS ARE IN MILLIMETERS.
TOLERANCES UNLESS OTHERWISE STATED
± 0..2MM OR TO STANDARDS DICTATED BY
MATERIALS USED. ANGLES IN DEGREES ± 0.5 °

UNIVERSITY OF THE WITWATERSRAND
SCHOOL OF MECHANICAL, AERONAUTICAL AND INDUSTRIAL ENGINEERING

TITLE: Slanted section: 15 degree
Std steel U-channel (50x100)

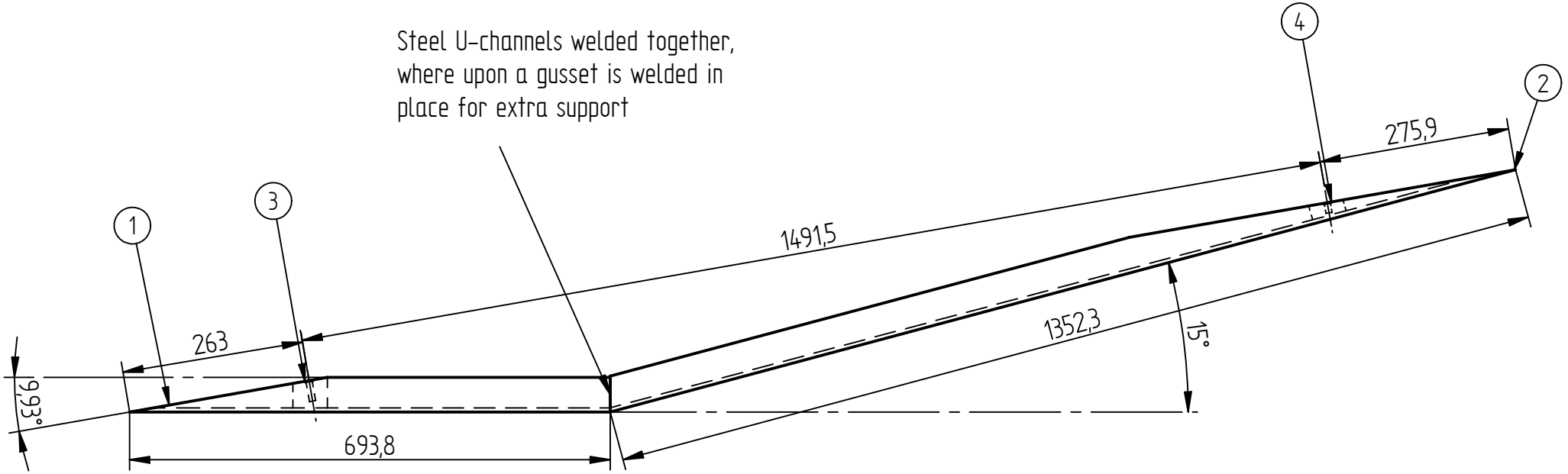
QUANTITY: 1 | REV

SCALE: 1 : 5.56 | WEIGHT: | 1 of

SOLID EDGE ACADEMIC COPY

Item Number	Title	Material	Quantity
1	Horizontal 15 deg U-channel	Steel	1
2	15 degree U-channel	Steel	1
3	Horiz support insert	Steel	1
4	15 degree support insert	Steel	1

Steel U-channels welded together, where upon a gusset is welded in place for extra support



	NAME
DRAWN BY	Andre Cachucho (0501252N)
SUPERVISOR	Prof. B. W. Skews
ENG APPR	
DATE	07/10/2009

ALL DIMENSIONS ARE IN MILLIMETERS.
TOLERANCES UNLESS OTHERWISE STATED
± 0..2MM OR TO STANDARDS DICTATED BY
MATERIALS USED. ANGLES IN DEGREES ± 0.5 °

UNIVERSITY OF THE WITWATERSRAND
SCHOOL OF MECHANICAL, AERONAUTICAL AND INDUSTRIAL ENGINEERING

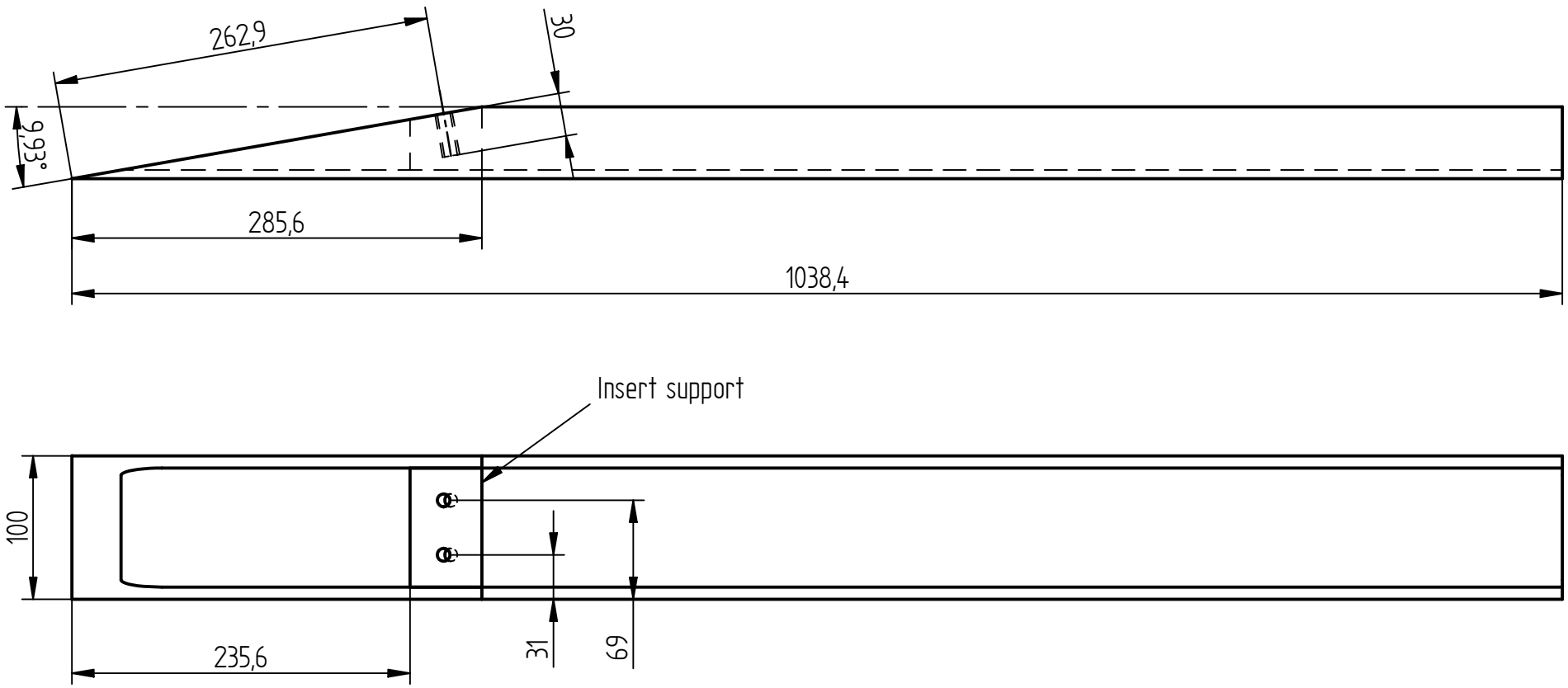
TITLE: 15 degree U-channel insert Assembly

QUANTITY: 1

REV

SCALE: 1 : 8.33 | WEIGHT: | 1 of

SOLID EDGE ACADEMIC COPY



NB: Weld support inserts (Blocks) before machining

	NAME
DRAWN BY	Andre Cachucho (0501252N)
SUPERVISOR	Prof. B. W. Skews
ENG APPR	
DATE	07/10/2009

ALL DIMENSIONS ARE IN MILLIMETERS.
TOLERANCES UNLESS OTHERWISE STATED
± 0..2MM OR TO STANDARDS DICTATED BY
MATERIALS USED. ANGLES IN DEGREES ± 0.5 °

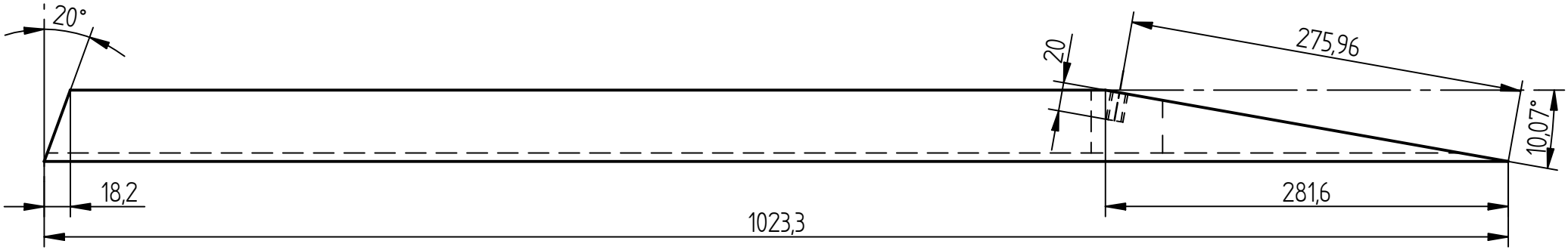
UNIVERSITY OF THE WITWATERSRAND
SCHOOL OF MECHANICAL, AERONAUTICAL AND INDUSTRIAL ENGINEERING

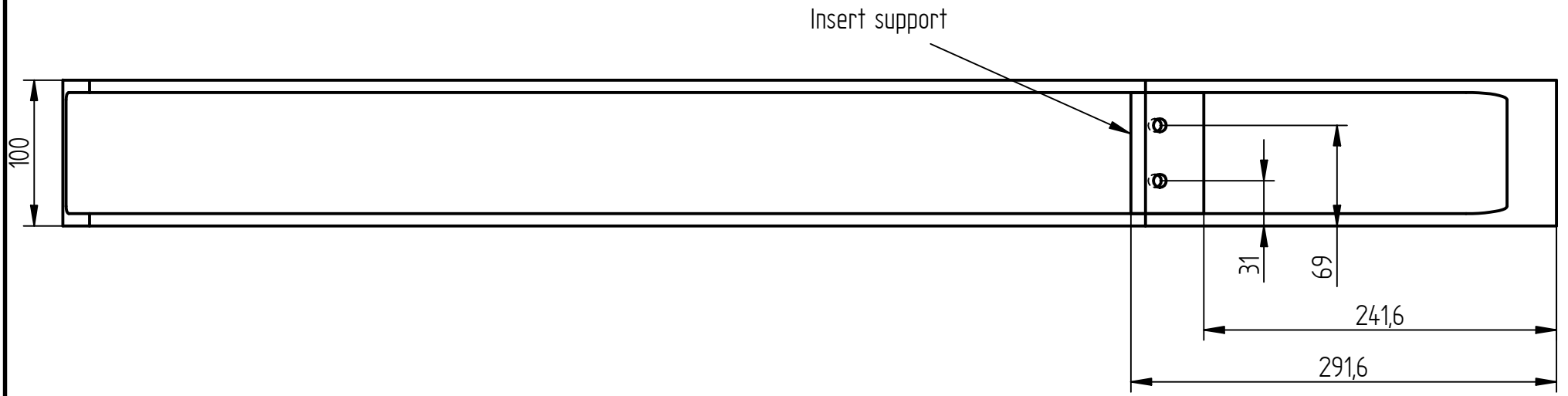
TITLE: Horizontal section: 20 degree
Std steel U-channel (50x100)

QUANTITY: 1 | REV

SCALE: 1 : 4.35 | WEIGHT: | 1 of

SOLID EDGE ACADEMIC COPY





NB: Weld support inserts (Blocks) before machining

	NAME
DRAWN BY	Andre Cachucho (0501252N)
SUPERVISOR	Prof. B. W. Skews
ENG APPR	
DATE	07/10/2009

ALL DIMENSIONS ARE IN MILLIMETERS.
TOLERANCES UNLESS OTHERWISE STATED
± 0..2MM OR TO STANDARDS DICTATED BY
MATERIALS USED. ANGLES IN DEGREES ± 0.5 °

UNIVERSITY OF THE WITWATERSRAND

SCHOOL OF MECHANICAL, AERONAUTICAL AND INDUSTRIAL ENGINEERING

TITLE: Slanted section: 20 degree
Std steel U-channel (50x100)

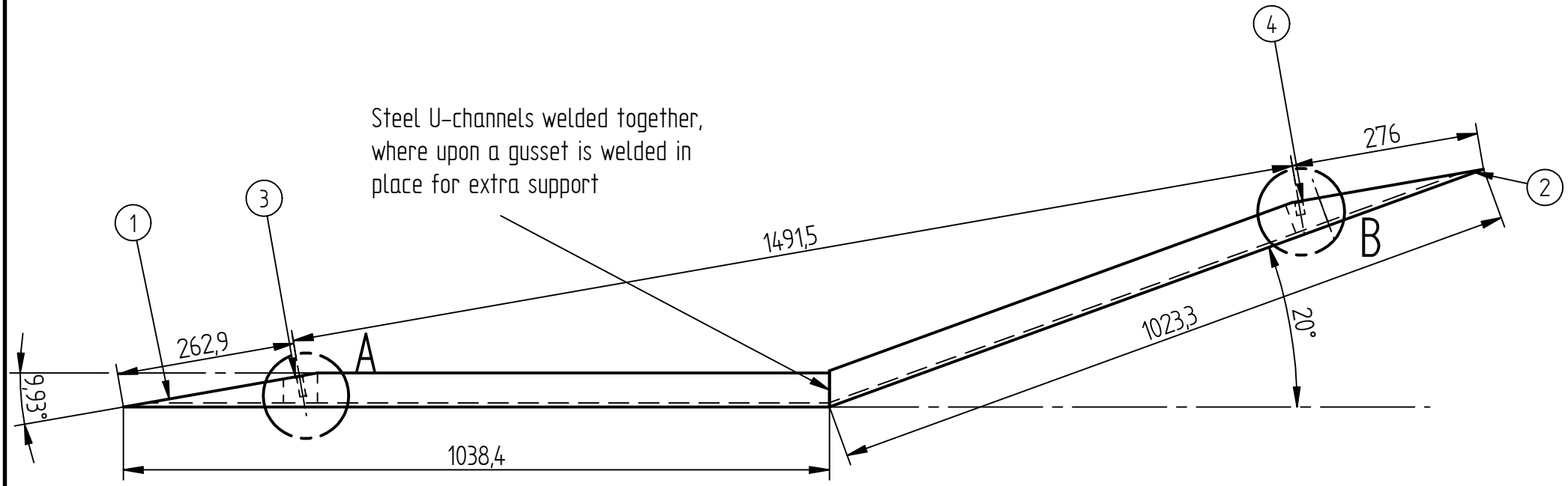
QUANTITY: 1

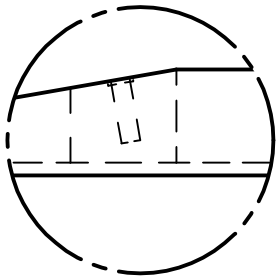
REV

SCALE: 1 : 4.35 | WEIGHT: | 1 of

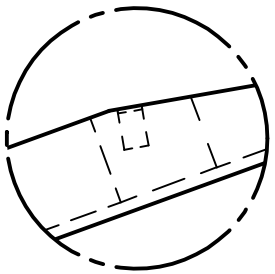
SOLID EDGE ACADEMIC COPY

Item Number	Title	Material	Quantity
1	Horizontal 20 deg U-channel	Steel	1
2	20 degree U-channel	Steel	1
3	Horiz support insert	Steel	1
4	20 degree support insert	Steel	1





DETAIL A



DETAIL B

	NAME
DRAWN BY	Andre Cachucho (0501252N)
SUPERVISOR	Prof. B. W. Skews
ENG APPR	
DATE	07/10/2009

ALL DIMENSIONS ARE IN MILLIMETERS.
TOLERANCES UNLESS OTHERWISE STATED
± 0..2MM OR TO STANDARDS DICTATED BY
MATERIALS USED. ANGLES IN DEGREES ± 0.5 °

UNIVERSITY OF THE WITWATERSRAND

SCHOOL OF MECHANICAL, AERONAUTICAL AND INDUSTRIAL ENGINEERING

TITLE: 20 degree U-channel insert Assembly

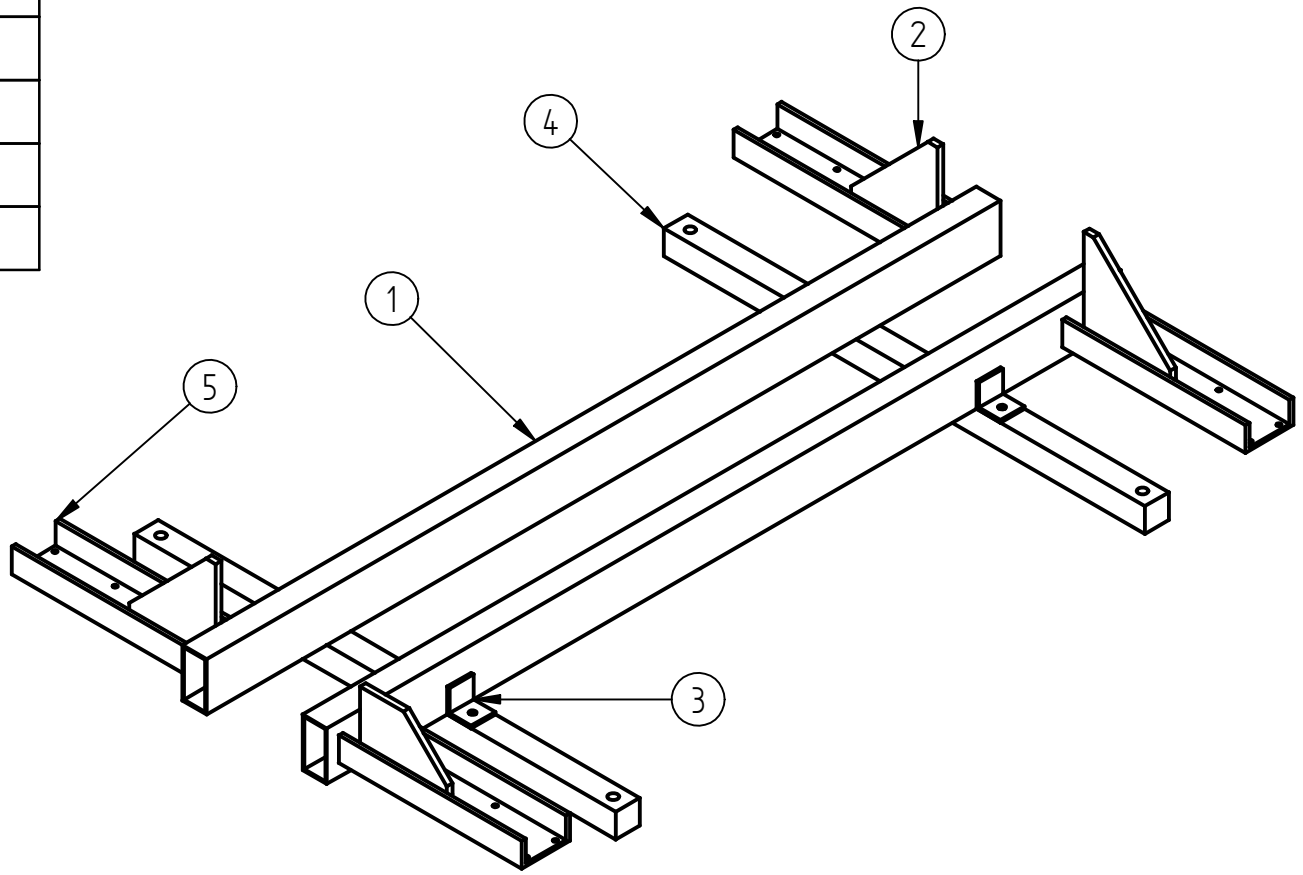
QUANTITY: 1

REV

SCALE: 1 : 8.33 | WEIGHT: | 1 of

SOLID EDGE ACADEMIC COPY

Item Number	Title	Quantity
1	Castor support rail	2
2	Caster support angle	4
3	Trolley stabiliser flange	4
4	Trolley stabiliser bar	2
5	Caster support assembly	4



	NAME
DRAWN BY	Andre Cachucho
SUPERVISOR	Prof. B. W. Skews
ENG APPR	
DATE	13/09/2009

ALL DIMENSIONS ARE IN MILLIMETERS.
TOLERANCES UNLESS OTHERWISE STATED
± 0..2MM OR TO STANDARDS DICTATED BY
MATERIALS USED. ANGLES IN DEGREES ± 0.5 °

UNIVERSITY OF THE WITWATERSRAND

SCHOOL OF MECHANICAL, AERONAUTICAL AND INDUSTRIAL ENGINEERING

TITLE Stand assembly layout

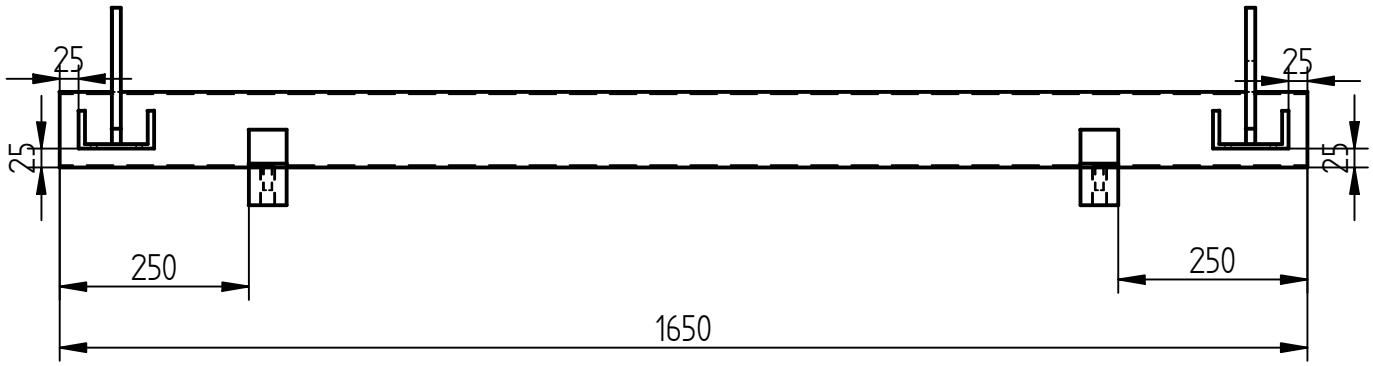
QUANTITY: 1

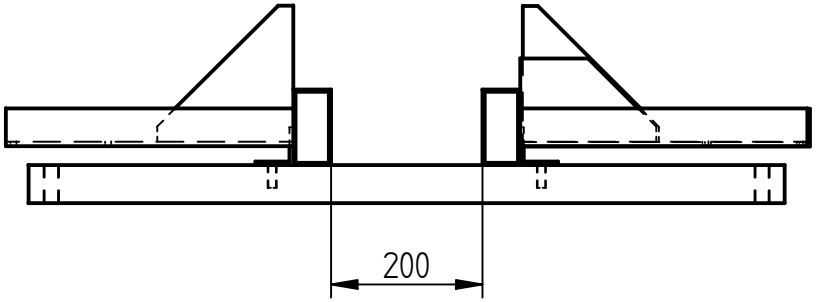
REV

SCALE: 1 : 5

WEIGHT:

SOLID EDGE ACADEMIC COPY





	NAME
DRAWN BY	LORENZO LACOVIG
SUPERVISOR	Prof. B. W. Skews
ENG APPR	
DATE	13/09/2009

ALL DIMENSIONS ARE IN MILLIMETERS.
TOLERANCES UNLESS OTHERWISE STATED
± 0..2MM OR TO STANDARDS DICTATED BY
MATERIALS USED. ANGLES IN DEGREES ± 0.5 °

UNIVERSITY OF THE WITWATERSRAND

SCHOOL OF MECHANICAL, AERONAUTICAL AND INDUSTRIAL ENGINEERING

TITLE Castor stand assembly

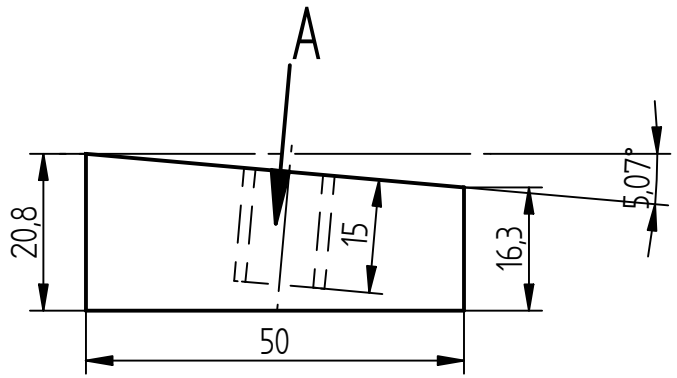
QUANTITY: 1

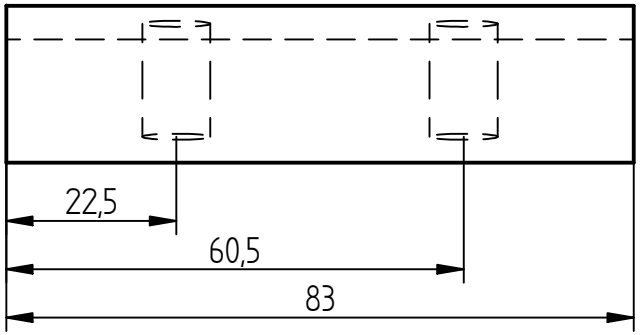
REV

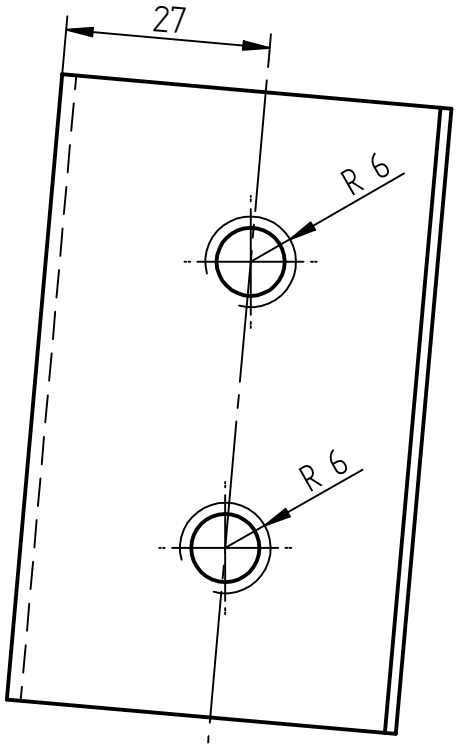
SCALE: 1 : 5

WEIGHT:

SOLID EDGE ACADEMIC COPY







VIEW A

Both holes are threaded

	NAME
DRAWN BY	Andre Cachucho (0501252N)
SUPERVISOR	Prof. B. W. Skews
ENG APPR	
DATE	07/10/2009

ALL DIMENSIONS ARE IN MILLIMETERS.
TOLERANCES UNLESS OTHERWISE STATED
± 0..2MM OR TO STANDARDS DICTATED BY
MATERIALS USED. ANGLES IN DEGREES ± 0.5 °

UNIVERSITY OF THE WITWATERSRAND

SCHOOL OF MECHANICAL, AERONAUTICAL AND INDUSTRIAL ENGINEERING

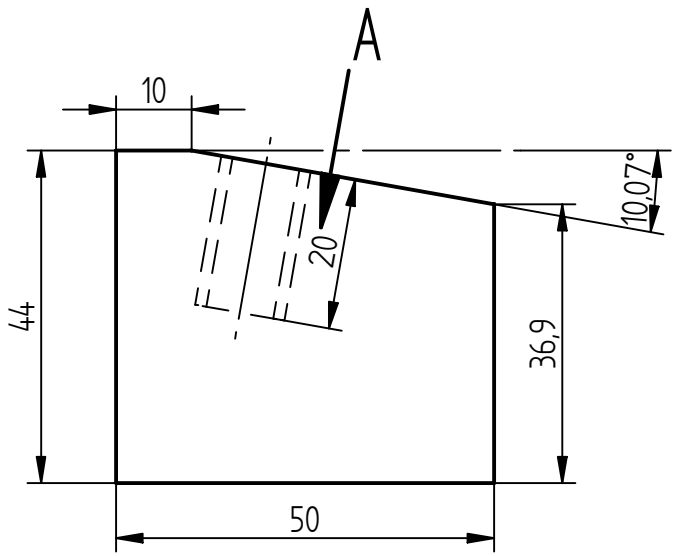
TITLE: 15 deg channel section: Support insert

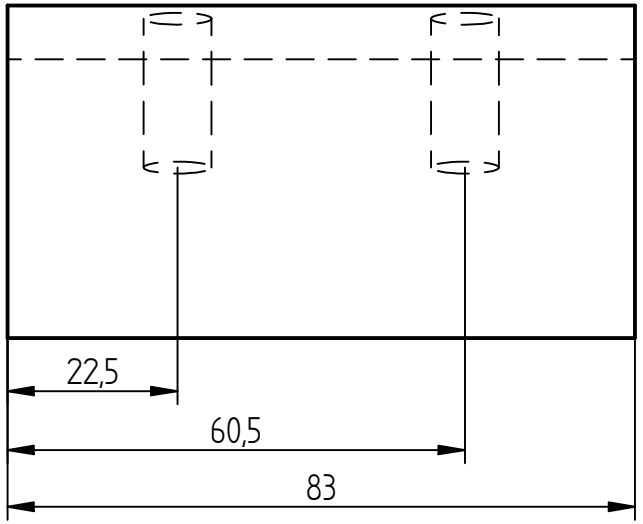
QUANTITY: 1

REV

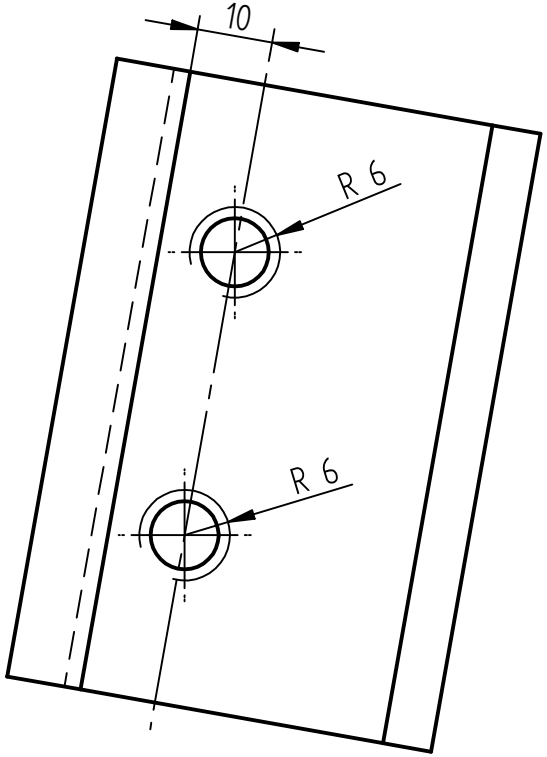
SCALE: 1 : 1 | WEIGHT: | 1 of

SOLID EDGE ACADEMIC COPY





Both holes are threaded



VIEW A

	NAME
DRAWN BY	Andre Cachucho (0501252N)
SUPERVISOR	Prof. B. W. Skews
ENG APPR	
DATE	07/10/2009

ALL DIMENSIONS ARE IN MILLIMETERS.
TOLERANCES UNLESS OTHERWISE STATED
± 0..2MM OR TO STANDARDS DICTATED BY
MATERIALS USED. ANGLES IN DEGREES ± 0.5 °

UNIVERSITY OF THE WITWATERSRAND
SCHOOL OF MECHANICAL, AERONAUTICAL AND INDUSTRIAL ENGINEERING

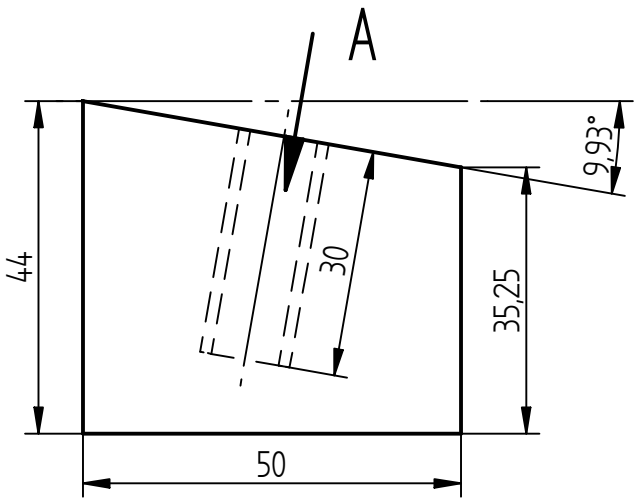
TITLE: Support insert: 20 deg channel section

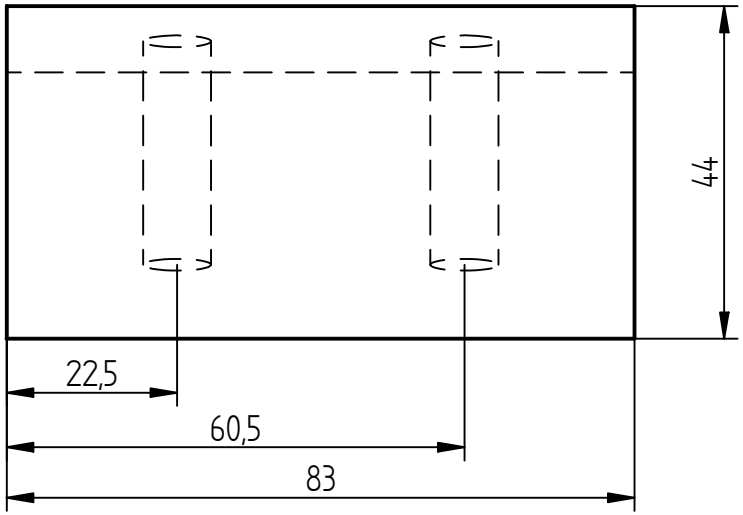
QUANTITY: 1

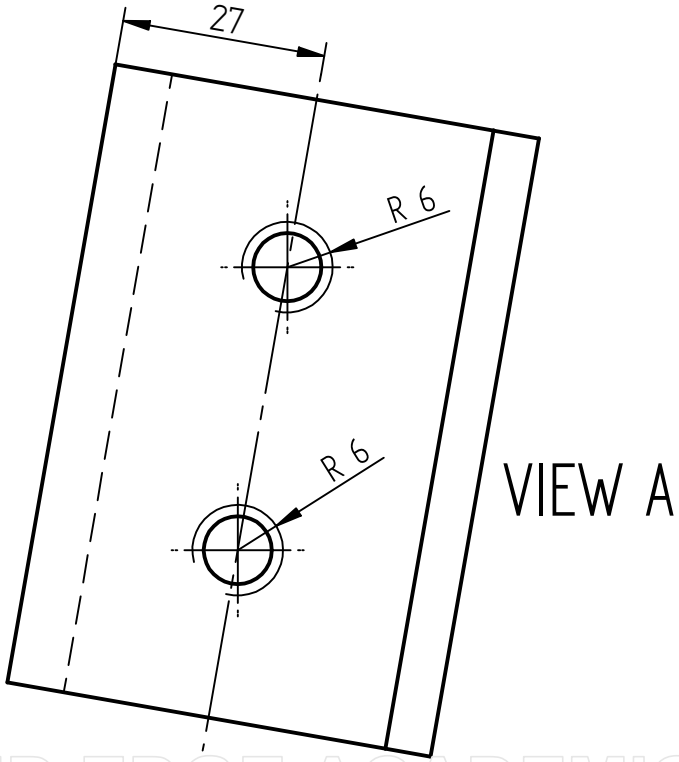
REV

SCALE: 1 : 1 | WEIGHT: | 1 of

SOLID EDGE ACADEMIC COPY







VIEW A

Both holes are threaded

	NAME
DRAWN BY	Andre Cachucho (0501252N)
SUPERVISOR	Prof. B. W. Skews
ENG APPR	
DATE	07/10/2009

ALL DIMENSIONS ARE IN MILLIMETERS.
TOLERANCES UNLESS OTHERWISE STATED
± 0..2MM OR TO STANDARDS DICTATED BY
MATERIALS USED. ANGLES IN DEGREES ± 0.5 °

UNIVERSITY OF THE WITWATERSRAND

SCHOOL OF MECHANICAL, AERONAUTICAL AND INDUSTRIAL ENGINEERING

TITLE: Support insert: Horizontal section

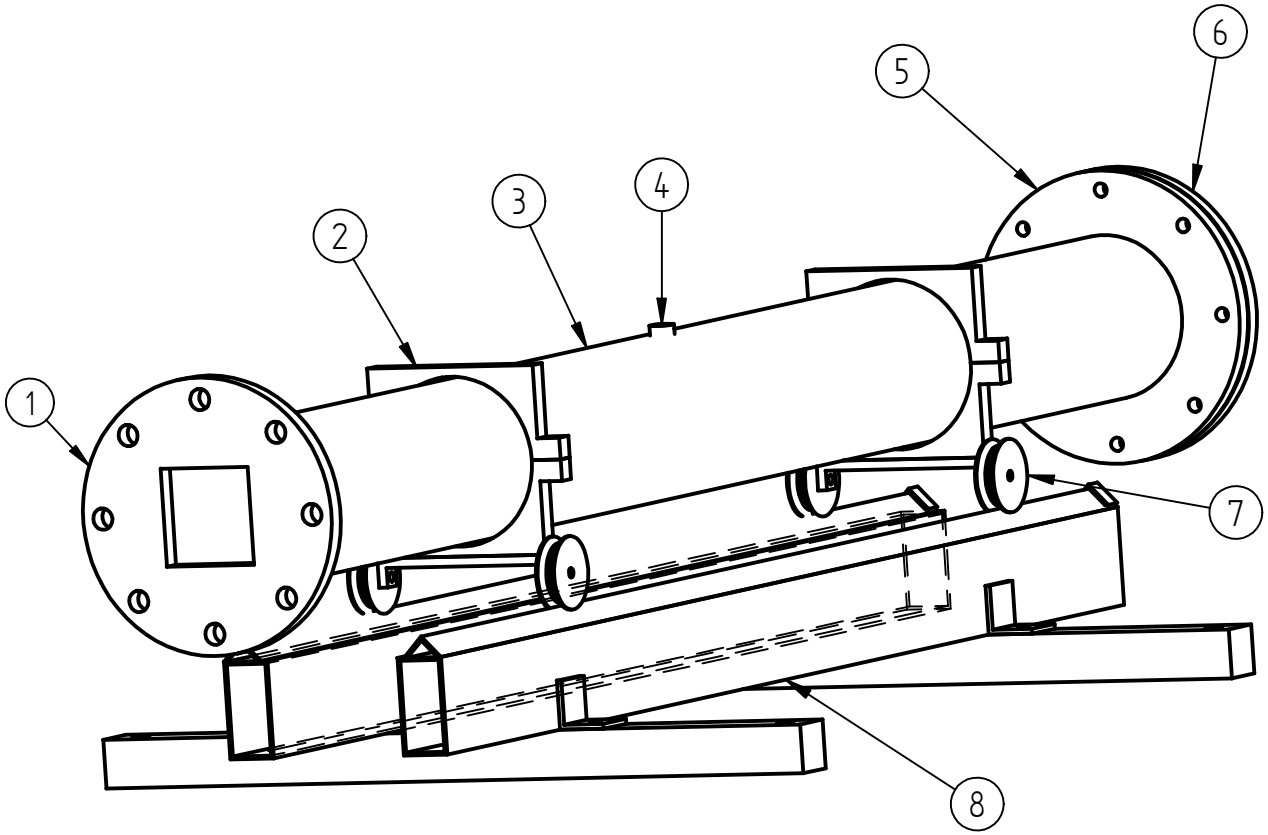
QUANTITY: 2

REV

SCALE: 1 : 1 | WEIGHT: | 1 of

SOLID EDGE ACADEMIC COPY

Item Number	Title	Quantity
1	Front driver flange	1
2	Wheel supports	2
3	Round tube	1
4	Valve plugin	2
5	Driver 1st end flange	1
6	Driver 2nd end flange	1
7	Wheel	4
8	Driver stand assembly	1



The manufacturing of the driver will be outsourced to Arlec Engineering Works CC.

	NAME
DRAWN BY	Andre Cachucho (0501252N)
SUPERVISOR	Prof. B. W. Skews
ENG APPR	
DATE	07/10/2009

ALL DIMENSIONS ARE IN MILLIMETERS.
TOLERANCES UNLESS OTHERWISE STATED
± 0..2MM OR TO STANDARDS DICTATED BY
MATERIALS USED. ANGLES IN DEGREES ± 0.5 °

UNIVERSITY OF THE WITWATERSRAND
SCHOOL OF MECHANICAL, AERONAUTICAL AND INDUSTRIAL ENGINEERING

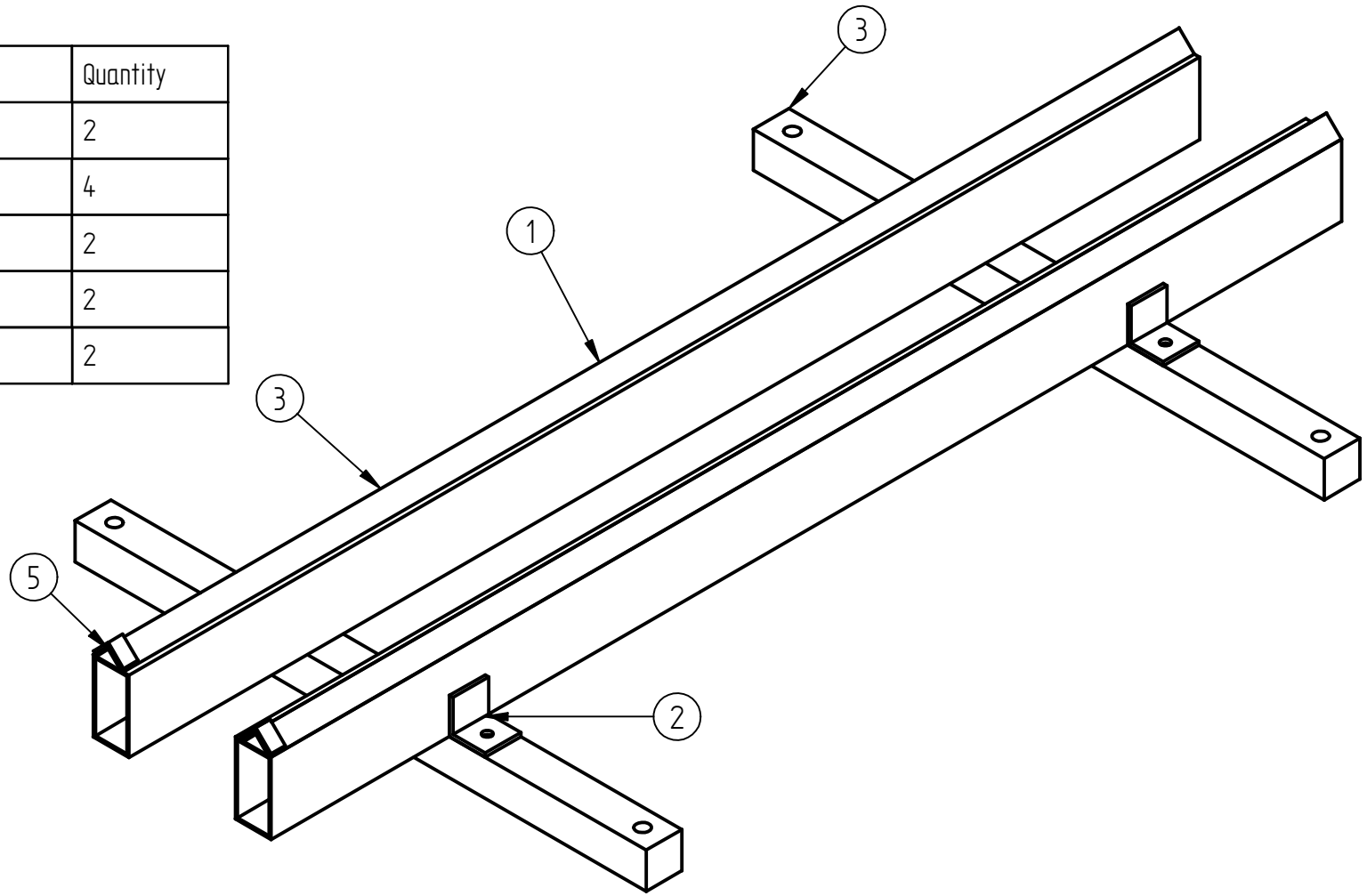
TITLE: Driver and support assembly

QUANTITY: 1 | REV

SCALE: 1 : 7.69 | WEIGHT: | 1 of

SOLID EDGE ACADEMIC COPY

Item Number	Title	Quantity
1	Castor support rail	2
2	Trolley stabiliser flange	4
3	Trolley stabiliser bar	2
4	Trolley V-rail	2
5	Stopper V-rail	2



	NAME
DRAWN BY	Andre Cachucho (0501252N)
SUPERVISOR	Prof. B. W. Skews
ENG APPR	
DATE	07/10/2009

ALL DIMENSIONS ARE IN MILLIMETERS.
TOLERANCES UNLESS OTHERWISE STATED
± 0..2MM OR TO STANDARDS DICTATED BY
MATERIALS USED. ANGLES IN DEGREES ± 0.5 °

UNIVERSITY OF THE WITWATERSRAND
SCHOOL OF MECHANICAL, AERONAUTICAL AND INDUSTRIAL ENGINEERING

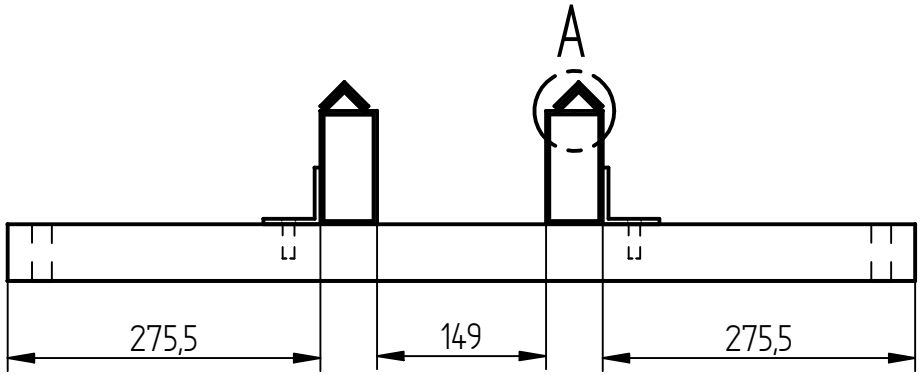
TITLE: Driver stand assembly

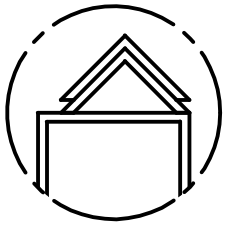
QUANTITY: 1

REV

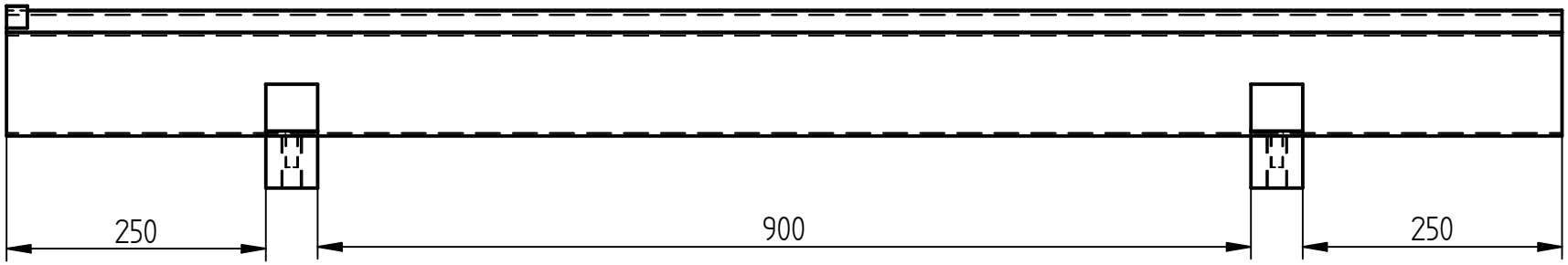
SCALE: 1 : 7.69 | WEIGHT: | 1 of

SOLID EDGE ACADEMIC COPY





DETAIL A



	NAME
DRAWN BY	Andre Cachucho (0501252N)
SUPERVISOR	Prof. B. W. Skews
ENG APPR	
DATE	07/10/2009

ALL DIMENSIONS ARE IN MILLIMETERS.
TOLERANCES UNLESS OTHERWISE STATED
± 0..2MM OR TO STANDARDS DICTATED BY
MATERIALS USED. ANGLES IN DEGREES ± 0.5 °

UNIVERSITY OF THE WITWATERSRAND

SCHOOL OF MECHANICAL, AERONAUTICAL AND INDUSTRIAL ENGINEERING

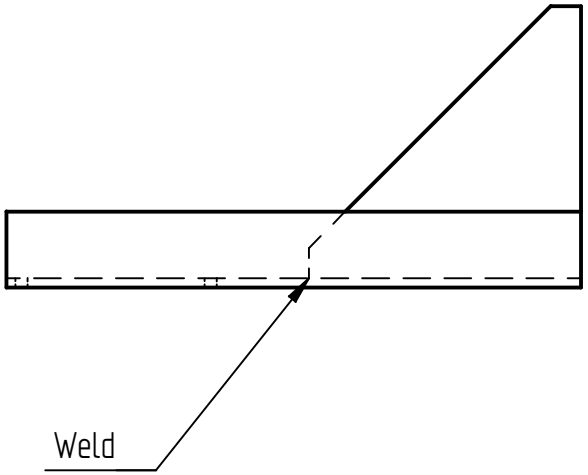
TITLE: Driver stand assembly

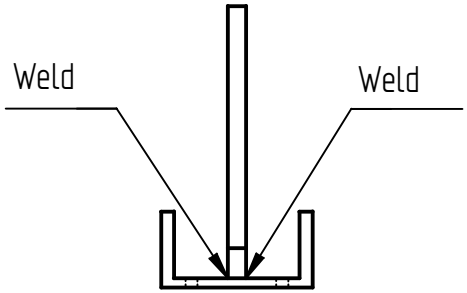
QUANTITY: 1

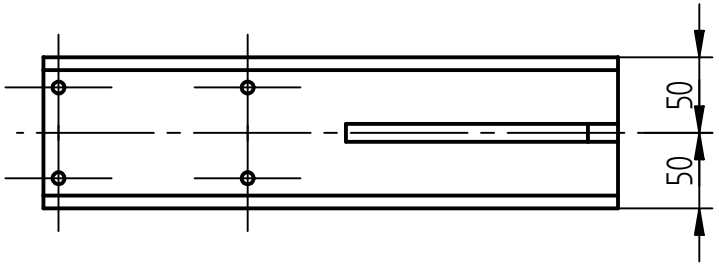
REV

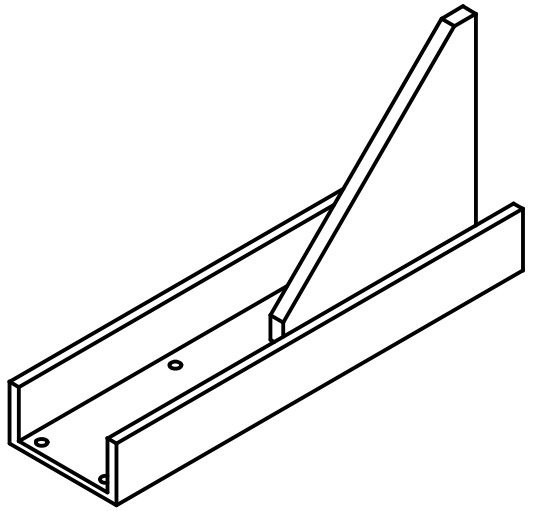
SCALE: 1 : 6.67 | WEIGHT: | 1 of

SOLID EDGE ACADEMIC COPY









	NAME
DRAWN BY	LORENZO LACOVIG
SUPERVISOR	Prof. B. W. Skews
ENG APPR	
DATE	02/05/2007

ALL DIMENSIONS ARE IN MILLIMETERS.
TOLERANCES UNLESS OTHERWISE STATED
± 0..2MM OR TO STANDARDS DICTATED BY
MATERIALS USED. ANGLES IN DEGREES ± 0.5 °

UNIVERSITY OF THE WITWATERSRAND

SCHOOL OF MECHANICAL, AERONAUTICAL AND INDUSTRIAL ENGINEERING

TITLE Castor Support Assembly

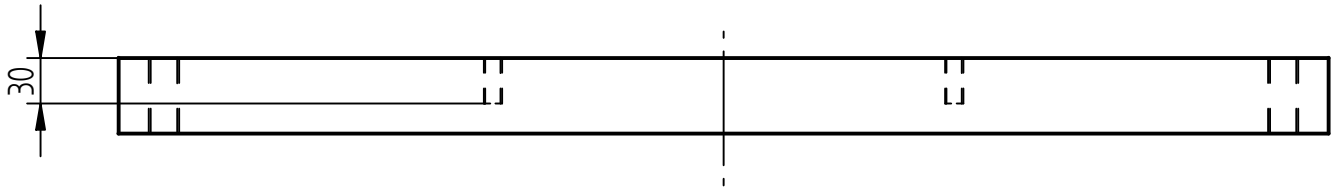
QUANTITY: 4

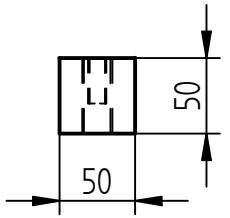
REV

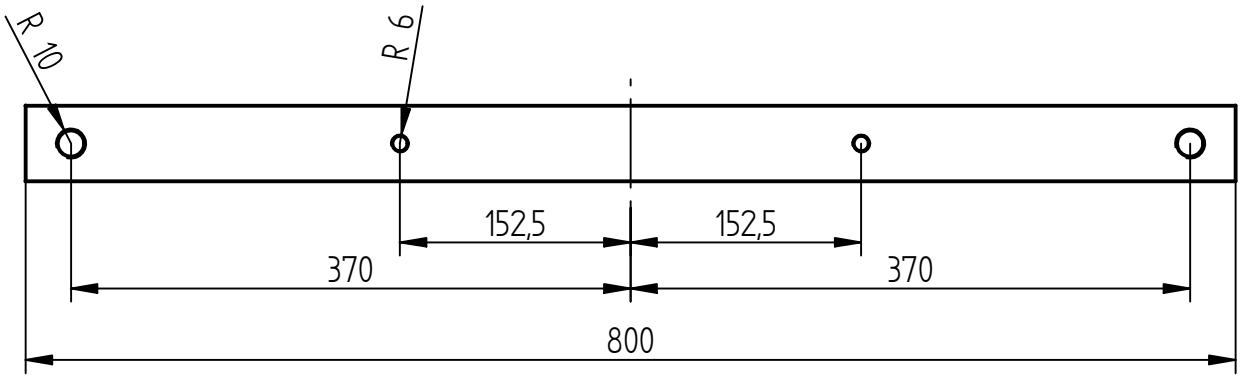
SCALE: 1 : 5

WEIGHT:

SOLID EDGE ACADEMIC COPY







NB: ALL HOLES ARE TAPPED

	NAME
DRAWN BY	Andre Cachucho (0501252N)
SUPERVISOR	Prof. B. W. Skews
ENG APPR	
DATE	07/10/2009

ALL DIMENSIONS ARE IN MILLIMETERS.
TOLERANCES UNLESS OTHERWISE STATED
± 0..2MM OR TO STANDARDS DICTATED BY
MATERIALS USED. ANGLES IN DEGREES ± 0.5 °

UNIVERSITY OF THE WITWATERSRAND

SCHOOL OF MECHANICAL, AERONAUTICAL AND INDUSTRIAL ENGINEERING

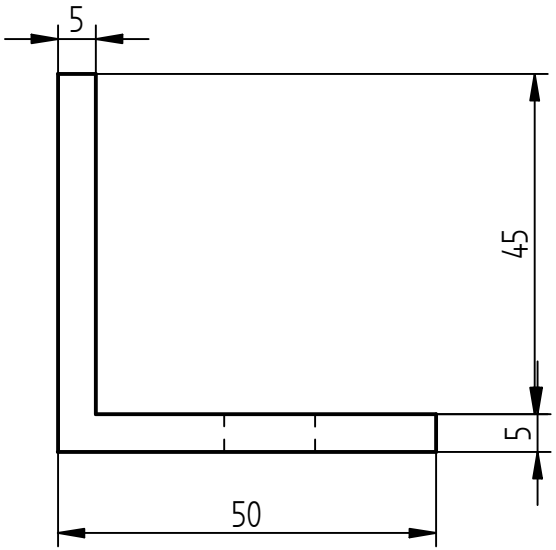
TITLE: Driver stabilising bar
std 50 X 50 steel bar

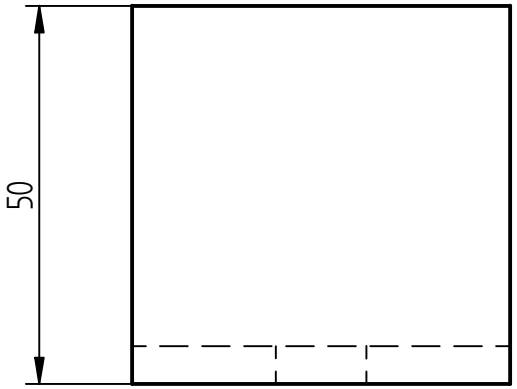
QUANTITY: 2

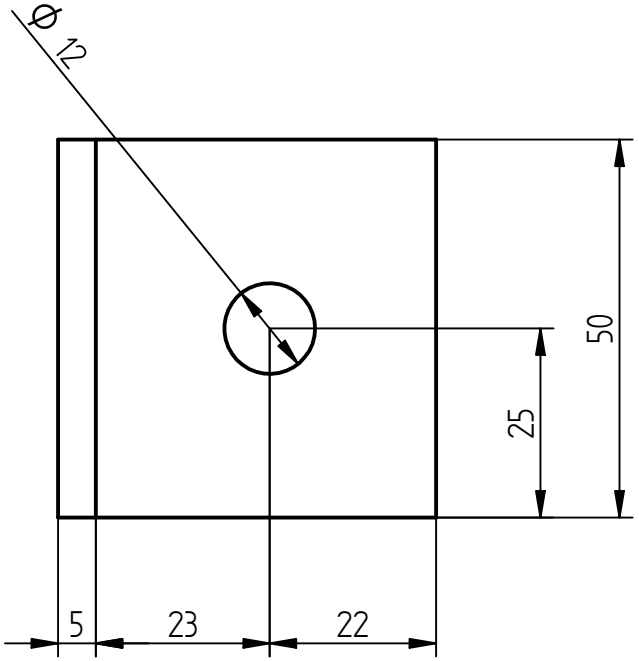
REV

SCALE: 1 : 5 | WEIGHT: | 1 of

SOLID EDGE ACADEMIC COPY







	NAME
DRAWN BY	LORENZO LACOVIG
SUPERVISOR	Prof. B. W. Skews
ENG APPR	
DATE	23/10/2007

ALL DIMENSIONS ARE IN MILLIMETERS.
TOLERANCES UNLESS OTHERWISE STATED
± 0..2MM OR TO STANDARDS DICTATED BY
MATERIALS USED. ANGLES IN DEGREES ± 0.5 °

UNIVERSITY OF THE WITWATERSRAND

SCHOOL OF MECHANICAL, AERONAUTICAL AND INDUSTRIAL ENGINEERING

TITLE Driver Stabilizer Flange
[mild steel plate]

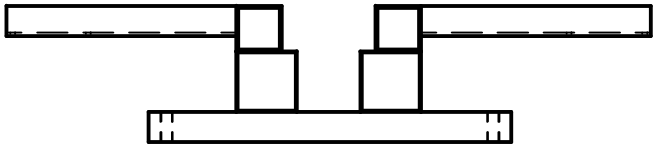
QUANTITY: 4

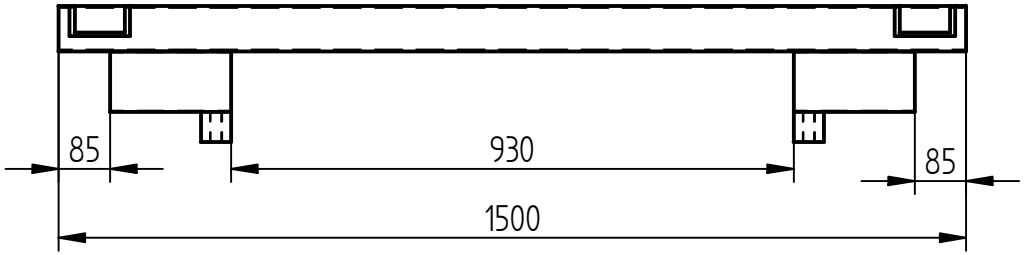
REV

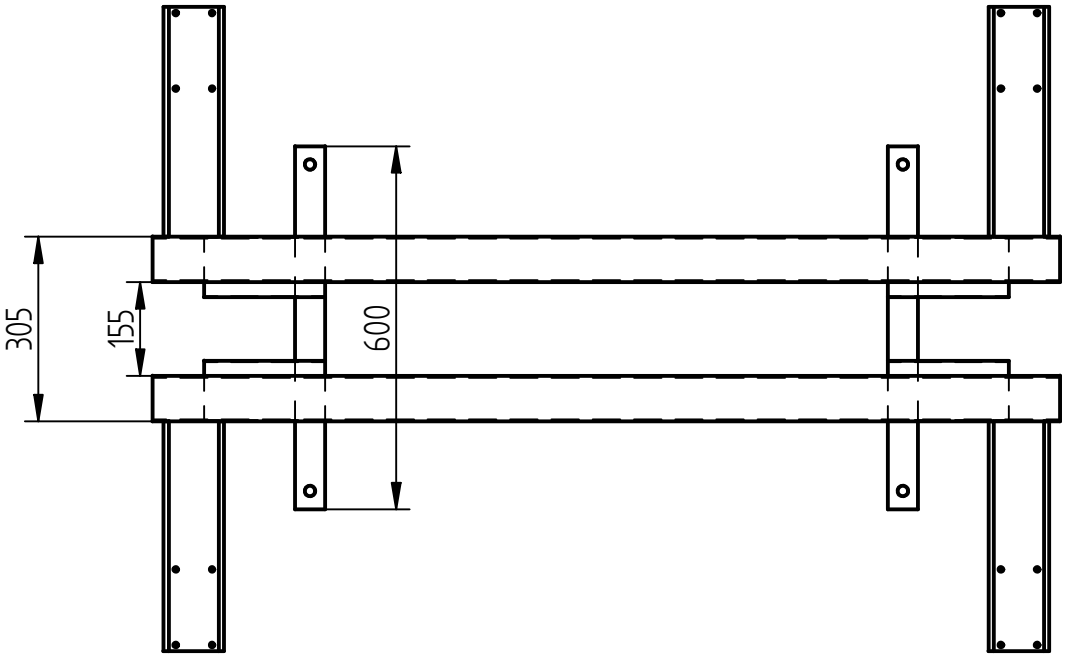
SCALE: 1 : 1

WEIGHT:

SOLID EDGE ACADEMIC COPY







	NAME
DRAWN BY	Andre Cachucho (0501252N)
SUPERVISOR	Prof. B. W. Skews
ENG APPR	
DATE	07/10/2009

ALL DIMENSIONS ARE IN MILLIMETERS.
TOLERANCES UNLESS OTHERWISE STATED
± 0..2MM OR TO STANDARDS DICTATED BY
MATERIALS USED. ANGLES IN DEGREES ± 0.5 °

UNIVERSITY OF THE WITWATERSRAND

SCHOOL OF MECHANICAL, AERONAUTICAL AND INDUSTRIAL ENGINEERING

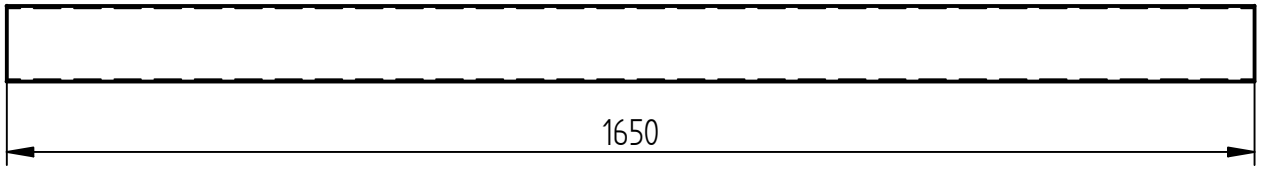
TITLE: New driver supports

QUANTITY: 2

REV

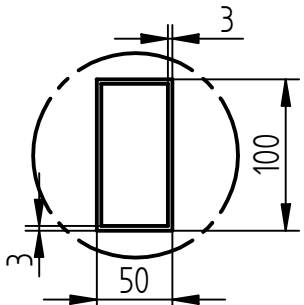
SCALE: 1 : 12.5 | WEIGHT: | 1 of

SOLID EDGE ACADEMIC COPY





A



DETAIL A

	NAME
DRAWN BY	LORENZO LACOVIG
SUPERVISOR	Prof. B. W. Skews
ENG APPR	
DATE	02/05/2007

UNIVERSITY OF THE WITWATERSRAND

SCHOOL OF MECHANICAL, AERONAUTICAL AND INDUSTRIAL ENGINEERING

TITLE Castor Support Rail
std 100 x 50 x 3 Rectangular Steel Tube

ALL DIMENSIONS ARE IN MILLIMETERS.
TOLERANCES UNLESS OTHERWISE STATED
± 0..2MM OR TO STANDARDS DICTATED BY
MATERIALS USED. ANGLES IN DEGREES ± 0.5 °

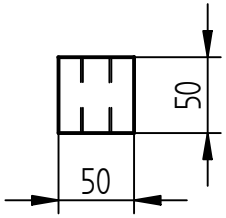
QUANTITY: 2

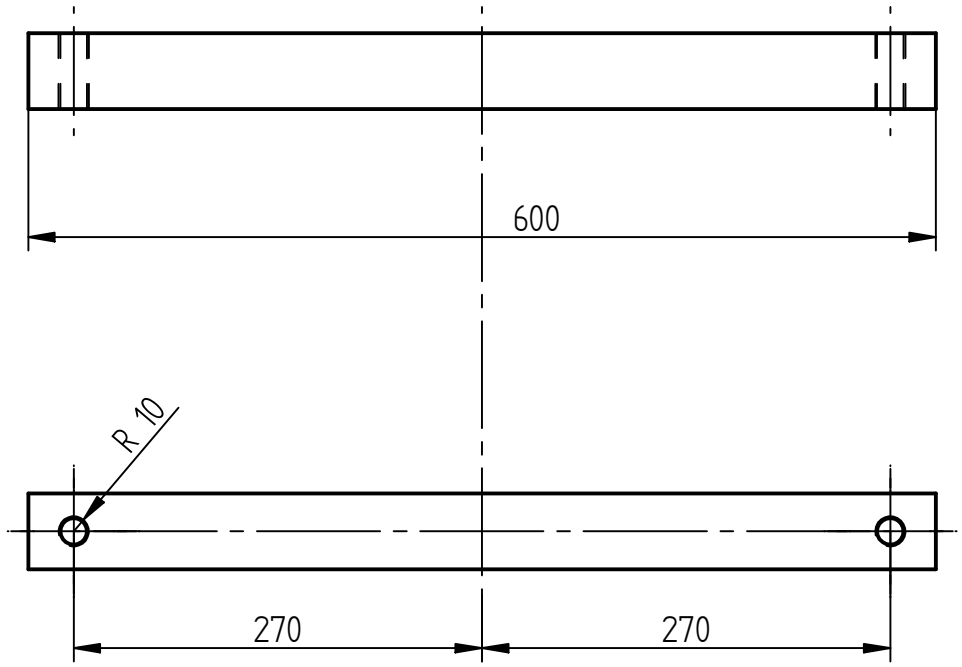
REV

SCALE: 1 : 10

WEIGHT:

SOLID EDGE ACADEMIC COPY





All holes are threaded

	NAME
DRAWN BY	Andre Cachucho (0501252N)
SUPERVISOR	Prof. B. W. Skews
ENG APPR	
DATE	07/10/2009

ALL DIMENSIONS ARE IN MILLIMETERS.
TOLERANCES UNLESS OTHERWISE STATED
± 0..2MM OR TO STANDARDS DICTATED BY
MATERIALS USED. ANGLES IN DEGREES ± 0.5 °

UNIVERSITY OF THE WITWATERSRAND

SCHOOL OF MECHANICAL, AERONAUTICAL AND INDUSTRIAL ENGINEERING

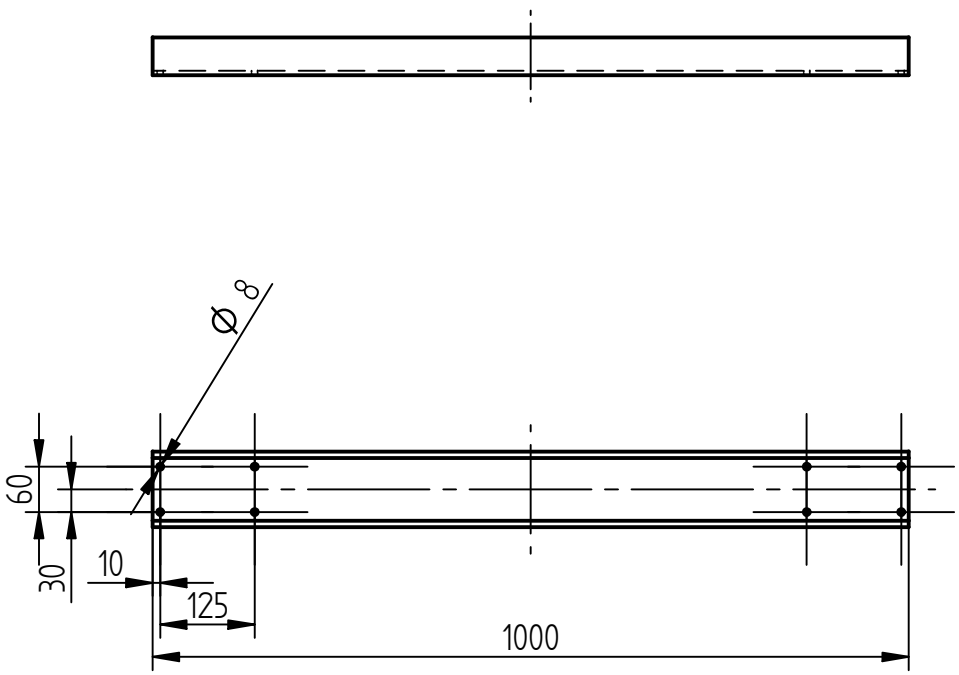
TITLE: Driver stabilising bar
std 50 X 50 steel bar

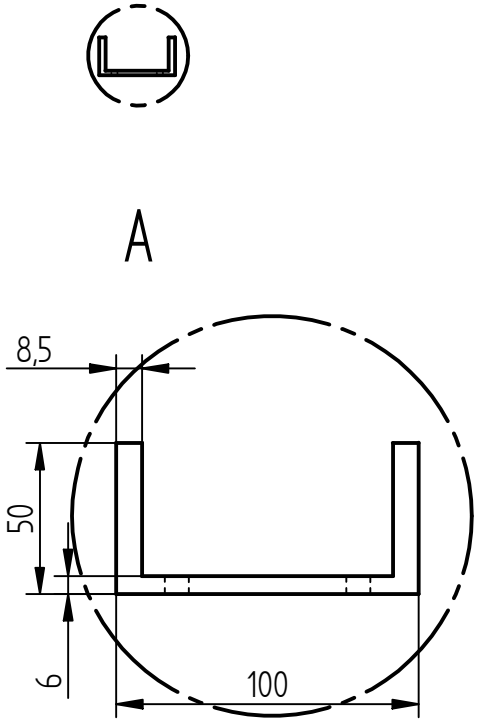
QUANTITY: 2

REV

SCALE: 1 : 5 | WEIGHT: | 1 of

SOLID EDGE ACADEMIC COPY





DETAIL A

	NAME
DRAWN BY	LORENZO LACOVIG
SUPERVISOR	Prof. B. W. Skews
ENG APPR	
DATE	13/06/2007

ALL DIMENSIONS ARE IN MILLIMETERS.
TOLERANCES UNLESS OTHERWISE STATED
± 0..2MM OR TO STANDARDS DICTATED BY
MATERIALS USED. ANGLES IN DEGREES ± 0.5 °

UNIVERSITY OF THE WITWATERSRAND
SCHOOL OF MECHANICAL, AERONAUTICAL AND INDUSTRIAL ENGINEERING

TITLE Trolley Caster Support

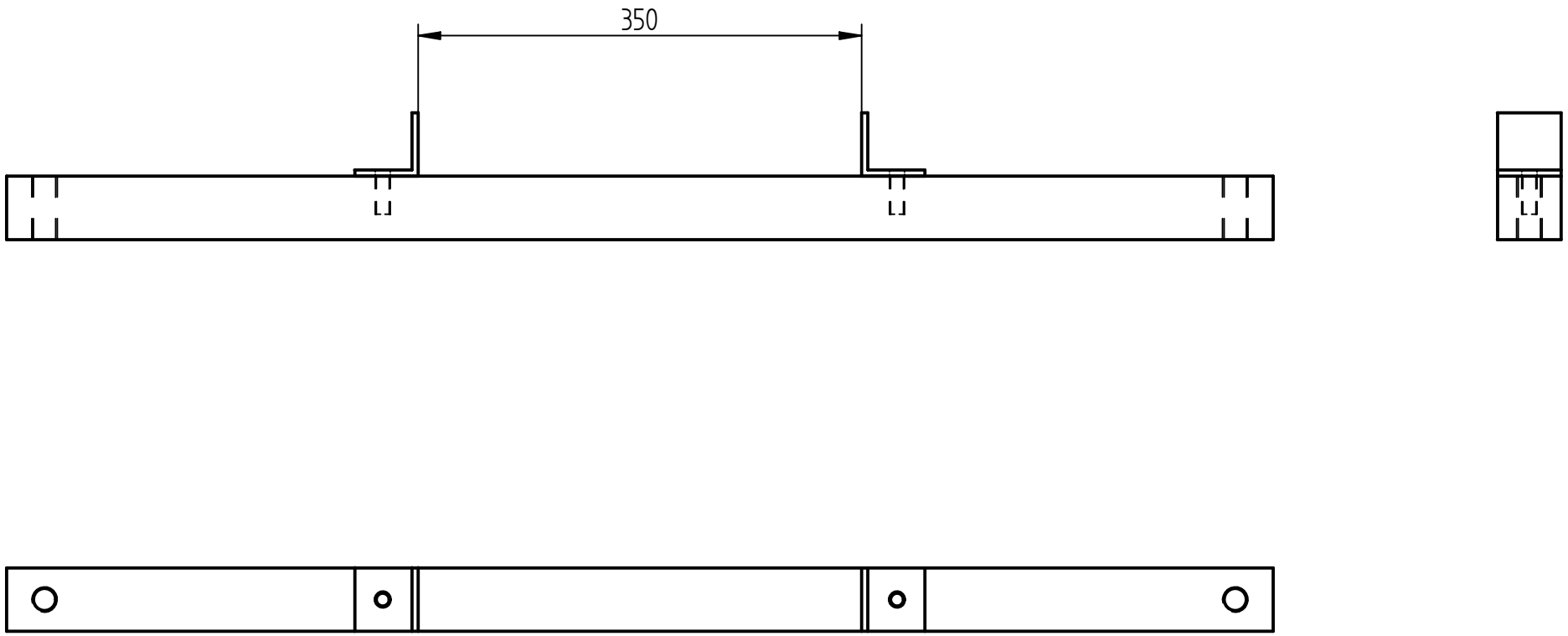
QUANTITY: 2

REV

SCALE: 1 : 10

WEIGHT:

SOLID EDGE ACADEMIC COPY



	NAME
DRAWN BY	LORENZO LACOVIG
SUPERVISOR	Prof. B. W. Skews
ENG APPR	
DATE	23/10/2007

ALL DIMENSIONS ARE IN MILLIMETERS.
TOLERANCES UNLESS OTHERWISE STATED
± 0..2MM OR TO STANDARDS DICTATED BY
MATERIALS USED. ANGLES IN DEGREES ± 0.5 °

UNIVERSITY OF THE WITWATERSRAND

SCHOOL OF MECHANICAL, AERONAUTICAL AND INDUSTRIAL ENGINEERING

TITLE Trolley Stabilizer Assembly

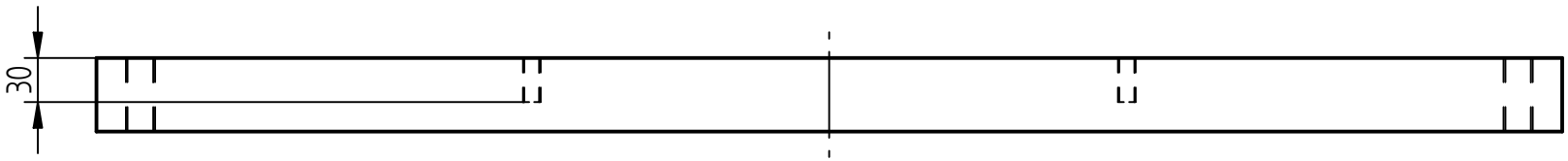
QUANTITY: 2

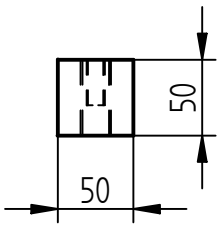
REV

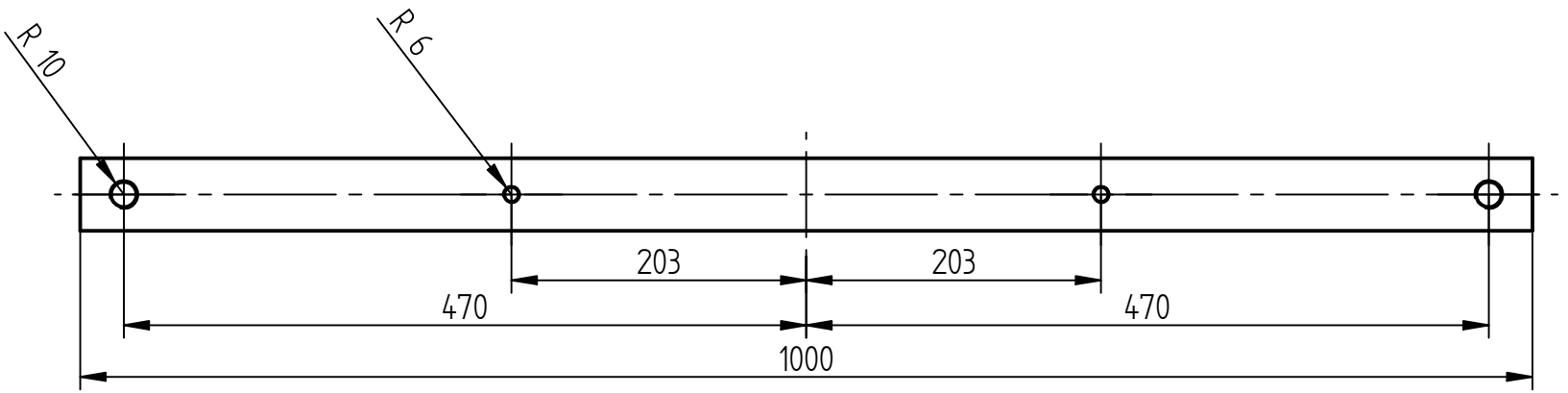
SCALE: 1 : 5

WEIGHT:

SOLID EDGE ACADEMIC COPY







NB: ALL HOLES ARE TAPPED

	NAME
DRAWN BY	LORENZO LACOVIG
SUPERVISOR	Prof. B. W. Skews
ENG APPR	
DATE	23/10/2007

ALL DIMENSIONS ARE IN MILLIMETERS.
TOLERANCES UNLESS OTHERWISE STATED
± 0..2MM OR TO STANDARDS DICTATED BY
MATERIALS USED. ANGLES IN DEGREES ± 0.5 °

UNIVERSITY OF THE WITWATERSRAND

SCHOOL OF MECHANICAL, AERONAUTICAL AND INDUSTRIAL ENGINEERING

TITLE Trolley Stabilizer Bar
std 50 X 50 steel bar

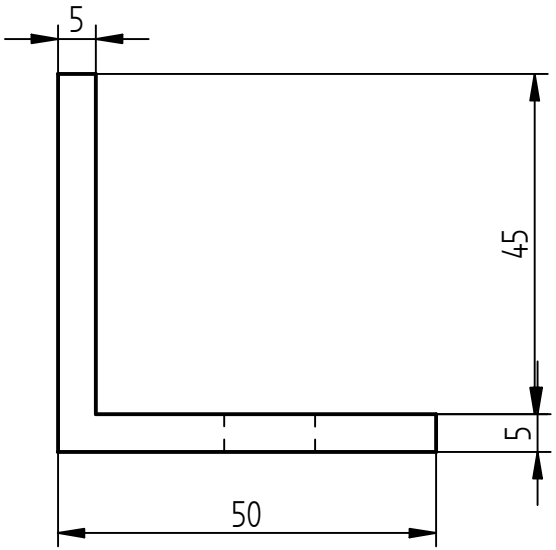
QUANTITY: 2

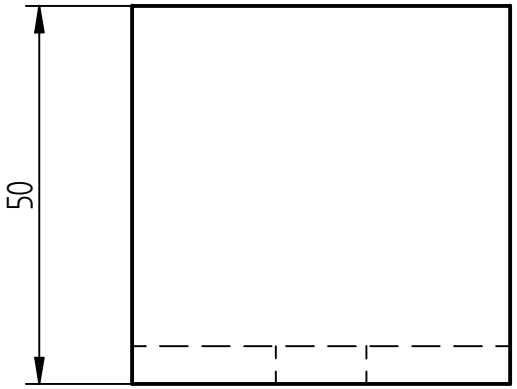
REV

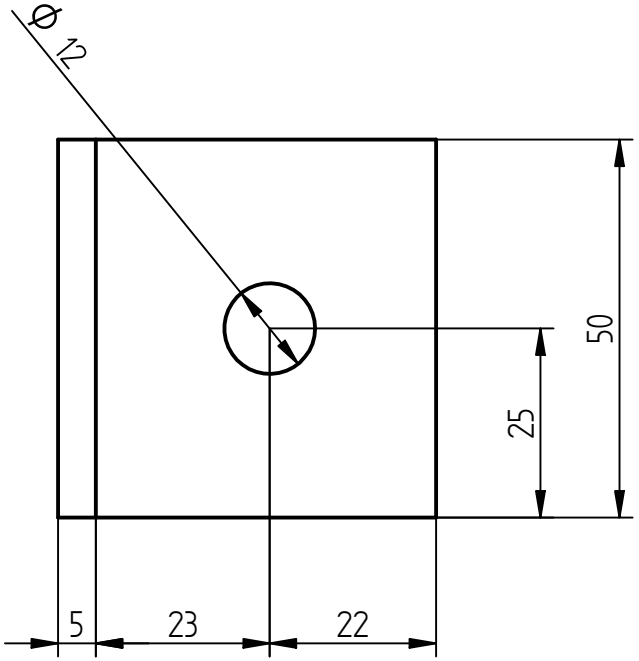
SCALE: 1 : 5

WEIGHT:

SOLID EDGE ACADEMIC COPY







	NAME
DRAWN BY	LORENZO LACOVIG
SUPERVISOR	Prof. B. W. Skews
ENG APPR	
DATE	23/10/2007

ALL DIMENSIONS ARE IN MILLIMETERS.
TOLERANCES UNLESS OTHERWISE STATED
± 0..2MM OR TO STANDARDS DICTATED BY
MATERIALS USED. ANGLES IN DEGREES ± 0.5 °

UNIVERSITY OF THE WITWATERSRAND

SCHOOL OF MECHANICAL, AERONAUTICAL AND INDUSTRIAL ENGINEERING

TITLE Trolley Stabilizer Flange
[mild steel plate]

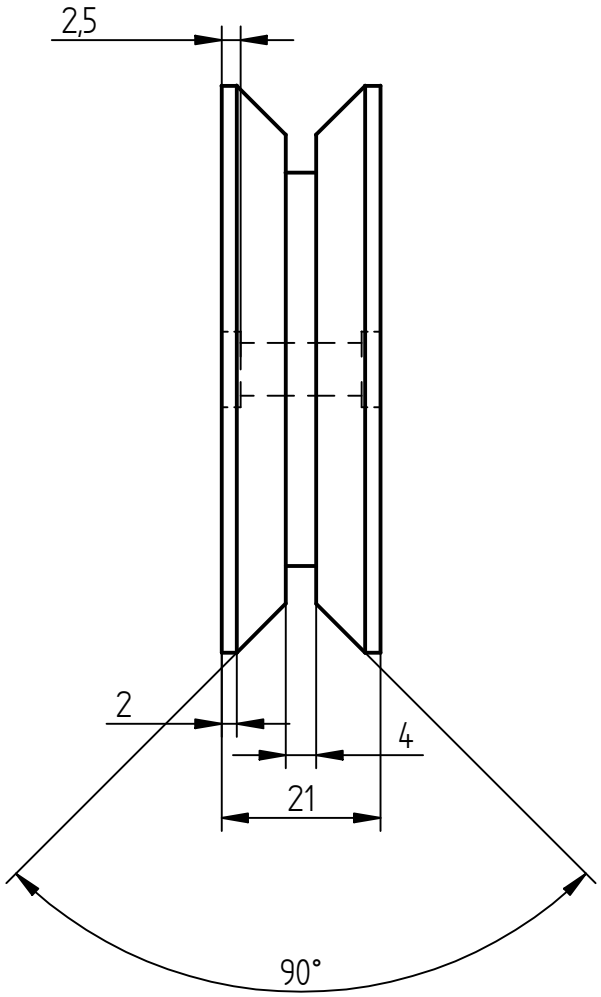
QUANTITY: 4

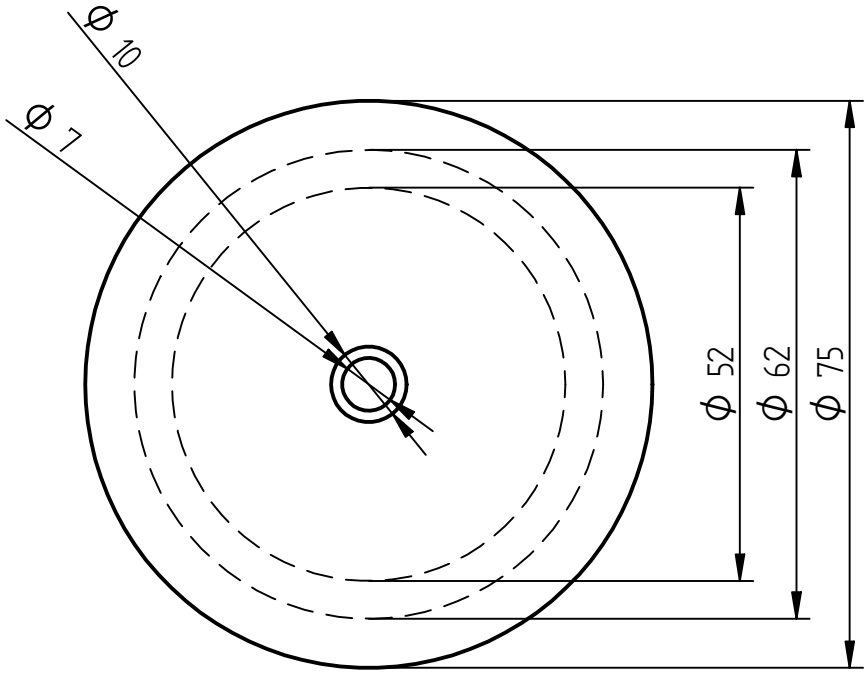
REV

SCALE: 1 : 1

WEIGHT:

SOLID EDGE ACADEMIC COPY





	NAME
DRAWN BY	LORENZO LACOVIG
SUPERVISOR	Prof. B. W. Skews
ENG APPR	
DATE	03/12/2007

ALL DIMENSIONS ARE IN MILLIMETERS.
TOLERANCES UNLESS OTHERWISE STATED
± 0..2MM OR TO STANDARDS DICTATED BY
MATERIALS USED. ANGLES IN DEGREES ± 0.5 °

UNIVERSITY OF THE WITWATERSRAND

SCHOOL OF MECHANICAL, AERONAUTICAL AND INDUSTRIAL ENGINEERING

TITLE V-Groove Wheel (mild steel)

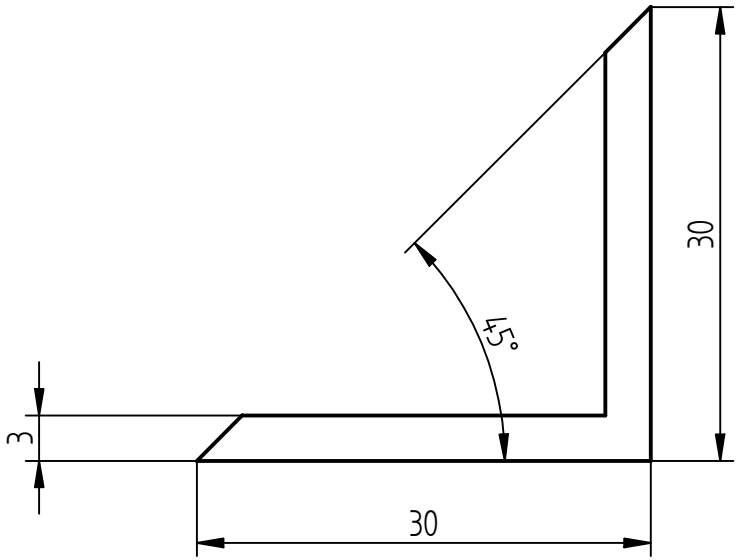
QUANTITY: 4

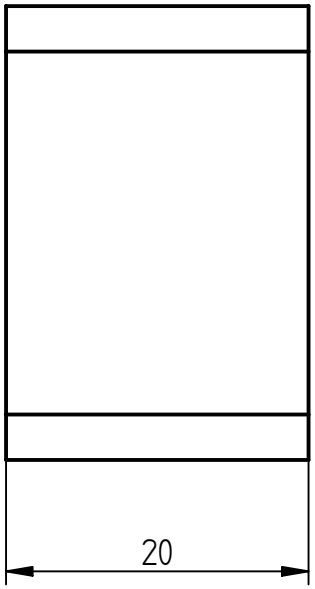
REV

SCALE: 1 : 1

WEIGHT:

SOLID EDGE ACADEMIC COPY





	NAME
DRAWN BY	Andre Cachucho (0501252N)
SUPERVISOR	Prof. B. W. Skews
ENG APPR	
DATE	07/10/2009

ALL DIMENSIONS ARE IN MILLIMETERS.
TOLERANCES UNLESS OTHERWISE STATED
± 0..2MM OR TO STANDARDS DICTATED BY
MATERIALS USED. ANGLES IN DEGREES ± 0.5 °

UNIVERSITY OF THE WITWATERSRAND

SCHOOL OF MECHANICAL, AERONAUTICAL AND INDUSTRIAL ENGINEERING

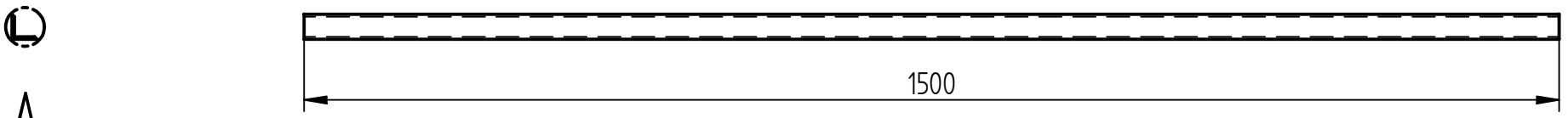
TITLE: V-rail
Std. 30x30x3 Steel rectangular tube

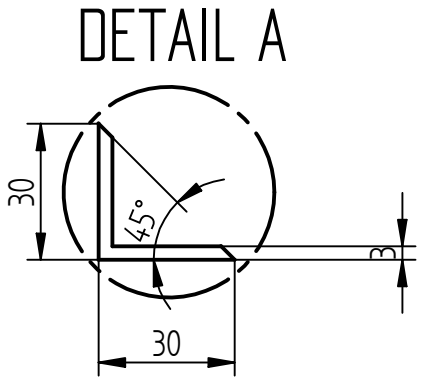
QUANTITY: 2

REV

SCALE: 1 : 7.69 | WEIGHT: | 1 of

SOLID EDGE ACADEMIC COPY





	NAME
DRAWN BY	Andre Cachucho (0501252N)
SUPERVISOR	Prof. B. W. Skews
ENG APPR	
DATE	07/10/2009

ALL DIMENSIONS ARE IN MILLIMETERS.
TOLERANCES UNLESS OTHERWISE STATED
± 0..2MM OR TO STANDARDS DICTATED BY
MATERIALS USED. ANGLES IN DEGREES ± 0.5 °

UNIVERSITY OF THE WITWATERSRAND
SCHOOL OF MECHANICAL, AERONAUTICAL AND INDUSTRIAL ENGINEERING

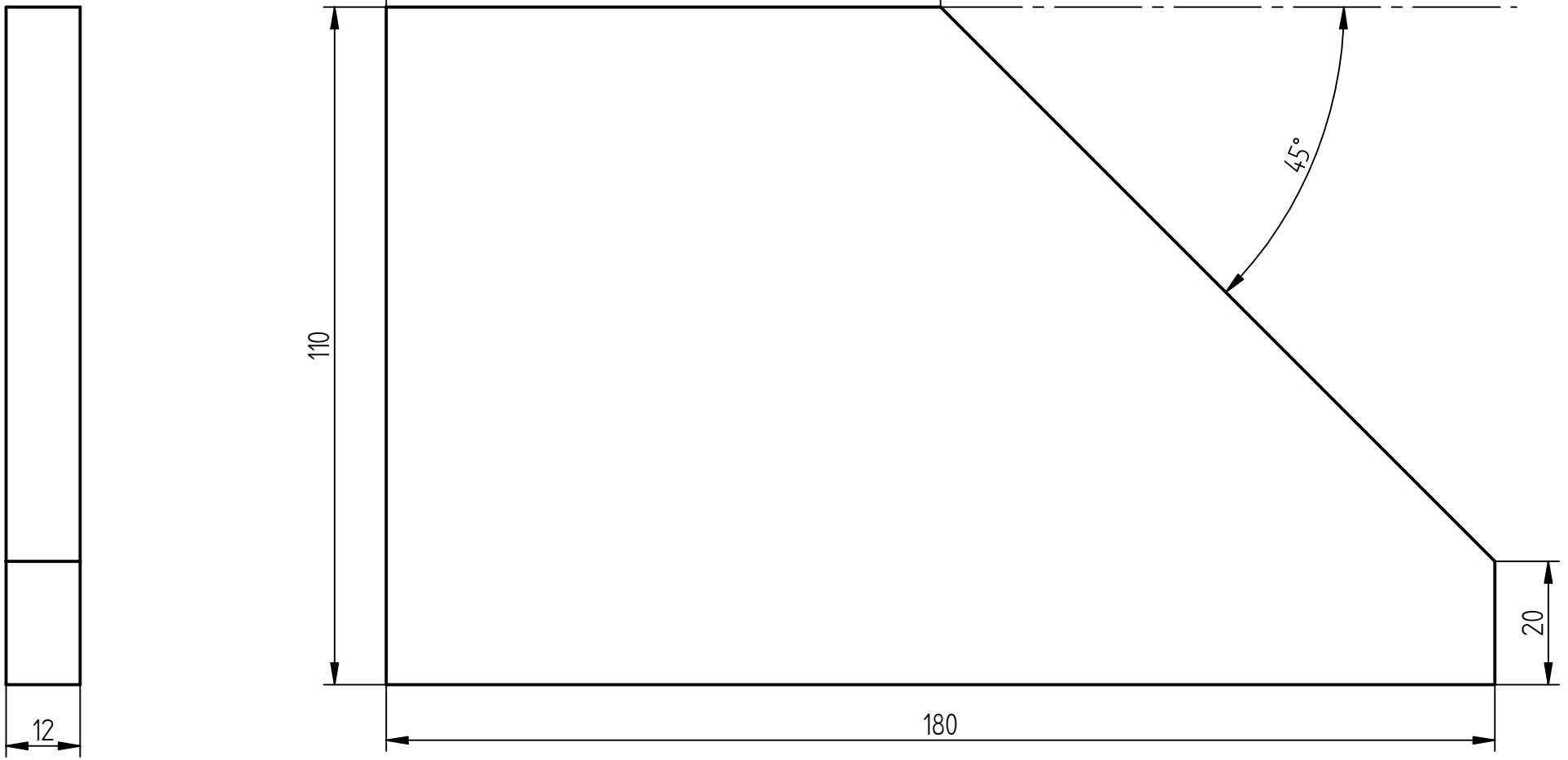
TITLE: V-rail
Std. 30x30x3 Steel rectangular tube

QUANTITY: 2

REV

SCALE: 1 : 7.69 | WEIGHT: | 1 of

SOLID EDGE ACADEMIC COPY



	NAME
DRAWN BY	LORENZO LACOVIG
SUPERVISOR	Prof. B. W. Skews
ENG APPR	
DATE	09/06/2007

ALL DIMENSIONS ARE IN MILLIMETERS.
TOLERANCES UNLESS OTHERWISE STATED
± 0..2MM OR TO STANDARDS DICTATED BY
MATERIALS USED. ANGLES IN DEGREES ± 0.5 °

UNIVERSITY OF THE WITWATERSRAND

SCHOOL OF MECHANICAL, AERONAUTICAL AND INDUSTRIAL ENGINEERING

TITLE Castor Support Angle
(pricker foot) [mild steel plate]

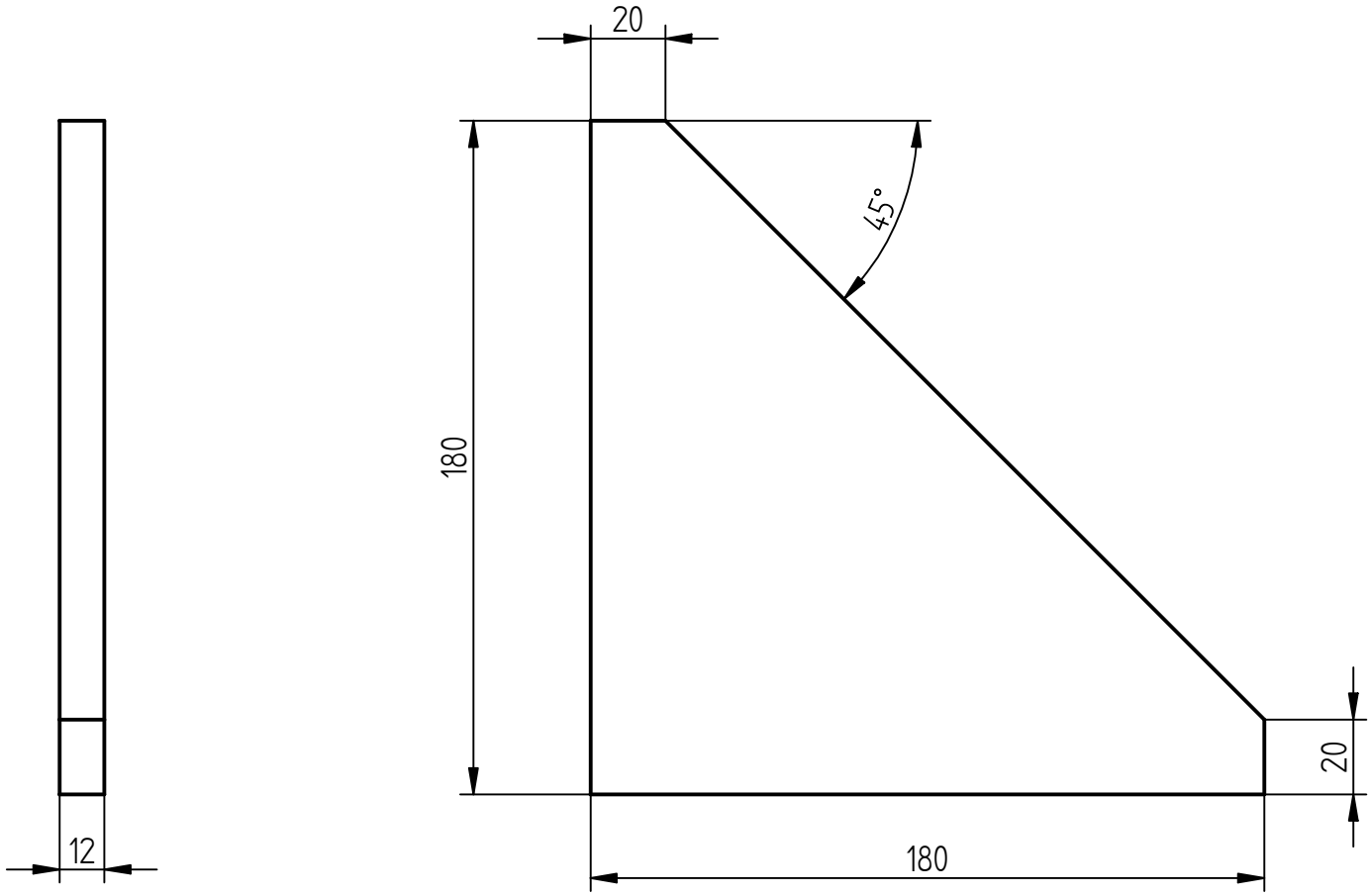
QUANTITY: 1

REV

SCALE: 1 : 1

WEIGHT:

SOLID EDGE ACADEMIC COPY



	NAME
DRAWN BY	LORENZO LACOVIG
SUPERVISOR	Prof. B. W. Skews
ENG APPR	
DATE	09/06/2007

ALL DIMENSIONS ARE IN MILLIMETERS.
TOLERANCES UNLESS OTHERWISE STATED
± 0..2MM OR TO STANDARDS DICTATED BY
MATERIALS USED. ANGLES IN DEGREES ± 0.5 °

UNIVERSITY OF THE WITWATERSRAND

SCHOOL OF MECHANICAL, AERONAUTICAL AND INDUSTRIAL ENGINEERING

TITLE Castor Support Angle
[mild steel plate]

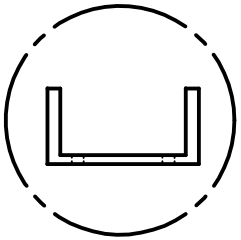
QUANTITY: 3

REV

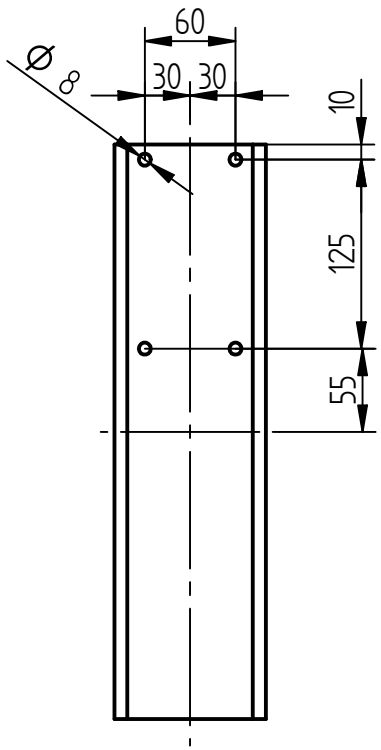
SCALE: 1 : 2

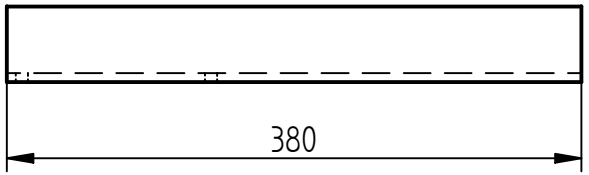
WEIGHT:

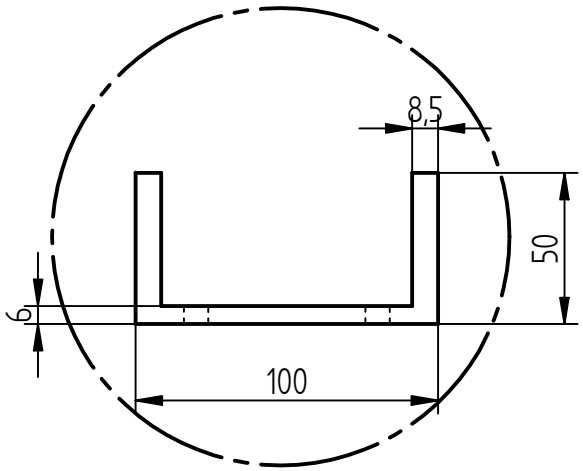
SOLID EDGE ACADEMIC COPY



A







DETAIL A

	NAME
DRAWN BY	LORENZO LACOVIG
SUPERVISOR	Prof. B. W. Skews
ENG APPR	
DATE	02/05/2007

UNIVERSITY OF THE WITWATERSRAND

SCHOOL OF MECHANICAL, AERONAUTICAL AND INDUSTRIAL ENGINEERING

TITLE Castor Support Arm
std 100 x 50 steel channel

ALL DIMENSIONS ARE IN MILLIMETERS.
TOLERANCES UNLESS OTHERWISE STATED
± 0..2MM OR TO STANDARDS DICTATED BY
MATERIALS USED. ANGLES IN DEGREES ± 0.5 °

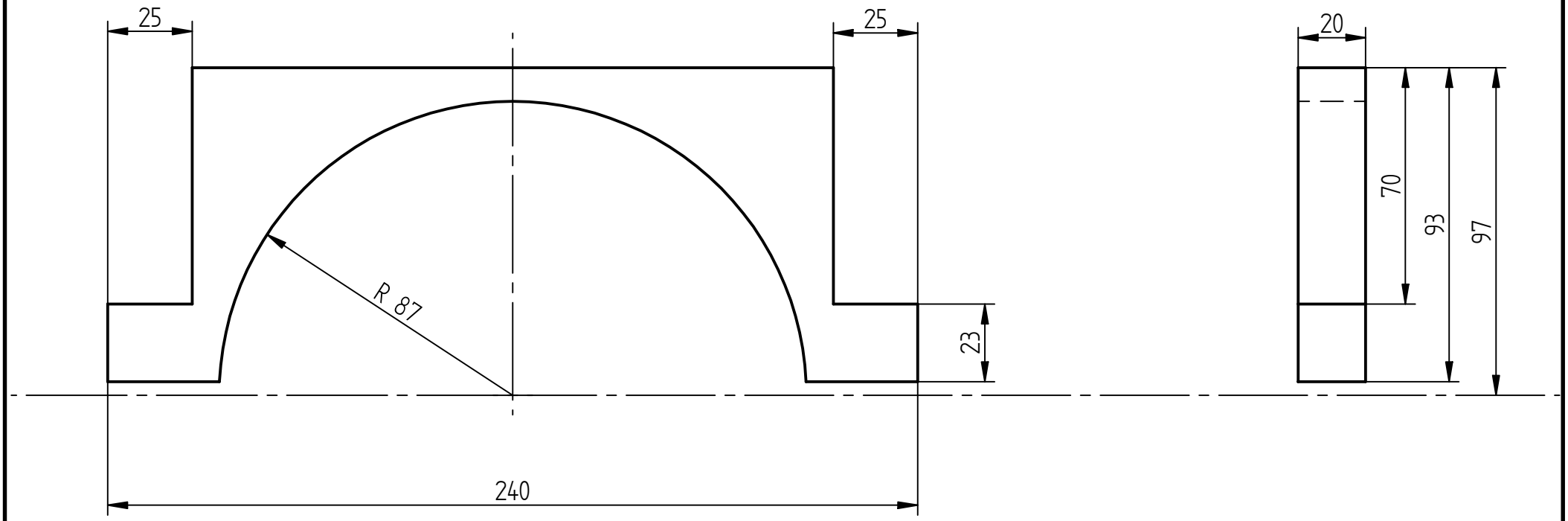
QUANTITY: 4

REV

SCALE: 1 : 5

WEIGHT:

SOLID EDGE ACADEMIC COPY



The following parts will be cut by water jet.

	NAME
DRAWN BY	Andre Cachucho (0501252N)
SUPERVISOR	Prof. B. W. Skews
ENG APPR	
DATE	25/03/2010

ALL DIMENSIONS ARE IN MILLIMETERS.
TOLERANCES UNLESS OTHERWISE STATED
± 0..2MM OR TO STANDARDS DICTATED BY
MATERIALS USED. ANGLES IN DEGREES ± 0.5 °

UNIVERSITY OF THE WITWATERSRAND

SCHOOL OF MECHANICAL, AERONAUTICAL AND INDUSTRIAL ENGINEERING

TITLE: Wheel frame support

QUANTITY: 4

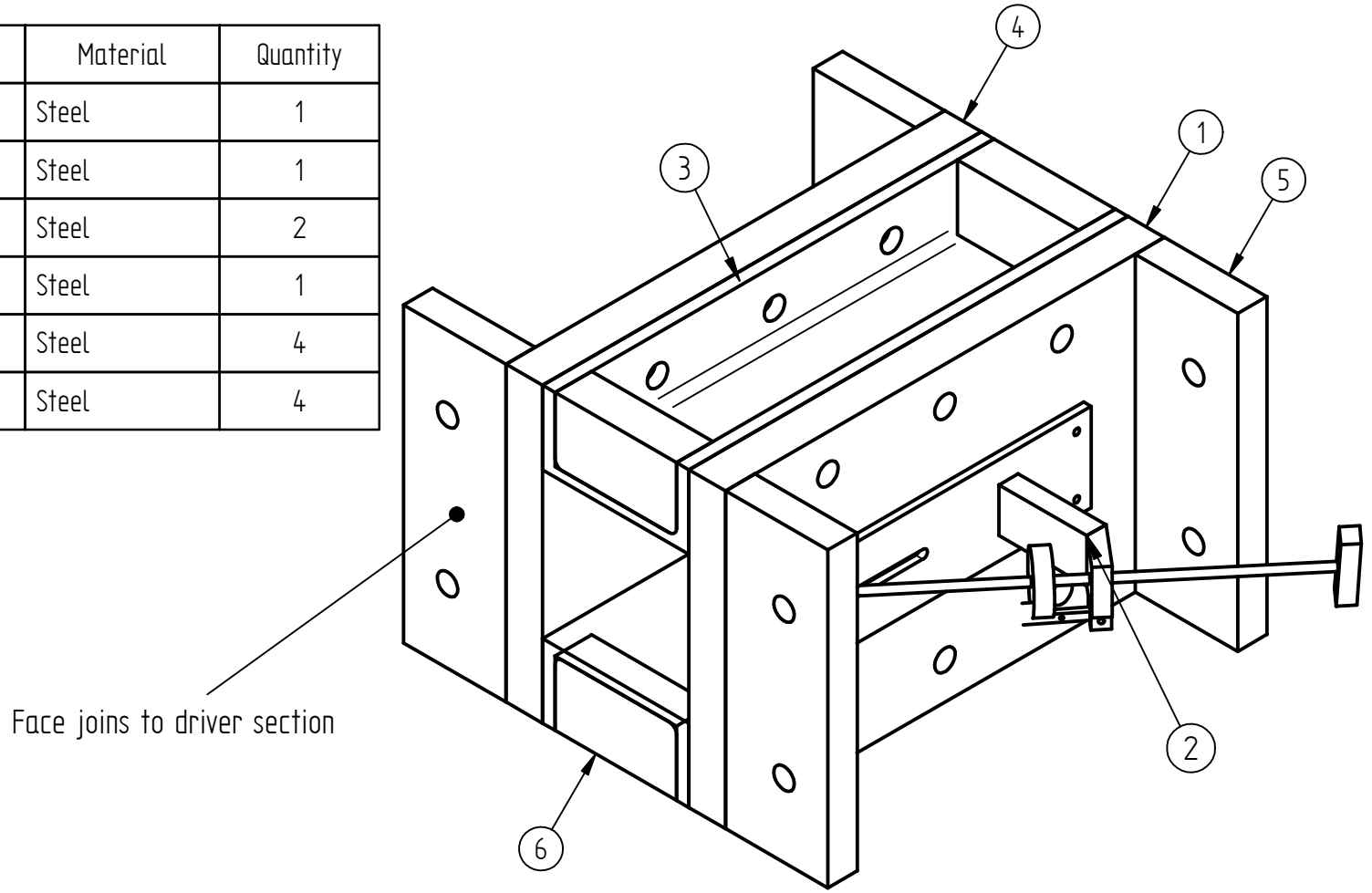
REV

SCALE: 1 : 0.5 | WEIGHT: | 1 of

SOLID EDGE ACADEMIC COPY

D.3 Plunger section

Item Number	Title	Material	Quantity
1	Plunger pricker wall	Steel	1
2	Pricker assembly	Steel	1
3	Plunger U-channel	Steel	2
4	Plunger side wall	Steel	1
5	Driver flanges	Steel	4
6	U-channel inserts	Steel	4



	NAME
DRAWN BY	Andre Cachucho (0501252N)
SUPERVISOR	Prof. B. W. Skews
ENG APPR	
DATE	07/10/2009

ALL DIMENSIONS ARE IN MILLIMETERS.
TOLERANCES UNLESS OTHERWISE STATED
± 0..2MM OR TO STANDARDS DICTATED BY
MATERIALS USED. ANGLES IN DEGREES ± 0.5 °

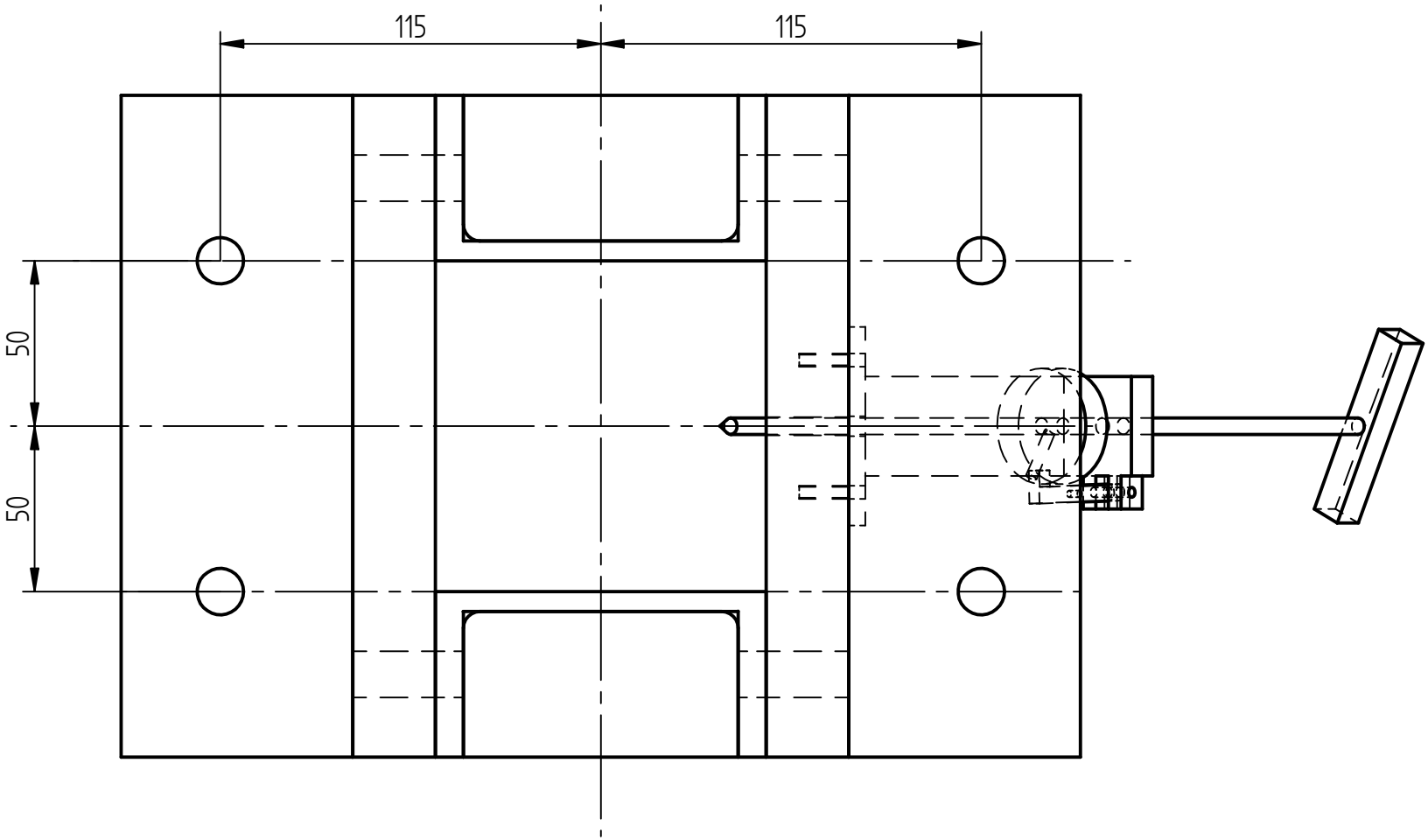
UNIVERSITY OF THE WITWATERSRAND
SCHOOL OF MECHANICAL, AERONAUTICAL AND INDUSTRIAL ENGINEERING

TITLE: Plunger section assembly

QUANTITY: 1 | REV

SCALE: 1 : 3.33 | WEIGHT: | 1 of

SOLID EDGE ACADEMIC COPY



All holes on this face are M14

Face to join with driver section

	NAME
DRAWN BY	Andre Cachucho (0501252N)
SUPERVISOR	Prof. B. W. Skews
ENG APPR	
DATE	07/10/2009

ALL DIMENSIONS ARE IN MILLIMETERS. TOLERANCES UNLESS OTHERWISE STATED ± 0..2MM OR TO STANDARDS DICTATED BY MATERIALS USED. ANGLES IN DEGREES ± 0.5 °

UNIVERSITY OF THE WITWATERSRAND

SCHOOL OF MECHANICAL, AERONAUTICAL AND INDUSTRIAL ENGINEERING

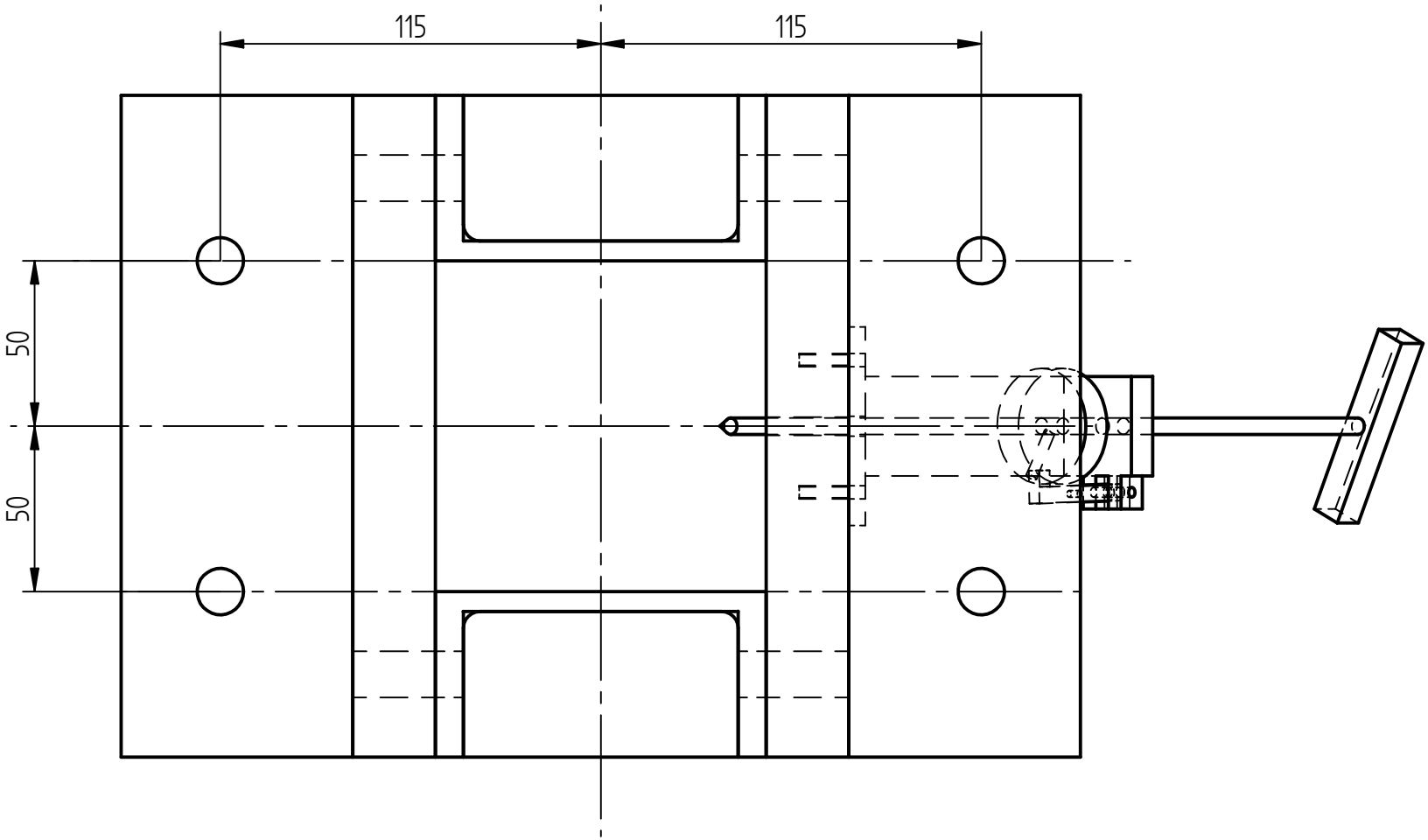
TITLE: Plunger assembly – driver view

QUANTITY: 1

REV

SCALE: 1 : 2 | WEIGHT: | 1 of

SOLID EDGE ACADEMIC COPY



All holes on this face are M14

Face to join with driver section

	NAME
DRAWN BY	Andre Cachucho (0501252N)
SUPERVISOR	Prof. B. W. Skews
ENG APPR	
DATE	07/10/2009

ALL DIMENSIONS ARE IN MILLIMETERS. TOLERANCES UNLESS OTHERWISE STATED ± 0..2MM OR TO STANDARDS DICTATED BY MATERIALS USED. ANGLES IN DEGREES ± 0.5 °

UNIVERSITY OF THE WITWATERSRAND

SCHOOL OF MECHANICAL, AERONAUTICAL AND INDUSTRIAL ENGINEERING

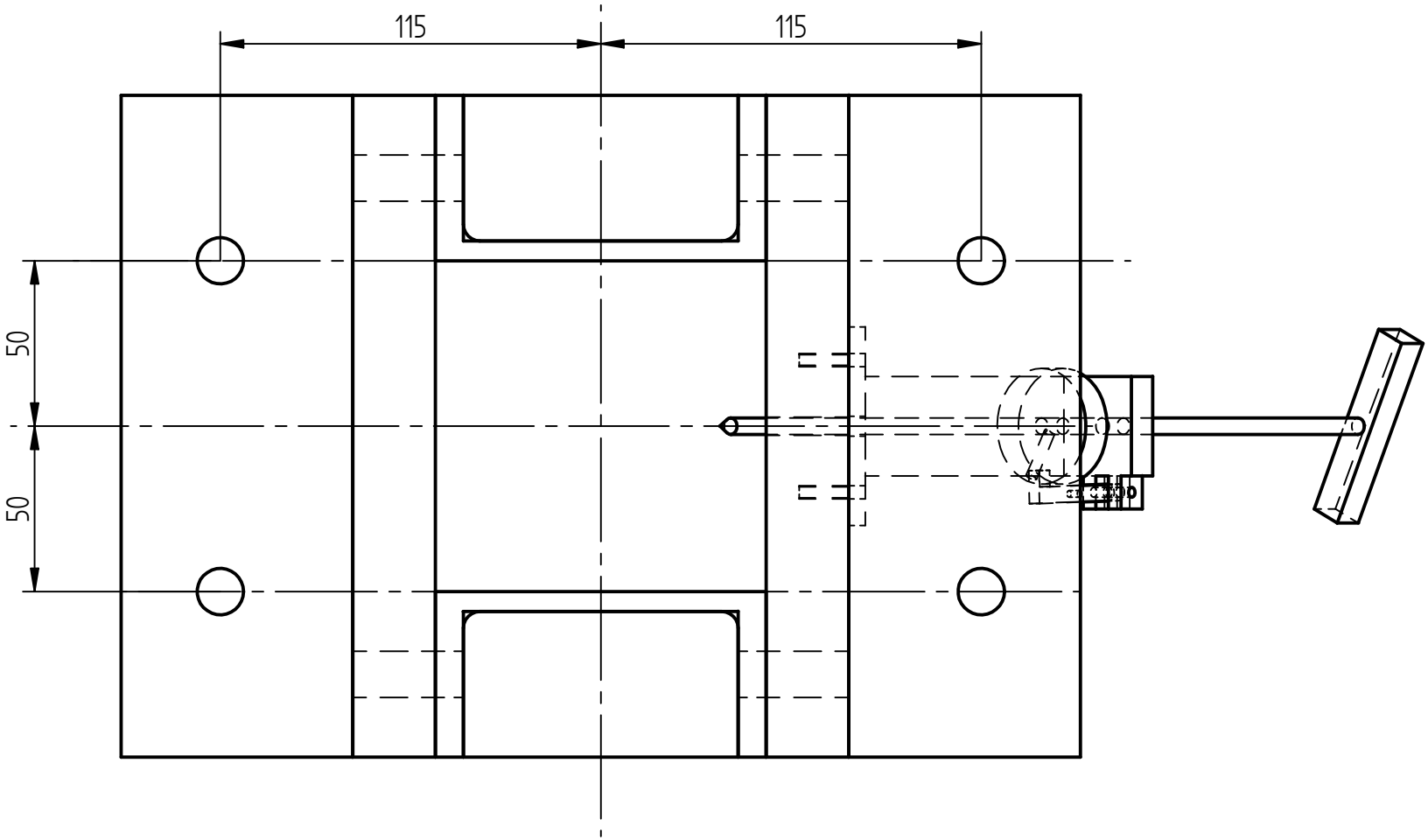
TITLE: Plunger assembly – driver view

QUANTITY: 1

REV

SCALE: 1 : 2 | WEIGHT: | 1 of

SOLID EDGE ACADEMIC COPY



All holes on this face are M14

Face to join with driver section

	NAME
DRAWN BY	Andre Cachucho (0501252N)
SUPERVISOR	Prof. B. W. Skews
ENG APPR	
DATE	07/10/2009

ALL DIMENSIONS ARE IN MILLIMETERS. TOLERANCES UNLESS OTHERWISE STATED ± 0..2MM OR TO STANDARDS DICTATED BY MATERIALS USED. ANGLES IN DEGREES ± 0.5 °

UNIVERSITY OF THE WITWATERSRAND

SCHOOL OF MECHANICAL, AERONAUTICAL AND INDUSTRIAL ENGINEERING

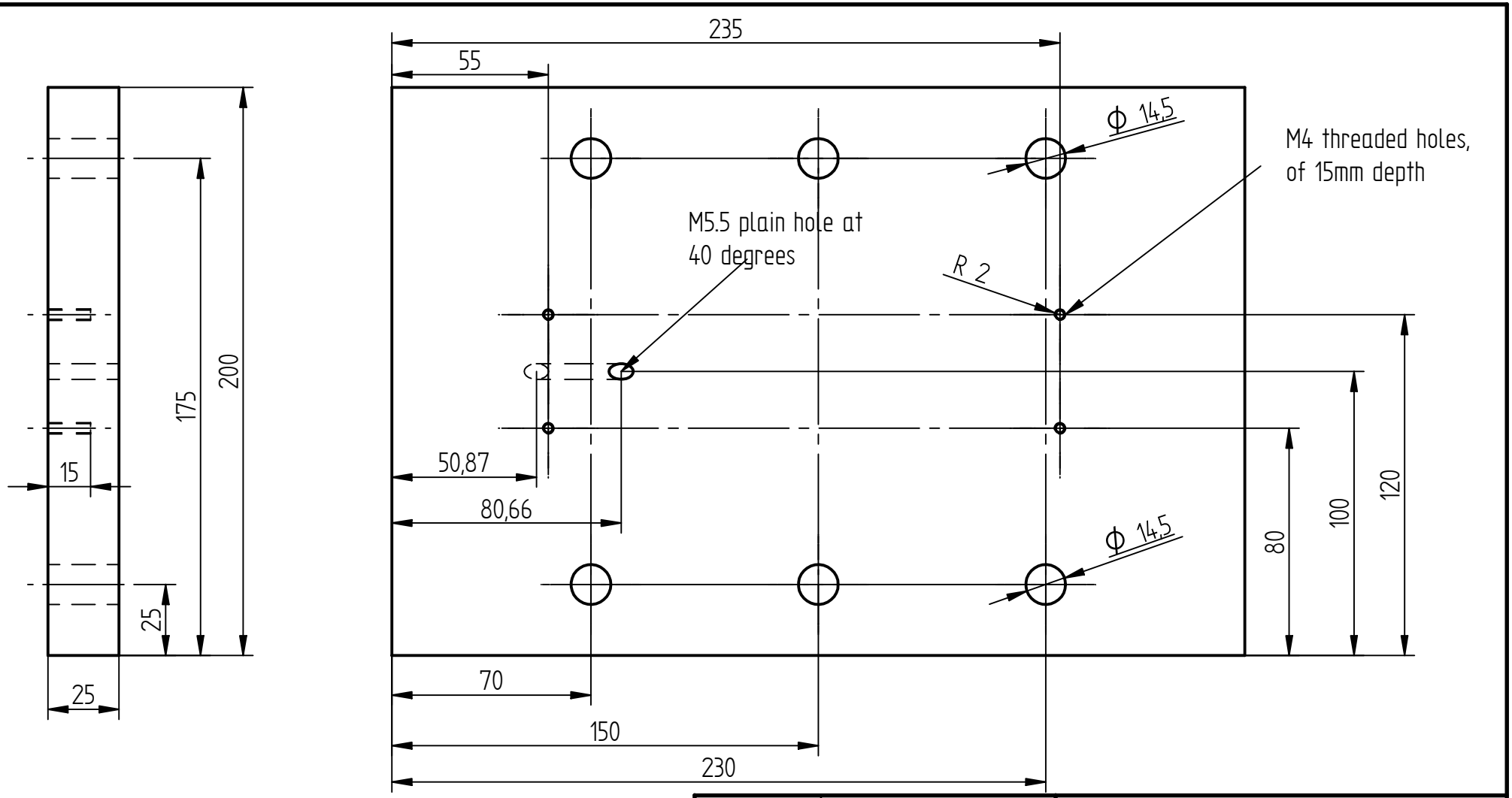
TITLE: Plunger assembly – driver view

QUANTITY: 1

REV

SCALE: 1 : 2 | WEIGHT: | 1 of

SOLID EDGE ACADEMIC COPY



	NAME
DRAWN BY	Andre Cachucho (0501252N)
SUPERVISOR	Prof. B. W. Skews
ENG APPR	
DATE	07/10/2009

ALL DIMENSIONS ARE IN MILLIMETERS.
TOLERANCES UNLESS OTHERWISE STATED
± 0..2MM OR TO STANDARDS DICTATED BY
MATERIALS USED. ANGLES IN DEGREES ± 0.5 °

UNIVERSITY OF THE WITWATERSRAND

SCHOOL OF MECHANICAL, AERONAUTICAL AND INDUSTRIAL ENGINEERING

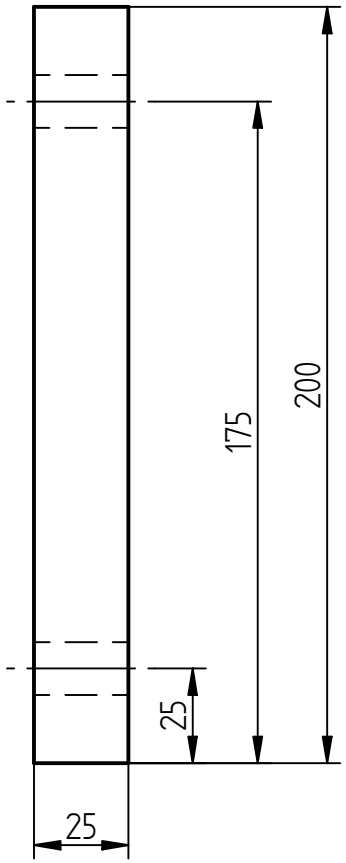
TITLE: Plunger pricker wall section

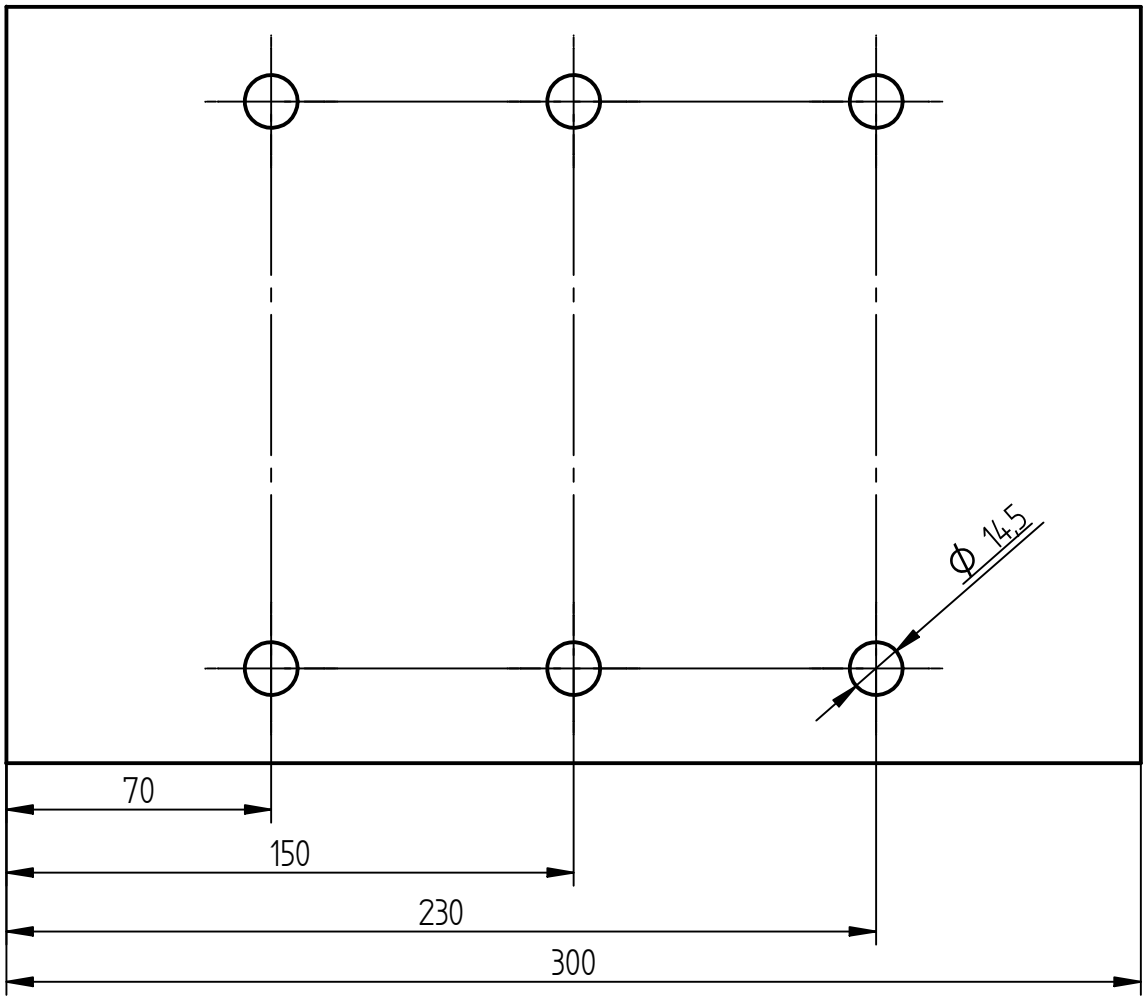
QUANTITY: 1

REV

SCALE: 1 : 2 | WEIGHT: | 1 of

SOLID EDGE ACADEMIC COPY





All holes on this face are M14.5

	NAME
DRAWN BY	Andre Cachucho (0501252N)
SUPERVISOR	Prof. B. W. Skews
ENG APPR	
DATE	07/10/2009

ALL DIMENSIONS ARE IN MILLIMETERS.
TOLERANCES UNLESS OTHERWISE STATED
± 0..2MM OR TO STANDARDS DICTATED BY
MATERIALS USED. ANGLES IN DEGREES ± 0.5 °

UNIVERSITY OF THE WITWATERSRAND

SCHOOL OF MECHANICAL, AERONAUTICAL AND INDUSTRIAL ENGINEERING

TITLE: Plunger pricker wall section

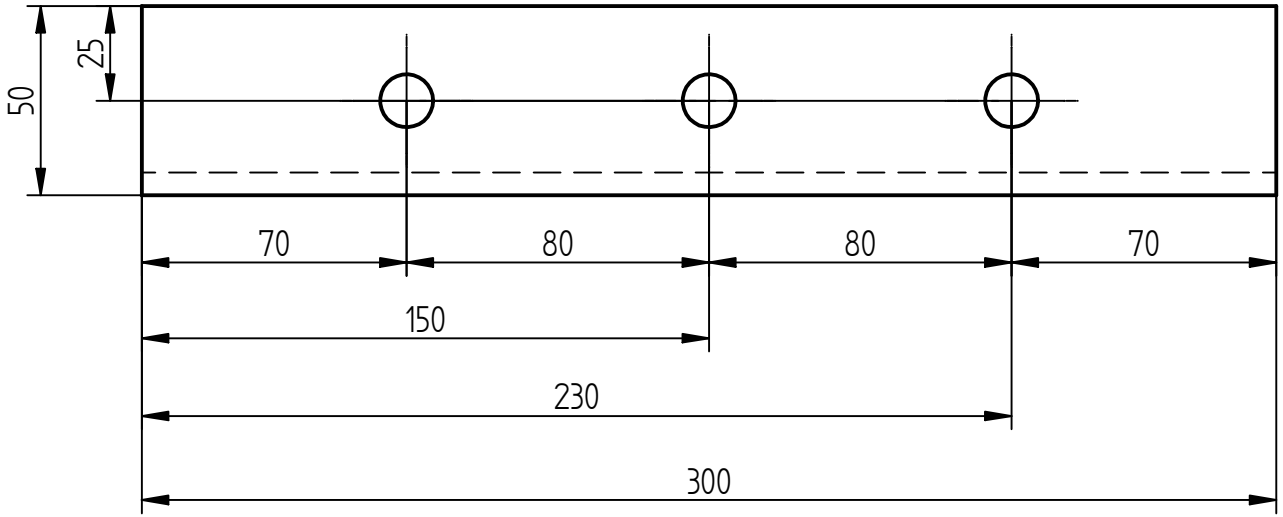
QUANTITY: 1

REV

SCALE: 1 : 2 | WEIGHT: | 1 of

SOLID EDGE ACADEMIC COPY

All holes on this face are M14.5



	NAME
DRAWN BY	Andre Cachucho (0501252N)
SUPERVISOR	Prof. B. W. Skews
ENG APPR	
DATE	07/10/2009

ALL DIMENSIONS ARE IN MILLIMETERS.
TOLERANCES UNLESS OTHERWISE STATED
± 0..2MM OR TO STANDARDS DICTATED BY
MATERIALS USED. ANGLES IN DEGREES ± 0.5 °

UNIVERSITY OF THE WITWATERSRAND
SCHOOL OF MECHANICAL, AERONAUTICAL AND INDUSTRIAL ENGINEERING

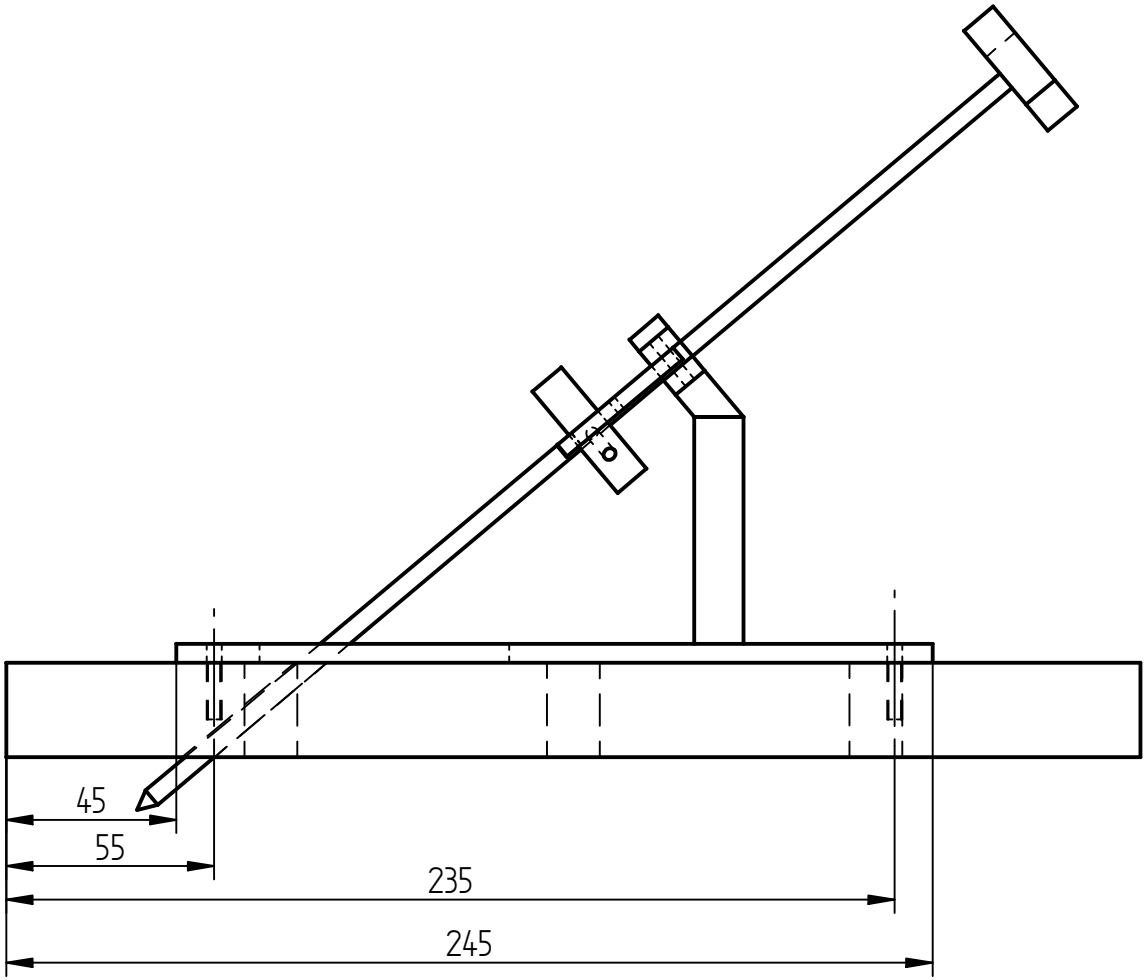
TITLE: Plunger U-channel
Std Steel 100x50 U-channel

QUANTITY: 1

REV

SCALE: 1 : 2 | WEIGHT: | 1 of

SOLID EDGE ACADEMIC COPY



	NAME
DRAWN BY	Andre Cachucho
SUPERVISOR	Prof. B. W. Skews
ENG APPR	
DATE	14/09/2000

ALL DIMENSIONS ARE IN MILLIMETERS.
TOLERANCES UNLESS OTHERWISE STATED
± 0..2MM OR TO STANDARDS DICTATED BY
MATERIALS USED. ANGLES IN DEGREES ± 0.5 °

UNIVERSITY OF THE WITWATERSRAND

SCHOOL OF MECHANICAL, AERONAUTICAL AND INDUSTRIAL ENGINEERING

TITLE Pricker Slider assembly

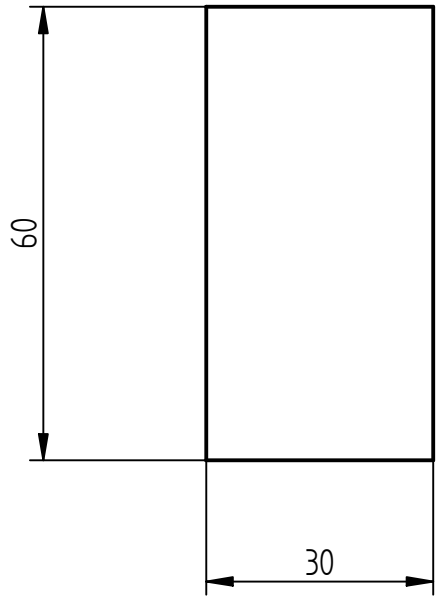
QUANTITY: 1

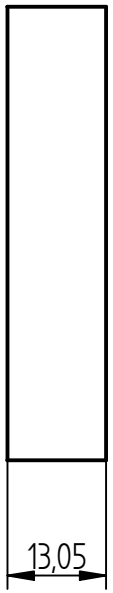
REV

SCALE: 1 : 10

WEIGHT:

SOLID EDGE ACADEMIC COPY





	NAME
DRAWN BY	LORENZO LACOVIG
SUPERVISOR	Prof. B. W. Skews
ENG APPR	
DATE	05/06/2007

ALL DIMENSIONS ARE IN MILLIMETERS.
TOLERANCES UNLESS OTHERWISE STATED
± 0..2MM OR TO STANDARDS DICTATED BY
MATERIALS USED. ANGLES IN DEGREES ± 0.5 °

UNIVERSITY OF THE WITWATERSRAND

SCHOOL OF MECHANICAL, AERONAUTICAL AND INDUSTRIAL ENGINEERING

TITLE Pricker Arm (Bottom)

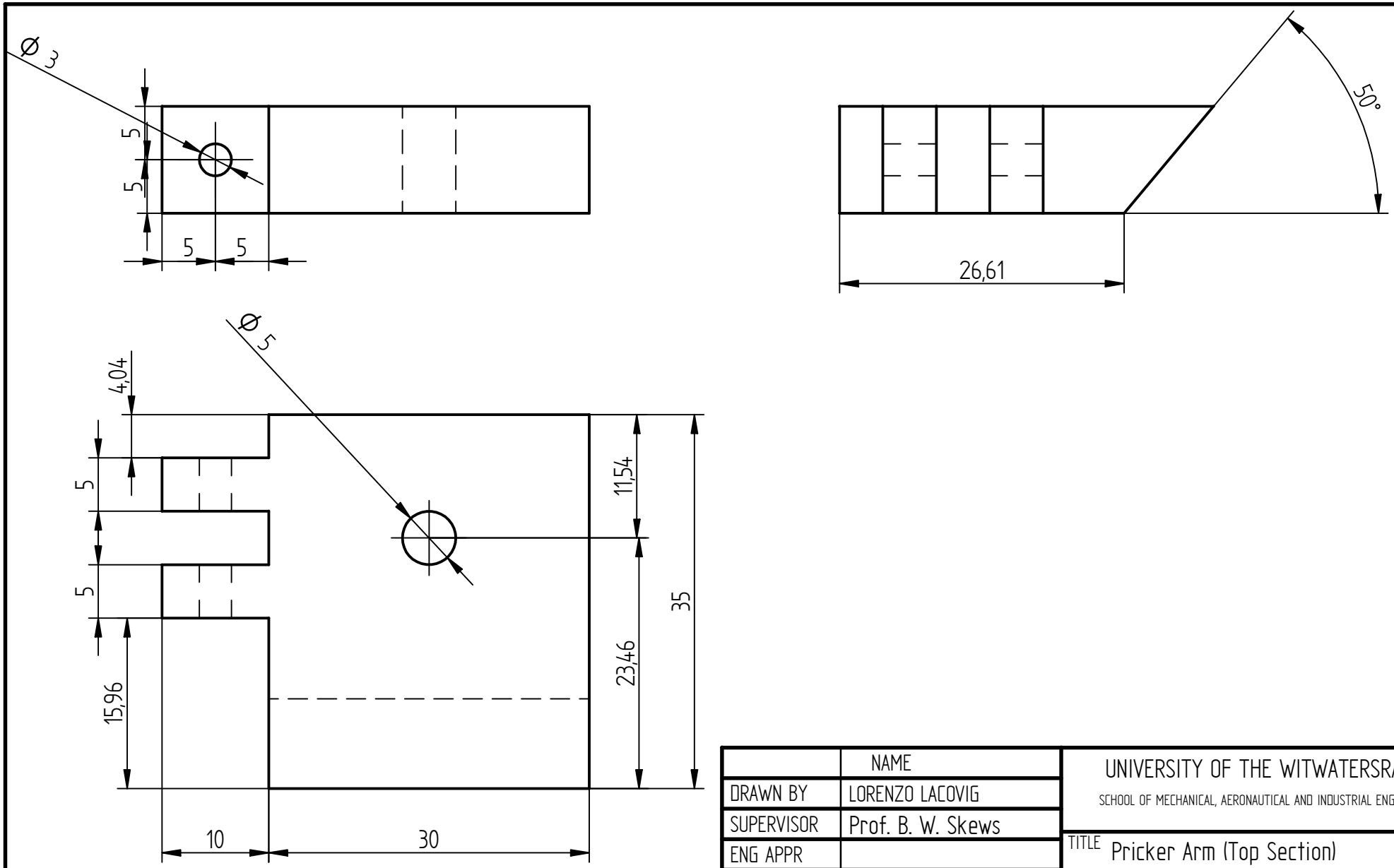
QUANTITY: 1

REV

SCALE: 1 : 1

WEIGHT:

SOLID EDGE ACADEMIC COPY



	NAME
DRAWN BY	LORENZO LACOVIG
SUPERVISOR	Prof. B. W. Skews
ENG APPR	
DATE	13/06/2007

ALL DIMENSIONS ARE IN MILLIMETERS.
TOLERANCES UNLESS OTHERWISE STATED
± 0..2MM OR TO STANDARDS DICTATED BY
MATERIALS USED. ANGLES IN DEGREES ± 0.5 °

UNIVERSITY OF THE WITWATERSRAND

SCHOOL OF MECHANICAL, AERONAUTICAL AND INDUSTRIAL ENGINEERING

TITLE Pricker Arm (Top Section)

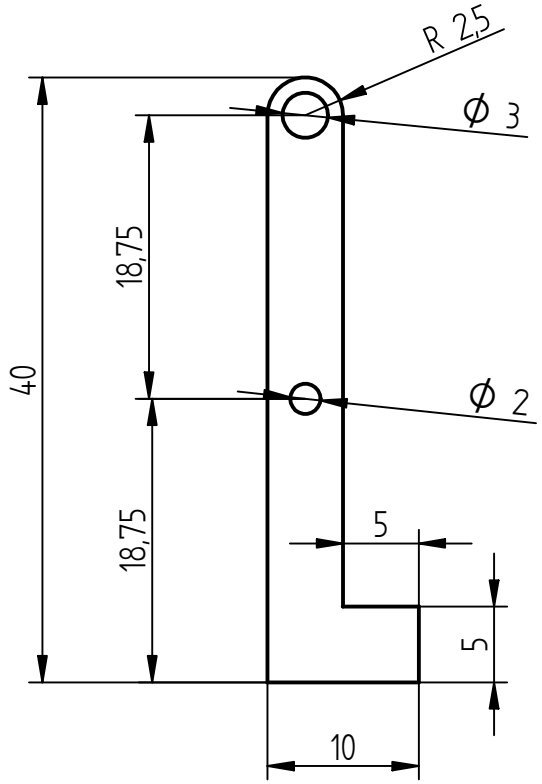
QUANTITY: 1

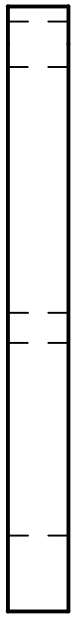
REV

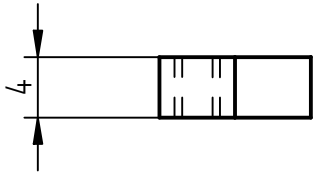
SCALE: 2 : 1

WEIGHT:

SOLID EDGE ACADEMIC COPY







	NAME
DRAWN BY	LORENZO LACOVIG
SUPERVISOR	Prof. B. W. Skews
ENG APPR	
DATE	13/06/2007

ALL DIMENSIONS ARE IN MILLIMETERS.
TOLERANCES UNLESS OTHERWISE STATED
± 0..2MM OR TO STANDARDS DICTATED BY
MATERIALS USED. ANGLES IN DEGREES ± 0.5 °

UNIVERSITY OF THE WITWATERSRAND

SCHOOL OF MECHANICAL, AERONAUTICAL AND INDUSTRIAL ENGINEERING

TITLE Pricker Lever

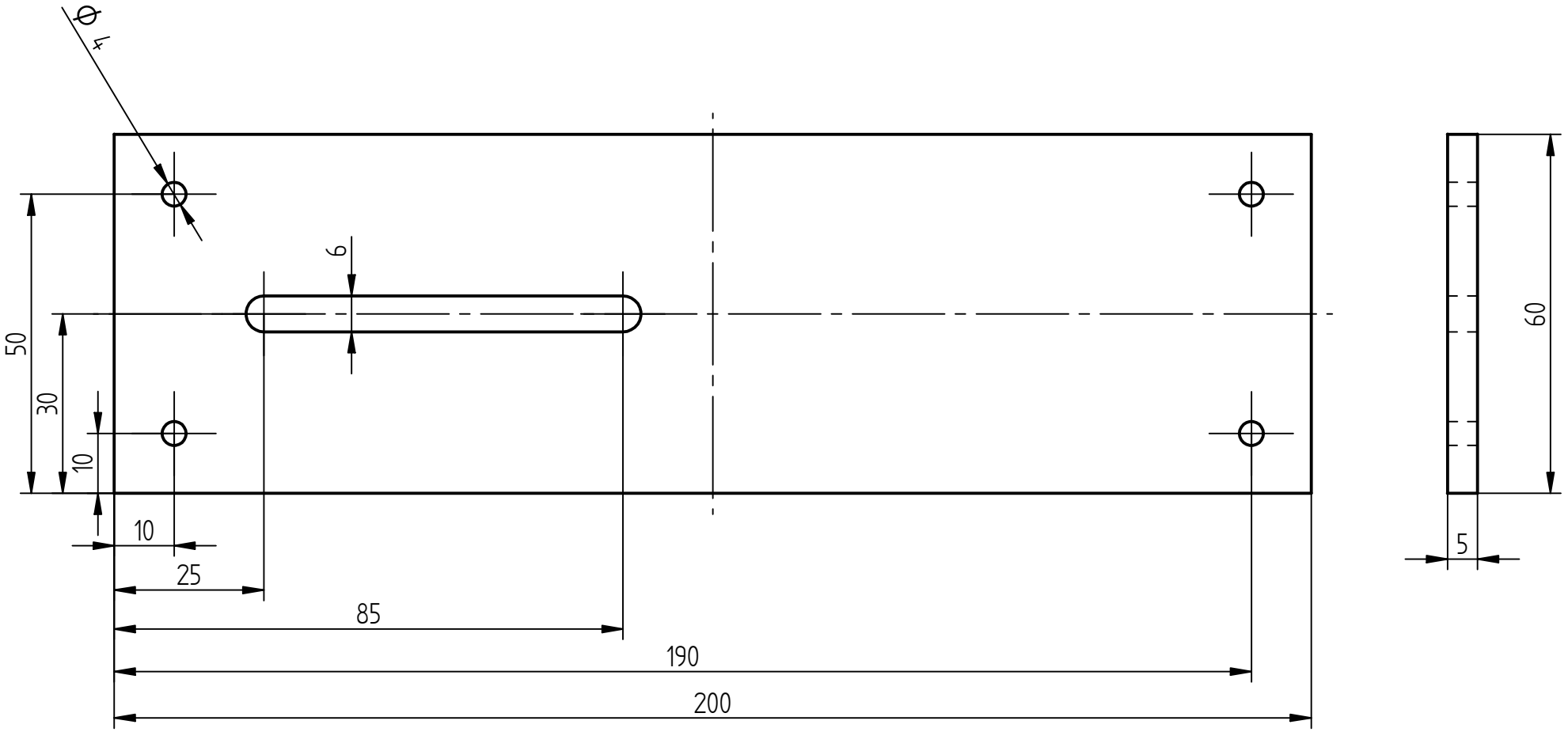
QUANTITY: 1

REV

SCALE: 2 : 1

WEIGHT:

SOLID EDGE ACADEMIC COPY



	NAME
DRAWN BY	LORENZO LACOVIG
SUPERVISOR	Prof. B. W. Skews
ENG APPR	
DATE	05/11/2007

ALL DIMENSIONS ARE IN MILLIMETERS.
TOLERANCES UNLESS OTHERWISE STATED
± 0..2MM OR TO STANDARDS DICTATED BY
MATERIALS USED. ANGLES IN DEGREES ± 0.5 °

UNIVERSITY OF THE WITWATERSRAND

SCHOOL OF MECHANICAL, AERONAUTICAL AND INDUSTRIAL ENGINEERING

TITLE Pricker Plate

QUANTITY: 1

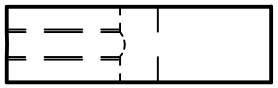
REV

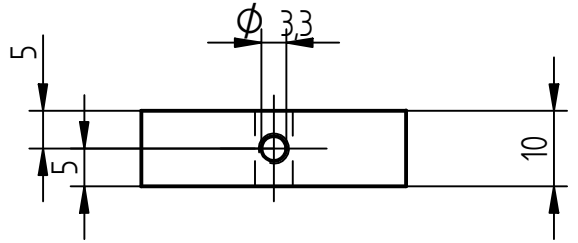
SCALE: 1 : 1

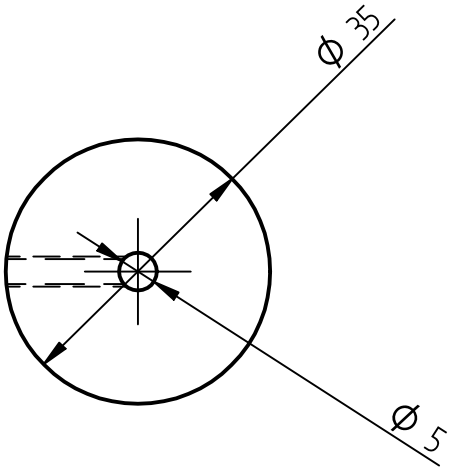
WEIGHT:

SOLID EDGE ACADEMIC COPY

M4 Threaded Hole







	NAME
DRAWN BY	LORENZO LACOVIG
SUPERVISOR	Prof. B. W. Skews
ENG APPR	
DATE	05/11/2007

ALL DIMENSIONS ARE IN MILLIMETERS.
TOLERANCES UNLESS OTHERWISE STATED
± 0..2MM OR TO STANDARDS DICTATED BY
MATERIALS USED. ANGLES IN DEGREES ± 0.5 °

UNIVERSITY OF THE WITWATERSRAND

SCHOOL OF MECHANICAL, AERONAUTICAL AND INDUSTRIAL ENGINEERING

TITLE Pricker Stopper

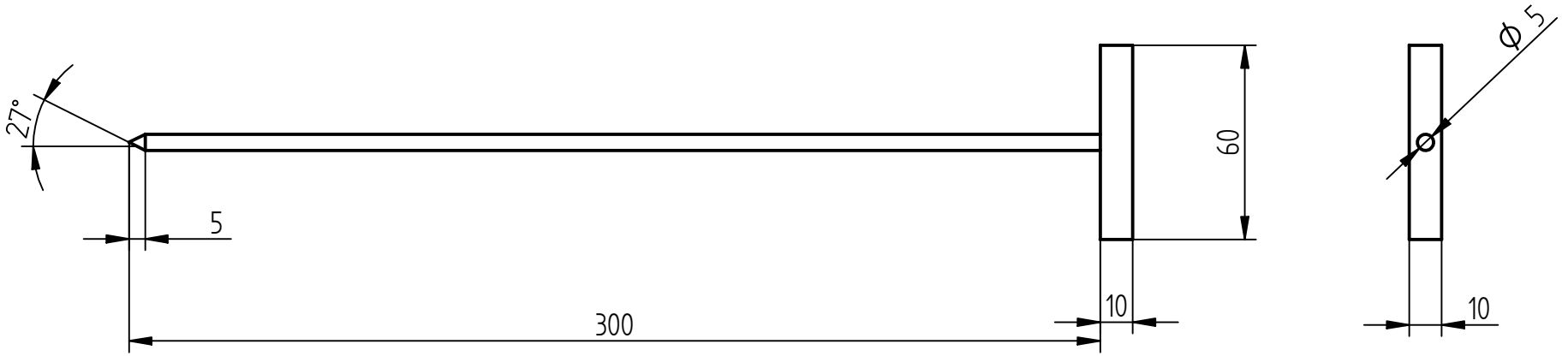
QUANTITY: 1

REV

SCALE: 1 : 1

WEIGHT:

SOLID EDGE ACADEMIC COPY



	NAME
DRAWN BY	LORENZO LACOVIG
SUPERVISOR	Prof. B. W. Skews
ENG APPR	
DATE	13/06/2007

ALL DIMENSIONS ARE IN MILLIMETERS.
TOLERANCES UNLESS OTHERWISE STATED
± 0..2MM OR TO STANDARDS DICTATED BY
MATERIALS USED. ANGLES IN DEGREES ± 0.5 °

UNIVERSITY OF THE WITWATERSRAND

SCHOOL OF MECHANICAL, AERONAUTICAL AND INDUSTRIAL ENGINEERING

TITLE Pricker

QUANTITY: 1

REV

SCALE: 1 : 2

WEIGHT:

SOLID EDGE ACADEMIC COPY